MATERIALS RESEARCH SOCIETY
SYMPOSIUM PROCEEDINGS VOLUME 758

Rapid Prototyping Technologies

Symposium held December 3–5, 2002, Boston, Massachusetts, U.S.A.

EDITORS:

Alberto Piqué
Naval Research Laboratory
Washington, D.C., U.S.A.

Andrew S. Holmes
Imperial College London
London, United Kingdom

Duane B. Dimos
Sandia National Laboratories
Albuquerque, New Mexico, U.S.A.

Materials Research Society
Warrendale, Pennsylvania

This material is based upon work supported by the National Science Foundation under Grant Number DMI-0228896. Any opinions, findings, and conclusions or recommendations expressed in this material are those of the author(s) and do not necessarily reflect the views of the National Science Foundation.

This work was supported in part by the Office of Naval Research under Grant Number N00014-02-1-0820. The United States Government has a royalty-free license throughout the world in all copyrightable material contained herein.

Single article reprints from this publication are available through
University Microfilms Inc., 300 North Zeeb Road, Ann Arbor, Michigan 48106

CODEN: MRSPDH

Published by:

Materials Research Society
506 Keystone Drive
Warrendale, PA 15086
Telephone (724) 779-3003
Fax (724) 779-8313
Web site: http://www.mrs.org/

Manufactured in the United States of America

CONTENTS

*Invited Paper

DIRECT-WRITE OF MICROELECTRONICS

NANOSCALE RAPID PROTOTYPING

*Invited Paper

TISSUE ENGINEERING AND BIOMEDICAL APPLICATIONS

*Invited Paper

PREFACE

Symposium LL, "Rapid Prototyping Technologies," was held December 3–5 at the 2002 MRS Fall Meeting in Boston, Massachusetts. The symposium highlighted a broad range of international research activities in the areas of direct-write (DW), solid freeform (SFF) and microstereolithography (MSL). Five sessions were held, covering layered manufacturing and laser sintering, solution and spray processing, direct-write of microelectronics, nanoscale rapid prototyping, and biological tissue engineering and biomedical applications. In total thirty-five papers were presented, with a good balance achieved between invited reviews and presentations of the latest research results.

This was the third MRS symposium on rapid prototyping (RP) and related technologies, following successful symposia at the Spring 2000 and Fall 2001 Meetings. This year we were able to continue themes developed in the earlier meetings, while also expanding the scope to include new and exciting developments, particularly in the areas of nano-scale patterning and biomedical applications. The standard of presentations was extremely high throughout, and all five sessions were well attended by audiences keen to engage in lively discussion and debate.

This volume contains a selection of twenty-four papers from the symposium. Papers from all sessions are included, with particularly good coverage of the sessions on layer manufacturing, nanoscale RP, and tissue engineering and biomedical applications. The volume provides a comprehensive overview of RP technologies, together with an update on the most recent advances in the field. It will be of interest both to the RP community, and also to researchers in other fields who have an interest in the development of new materials and structures that cannot be realized by traditional manufacturing techniques.

We wish to thank the staff of the MRS for their help with the organization and running of the symposium, and for their assistance with the production of this proceedings volume. We gratefully acknowledge the financial support of the Defence Advanced Research Projects Agency, the National Science Foundation, and the Office of Naval Research.

Alberto Piqué
Andrew S. Holmes
Duane B. Dimos

April 2003

MATERIALS RESEARCH SOCIETY SYMPOSIUM PROCEEDINGS

Volume 715— Amorphous and Heterogeneous Silicon-Based Films—2002, J.R. Abelson, J.B. Boyce, J.D. Cohen, H. Matsumura, J. Robertson, 2002, ISBN: 1-55899-651-6
Volume 716— Silicon Materials—Processing, Characterization and Reliability, J. Veteran, D.L. O'Meara, V. Misra, P. Ho, 2002, ISBN: 1-55899-652-4
Volume 717— Silicon Front-End Junction Formation Technologies, D.F. Downey, M.E. Law, A. Claverie, M.J. Rendon, 2002, ISBN: 1-55899-653-2
Volume 718— Perovskite Materials, K. Poeppelmeier, A. Navrotsky, R. Wentzcovitch, 2002, ISBN: 1-55899-654-0
Volume 719— Defect and Impurity Engineered Semiconductors and Devices III, S. Ashok, J. Chevallier, N.M. Johnson, B.L. Sopori, H. Okushi, 2002, ISBN: 1-55899-655-9
Volume 720— Materials Issues for Tunable RF and Microwave Devices III, S.C. Tidrow, J.S. Horwitz, J. Levy, X. Xi, 2002, ISBN: 1-55899-656-7
Volume 721— Magnetic and Electronic Films—Microstructure, Texture and Application to Data Storage, P.W. DeHaven, D.P. Field, S.D. Harkness IV, J.A. Sutliff, J.A. Szpunar, L. Tang, T. Thomson, M.D. Vaudin, 2002, ISBN: 1-55899-657-5
Volume 722— Materials and Devices for Optoelectronics and Microphotonics, R.B. Wehrspohn, S. Noda, C. Soukoulis, R. März, 2002, ISBN: 1-55899-658-3
Volume 723— Molecularly Imprinted Materials—Sensors and Other Devices, K.J. Shea, M.J. Roberts, M. Yan, 2002, ISBN: 1-55899-659-1
Volume 724— Biological and Biomimetic Materials—Properties to Function, J. McKittrick, J. Aizenberg, C. Orme, P. Vekilov, 2002, ISBN: 1-55899-660-5
Volume 725— Organic and Polymeric Materials and Devices—Optical, Electrical and Optoelectronic Properties, G.E. Jabbour, N.S. Sariciftci, S.T. Lee, S. Carter, J. Kido, 2002, ISBN: 1-55899-661-3
Volume 726— Organic/Inorganic Hybrid Materials—2002, R.M. Laine, C. Sanchez, S. Yang, C.J. Brinker, 2002, ISBN: 1-55899-662-1
Volume 727— Nanostructured Interfaces, G. Duscher, J.M. Plitzko, Y. Zhu, H. Ichinose, 2002, ISBN: 1-55899-663-X
Volume 728— Functional Nanostructured Materials through Multiscale Assembly and Novel Patterning Techniques, Steven C. Moss, 2002, ISBN: 1-55899-664-8
Volume 729— BioMEMS and Bionanotechnology, L.P. Lee, J.T. Borenstein, R.P. Manginell, M. Okandan, P.J. Hesketh, 2002, ISBN: 1-55899-665-6
Volume 730— Materials for Energy Storage, Generation and Transport, G. Ceder, S.A. Ringel, R.B. Schwarz, 2002, ISBN: 1-55899-666-4
Volume 731— Modeling and Numerical Simulation of Materials Behavior and Evolution, V. Tikare, E.A. Olevsky, A. Zavaliangos, 2002, ISBN: 1-55899-667-2
Volume 732E—Chemical-Mechanical Planarization, S.V. Babu, R. Singh, N. Hayasaka, M. Oliver, 2002, ISBN: 1-55899-668-0
Volume 733E—Polymer Nanocomposites, S. Nutt, R. Vaia, W. Rodgers, G.L. Hagnauer, G.W. Beall, 2002, ISBN: 1-55899-669-9
Volume 734— Polymer/Metal Interfaces and Defect Mediated Phenomena in Ordered Polymers, E.D. Manias, G.G. Malliaras, 2003, ISBN: 1-55899-671-0
Volume 735— Bioinspired Nanoscale Hybrid Systems, G. Schmid, U. Simon, S.J. Stranick, S.M. Arrivo, S. Hong, 2003, ISBN: 1-55899-672-9
Volume 736— Electronics on Unconventional Substrates—Electrotextiles and Giant-Area Flexible Circuits, M.S. Shur, P. Wilson, D. Urban, 2003, ISBN: 1-55899-673-7
Volume 737— Quantum Confined Semiconductor Nanostructures, J.M. Buriak, D.D.M. Wayner, F. Priolo, B. White, V. Klimov, L. Tsybeskov, 2003, ISBN: 1-55899-674-5
Volume 738— Spatially Resolved Characterization of Local Phenomena in Materials and Nanostructures, D.A. Bonnell, J. Piqueras, A.P. Shreve, F. Zypman, 2003, ISBN: 1-55899-675-3
Volume 739— Three-Dimensional Nanoengineered Assemblies, T.M. Orlando, L. Merhari, K. Ikuta, D.P. Taylor, 2003, ISBN: 1-55899-676-1
Volume 740— Nanomaterials for Structural Applications, C. Berndt, T.E. Fischer, I. Ovid'ko, G. Skandan, T. Tsakalakos, 2003, ISBN: 1-55899-677-X

MATERIALS RESEARCH SOCIETY SYMPOSIUM PROCEEDINGS

Volume 741— Nano- and Microelectromechanical Systems (NEMS and MEMS) and Molecular Machines, A.A. Ayon, T. Buchheit, D.A. LaVan, M. Madou, 2003, ISBN: 1-55899-678-8
Volume 742— Silicon Carbide 2002—Materials, Processing and Devices, S.E. Saddow, D.J. Larkin, N.S. Saks, A. Schoener, 2003, ISBN: 1-55899-679-6
Volume 743— GaN and Related Alloys—2002, E.T. Yu, C.M. Wetzel, J.S. Speck, A. Rizzi, Y. Arakawa, 2003, ISBN: 1-55899-680-X
Volume 744— Progress in Semiconductors II—Electronic and Optoelectronic Applications, B.D. Weaver, M.O. Manasreh, C.C. Jagadish, S. Zollner, 2003, ISBN: 1-55899-681-8
Volume 745— Novel Materials and Processes for Advanced CMOS, M.I. Gardner, J-P. Maria, S. Stemmer, S. De Gendt, 2003, ISBN: 1-55899-682-6
Volume 746— Magnetoelectronics and Magnetic Materials—Novel Phenomena and Advanced Characterization, S. Zhang, W. Kuch, G. Guentherodt, C. Broholm, A. Kent, M.R. Fitzsimmons, I. Schuller, J.B. Kortright, T. Shinjo, Y. Zhu, 2003, ISBN: 1-55899-683-4
Volume 747— Crystalline Oxide-Silicon Heterostructures and Oxide Optoelectronics, D.S. Ginley, S. Guha, S. Carter, S.A. Chambers, R. Droopad, H. Hosono, D.C. Paine, D.G. Schlom, J. Tate, 2003, ISBN: 1-55899-684-2
Volume 748— Ferroelectric Thin Films XI, D. Kaufman, S. Hoffmann-Eifert, S.R. Gilbert, S. Aggarwal, M. Shimizu, 2003, ISBN: 1-55899-685-0
Volume 749— Morphological and Compositional Evolution of Thin Films, N. Bartelt, M.J. Aziz, I. Berbezier, J.B. Hannon, S. Hearne, 2003, ISBN: 1-55899-686-9
Volume 750— Surface Engineering 2002—Synthesis, Characterization and Applications, A. Kumar, W.J. Meng, Y-T. Cheng, J. Zabinski, G.L. Doll, S. Veprek, 2003, ISBN: 1-55899-687-7
Volume 751— Structure-Property Relationships of Oxide Surfaces and Interfaces II, X. Pan, K.B. Alexander, C.B. Carter, R.W. Grimes, T. Wood, 2003, ISBN: 1-55899-688-5
Volume 752— Membranes—Preparation, Properties and Applications, V.N. Burganos, R.D. Noble, M. Asaeda, A. Ayral, J.D. LeRoux, 2003, ISBN: 1-55899-689-3
Volume 753— Defect Properties and Related Phenomena in Intermetallic Alloys, E.P. George, H. Inui, M.J. Mills, G. Eggeler, 2003, ISBN: 1-55899-690-7
Volume 754— Supercooled Liquids, Glass Transition and Bulk Metallic Glasses, A.L. Greer, T. Egami, A. Inoue, S. Ranganathan, 2003, ISBN: 1-55899-691-5
Volume 755— Solid-State Chemistry of Inorganic Materials IV, M. Greenblatt, M.A. Alario-Franco, M.S. Whittingham, G. Rohrer, 2003, ISBN: 1-55899-692-3
Volume 756— Solid-State Ionics—2002, P. Knauth, J-M. Tarascon, E. Traversa, H.L. Tuller, 2003, ISBN: 1-55899-693-1
Volume 757— Scientific Basis for Nuclear Waste Management XXVI, R.J. Finch, D.B. Bullen, 2003, ISBN: 1-55899-694-X
Volume 758— Rapid Prototyping Technologies, A.S. Holmes, A. Piqué, D.B. Dimos, 2003, ISBN: 1-55899-695-8
Volume 759— Granular Material-Based Technologies, S. Sen, M.L. Hunt, A.J. Hurd, 2003, ISBN: 1-55899-696-6
Volume 760E—The Undergraduate Curriculum in Materials Science and Engineering, E.P. Douglas, O.D. Dubón Jr., J.A. Isaacs, W.B. Knowlton, M. Stanley Whittingham, 2003, ISBN: 1-55899-697-4
Volume 761E—Molecular Electronics, M-I. Baraton, E.L. Garfunkel, D.C. Martin, S.S.P. Parkin, 2003, ISBN: 1-55899-698-2

Prior Materials Research Society Symposium Proceedings available by contacting Materials Research Society

Layer Manufacturing and Selective Laser Sintering

Mat. Res. Soc. Symp. Proc. Vol. 758 © 2003 Materials Research Society LL1.1

Microstereolithography: a Review

Arnaud Bertsch, Sébastien Jiguet, Paul Bernhard[1], Philippe Renaud
Swiss Federal Institute of Technology, Lausanne (EPFL), STI – IMM – LMIS4
1015 Lausanne, Switzerland
[1]Proform AG, Route de Chésalles 60, ZI les Fontanettes
1723 Marly, Switzerland

ABSTRACT

Microstereolithography is a technology at the interface of the microengineering and rapid prototyping domains. It has evolved from the stereolithography technique, and is also based on a light-induced layer-stacking manufacturing. As the resolution of the microstereolithography technique is far better than the one of rapid prototyping technologies, this technique is of particular interest in the microengineering domain where its 3D capability allows the production of components no other microfabrication technique can create.

The first developments of the microstereolithography technique have started in 1993 and different research teams have developed machines since, using different approaches. This paper reviews the major microstereolithography processes developed until now.

Microstereolithography is starting to be a commercially available manufacturing process. As the market for miniaturized products grows rapidly, there is an increasing need for high-resolution small size prototype parts. If the production of small mechanical components is the first commercial application of microstereolithography, this technology can also produce useful components for the microrobotic, microfluidic, microsystems and biomedical fields. Current research in the microstereolithography field is focused on using ceramic composites as material to manufacture complex three-dimensional parts that can be sintered to produce pure alumina microcomponents.

INTRODUCTION

Microstereolithography is the general designation of various microfabrication technologies based on the principle used in stereolithography, a rapid prototyping technology patented in 1984[1,2] and used in the automotive and aerospace industries as well as in all industrial and technological fields requiring the manufacturing of three dimensional prototype parts. If the word "Microstereolithography" is now commonly accepted by almost every user and developer of this technology, many different names (micro-photoforming, IH process, spatial forming, 3D optical modeling, microstereophotolithography, optical forming, etc...) have been used by the research teams who published the first reports on this technique, corresponding to variations in the design of the built apparatuses. Nevertheless, whatever their name can be, all microstereolithography machines have the same aim and the same basic principle: They allow to build small-size, high-resolution three-dimensional objects, by superimposing a certain number of layers obtained by a light-induced and space-resolved polymerization of a liquid resin into a solid polymer.

IMPROVEMENT OF THE STEREOLITHOGRAPHY RESOLUTION

To understand how stereolithography, a rapid prototyping technology with a 150μm resolution, could evolve towards microfabrication, a quick recall on its principle and on the photo-polymerization mechanism will show the possible paths that have been followed by the different research teams working in this field.

Of course, many factors (machine-, software-, process-, resin-related, etc..) affect the resolution of the stereolithography parts. The aim of this section is not to inventory all of them, but to define the principal directions that can lead to an important improvement of the resolution and which can be the starting point in the creation of high-resolution stereolithography processes for manufacture of small-sized parts.

Stereolithography

The stereolithography process is the first and most widely used rapid prototyping technique. It allows to build a part layer by layer by laser induced polymerization. The laser beam is focused and scanned on the open surface of the photosensitive liquid and a liquid/solid transformation occurs locally, which allows to create the shape of one layer of the object. When a layer is finished, fresh resin is spread on top of the already manufactured part of the object, and the light-induced solidification of the next layer is started.

Photopolymerization

Photopolymerization is the chemical reaction underlying the change of state that makes it possible to create the layers composing the objects in the stereolithography process: the absorption of a given quantity of photons per volume unit of photosensitive medium creates reactive species, which induces the polymerization of the liquid monomer into a solid polymer by a chain reaction. This polymer is generally cross-linked and cannot dissolve again in a monomer bath.

The evolution of the polymerized depth with the irradiation time in stereolithography can be easily predicted and is presented extensively in the literature [3,4]. Equation 1 gives the temporal evolution of the polymerized depth e:

$$e = \frac{1}{\alpha c} Ln\left(\frac{t}{t_0}\right) \qquad (1)$$

where t (s) is the irradiation time, t_0 (s) the irradiation time at the threshold, α (l.mol^{-1}.cm^{-1}) the Napierian coefficient of molar extinction, c (mol.l^{-1}) the concentration of the absorbing substance. This relation shows that the evolution of the polymerized depth e with the irradiation time is logarithmic. This simple model is in good agreement with experimental results in the case of resins that do not undergo changes in their absorption coefficient during the polymerization process.

Reduction of the polymerized depth

To improve the resolution of the stereolithography process in the vertical direction, thinner layers have to be created. Making smaller layers mechanically by spreading a thinner layer of fresh resin on the surface of the object to be manufactured is not sufficient to control the vertical resolution. The most important parameter is the light penetration depth in the medium [4,5]: If it is not correctly controlled, the light could penetrate deep in the chemical medium and go through some already polymerized layers, which could result in a loss of resolution in the already polymerized part of the object. To control accurately the polymerization depth, different solution can be imagined:

a) Irradiating the resin in conditions close to the polymerization threshold

When the photosensitive chemical medium is irradiated during a short time so that the energy received by the resin is close to the critical energy E_c required to start the polymerization process, equation 1 can be simplified and written:

$$e \cong \frac{1}{\alpha c} \frac{t - t_0}{t_0} \qquad (2)$$

Thin polymerized layers can be obtained and their thickness can be controlled by the choice of the irradiation time, but as the incident energy received by the resin is close to the critical energy required to start the polymerization phenomenon, they have in general poor mechanical properties. Moreover, a small variation of the irradiation energy leads to important changes in the polymerized depth, which is not compatible with vector-by-vector fabrication processes. In particular, when two polymerized vectors are secant, the intersection point is irradiated with twice the energy of other points, which makes it impossible to control accurately the polymerized depth (figure. 1).

b) Using a highly absorbing chemical medium

When the irradiation energy is significant compared to the critical energy, equation 1 can be written:

$$e \cong \frac{R_1}{\alpha c} \quad \text{where} \quad R_1 = Ln\left(\frac{t}{t_0}\right) \qquad (3)$$

There are only very small variations of R_1 with small variations of the irradiation time t, when $t >> t_0$. In this case, the polymerized thickness does not depend much on small variations of the irradiation time, which is better adapted to vector-by-vector fabrication. The polymerized thickness can be reduced by using reactive resins with low value of the optical thickness $\mu = 1/\alpha c$. Such resins show a strong absorption of the irradiation wavelength and can be obtained by formulating chemical media containing high concentrations of highly absorbing chemicals (initiators or non-reactive chemicals).

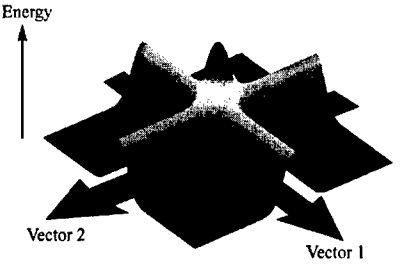

Figure 1. When two polymerized vectors are secant, the intersection point receives a double energetic dose. When the irradiation energy is close to the critical energy, this leads to significant changes in the polymerized thickness.

Improving the transverse resolution of stereolithography

The horizontal resolution of the stereolithography process is mainly a function of the resolution of the scanning system and quality and stability of the laser beam. The laser diameter on a standard SLA-250, the most widespread commercial stereolithography machine commercialized by the company 3D Systems, (0.25 mm) sets a lower limit to the resolution and feasibility of small size features. Given a stable laser beam profile, accurate correction factors for the width of the scanning beam and resin shrinkage, a horizontal precision in the order of the half of the laser beam width, as a rule of thumb, can be routinely achieved.

A significant improvement in the horizontal resolution can be achieved by using a single mode instead of the common multimode HeCd laser on a conventional SLA-250 machine. The spot size at the focal point can be reduced from 0.25mm to about 0.08-0.1mm, which pushes down the lower limit of feature feasibility [6]. This technique has found applications in the area of watch making, electronics [7] and in the electro- and medico-technical industry (hearing aids). A few specialized service bureaus worldwide commercially produce small size high-resolution prototypes made with the small spot stereolithography technology.

Further improvements of the horizontal resolution of the stereolithography process requires the reduction of the interaction volume between light and matter. This leads to different microstereolithography concepts that will be discussed in the next paragraph.

MICROSTEREOLITHOGRAPHY: CONCEPTS AND PROCESSES

Vector-by-vector microstereolithography

The basic principle of all vector-by-vector microstereolithography machines is very similar to the one of the stereolithography technique: every layer of the object is made by scanning a focused light beam on the surface of a photosensitive resin. To get a better resolution than stereolithography, the beam is focused more precisely in order to reduce the spot size to a few micrometers in diameter, which requires additional technological developments in the designed microstereolithography machines. In particular it is necessary to measure precisely and continuously the position of the surface on which the beam is scanned and to dynamically focus

it with a sufficient precision. A first kind of microstereolithography processes based on this principle has been developed, and the vector by vector scanning of every layer is in general not realized with scanning mirrors but by moving the photoreactor with x-y translation stages.

a) Constrained surface technique

The first papers published at an international conference on microstereolithography were issued in 1993, one at the MHS conference by Takagi et al. [8] and a second at the MEMS conference by Ikuta et al. [9]. The processes that are described in those papers and which are more extensively presented later in other publications, are relatively similar. They are based on a vector by vector tracing of every layer of the object with a light beam, focused on the reactive resin through a transparent window. In this variation of the microstereolithography process, the point on which the light beam is focused remains fixed, but x-y translation stages are used to move either all the optical system focusing the light beam on the resin surface, or the photoreactor in which the object is made. A shutter occults the light during translation without polymerization or when a new layer is made (Figure 2a).

The use of a glass window to push on the liquid and obtain a layer of constant thickness avoids the problem related to spreading the fresh resin on the already polymerized part of the object. However, polymerizing through a transparent window has a major disadvantage: the formed polymer sticks to it, which can result in partial or total destruction of the part during the manufacturing process.

Apparatus described by:	Takagi et al. (1993)	Ikuta et al. (1993)
Name of process	Photo forming	IH process
Light source	He-Cd laser, UV (325 nm)	Xenon lamp, UV
Constrained surface with	Quartz window +PFA tape	Transparent window
Irradiation	From bottom	From top
Maximum size of structure	20x20x20mm	10x10x10mm
Announced resolution	5 x 5 x 3 μm (x,y,z)	60μm, up to 8μm
Resin type	Acrylic	Not specified

Table I. Characteristics of vector-by-vector microstereolithography machines operating with the constrained surface technique, described by Takagi and Ikuta in 1993.

b) Free surface technique

To avoid the adhesion of the polymer to the transparent window in the constrained surface processes, some research teams developed vector-by vector microstereolithography processes based on a free surface technique (Figure 2b). These processes are very similar to the ones presented in the previous paragraph, except the surface of the liquid resin is not constrained by a transparent window. The main disadvantage of this method is the difficulty in controlling the thickness of the deposited liquid layer: Once the liquid layer is spread on the surface, it is necessary to wait for the gravity forces to level the surface. The time required to obtain a horizontal fresh layer of resin depends on the rheological properties of the resin. Low viscosity monomers have to be used as often as possible.

Zissi et al. published a first paper describing a vector-by-vector microstereolithography process using the free surface technique in 1994 [10], and another was presented in 1998[11] by Zhang et al.

Apparatus described by:	Zissi et al. (1994)	Zhang et al. (1998)
Name of process	Microstereophotolithography	Micro-stereolithography
Light source	Argon ion laser	Argon ion laser
Surface monitoring	IR laser diode	CCD camera
Announced resolution	30 x 30 x 20 μm (x,y,z)	Spot has 1-2 μm
Resin type	Acrylate based resin containing non-reactive absorbers and polymerization inhibitors	HDDA monomer containing 4wt% of benzoin ethly ether as photoinitiator

Table II. Characteristics of the vector-by-vector microstereolithography machines operating with the free surface technique, described by Zissi and Zhang.

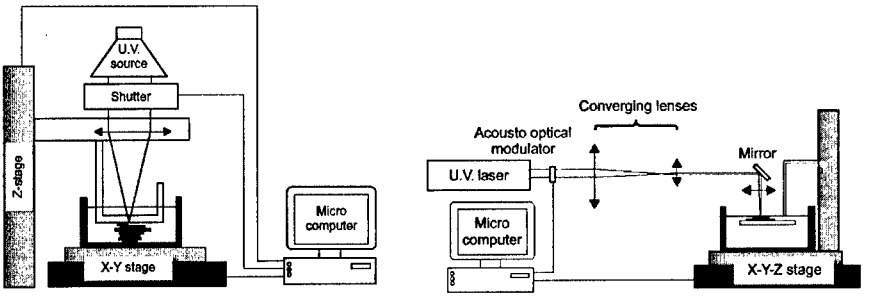

(a) Constrained surface technique *(b) Free surface technique*

Figure 2. Schematic diagram of vector by vector microstereolithography processes (from [12]).

Integral microstereolithography

Integral microstereolithography has started to be studied more recently than vector-by-vector microstereolithography because integral processes are much more different from conventional rapid prototyping techniques than vector-by-vector processes. Moreover, the components that could be used as dynamic pattern-generators, which are the key components in integral processes, were not commercially available with a sufficient resolution until 1995.

In integral microstereolithography, every layer of the object is made in one irradiation step by projecting its image on the surface of the photopolymerizable resin, with a high resolution an a certain depth of focus. This avoids the problems related to the fine focusing of a light beam in one point on the liquid surface, which is often limiting vector-by-vector microstereolithography processes. A pattern generator allows to shape the light, such that it contains the image of the layer to be solidified. This image is then reduced and focused on the surface of the reactive medium with the appropriate optical system. The superimposition of the different layers composing the object is done in the same way as in conventional stereolithography (Figure 3a). Integral microstereolithography processes are fast, because the irradiation of an entire layer is done in one step, whatever its pattern may be.

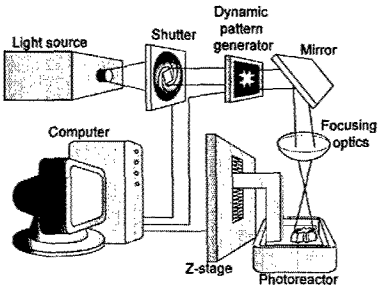

(a) Principle

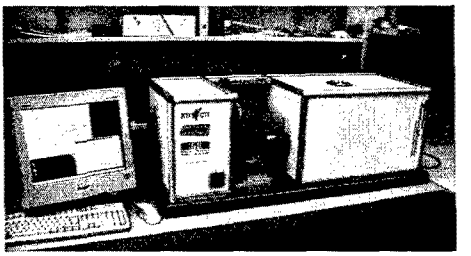

(b) DMD™ based machine at EPFL

Figure 3. Integral microstereolithography.

a) Liquid crystal displays (LCDs) as pattern generators

The first paper presenting an integral microstereolithography machine was published in 1995 by Bertsch et al. [13] and the component used as dynamic pattern generator was a LCD panel developed for rear projection applications. Every pixel of such LCD panels is a small cell that can be set either to its transparent state or to its opaque state, by changing the orientation of the molecules it contains. By inserting a liquid crystal display on the optical path of the light beam, the transmitted light can be modulated, which allows to use successfully those LCD screens to manufacture complex in shape objects by microstereolithography [12].

When the first experiments were started on the use of LCDs as spatial light modulators in microstereolithography, this component was not compatible with UV light. A visible light source was required in the apparatus and a photopolymerizable resin reacting with visible wavelengths had to be developed.

In 1998, Loubère at al. [14] presented another integral microstereolithography process using a LCD display as pattern generator and performing the resin irradiation with visible wavelengths. Chatwin et al. [15] presented in 1998 an integral microstereolithography process operating in the UV that uses a special LCD display, transparent to wavelength above 350nm. It is a polysilicon thin film twisted nematic liquid crystal display manufactured by CRL Smectic Technologies Ltd.

Apparatus described by:	Bertsch et al. (1995)	Chatwin et al. (1998)	Loubère et al. (1998)
Light source	Ar+ laser (515nm)	Ar+ laser (351.1nm)	Halogen lamp
LCD display resolution	260x260 pixels	600x800 pixels	640x480 pixels
Speed	90 layers per hour	< 60 layers per hour	60 layers per hour
Announced resolution	5 x 5 x 5 μm (x,y,z)	? x ? x 50μm (x,y,z)	5 x 5 x 10 μm (x,y,z)
Resin	PETIA with EosinY as photo-sensitiser and amine as co-initiator	Cibatool 5180 (low viscosity epoxy-based resin)	PETIA with EosinY as photo-sensitiser and amine as co-initiator

Table III. Characteristics of the integral microstereolithography machines described by Bertsch, Chatwin and Loubère.

b) Digital Micromirror Device™ as pattern generator

The Digital Micromirror Device (DMD™) produced by Texas Instruments, which is an array of micromirrors actuated by electrostatic forces can also be successfully used as pattern generator for microstereolithography. This component is a microelecromechanical system working as a light switch [16].

The DMD™ is monolithically fabricated by CMOS-like processes over a CMOS memory, and is made of 16 μm square aluminum mirrors that can reflect the light in one of two directions, depending on the state of the underlying memory cell. The rotation of the mirror is accomplished through electrostatic attraction. By combining the DMD™ with a suitable light source and optical system, each mirror reflects the incident light either into or out of the pupil of the projection lens by a simple beam-steering technique. When the mirror is rotated to +10 degrees, the corresponding pixel in the image appears bright, whereas when the mirror is rotated to –10 degrees, the corresponding pixel appears dark.

To demonstrate the feasibility of the technology, an array of micromirrors having a VGA resolution (640 x 480) was used in a first prototype developed to work with visible wavelengths by Bertsch et al [3]. The typical manufacturing speed of this machine is of about 200 to 300 layers per hour, depending on the shape of the layers, and the resolution , up to $3x3x3\mu m^3$.

In a second microstereolithography machine created to operate in the UV, a DMD™ chip having a XGA (1024 x 768) resolution was used. This apparatus was developed at the Swiss Federal Institute of Technology in Lausanne, EPFL (figure 3b) for use in an industrial context. An acrylate-based resin has been formulated to be used with this apparatus. It is highly absorbing for the irradiation wavelengths and has mechanical properties close to the ones of conventional stereolithography resins.

Creating an object inside the reactive medium

There are of course many advantages to creating the object directly in the resin, without superimposing layers: No support parts are needed. No time is spent spreading the liquid on the part being manufactured, which potentially can speed-up the process significantly. Freely movable structures can be fabricated without the need of sacrificial layers. Many attempts have been done to develop such kind of processes in the rapid prototyping domain, for creating big objects, but they have never been successful. However, when making micro objects some solutions have been found to create them directly inside the reactive medium.

When objects are created by microstereolithography by polymerizing directly inside the reactive medium, the energetic density of the light beam has to be maximal under the surface, which requires adapted chemical media and complex optical systems. This approach allows to create very small objects because very small increments are possible in both the vertical and transverse direction.

a) Two-photon process

Two-photon absorption is an optical nonlinear phenomenon that occurs at sufficiently high level of irradiance in all materials, when the combined energy of two photons matches the transition energy between the ground state and the excited state. The rate of two-photon absorption is proportional to the square of the incident light intensity. The quadratic dependence of the two-photon absorption rate on the light intensity confines the absorption to the area at the

focal point. As the two-photon transition rate is extremely small, the power of the light source has to be extremely high.

Maruo et al., who developed the first two-photon microstereolithography apparatus in 1996 [17], used a mode locked Ti:Sapphire laser emitting at 770nm. The beam power at peak in the resin was about 3kW with a repetition rate of 76 MHz and a pulse width of 130fs. The resin was transparent to IR light and did not attenuate the light beam, which could be focused inside the resin without polymerization at the surface. This process was the first microstereolithography process having a submicron resolution.

Kawata et al. developed a microstereolithography apparatus based on the same principle with a 120nm resolution, which is smaller than the diffraction limit (the nonlinear effects allow to exceed it). To demonstrate the very high resolution obtained with this process, Kawata et al. built a micro-bull, which is 10μm long and 7 μm high [18].

b) Single-photon process

In a single-photon under-surface manufacturing microstereolithography process, the nonlinearity of the photopolymerization reaction in response to the irradiation intensity is used. The presence of oxygen molecules dissolved in the resin inhibits the polymerization reaction. As a result, if the light intensity is adequately low, polymerization does not start. This phenomenon can be exploited to selectively solidify the resin by regulating the intensity of the light. A radiation that is weakly absorbed by the resin can be tightly focused inside the photoreactor under optimal conditions, such that the intensity is sufficient to solidify the resin near the focal point but not in the out-of-focus region.

Maruo et al. presented a microstereolithography process based on the single-photon under surface polymerization at the MEMS conference in 1998 [19]. The single photon photopolymerization is stimulated not by a pulsed laser but by a continuous wave blue He-Cd laser. As conventional UV-initiated resins weakly absorb the blue wavelength at 441.6nm, conditions in which the single photon process can be exploited exist. The process resolution is close to the one of the 2-photon technique: the best lateral and depth resolutions attained were 0.43 and 1.4 μm respectively.

APPLICATIONS OF MICROSTEREOLITHOGRAPHY

Microstereolithography is starting to be a commercially available manufacturing process. There is a growing need for high-resolution small size components in the rapid prototyping domain. As the market for miniaturized products grows rapidly, there is also an increasing need for high-resolution prototype parts. When small size objects have to be built with dimensions of only a few millimeters or less, current rapid prototyping technologies are limited with respect to the feasibility of small features: openings and small holes are difficult to make and have to be re-drilled once the prototype is built, which is particularly difficult. Another aspect, which has to be taken into consideration for small components, is that manual surface finishing can be a very tedious, if not impossible task.

The small-spot laser stereolithography technology is the first step towards high-resolution rapid prototyping, and this process is made commercially available by a few service bureaus around the world. The resolution obtained with this technology is sufficient for a large number of

products; however, there are still many applications that demand substantially higher resolution and precision.

The first commercial application of microstereolithography is the production of components for rapid prototyping applications. The first company that started to sell such prototype parts is microTEC in Duisbourg, Germany [20]. Recently, Proform AG, in Marly, a Swiss service bureau already specialized in high-resolution prototype parts also started such activity. If the production of small mechanical components is the only current commercial application of microstereolithography, all universities and research institutes who investigated this technology manufactured interesting objects and tried to find potential applications for this process.

Objects with a geometric complexity

All research teams who realized microstereolithography machines tried to validate the concept they developed by manufacturing components that are difficult or impossible to build with conventional microfabrication processes, like bending pipes [9], micro coil springs [9], spiral structures [21], microgears of different shapes [11,12,22,23], freely movable microstructures [19,23], 3D networks, scale models [3,6], (small car, statue of liberty (figure 4c), micro turbines, Christmas tree) etc... Of course all these test objects have no real use, but they illustrate the wide diversity of shapes and the intricate details that can be produced with the microstereolithography processes.

Small mechanical components

The manufacturing of small size high-resolution components that rapid prototyping technologies are unable to create with adequate detail is of course the first domain in which microstereolithography could be successful (figure 4a). Most research teams have investigated more microsystem/microfluidic related uses of this technology, but have neglected to investigate thoroughly this field. There is a growing demand of high-resolution prototype objects in particular in the medico-technical industry. Medical probe heads in which optical and chemical sensors could be embedded will be less invasive if they could be created with a smaller size [6]. Hearing-aid manufacturers try to design lightweight products small enough not to be detected, comfortable, with rounded shapes to be close from the natural geometry of the ear canal. For such applications it is necessary to prototype small mechanical components with intricate details. In the medical domain, 3D models made by microstereolithography can also be used to train the surgeons before a very difficult operation (At the HARMST'01 workshop MicroTec presented a model of the ear canal that was used for this purpose).

In the electro-technical industry microstereolithography can be advantageously used for the prototyping of small connectors, and many other examples can be found in different domains.

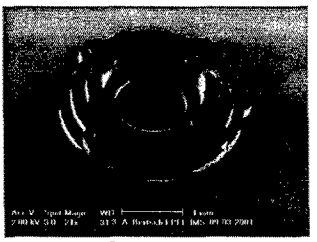

(a) Prototype part

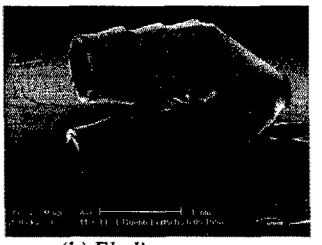

(b) Fludic connector

(c) Scale model

Figure 4. Objects made by microstereolithography.

Microsystem components

As microstereolithography has evolved from rapid prototyping technologies and does not yet allow a wafer-level manufacturing, different research teams have investigated its possible combination to conventional silicon-based micro-machining technologies in order to integrate new functions on planar structures and create original microsystem components. In this context, microstereolithography has been combined to thick-resist UV lithography to associate curved and conical structures with the smooth and vertical walls and micrometer accuracy of SU-8 technology [24]. It has been combined to piezoelectric elements [25] and shape memory alloy wires[26] to create actuators. Microstereolithography has also been used for prototyping MEMS components and optimizing their geometry, before investing in photomasks and using more conventional cleanroom technologies for mass production [27]. In the future, the manufacturing of hybrid polymer structures by combining various types of polymers, such as conductive polymers, polymers of various refractive index or flexible polymers could also lead to the creation of new optical, chemical and biochemical microsystems with the microstereolithography technology [28].

Microfluidic components

Many authors studied the possibility to create microfluidic components with the microstereolithography process. It is indeed relatively easy to create pipes and connectors having shapes that are impossible to be obtained by conventional microfabrication technologies with this technique (figure 4b). Different passive microfluidic components are presented in the literature: pipes, channels, connectors, mixers, etc. More complex passive microfluidic components have also been presented, obtained either by combining different technologies or by inserting membranes or films during the patterning process (a cell-free biochemical chip for Luciferase synthesis, a micro-osmotic valve prototype for insulin injection, a concentrator chip, etc...)

By combining structures made by microstereolithography with piezoelectric actuators or shape memory alloy components, active fluidic components can also be obtained (micropumps [29], switching valves, etc...) Once active and passive microfluidic components can be produced, their assembly can lead to complex fluidic systems. Ikuta et al. developed a simple method for holding and connecting fluidic components to obtain chemical and biochemical chips. This versatile fluidic device has been named "Biochemical IC"[30].

CONCLUSION - MICROSTEREOLITHOGRAPHY OF COMPOSITE MATERIALS

One of the major limitations of the microstereolithography technology is related to the materials that can be used in this manufacturing technique: Only a few polymers can be used, acrylates in general or eventually epoxies. Because of their three dimensional geometry, most objects produced by microstereolithography cannot be molded, which implies that, for some applications, microstereolithography is no longer a rapid prototyping technology but a manufacturing technique. In this case, the produced objects need to have adequate mechanical, chemical or physical characteristics. As a result, studies on the use of new materials for microstereolithography have been started, and in particular on the use of composite materials made of ceramic particles embedded in a polymer matrix as reactive medium in this technology. The ultimate aim is of course the production of micro-components in ceramic materials, which can be obtained by sintering the composite. However, for sintering successfully such composite components, the load of particles embedded in the resin has to be sufficiently high, which increases significantly the viscosity of the chemical media. If different teams have started to work in this field, no satisfactory solution has been obtained yet, but this research in the material domain are very promising for the utilization of microstereolithography not only as a prototyping technology but as a manufacturing technique.

REFERENCES

1. C. W. Hull, US Patent Patent No. 4,575,330 (1986).
2. J. C. André, A. Le Méhauté, and O. De Witte, French Patent Patent No. 84,11,241 (1984).
3. L. Beluze, A. Bertsch, and P. Renaud, presented at the SPIE Symposium on Design, Test and microfabrication of MEMs/MOEMs, Paris, France, 1999.
4. S. Zissi, A. Bertsch, J. Y. Jézéquel, S. Corbel, J. C. André, and D. J. Lougnot, Microsystem Technologies **2** (2), 97 (1996).
5. T. Nakamoto, K. Yamaguchi, P. A. Abraha, and K. Mishima, J. Micromech. Microeng. **6** (2), 240 (1996).
6. A. Bertsch, P. Bernhard, C. Vogt, and P. Renaud, Rapid Prototyping Journal **6** (4), 259 (2000).
7. P. Bernhard, Rapid prototyping report **Dec. 1997** (1997).
8. T. Takagi and N. Nakajima, presented at the 4th International Symposium on Micro Machine and Human Science (MHS'93), 1993.
9. K. Ikuta and K. Hirowatari, presented at the 6th IEEE Workshop on Micro Electro Mechanical Systems (MEMS'93), 1993.
10. S. Zissi, A. Bertsch, S. Ballandras, S. Corbel, J. Y. Jézéquel, C. Belin, D. J. Lougnot, and J. C. André, presented at the 3e Assises Européennes du Prototypage Rapide, Paris, France, 1994.
11. X. Zhang, X. N. Jiang, and C. Sun, Micro Electro Mechanical Systems (MEMS) ASME **66**, 3 (1998).
12. A. Bertsch, S. Zissi, J. Y. Jézéquel, S. Corbel, and J. C. André, Micro. Tech. **3** (2), 42 (1997).

13. A. Bertsch, S. Zissi, J. Y. Jézéquel, S. Corbel, and J. C. André, presented at the 4èmes assises européennes du prototypage rapide, Paris, France, 1995.
14. V. Loubère, S. Monneret, and S. Corbel, presented at the the 4th Japan-France Congress and 2nd Asia-Europe Congress on Mechatronics, Kitakyushu, Japan, 1998.
15. C. R. Chatwin, M. Farsari, S. Huang, M. I. Heywood, P. M. Birch, R. C. D. Young, and J. D. Richardson, Applied optics **37** (32), 7514 (1998).
16. L. J. Hornbeck, presented at the Electronic Imaging (EI'97) - Projection displays III, San Jose, California, USA, 1997.
17. S. Maruo, O. Nakamura, and S. Kawata, presented at the SPIE - Optics for Science and New Technology, 1996.
18. S. Kawata, H.-B. Sun, T. Tanaka, and K. Takada, Nature **412**, 697 (2001).
19. K. Ikuta, S. Maruo, and S. Kojima, presented at the 11th IEEE Workshop on Micro Electro Mechanical Systems (MEMS'98), Heidelberg, Germany, 1998.
20. H. Bohlmann and R. Götzen, presented at the 4th International Workshop on High Aspect Ratio Micro Structure Technology (HARMST'01), Baden-Baden, Germany, 2001.
21. S. Maruo, O. Nakamura, and S. Kawata, Optics Letters **22** (2), 132 (1997).
22. M. Farsari, S. Huang, P. M. Birch, F. Clarte-Tournier, R. C. D. Young, D. Budgett, C. Bradfield, and C. R. Chatwin, optics letters **24** (8), 549 (1999).
23. S. Maruo and K. Ikuta, Applied Physics Letters **76** (19), 2656 (2000).
24. A. Bertsch, H. Lorenz, and P. Renaud, Sensors and Actuators: A **73**, 14 (1999).
25. T. Takagi and N. Nakajima, presented at the 7th IEEE Workshop on Micro Electro Mechanical Systems (MEMS'94), Oiso, Japan, 1994.
26. S. Ballandras, M. Calin, S. Zissi, A. Bertsch, J. C. André, and D. Hauden, Sensors and actuators A **62**, 741 (1997).
27. T. S. Ji, K. J. Vinoy, and V. K. Varadan, Smart Materials and Structures **10**, 1224 (2001).
28. S. Maruo, K. Ikuta, and T. Ninagawa, presented at the 14th IEEE International Conference on Micro Electro Mechanical Systems (MEMS2001), Interlaken, Switzerland, 2001.
29. K. Ikuta, T. Hasegawa, and T. Adachi, presented at the Transducers'01 Eurosensors XV Workshop, Munich, Germany, 2001.
30. K. Ikuta, presented at the International Microprocesses and Nanotechnology Conference, 2000.

Mat. Res. Soc. Symp. Proc. Vol. 758 © 2003 Materials Research Society LL1.2

Rapid Manufacturing with Direct Metal Laser Sintering

J-E. Lind, J. Hanninen, J. Kotila, O. Nyrhila and T. Syvanen
Rapid Manufacturing Development Group
EOS Finland
Aholantie 17
21290 Rusko, Finland

ABSTRACT

The term Rapid Manufacturing is today very often used as a substitute for Rapid Prototyping, because the manufacturing processes and materials have developed so much that the parts produced with the machines can even be used as functional production parts. For Direct Metal Laser Sintering (DMLS) this was enabled by the introduction of the powders for 20 micron layer thickness; steel-based powder in 2001 and bronze-based powder in 2002. Successful rapid manufacturing with DMLS does not only mean the reduction of layer thickness, but it is a sum of many factors that had to be optimized in order to make the process work with the 20 micron layer thickness: the metal powder behavior in very thin layers is not the same as with thicker layers, the demands for the support structures are higher and the possibility of using multiples of the layer thickness gives additional freedom. By optimizing the process parameters the UTS values for the steel-based powder increased up to 600 MPa and for the bronze-based powder up to 400 MPa. At the same time the surface roughness (Ra) values after shot peening were 3 microns and 2 microns, respectively. Although using thinner layers also increases the building time the advantage is gained in drastically reduced finishing times due to increased surface quality and detail resolution. Typical geometries produced by DMLS are difficult-to-manufacture components and components typically produced by P/M or even by die-casting. The paper covers the development aspects in both material and process development and also presents some realized case studies.

INTRODUCTION

Rapid manufacturing (RM) can be briefly described as any manufacturing that is able to fabricate products in a time, which is short in a relative sense. The definition of short in time always refers to the present knowledge of available and established technologies and process chains. In addition, using a single additive technology may not always be the most effective way of fabricating parts. Instead, a combination of additive and conventional technologies exploiting their strengths is usually the fastest and most economical way of minimizing the project lead-time. Since the beginning of the Rapid Prototyping (RP) era in the beginning of the nineties the definition of a short lead-time has step by step changed from months to days. However, this change still can not be applied to every case and application, the larger and more complex the part is the longer is the fabrication time.

DMLS was first developed to be a Rapid Tooling (RT) method for injection molding tools. The development was done in cooperation by EOS Gmbh and Electrolux Rapid Development (now Rapid Product Innovations). The cooperation achieved success in 1995 when the first bronze-based powder for 100 μm layer thickness (DirectMetal 100) and a laser-sintering

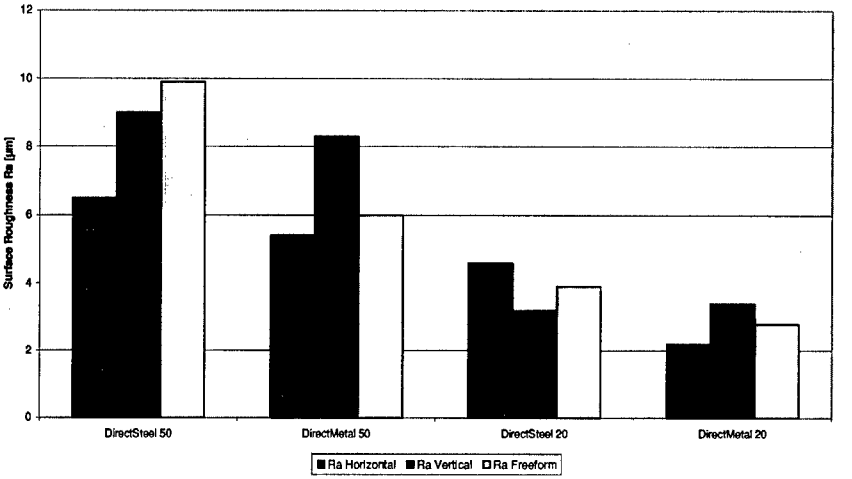

Figure 1. Surface roughness of the DMLS materials after shot peening.

machine for the powder were introduced [1]. Immediately after the introduction, the demand for more materials and better surface quality was evident. This led to further development of both the material and the process. The next step was the introduction of a bronze-based powder for 50 µm layer thickness (DirectMetal 50) in 1997 and a year later a new steel powder (DirectSteel 50) for the same layer thickness was also introduced [2]. At the same time an improved machine was also introduced with e.g. more accurate mechanics, more powerful laser and an atmosphere module for the generation of an inert atmosphere for laser-sintering of the steel-based powder. Although the surface properties of the bronze-based material were improved considerably, the use of 50 µm layers was not sufficient for the parts made of the steel-based powder. There was still need for too much post-processing. The latest solution to this problem was to develop a steel-based powder for 20 µm layer thickness (DirectSteel 20), which was introduced in 2001. In most cases the stair-stepping effect is not visible when using the 20 µm layer thickness. In fact, the surface quality of the parts produced of the powder was so good that in some injection molding cases no finishing was needed. After this the same development work was done for the bronze-based material and the result was introduced in early 2002 as the 20 µm bronze-based powder (DirectMetal 20), which in addition to the improved surface quality had also much improved mechanical properties. In fact, the tensile strength of the 20 µm bronze is almost the same as with the 50 µm steel. Figure 1 presents the surface roughness values of the current DMLS materials after shot peening [3]. Some of the properties of the DMLS materials can be seen in Table 1.

LASER-POWDER INTERACTION

The optimized metal powder mixes for DMLS are all based on the net-shape principle. Thus, the sintering and solidification shrinkages have to be compensated with volume expansion reactions [4,5]. The powder mixes contain only pure metals or metal alloys. With careful

Table 1. Properties of the DMLS materials.

	DirectMetal 100	DirectMetal 50	DirectMetal 20	DirectSteel 50	DirectSteel 20
Layer thickness	100 µm	50 µm	20 µm	50 µm	20 µm
Main constituent	Bronze	Bronze	Bronze	Steel	Steel
UTS	≤ 200 N/mm^2	≤ 200 N/mm^2	≤ 500 N/mm^2	≤ 500 N/mm^2	≤ 600 N/mm^2
Brinell hardness	90-120 HB	90-120 HB	100-120 HB	150-220 HB	180-230 HB
Minimum porosity	20 %	20 %	7 %	5 %	2 %
Max operating temperature	600°C	400°C	400°C	850°C	850°C

selection of the powder elements the materials can be laser-sintered with negligible shrinkage. During the laser sintering process each scanned powder layer maintains its x-y dimensions and thus accurate metal parts can be generated. However, as the process is based on liquid phase sintering, the solidifying liquid phase always causes some stresses in the matrix during sintering. These stresses are mostly relaxed by the heat conducted from the consecutive layers.

During the DMLS process a high intensity laser beam scans the surface of the metal powder layer. The powder particles absorb the high intensity laser radiation and heat is generated instantaneously in the powder layer, which causes partial and very local melting of the powder. The formed liquid phase wets the remaining solid particles. In addition, the melting causes a rearrangement of the orientation and position of the remaining solid particles. Due to thermocapillary and gravitational forces the melt penetrates deeper into the previously sintered structure.

These complex phenomena necessitate the use of support structures, when parts are sintered directly in the process. Although the powder underneath the current layer supports the sintered layer to some extent, it does not prevent the layer from warping or moving from its place due to thermal stresses or recoating. However, due to the very thin layers, down facing surfaces with angles even below 30° can be sintered on loose powder. If the distance from the closest sintered adjacent structure is not more than about 4 mm, even surfaces with 0° angle can be sintered without a support structure.

SUPPORTS AND EXPOSURE STRATEGIES

The direct fabrication of metal parts has been on the verge of mass commercialization for a few years already, but the progress has been slow due to problems that prevent the effective use of the technology. These problems are the need for supports on down facing surfaces and the surface quality on these surfaces. Most commercial software used for support generation are made for Stereolithography (SLA) and their suitability for a direct metal sintering process is not optimized.

The main functions of the supports are to prevent sintering on loose powder, fix the part to the building platform and conduct excess heat away from the part. Sintering on loose powder can be prevented by using a very dense mesh extruded in z-direction that is metallurgically bonded to both the building platform and the actual part. If the mesh is too large, heat is not conducted

away from the sintering zone quickly enough, which causes over melting. The over melting causes the formation of spherical droplets due to the surface tension of the liquid metal, which is also known as the balling phenomenon. If too many of these droplets are formed, the recoater may jam at this position during recoating of a new powder layer and can even break the support structure. The part has to be adequately bonded to the support in order to withstand the thermal stresses during the sintering. As mentioned previously, the stresses are mostly relaxed afterwards, but some remain in the matrix.

Fixing of the part and heat conduction benefit also from the dense mesh. However, in order to remove the support from the part easily the mesh cannot be too dense. In addition, the boundary between the support and the part has to be easily detectable and, even more importantly, easily breakable. This can be done by using serrated teeth on top of the support structure. With correct settings the teeth can be designed so that the support can be removed manually. However, this requires a slightly larger mesh for the support itself so that the bond between the support and the part is not too strong, i.e. the contact area between the support and the part becomes smaller. A drawback in using a larger mesh is that the surface quality on down facing surfaces becomes worse. If the support removal is not easy, machining has to be used, which usually lengthens the process chain to the extent that the use of an additive method may not be rational anymore. In conclusion, a proper support at the moment is a compromise between part fixing, heat conduction, support removal and surface quality.

The main drawback in the currently available support types is the poor surface quality on down facing surfaces. The use of supports based on sintering lines into a mesh is not very rational, because the line pattern and especially the teeth are copied onto the down facing surface. In addition, some hard to reach surfaces may have to be supported from another surface, which damages the surface quality of a surface that would otherwise be intact. Two examples of support marks on a surface can be seen in Figure 2. The figure on the left shows the marks of the support mesh as well as other marks on the vertical surface, which was used for supporting the other surface. The figure on the right shows support tooth marks after breaking off the support manually.

The most important factor in direct part manufacturing is that the user has to be aware of

Figure 2. Support marks on part surface after support removal.

how the part should be positioned for sintering. The correct positioning influences the resulting building time and also the post-processing time, as with correct positioning the amount of support can be minimized and the building time minimized. Another factor influencing on the amount of supports needed is the lack of variables in the exposure parameters. For example, with the EOS PSW process control software it is possible to use separate exposure parameters on the first layers on the down facing surfaces, i.e. downskin. However, there is a need to optimize certain other aspects of the building strategy to prevent e.g. the bulging material presented in Figure 2. At the moment, the best results in direct part fabrication are always compromises between the use of supports and exposure speeds and strategies.

CASES

Typical geometries that can be laser-sintered are conventionally produced by PM compacting, are cast or cannot be produced at all. In fact, the trend now seems to be that for some cases the conventional manufacturing methods are replaced by direct laser sintering by DMLS. Several applications require only a few components that would be very expensive to manufacture by conventional means. In these cases the parts could be produced by DMLS in just a few days without any tooling. Especially suitable for direct part manufacturing is the new 20 μm bronze powder, where a good mechanical strength is combined with an excellent surface quality.

There have been cases where direct laser-sintering has replaced conventional manufacturing totally. In a case where a customer needed 300 sets of a small locking device that consisted of three different parts (900 parts in total), casting was replaced by DMLS because of the speed and quality of the parts. At first the customer needed only a few prototypes, but after seeing the quality and consistency of the parts then decided to replace the whole series with the laser-sintered parts. Conventionally the customer would have needed three die-casting moulds or a number of investment casting "trees", both of which would have cost too much considering the number of parts and the lead-time would have been too long. With DMLS the project was carried out with 5 sintering jobs, which lasted 32 hours each. The supports were removed by snapping them off the part with pliers, which turned out to be a very fast method.

Figure 3 presents a fan wheel for a hand tool and a "spinning top" toy made of the same geometry. Both the parts are made of the 20 μm bronze-based material. The thin ribs in the fan

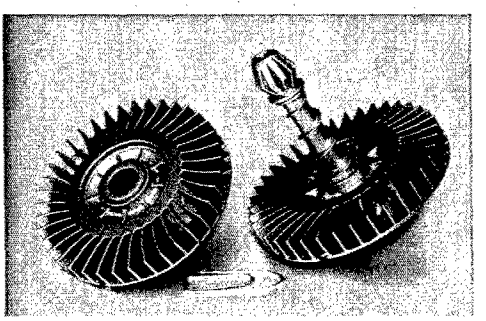

Figure 3. Parts made directly by DMLS. Fan wheel geometry by TransCAT GmbH.

wheel are only 0,6 mm thick, which is also the minimum feature thickness that can be fabricated with the technology. Injection molding inserts for the same geometry were also made and successful moldings were produced. The spinning top was made as a demonstration model of the technology, because it presents well the limits in detail resolution, but also the possibilities of freeform fabrication, because the part would be very difficult to make even by casting.

CONCLUSIONS

The state of the Rapid Tooling and Manufacturing industry has changed a lot over the past decade. For DMLS it has meant expansion of material selection from bronze to steel materials and also reduction of the layer thickness from 100 µm to 20 µm. The properties of the sintered materials have improved significantly: the tensile strength has increased from 200 N/mm^2 to 600 N/mm^2 and the surface roughness has reduced from nearly 10 µm to about 2-3 µm. The improved properties have widened the application field from the original injection molding to direct part manufacturing. In addition, the technology has shifted from a prototyping method permanently to a production method also. This applies to both mold manufacturing and direct part manufacturing.

Today, more complex shapes and more varieties of the same product are produced. Therefore, production costs would rise very much if conventional technologies would be used in the production. This serves as a driving force for further development of the DMLS process for rapid manufacturing. There is still need for an even better surface quality, accuracy, different materials and a faster process. Some of these problems could be resolved by simply developing a better software for support generation and by making some modifications to the exposure strategies in the EOS PSW software. The development work continues in this direction.

REFERENCES

1. T. Syvänen, *Direct Laser Sintering of Metals – Material and Process Development*, M.Sc. Thesis, Tampere University of Technology, 1996.
2. J. Kotila, *Development of Steel Based Metal Powder for DMLS-Process*, M.Sc.Thesis, Tampere University of Technology, 1998.
3. J-E. Lind, T. Syvanen, J. Hanninen, O. Nyrhila and J. Kotila, "*Direct Metal Laser Sintering – From 100 µm to 20 µm layers*", Proc. of Metal Powder Deposition for Rapid Manufacturing Conference 2002, MPIF, pp. 225-232.
4. R. M. German, *Sintering Theory and Practice*, John Wiley & Sons, New York, NY, 1996, p. 225.
5. A. P. Savitskii: *Liquid Phase Sintering of the Systems with Interacting Components*, Russian Academy of Sciences Siberian Branch, Tomsk, Russia, (1993) p. 66.

Mat. Res. Soc. Symp. Proc. Vol. 758 © 2003 Materials Research Society LL1.4

Layered Manufacturing: Challenges and Opportunities

Khershed P. Cooper
Materials Science and Technology Division, Naval Research Laboratory
Washington, DC 20375-5343, U.S.A.

ABSTRACT

Layered Manufacturing (LM) refers to computer-aided manufacturing processes in which parts are made in sequential layers relatively quickly. Parts that are produced by LM can be formed from a wide range of materials such as photosensitive polymers, metals and ceramics in sizes from a centimeter to a few meters with sub-millimeter feature resolutions. LM has found use in diverse areas including biomedical engineering, pharmaceuticals, aerospace, defense, electronics and design engineering. The promise of LM is the capability to make customized complex-shaped functional parts without specialized tooling and without assembly. LM is still a few years away from fully realizing its promise but its potential for manufacturing remains high. A few of the fundamental challenges in materials processing confronting the community are improving the quality of the surface finish, eliminating residual stress, controlling local composition and microstructure, achieving fine feature size and dimensional tolerance and accelerating processing speed. Until these challenges are met, the applicability of LM and its commercialization will be restricted. Sustained scientific activity in LM has advanced over the past decade into many different areas of manufacturing and has enabled exploration of novel processes and development of hybrid processes. The research community of today has the opportunity to shape the future direction of science research to realize the full potential of LM.

INTRODUCTION

Metallic parts are made by one of several technologies, machined from the bulk, cast in a mold and densified in a HIP. Ceramic parts are made by sintering powder compacts, plastic parts by injection molding. Metallic, ceramic or plastic parts can also be made by layered manufacturing. Layered Manufacturing (LM) refers to building a three-dimensional object layer-by-layer, with the architecture of each layer dictated by a CAD drawing. The form is made without support, hence the technology is also known as Solid Freeform Fabrication (SFF). The part could be a solid model designed to serve as a visualization tool in the design of a component, a device or a system. The part could be a functional part, having the same attributes as one made conventionally. The foremost advantage of LM is the ability to make a prototype fairly rapidly, hence the term Rapid Prototyping (RP) is also applied to this technology. In fact, it is in the area of RP that the technology has seen most commercialization. Design engineers and course instructors routinely utilize RP machines for design and instruction. A significant body of research and development work has taken place in LM/SFF/RP over the last 15 years. Today, it can be considered a mature science. Technological maturity is on the horizon. During this period of time, a myriad of techniques has sprouted, driven by the need to fabricate parts from a variety of materials and for a variety of applications. Some methods have achieved commercial status, having graduated from the university level, others are in various stages of research. However, the most pressing question today is whether LM has achieved the status of a viable manufacturing alternative. Will it achieve the same standing as CNC machining? Will it be able to produce parts

and components that can be inserted without qualification into service? The intent of this paper is many-fold. However, it will not try to answer the above questions. This paper will briefly describe the LM principle and the various techniques that have sprouted. It will list the scientific and processing challenges and how they are being met. It will highlight the promise of LM and identify a few success stories. It will talk about scientific opportunities for the technology.

LAYERED MANUFACTURING

"From Art to Part", that is the slogan for LM. The LM process is illustrated in Figure 1. We start with a rendition of the object in a *CAD system.* The CAD drawings (e.g., Unigraphics, CATIA or ProEngineer) are sent to an automated *process planner* in a data exchange format. In the process planner, the CAD model is "sliced" by one of many slicing programs. Depending upon the geometry of the slice, the process planner also determines motion control trajectories for each slice. These trajectories are fed into an *automated fabrication machine* where the slice is traced or deposited on a suitable substrate, guided by the x-y motion of the build platform or that of the deposition head. Alternatively, the slice is patterned on the substrate using masks. Similarly, the next slice is formed after incremental displacement of the platform in the build or z-direction. Sequential stacking of such slices results in the building of a 3D object. In short, a *computerized solid model* is directly converted to a *physical solid model.*

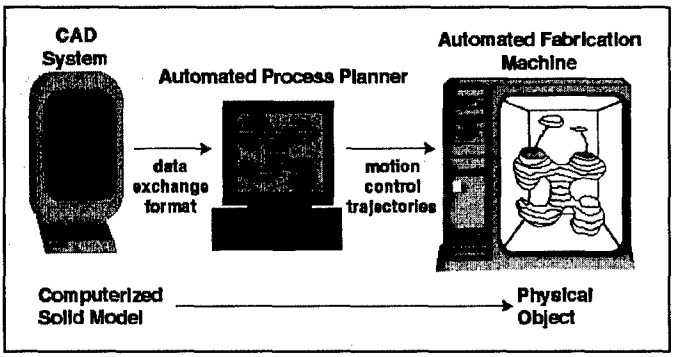

Figure 1. Schematic representation of the LM process.

LM is mainly an additive process. Each slice is added to the previous slice. While most of LM fabrication is usually done with single material processing, multi-material processing is also being developed, especially when support structures are necessary for complex geometries such as internal cavities and overhangs. In fact, most deposition techniques allow for the deposition of at least two materials, part material and support material. Support material is usually sacrificial and is removed after building is complete. Multi-material deposition systems are designed to fabricate multi-component systems and devices. Another variation is to incorporate a light machining operation (subtractive process) along with the additive process to ensure dimensionality and surface finish. Every added complication to the basic additive LM process imposes a fundamental challenge with the digital representation of process that enables designers to capture the full range of design possibilities offered by LM. LM technology can also be

exploited for depositing structures such as flanges and stiffeners on existing parts and for repairing certain part defects. Key parameters that characterize a LM technique are the build rate and the build envelope, ability to make parts of different materials, dimensional accuracy and feature size.

LAYERED MANUFACTURING TECHNIQUES

A plethora of techniques have been developed during the research phase of LM. The development of each technique probably owes more to inventiveness than to problem-solving. A broad classification of LM techniques based on the nature of the build material that will define the nascent form or shape is given in Table 1. The build materials are classified as liquid, gas, powder, binder, wire or sheet. The main purpose in preparing this list is to highlight the wide variety of concepts involved and the wide variety of materials processed. Brief descriptions of the techniques follow with references for further details.

Table 1. Classification of LM techniques.

LIQUID-based Photocurable Slurries Curing with UV-Laser ○ Stereolithography (SLA) - *3D Systems* Curing with Visible Light and DMD ● Direct Photo Shaping (DPS) - *SRI Int.* Curing with light through masks ● Microstereolithography (μSLA)- *Lausanne* Electrolyte Electroplating ● Electrochemical Fab. (EFAB) - *USC* Drops Printing with Inkjet ○ Multi Jet Modeling (MJM) - *3D Systems* ○ 3D Plotter - *Solidscape* Casting ● Shape Deposition Mfg (SDM) - *Stanford* ● Drop-by-Drop Mfg - *UC-Irvine* ● Robocasting - *Sandia* Freezing Water ● Rapid Freeze Prototype (RFP) - *Missouri* GAS-based Chemical Vapor ● Laser-asst. CVD (LCVD) - *Georgia Tech* Laser ● Selected Area Laser Dep. (SALD) - *Connecticut*	POWDER-based Sintering with Lasers ○ Selective Laser Sintering (SLS) - *3D Systems* Melting with Lasers ○ Laser Eng. Net Shaping (LENS) - *Optomec* ○ Laser Additive Mfg (LAM) - *AeroMet* ○ Direct Metal Dep. (DMD) - *POM* BINDER-based Binding Powder ○ 3D Printing (3DP) - *Extrudehone/Z Corp* Extruding Filament ○ Fused Dep. Modeling (FDM) - *Stratasys* ● Fused Dep. of Ceramics (FDC) - *Rutgers* ● Extrusion Freeform Fab. (EFF) - *ACR* WIRE-based Wire Feed ● E-beam Freeform Fab. (EBF^3) *by MIT/NASA* SHEET-based Lamination ○ Laminated Object Mfg (LOMS) - *Cubic* ○ Commercial ● Research

Within the LIQUID-based category are build materials such as photocurable slurries, electrolytes and liquid drops. Photocurable slurry techniques vary depending upon the form of energy and level of masking utilized to cure the liquid. *Stereolithography* (SLA) uses a rastered UV laser, *direct photo shaping* (DPS) uses visible light and masks or digital mirror devices and *microstereolithography* (μSLA) uses visible light and masks on the μm-scale. While SLA has achieved commercial status through the efforts of 3D Systems [1], DPS and μSLA, developed by Ventura et al [2] and Beluze et al [3], respectively, are in the research stage. SLA and μSLA are primarily suitable for materials that polymerize, e.g., plastics. With DPS, ceramic parts have been successfully made by binding .the ceramic powder with a photocurable liquid and curing by exposure to light. A novel technique developed by Cohen et al [4] is *electrochemical fabrication* (EFAB), which involves electroplating metallic layers sequentially. Liquid drops make ideal media for precision deposition. Printing with inkjets mimics ink-jet printers, with the ink composed of different kinds of liquids. *Multi-jet modeling* (MJM), marketed by 3D Systems [1], uses multiple ink jets and enjoys increased throughput. The *3D Plotter* is a single ink-jet process and is marketed by Solidscape [5]. Both methods appear to be restricted to a variety of polymeric materials. It must be pointed out that in the case of polymeric materials, the formulations are unique and proprietary and are usually marketed by the system vendor.

Shape deposition manufacturing (SDM), developed by Prinz and Weiss et al [6] uses drops from low-melting wax to high melting metals and alloys to build layered structures with each layer shaped by a suitable machining operation. A variant is Mold SDM [7] in which a ceramic part is gel-cast into a SDM mold usually made of a sacrificial material such as wax. Another interesting method is *drop-by-drop manufacturing* developed by Orme et al [8], which involves directing mono-sized charged drops of liquid metal, generated by an ultrasonic nozzle, to specific locations on a substrate. Research has been restricted to low-melting metals such as solders and aluminum-silicon. *Robocasting*, developed by Cesarano [9], involves depositing drops of water-based ceramic slurries in a predetermined pattern. Leu et al [10] have developed the *rapid freezing prototyping* (RFP) process that freezes water drops into the desired shape. The frozen shape is then used as a pattern for investment casting of metals.

At present, the GAS-based techniques are confined to the laboratory. The principle is to use the thermal energy from a laser to induce a chemical reaction within special reagent gases to produce a solid deposit. Lackey et al [11] have developed *laser-assisted chemical vapor deposition* (LCVD) and Marcus et al [12] have developed *selected area laser deposition* (SALD). There are variations to SALD, in the form of SALDVI, which is vapor infiltration to form a cermet and SALD-Joining, which is joining two ceramic pieces. Gas-based techniques suffer from very low deposition rates, but may have an application involving fabrication of *in situ* sensors such as thermocouples.

POWDER-based techniques appear to have achieved the highest level of commercialization and involve either a powder bed or a powder spray. *Selective laser sintering* (SLS) uses a laser to sinter the uppermost layer on a powder bed in a predetermined pattern. The powder bed is incrementally lowered and the next layer is similarly formed. A sintered shape forms and is supported by the surrounding packed powder. The powder can be a polymer, sand, a ceramic or a metal. For the high melting powder, a binder may be mixed in and, as the laser sweeps the layer, a bound shape emerges. A variation is SLS/HIP in which the outer surface of metallic components is sintered before hot isostatic pressing. Developed by Beaman et al [13], the SLS process is today marketed by 3D Systems [1]. A similar laser-sintering process is EOSINT, which is marketed by Electro Optical Systems [14]. Another powder-based technique

involves feeding powder into a laser melt pool and is mainly applied to metals. In laser additive processes, the reinforced melt pool solidifies into a layer the shape of which is determined by the path followed by the laser beam. Layer-by-layer fusion of such shapes results in a 3D form whose dimensional tolerance, surface finish, microstructure and properties will depend upon how well the processing conditions have been optimized and how accurate a closed-loop control is achieved. *Laser engineered net shaping* (LENS), developed by Griffith et al [15] and marketed by Optomec [16], strives to achieve finer feature size, higher degree of complexity and a smooth surface finish, but at the expense of throughput. To achieve these part attributes requires finer powder and smaller melt pool size. *Laser additive manufacturing* (LAM) is commercialized by AeroMet [17] and involves higher throughput net-shape forming of high-end metallic parts. LAM makes a preform, which is subsequently light machined to the final dimensions and surface finish. *Direct metal deposition* (DMD) was developed by Mazumder et al [18] and is commercialized by Precision Optical Manufacturing [19]. Its claim is a proprietary closed-loop feedback control system for accurate metallic part reproduction.

BINDER-based techniques fall into two categories, binding a powder bed and extruding filaments. The *3D Printing* (3DP) process was developed by Sachs et al [20] and is marketed by a series of licensees such as Z-Corp [21] and Extrudehone [22]. 3DP involves binding the uppermost layers of a powder bed using a series of streams of a suitable binder. The unbound powder provides the support structure. The powder can be a polymer, starch, ceramic or metal. Metallic parts for tooling are fabricated by debinding the printed structure and melt-infiltrating the skeleton with a lower melting alloy to retain part dimensional fidelity. *Fused deposition modeling* (FDM) is marketed by Stratasys [23] and involves the deposition of a binder-containing filament. Danforth et al [24] developed the *fused deposition of ceramics* (FDC) process, which uses ceramic-loaded filaments and the *fused deposition of metals* (FDMet) process, which uses metal-loaded filaments. Proceeding further, a *multi-material deposition* system (FDMM) was developed with the goal of depositing at least two ceramic materials or a metal and a ceramic along with support material. While FDM and FDC involve fabricating carefully formulated filaments and feeding them fused onto the substrate, *extrusion freeform fabrication* (EFF), developed by Vaidyanathan et al [25], involves extruding a binder-ceramic mixture and feeding the filament, unfused, onto the substrate. In all these methods, the green part is later debound and sintered to full density.

WIRE-based SFF involves feeding a metallic wire into a melt pool formed by a laser beam or an e-beam. Preliminary work was done by Eagar et al [26] using a high power e-beam. Recently, Taminger et al [27] have revived the method with their *e-beam freeform fabrication* (EBF^3) process with the goal to develop a fabrication system that could be deployed in a remote setting such as outer space. Advantages of wire feeding are full material utilization and no particulate contamination of the environment, which would be a requirement for space-flight. Finally, in the SHEET-based category is the *laminated object manufacturing* system (LOMS) process marketed by Cubic Technologies [28]. LOMS involves precisely carving out and stacking sheets or laminates made of paper, plastic or bound ceramic using a laser. With the same laser, the support structure is crosshatched and later removed.

By no means is the list in Table 1 complete. However, processes not described would probably fall under one category or the other. While some techniques are dedicated to one material, e.g., LAM or EBF^3 for metals, other techniques can be quite adaptable and have demonstrated capability in fabricating parts from a variety of materials. A listing of some of the commercial rapid prototyping machines, their representative vendors, their capabilities, system

price and materials costs is available on the web [29]. While these machines are capable of fabricating prototypes out of plastic, some of them are designed to fabricate objects and even parts out of metals and ceramics. Prototyping is still the main utility of these commercial systems. Most of the commercial machines are single material systems. Commercial multi-material systems are in the distant future.

MATERIALS AND PROCESSING CHALLENGES

Prior to the advent of layered manufacturing as a fabrication technology, parts were made by processes such as injection molding, powder consolidation, metal casting, gel casting and machining. The materials and processing challenges for these single-step, single material processes were important, but few and relatively straightforward to tackle. For instance, in metal casting, the practitioner had to deal with solidification of liquid metals, in powder metallurgy, consolidation behavior, in injection molding, material flow. LM technologists have to study and understand a host of materials- and process-related issues. A list of these challenges is given in Table 2. Each of these factors can play an important role in the economical manufacture of reliable and functional parts.

Table 2. Materials and processing challenges.

Materials	Process Planning	Processing	Post-processing	Properties
♦ Powders ♦ Binders ♦ Filaments ♦ Gas precursors ♦ Wires ♦ Sheets ♦ Support material ♦ Green strength	♦ Tool path ♦ Masking ♦ Road dimensions ♦ Layer increment ♦ Preheat ♦ Process control • Temperature • Dimension	♦ Binding ♦ Curing ♦ Sintering ♦ Powder or wire feeding ♦ Molten pool forming ♦ Solidification ♦ Reaction zone ♦ Gel casting	♦ Debinding ♦ Firing ♦ Co-firing ♦ Resin infiltration ♦ Melt infiltration ♦ Densification ♦ Heat treatment ♦ Machining	♦ Porosity ♦ Bonding ♦ Shrinkage ♦ Residual stress ♦ Distortion ♦ Dimensional accuracy ♦ Surface finish ♦ Microstructure ♦ Mechanical properties

Materials issues involve selection of powders, binders, filaments and support with the correct particulate size, shape, formulation, composition, and physical properties. An important factor to consider is the green strength of the part after it is fabricated and before it is densified. Handling issues, among others, will dictate material formulations. Optimized *process planning* for defect-free deposition is important. This involves control of parameters such as tool path, road dimensions, masking, layer increment and, in thermal processes, temperature. Devising optimal trajectories for the deposition head for good inter-road and inter-layer bonding is critical. Designing and fabricating masks optimally is important for precision. Determining the correct conditions for *processing* such as binding, curing, sintering, melting and solidification is important. Determining the correct schedules for *post processing* such as debinding, firing or co-firing, liquid infiltration, densification, heat treatment and light machining are important. Finally, the utility of a part depends on the presence or absence of defects such as porosity, poor bonding,

shrinkage, residual stress and distortion, and *properties* such as dimensional accuracy, surface finish, microstructure and mechanical and other properties.

Understanding materials behavior, whether it be solidification of melted powder or formulation of binder-particulate mixtures, whether it be thermally-induced residual stresses in metals or curing cycles for polymers, is the first step towards reliable fabrication by LM. The next step is to determine processing parameters by experimentation, guided by process models based on prior experience and theories involving heat and fluid flow. For instance, in the case of laser additive processes, Beuth and Klingbeil [30] have developed process maps that link melt pool dimensions with laser power density. Hofmiester et al [31] have developed techniques to visualize the dynamic melt pool and monitor its dimensions and temperature distributions in real time. Combining these two diagnostic tools, active process control is envisioned with the possibility of making metallic parts with high dimensional tolerance and low residual stress. Another example of process development is the anti-alias filtering incorporated in the DPS process by Ventura [32], which turns sharp black and white stair-steps into smooth gray-scale boundaries. Improved surface finish for ceramic parts was demonstrated by achieving a 6-fold reduction in the average stair-step height. Jafari et al [33] developed "tool path based deposition planning" for fused deposition processes. Porosity-free, accurate deposited structures were achieved by a plan involving varying roller (filament feed) speeds. Binder burnout and co-firing are challenges facing multi-material deposition. Allahverdi et al [34] showed that differential expansion caused cracking and delamination in FDMM fabricated PZT tube actuators having helical Ag/Pd electrodes. One solution was to use pre-oxidized metallic powder and deoxidize the electrode after sintering. A pressing need before LM becomes an acceptable manufacturing tool is the characterization of the microstructure and properties of the fabricated part. Rhenium fabricated by LAM was found to be essentially fully dense and reasonably accurate in dimensions, but it had coarse grain size requiring some means of grain refinement such as alloying [35]. Another observation was oxygen pick-up, but this was mainly confined to the surface, which would be ground away. Rhenium is also made by EB-CVD. Grain size and grain orientation have implications for mechanical behavior of shapes such as missile thruster nozzle. EB-CVD will result in grains oriented parallel to the hoop stress formed by the exiting gases, while LAM will result in grains oriented perpendicular to the stress.

THE PROMISE OF LM

Like many new technologies that capture the imagination, LM comes with many promises. A laundry list of benefits, not available with traditional fabrication methods, is touted. The promise of LM falls under three categories: *Unique Fabrication Capabilities, Important Applications and Commercial Implications.* Under unique fabrication capabilities are *avoiding conventional tooling* as there is no need for specialized tooling or part fixturing; *geometric flexibility*, which is the ability to fabricate complex part geometries and arbitrary shapes; and *local composition control*, which is the ability to form graded structures and compositions. Among important applications, LM has made most headway in the fabrication of *prototypes*, a designer's dream. Prototypes are non-functional solid models that are useful visualization aids. LM has made inroads in *machine tooling*, or the fabrication of tools and dies for high volume manufacturing such as injection molding. Manufacturing functional, form and fit *parts and components* is the holy grail for LM. With the transition in manufacturing from *mass production* to *mass customization*, LM is expected to play a major role. It is ideally poised for "lot size of

ONE", or the manufacture of highly individual products, but on a mass scale. With the gradual disappearance of skill-based fabrication, it is expected that LM will *replace handiwork*. There are commercial implications of LM technology. It is suitable for *agile and rapid manufacturing* and has potential to shorten product development time and mitigate logistical problems. Parts can be made *on-demand* instead of having stockpiles of inventory. Through *reverse engineering*, parts whose drawings are not available can be replicated. Through *remote manufacturing*, parts can be made on-board ships, submarines, space station or a remote location. On-line commerce for parts will flourish. Since machining is all but eliminated, an ancillary benefit is less exposure to hazardous material, e.g., lubricants, and less waste, e.g., turnings. It must be recognized that these promises of LM are not mutually exclusive, that two or more of the promises can act simultaneously.

LM has made significant strides in delivering on some of the promises. Sachs [36] gives two examples of *avoiding conventional tooling*. One is extensive use by Bell Helicopter of patterns made of SLA Quickcast for aluminum investment castings purely due to timing, not economic, considerations. The second is SLS-fabricated non-load bearing duraform polyamide parts for Boeing for military applications, which are now under study for certification. An example of *geometric flexibility* is the fabrication of tool dies with conformal-cooling channels. Enhanced heat extraction, increased production rate and reduced cost can thus be achieved. Conformal cooling channels can be made by depositing sacrificial material, which is later removed as with MIT's 3DP process [37], or can be made while fabricating the part as with Optomec's LENS process [16]. Another example of part complexity is the casting for a fuel cross over made for Rocketdyne by Soligen's 3DP process [36]. The *local composition control* capability of LM was demonstrated by cell phone casings made with color printed-in by Z Corp [36] and oral forms of medical "flash dosage" made with drugs in the interior and flavor masking on the exterior by Therics [36]. Both companies use the 3DP technique.

There are many examples of *prototypes*, *tooling* and *parts* made by LM in the literature. The ability to produce conformal cooling channels in tool dies will be a big benefit to the *machine tooling* industry. AeroMet. reports that their LAM-fabricated high-end titanium alloy *parts* are undergoing certification by the aerospace community [38]. A recent issue of The Economist magazine [39], defined *mass customization* as building to meet customer's individual orders rather than for stock. The goal is to deliver precisely the system that the customer wants and when he wants it. LM is poised to contribute to the mass customization or "build-to-order" concept. As an illustration of mass customization, Sachs [36] gives the example of plastic aligners for orthodontic work marketed by Align Technology. A sequence of plastic aligners, instead of wire braces, are used to move teeth. The aligners are thermoformed on molds of sequential models made by 3D Systems' SLA technique. The sequential models are computer-generated for teeth reorientation and are based on the initial plaster cast of the rubber impression of the crooked teeth. Conventionally, the aligners are milled, but details in regions where the teeth meet are best achieved by LM. An example of *replacing handiwork* is the hearing aid [36]. In conventional practice, substantial manual skill is needed to go from the rubber model to the final hearing aid. But, with the disappearance of these skills, these parts can now be built by LM. From a virtual model of the inner ear, Siemens Corporation created a shell by SLS. Electronics were later added to the shell to create the finished product.

Fabrication of spare parts and reproduction of components for which there is no engineering data are important benefits for several industries, especially the military. This *reverse engineering* concept is demonstrated by Anderson et al [40], who are adapting the 3DP

technique to fabricate metallic components. The plan is to start with an original component, perform a CT scan on it, generate the 3D data files, send it over the internet to a 3DP machine such as that marketed by Prometal, which produces a functional replica of the original part. Issues relating to reliable data transfer, logistics and internet security will have to be dealt with. The *remote manufacturing* promise of LM is being explored by the US Army TACOM division to produce replacement parts on demand in the field. For this purpose, the "Mobile Parts Hospital" program was conceived. The rapid manufacturing system consists of a LENS station for fabrication of metal parts and a multitask machining center to meet surface finish and tolerance requirements [41].

LM OPPORTUNITIES

It is recognized that progress is being made and will continue to be made towards realizing the promise of LM. However, LM is continuously evolving. While the bulk of the development work has been done in making single material, monolithic parts and objects for prototype and structural applications, programs exploiting the multi-material capability of LM are progressing. One goal is to develop functional and multi-functional materials with minimum post-processing. A multi-functional material could serve a dual purpose, e.g., structural and energy storage. Another goal is to fabricate systems with minimal assembly. Steps such as marking, drilling and soldering are time consuming and with every additional step in the manufacturing cycle the probability of defects and errors increase. With LM, "plug-and-play" modules can be readily made for modular devices. Minimizing assembly results in compact, lightweight, reliable and economical systems. Multi-material deposition machines, such as Rutgers' FDMM [42], are on-line and being utilized as experimental tools to manufacture a variety of functional parts. Opportunities for research are in the *biomedical engineering*, *electronics* and *sensor* areas, in the development of *hybrid manufacturing* systems and in *nanomanufacturing*.

In the *biomedical engineering* field considerable headway has been made in the orthopedic tissue engineering area. Strong scaffolds for bone growth having controlled porosity and made of bio-compatible polymers have been fabricated with techniques such as MIT's 3DP [20], Rutger's FDC [24] and ACR's EFF [25]. It is conceived that the scaffold will be in the shape of the degenerated or damaged bone, such as a broken jaw. The scaffold is impregnated with osteoinductive material to produce a polymer-calcium phosphate composite blend. After implantation, bone would replace the blend. In the *electronics* field, the goal is to replace the step-intensive tape casting/screen printing process of making MCMs with direct deposition of the individual passive and active components, the interconnects and the surrounding packaging media. Resistors, capacitors, conductors, through connections, all made of appropriate materials, are deposited, layer-by-layer, to achieve 3D device integration. It is envisaged that thermoelectric and other sensors, EMI shielding and heat sinks can also be integrated following a given design concept. Progress has been made with techniques such as NRL's MAPLE DW [43] by which a variety of electronic elements were accurately deposited on substrates and TA&T's stereo-photolithography [44] by which fully dense, narrow silver lines were deposited on ceramic substrates. The goal is to develop an automated process for electronic packaging having high resolution and high level of integration. A major scientific issue with multi-material deposition is determining the optimum densification (co-firing) conditions for defect-free and reliable components. In the *sensor* area, Li and Prinz [45] demonstrated embedding of optical

fiber in a structural element. The ability to continuously monitor structural health using embedded sensors would be very beneficial indeed.

Hybrid manufacturing processes utilize additive/subtractive operations such as Stanford's SDM [7]. Part quality, e.g., surface finish, is enhanced. Parts with internal channels such as miniaturized fuel cells and microfluidic devices are possible. Other permutations could involve a combination of techniques such as laser deposition and electroplating [45] or combining with MEMS and VLSI to realize products in the meso-scale regime. The ultimate goal is *integrative product synthesis.* Now that nanotechnology is here to stay, attention has shifted to *nanomanufacturing*. Cost effective, high throughput nanomanufacturing is the goal. Techniques such as Mirken et al's [46] dip-pen nanolithography (DPN), which involves depositing material via molecular transport using an AFM tip, and Chou et al's [47] nano imprint lithography (NIL), which involves imprinting by mold pressing and pattern transfer are being explored to realize this goal. Both approaches are ideally suited for layer-by-layer fabrication and would benefit from the LM concept of CAD-based intelligent manufacturing. It must be cautioned that in the nanometer world, gravity becomes negligible and surface tension, electrostatic and Van der Waals forces come into play, which will have implications for deposition and manipulation at the nano-scale. It is hoped that a multi-instrument (deposition-removal) machine possible with LM technology could be built to achieve fabrication, inspection, measurement and certification necessary for robust nanomanufacturing.

SUMMARY

A multitude of LM techniques has been described. Some have achieved commercial status, others are still in the laboratory stage. The aerospace, automotive, defense, electronics, and biomedical fields are poised to benefit from LM. LM is compatible with all classes of materials - metals, ceramics, polymers, composites, organics, and biomaterials. With this compatibility comes a host of materials and processing issues and challenges. Progress has been made to assuage some of these challenges. The current status of LM is that the science and engineering is mostly understood, however material properties such as microstructure and performance need to be documented thoroughly. For LM to achieve manufacturing status, full automation is a must, fabrication speed needs to be enhanced and engineering properties need to be measured and certified. LM is multi-disciplinary, involving manufacturing, robotics, mechanical, materials, information technology, computer science, chemistry, biomedical and electronics. It begs a system's approach. LM comes with many promises - avoiding conventional tooling, geometric flexibility, local composition control, mass customization, agile manufacturing, remote manufacturing and reverse engineering. Significant strides have been made in fulfilling some of these promises. Opportunities in LM are in bone scaffolds, 3D device integration, hybrid manufacturing and lithography-based nanomanufacturing.

ACKNOWLWDGEMENT

The author wishes to express his gratitude to several practitioners of LM, too many to be listed, for sharing their thoughts and their work for this paper. The author is indebted to various other sources for examples. The author is thankful to ONR for providing the funds and the inspiration to perform this research.

REFERENCES

1. http://www.3dsystems.com.
2. S. C. Ventura et al., "Direct Photo Shaping-A New SFF Process for Ceramic Components," Proceedings of the 7th International Conference on Rapid Prototyping, (1997), pp. 271-278.
3. L. Beluze, A. Bertsch and P. Renaud, *Proceedings of SPIE*, **3680**, (2), 808-817, (1999).
4. A. Cohen, G. Zhang, F-G. Tseng, F. Mansfeld, U. Frodis and P. Will, "EFAB: Batch Production of Functional, Fully-Dense Metal Parts with Micron-Scale Features", SFF Sym. Procs., (University of Texas-Austin, 1998), pp. 161-168.
5. http://www.solid-scape.com.
6. R. Merz, F. B. Prinz, K. Ramaswami, M. Terk and L. E. Weiss, "Shape Deposition Manufacturing", SFF Sym. Procs., (University of Texas-Austin, 1994), pp. 1-8.
7. J. W. Kietzman, A. G. Cooper, L. E. Weiss, L. Schultz, J. L. Lombardi, and F. B. Prinz , "Layered Manufacturing Material Issues for SDM of Polymers and Ceramics", SFF Sym. Procs., (University of Texas-Austin, 1997), pp. 133-140.
8. M. Orme and C. Huang, "Thermal Design Parameters Critical to the Development of Solid Freeform Fabrication of Structural Materials with Controlled Nano-Liter Droplets," SFF Sym. Procs., (University of Texas-Austin, 1995), pp 88 - 95.
9. http://www.sandia.gov/media/robocast.htm.
10. W. Zhang, M. C. Leu, G. Sui and Z. Ji, "An Experimental and analytical Study of Ice Part Fabrication with Rapid Freeze Prototyping", SFF Sym. Procs., (University of Texas-Austin, 1999), pp. 591-598.
11. C. E. Duty, D. L. Jean, and W. J. Lackey, *Cer. Eng. & Sci. Procs.*, **20** (4), 347-354, (1999).
12. J.E. Crocker, S. Harrison, L. Sun, L.L. Shaw and H.L. Marcus, *JOM*, **50**, (12), 21-23, (1998).
13. J. J. Beaman and C. R. Deckard, "Solid Freeform fabrication and Selective Laser Sintering," North American Manufacturing Research Conference Proceedings, (1987), pp. 636-640.
14. http://www.eos-gmbh.de/default.htm.
15. M. L. Griffith, D. M. Keicher, C. L. Atwood, J. A. Romero, J. E. Smugeresky, L. D. Harwell and D. L. Greene, "Free Form Fabrication of Metallic Components using Laser Engineered Net Shaping," SFF Sym. Procs., (University of Texas-Austin, 1996), p. 125.
16. P. Chavez, "From the Inside Out: The LENS™ Process is Fueling a Paradigm Shift in Modern Manufacturing Applications," *Technical Brief*, Optomec, (2000).
17. F. G. Arcella and F. H. Froes, *JOM*, **52**, (5), 28-30, (2000).
18. J. Mazumder, J. Choi, K. Nagarathnam, J. Koch and D. Hetzner, *JOM*, **49**, (5), 55-60, (1997).
19. http://www.pom.net.
20. E. Sachs, M. Cima, A. P. Williams, D. Brancazio and J. Cornie, *J of Eng for Industry*, **114**, (4), 481-488, (1992).
21. http://www.zcorp.com.
22. http://www.extrudehone.com.
23. http://www.stratasys.com.
24. S. C. Danforth, A. Safari, M. Jafari and N. Langrana, "Solid Freeform Fabrication of Functional Advanced Ceramic Components", *Naval Research Reviews*, vol. L, (Office of Naval Research, Three/1998), pp. 27-38.
25. R. Vaidyanathanan, J. Walish, J. L. Lombardi, S. Kasichainula, P. Calvert and K. C. Cooper, *JOM*, **52**, (12), 34-37, (2000).

26. D. Dave, J. Matz and T. W. Eagar, "Electron Beam Solid Freeform Fabrication of Metal Parts", SFF Sym. Procs., (University of Texas-Austin, 1995), pp. 64-71.
27. K. M. B. Taminger, R. A. Hafley and D. L. Dicus, "Solid Freeform Fabrication: An Enabling Technology for Future Space Missions", 2002 International Conference on Metal Powder Deposition for Rapid Manufacturing Proceedings, (MPIF, Princeton, NJ, 2002), pp. 51-60.
28. http://www.cubictechnologies.com.
29. http://home.att.net/~castleisland.
30. J. Beuth and N. Klingbeil, *JOM*, **53**, (9), 36-39, (2001).
31. W. Hofmeister, M. Wert, J. Smugeresky, J. A. Philliber, M. Griffith, and M. Ensz, *JOM-e*, **51**, (7), (1999).
32. S. Ventura et al, "Progress Report on Solid Freeform Fabrication Activities at SRI International," Presented at ONR's Wood's Hole Meeting, May 26, 2000.
33. W. Han, M.A. Jafari, S. Danforth and A. Safari, "Tool Path-Based Deposition Planning in Fused Deposition Processes," *J. of Mfcg. Sci. & Eng.*, ASME Transactions, in press, (2002).
34. M. Allahverdi, B. Jadidian, B. Harper, S. Rangarajan, M. Jafari, S.C. Danforth, and A. Safari, "Development of Tube Actuators with Helical Electrodes Using Fused Deposition of Ceramics", Proceedings of 12th IEEE International Symposium on Applications of Ferroelectrics, ISAF 2000, edited by S.K. Streiffer, B.J. Gibbons, and T. Tsurumi, (IEEE publication # 00CH37076, 2001), pp 381-384.
35. K. P. Cooper, F. G. Arcella and H. N. Jones, "Metallurgical Analysis of Laser Formed Rhenium", Rapid Prototyping of Materials, edited by F. D. S. marquis and D. l. Bourell, (TMS, Warrendale, PA, 2002), pp. 119-132.
36. E. Sachs, "Manufacturing by Solid Freeform Fabrication," SFF Sym. Procs., (University of Texas-Austin, 2001), pp. 596-618.
37. E. Sachs et al, "Production of Injection Molding Tooling with Conformal Cooling Channels using the 3DP Process," SFF Sym. Procs., (University of Texas-Austin, 1995), pp. 448-467.
38. F. G. Arcella, AeroMet Corp., Eden Prairie, MN, *private communication*.
39. A Long March, *The Economist*, July 14, 2001, p. 63.
40. R L. Anderson, J. Lembo and M. Rynerson, "Rapid Manufacturing of Metal Matrix Composite Materials using 3DP," Presented at Symposium on Rapid Prototyping of Materials, TMS Fall Meeting, Columbus, OH, October 7-10, 2002.
41. S. Kolisch, "Army to Produce replacement Parts on Demand in the Field," *The AMPTIAC Quarterly*, **6**, (3), 3-6, (2002).
42. M.A. Jafari, W. Han, F. Mohammadi, A. Safari, S.C. Danforth, and N. Langrana, "A Novel System for Fused Deposition of Advanced Multiple Ceramics," *J. Rapid Prototyping* (in press).
43. D. B. Chrisey, A. Pique, J. Fitz-Gerald, R. C. Y. Auyeung, R. A. McGill, H. D. Wu and M. Duignan, *Applied Surface Science*, **154-155**, 593-600, (2000).
44. W. R. Zimbeck, J. H. Jang, W. Schulze and R. W. Rice, "Automated Fabrication of Ceramic Electronic Packages by Stereo-photolithography," Materials Research Society Symposium Proceedings Vol. 625, (MRS, Warrendale, PA 2000), pp. 173-178.
45. X. Li and F. B. Prinz, "Embedding of Fiber Optic Sensors in Layered Manufacturing," SFF Sym. Procs., (University of Texas-Austin, 1995), pp. 314-324.
46. R. D. Piner, J. Zhu, F. Xu, S. Hong and C. A. Mirkin, *Science*, **283**, 661-663, (1999).
47. S. Y. Chou, P. R. Krauss and P. J. Renstrom, *Appl. Phys. Lett.*, **67**, 3114, (1995).

Mat. Res. Soc. Symp. Proc. Vol. 758 © 2003 Materials Research Society LL1.5

Alumina-Doped Silica Gradient-Index (GRIN) Lenses by Slurry-Based Three-Dimensional Printing (S-3DP™)

Hong-Ren Wang, Michael J. Cima and Emanuel M. Sachs[1]
Department of Materials Science and Engineering
Massachusetts Institute of Technology
77 Massachusetts Avenue
Cambridge, MA 02139
[1]Department of Mechanical Engineering
Massachusetts Institute of Technology
77 Massachusetts Avenue
Cambridge, MA 02139

ABSTRACT

The traditional Slurry-based Three-dimensional Printing (S-3DP™) process has been used to fabricate complex structure materials by printing organic binders in selected positions on each printing layer. This process is modified to fabricate functional graded materials, such as gradient index (GRIN) lenses, by depositing different concentrations of dopant at different positions. The modified S-3DP™ process offers advantages over conventional GRIN lens processes, including reduced processing time, improved compositional flexibility, and increased index profile dimensionality. Two different approximately parabolic dopant concentration profiles, which have maximum alumina concentrations of 1.63 mol% and 2.50 mol%, are printed into silica powder beds using S-3DP™. The samples with maximum alumina concentration of 1.63 mol% have been sintered into optical transparency at 1650 ^{0}C for 30 minutes in a vacuum furnace ($5x10^{-6}$ torr) while an additional dehydration process before sintering was required for the samples with maximum alumina concentration of 2.50 mol%. The magnifying effects of GRIN lenses with profiles of 1.63 mol% and 2.50 mol% alumina were observed, yielding effective focal lengths of 10 cm and 6.1 cm, respectively. Light diffraction, which results from the locally inhomogeneous dopant distribution and reduces the optical quality of GRIN lenses, was also observed.

INTRODUCTION

Conventional glass-based GRIN lenses have been fabricated by various methods, including molecular stuffing [1], ion exchange [2-7], and sol-gel [8,9] techniques, that rely on stuffing of base glass compositions with index altering cations. The diffusion-controlled nature of these processes requires long processing times (typically > 100 hours), thereby limiting feasible component sizes to less than 13 mm. In addition, GRIN materials fabricated by ion exchange techniques are not suitable for high temperature applications since the migration of alkali ions results in the distortion of the index profile [8]. Alternative materials systems or fabrication methods for large-scale GRIN components with desired optical characteristics and good environmental and thermal stability are needed.

The S-3DP™ technology is an agile, facile method of producing near-net shape advanced ceramic components. Parts are constructed in a layer-by-layer build sequence. Each layer of the

component is created by jetting a ceramic slurry onto a substrate, then selectively printing a binder into the dried layer in the desired pattern. The excess powder is then removed to produce a three dimensional structure. The S-3DP™ process can be modified to fabricate functionally graded materials, such as GRIN lenses, by replacing the binder with a dopant solution of varying concentration. The S-3DP™ process for GRIN lenses is shown schematically in Figure 1. Production of GRIN materials by S-3DP™ offers several advantages over conventional processing methods, including reduced processing times (< 70 hours) yielding economical fabrication of large-scale components, improved compositional flexibility, and increased index profile dimensionality. The improved flexibility and compositional control offered by S-3DP™ allows for a single component lens system with greater functionality. This reduces the number of optical components required, yielding considerable weight savings. The lens stacking required to overcome optical aberrations of a photographic lens system, for example, can be replaced by a single S-3DP™ GRIN lens.

This research focuses on developing an alumina-silica based materials system that can be used in the S-3DP™ process. The system was chosen because of the miscibility of alumina and silica at high temperature. The fabrication and properties of the resultant alumina-doped S-3DP™ GRIN lens are discussed in the following sections.

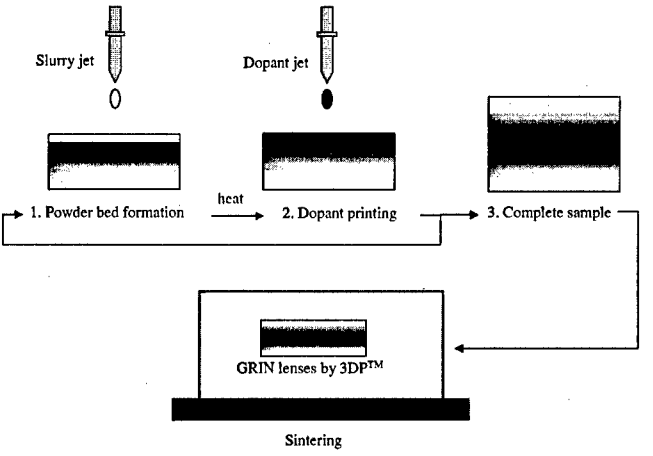

Figure 1. The schematic drawing of the S-3DP™ process for GRIN lenses.

EXPERIMENTAL PROCEDURE

The amorphous silica powder (Mitsubishi Chemical Company) used in this research had a median particle size of 1.4 μm and a surface area of 2.666 m^2/g. Aluminum nitrate nanohydrate ($Al(NO_3)_3*9H_2O$, Alfa Aesar) was used as the dopant source. The silica slurry with 30 vol% solid loading was prepared and ball-milled with glass media for 20 hours before printing. The chemical composition of the slurry is shown in Table I. Boric Acid was added to lower the sintering temperature. The alumina-doped powder beds were then made by S-3DP™. The

thickness of each printing layer was 73 μm. Two dopant concentration profiles, Design 2.5% max and Design 1.63% max, were deposited into the powder beds, as shown in Figure 2. The powder beds were heated to 900 °C for 4 hours to remove the hydroxyl groups introduced by the aluminum nitrate solution as well as the organic additives. Sintering was performed in a vacuum furnace (Centoor, MRF, pressure ~ $5x10^{-6}$ torr). Un-doped silica powder beds can be sintered to optical transparency at 1500 °C for 30 minutes. An additional dehydration process, 1000 °C for 24 hour in the vacuum furnace, was required for the powder beds with a maximum alumina concentration of 2.5 mol% before sintering. The alumina-doped powder beds were sintered at 1650 °C for 30 minutes. The sintered powder beds were polished and observed under an optical microscope. Electron Probe Micro Analysis (EPMA) was used to measure the dopant concentration profiles of the sintered samples.

Table I. The chemical composition of the silica slurry.

Silica Powder (vol%)	Deionized Water (vol%)	Methanol (vol%)	Poly(ethylene glycol) (MW:400)	NH_4OH (M)	H_3BO_3 (wt%)
30	35	35	3 wt% based on silica	0.20	1 wt% based on silica

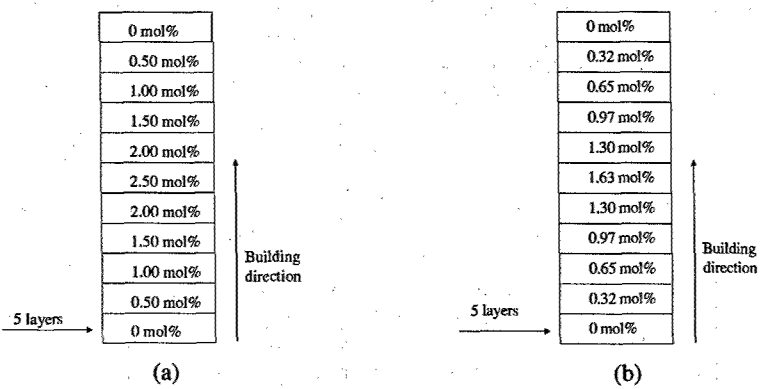

Figure 2. The concentration profiles of alumina in the GRIN lenses of (a) Design 2.5% max and (b) Design 1.63% max.

RESULTS AND DISCUSSION

The mixture of alumina and silica tends to form mullite ($3Al_2O_3+2SiO_2$) at temperatures higher than 950 °C [10]. The formation of mullite can be minimized by increasing the cooling rate and using an alumina concentration lower than 5 mol% [10]. The maximum alumina concentration in this study was 2.50 mol% (Figure 2). No crystallization in the alumina-doped

powder beds was found after heating at 900 °C for 4 hours. Several sintering conditions were tested. Optical transparency was achieved by sintering at 1650 °C for 30 minutes and cooling at the maximum rate (~500 °C per minute from the sintering temperature) allowed by the furnace. The magnifying effects of the sintered powder beds are shown in Figure 3. The MIT markers under the sintered GRIN lenses are enlarged in the vertical direction, as expected from the dopant concentration profiles shown in Figure 2. The object and image sizes in the vertical direction were measured, allowing the effective focal length (f_{eff}) to be determined by the following equation [11]:

$$\frac{1}{f_{\text{eff}}} = \frac{1}{S_1} - \frac{H_1}{H_2 * S_1} \tag{1}$$

where H_1 is the object size, H_2 is the image size, and S_1 is the distance between the lens and the object. The theoretical focal length (f_{th}) of a GRIN slab with a parabolic index of refraction profile is given by the following equation [12]:

$$f_{th} = \frac{1}{\left(\frac{n_{\max}^2 - n_{\min}^2}{0.25w^2}\right)^{1/2} \sin\left(\frac{d}{0.5w}\left(1 - \frac{n_{\min}^2}{n_{\max}^2}\right)^{1/2}\right)} \tag{2}$$

where w is the width of the GRIN slab, d is the thickness of the GRIN slab, n_{min} is the minimum index of refraction, and n_{max} is the maximum index of refraction. No direct measurement of index of refraction has been made. However, the index of refraction of the fused silicate (n) containing alumina has been studied and found to have a linear relationship with the alumina content [13] as:

$$n=1.4580+0.00192M \tag{3}$$

where M is the alumina concentration in mol%. The alumina concentration profiles of the Design 1.63% max and Design 2.5% max samples are shown in Figure 4. The profiles are fitted with parabolic curves. The maximum alumina concentrations of the Design 1.63% max and Design 2.5% max samples are found to be 1.04 mol% and 1.35 mol% and the maximum indexes of refraction (n_{max}) of both samples are calculated to be 1.46 and 1.4606 from Equation (3). The theoretical focal lengths of the sintered powder beds, assuming a parabolic index profile, are then calculated and compared with the effective focal lengths, as show in Table II. The effective focal length is very close to the theoretical values for the Design 1.63% max sample. The difference between the effective and theoretical values of the Design 2.5% max and Design 2.5% max(1) samples is due to the fact that the index profiles are not ideally parabolic. The actual concentrations are also lower than the designed values. This indicates that further research must be done to allow for more precise compositional control.

Observation of the sample perpendicular to the build direction shows a possibly problematic artifact of the printing process. The optical micrograph in Figure 5 and laser diffraction in Figure 6 show compositional variation within each layer. It is believed that the migration of dopant solution during the drying of each printed layer causes the non-uniform distribution of dopant within each layer. The locally high and low index regions within each layer diffract light

differently after the sample is sintered. Future research will focus on drying conditions and other methods to minimize this effect.

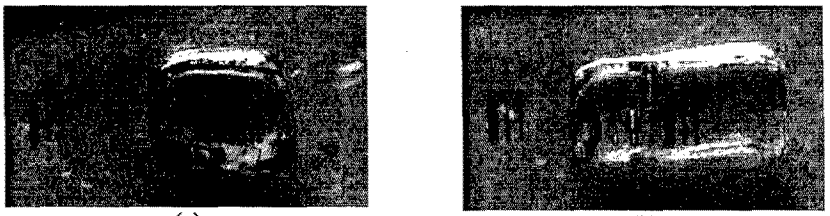

(a) (b)

Figure 3. The vertical enlargement with the GRIN lenses of (a) Design 2.5%(1) max and (b) Design 1.63% max above an MIT marker.

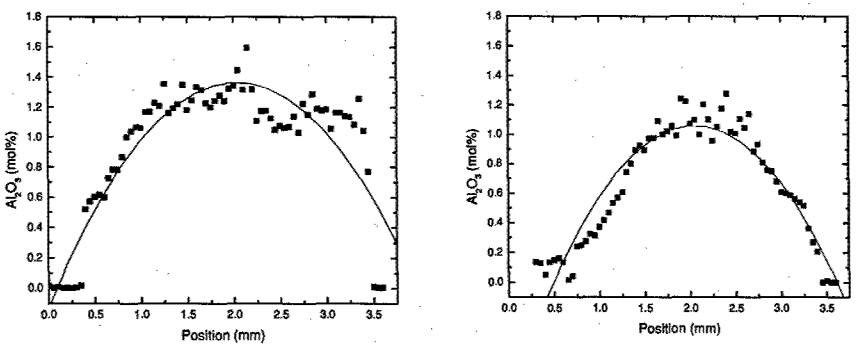

(a) (b)

Figure 4. The dopant distribution of the GRIN lenses of (a) Design 2.5% max(1) and (b) Design 1.63% max.

Table II. The effective (f_{eff}) and theoretical (f_{th}) focal lengths of different GRIN lenses.

	d (cm)	w (cm)	f_{eff}(cm)	f_{th} (cm)
Design 1.63% max	0.55	0.30	10	10.3
Design 2.5% max	0.70	0.30	4.68	6.27
Design 2.5% max (1)	0.60	0.30	6.10	7.28

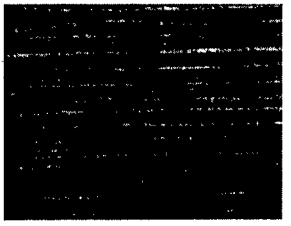

Figure 5. The layer merging problem investigated under the optical microscope.

Figure 6. The diffraction of the laser light shining through the sample.

CONCLUSIONS

The alumina-silica systems have been studied for the fabrication of GRIN lenses by S-3DP™. Optically transparent alumina-silica GRIN lenses were obtained by sintering at 1650 °C for 30 minutes. Three different GRIN lenses (Design 1.63% max, Design 2.5% max and Design 2.5% max(1)) with effective focal lengths of 10, 4.68, and 6.10 cm, respectively, have been successfully fabricated. EPMA results show the deviation of the actual dopant concentration from the designed value. Further research will focus on more precise local composition control and elimination of light diffraction due to locally inhomogeneous distribution of dopant.

REFERENCES

1. J. H. Simmons and *et al.*, *Applied Optics*, **18** [16] 2732-2733 (1979).
2. I. Kitano and *et al.*, *J. Japan Soc. App. Phys.*, **39**, 63-70 (1970).
3. J. E. Samuels and D.T. Moore, *Applied Optics*, **29** [28] 4042-4050 (1990).
4. S. Ohmi and *et al.*, *Applied Optics*, **27** [3] 496-499 (1988).
5. S. N. Houde-Walter and D.T. Moore, *Applied Optics*, **25** [19] 3373-3378 (1986).
6. A. R. Cooper and M.A. el-Leil, *Applied Optics*, **19** [7] 1087-1091 (1980).
7. A. D. Pearson, W.G. French, and E.G. Rawson, *Applied Physics Letters*, **15** [2] 76-77 (1969).
8. M. Yamane and *et al.*, SPIE Optical Engineering Press , 1993.
9. T. M. Che, J.B. Caldwell, and R.M. Mininni, Sol-Gel Optics, **1328,** 145-159 (1990).
10. J. F. MacDowell and G. H. Beall, *J. Am. Ceram. Soc.*, **52** [1] 17-25 (1969).
11. E. Hecht, "Optics," 4th edition, Addison-Wesley, 2002.
12. B. E. A. Saleh and M. C. Teich, "Fundamentals of Photonics," John Wiley & Sons Inc., New York, 1991.
13. K. Nassau, J. W. Shiever, and J. T. Krause, *J. Am. Ceram. Soc.*, **58** [9-10] 461 (1975).

Mat. Res. Soc. Symp. Proc. Vol. 758 © 2003 Materials Research Society LL1.6

Materials for Freeform Fabrication of GHz Tunable Dielectric Photonic Crystals

Paul G. Clem, James F. Carroll III[1] , Michael K. Niehaus[2], Joseph Cesarano III, James E. Smay[3], Jennifer A. Lewis[4], and Shawn-Yu Lin
Sandia National Laboratories,
Albuquerque, NM 87185-1411
[1] Also Alfred University, Alfred, NY
[2] Also New Mexico Institute of Mining and Technology, Socorro, NM
[3] Also University of Illinois, Urbana, IL
[4] Department of Materials Science and Engineering, University of Illinois, Urbana, IL

ABSTRACT

Photonic crystals are of interest for GHz transmission applications, including rapid switching, GHz filters, and phased-array technology. 3D fabrication by Robocasting enables moldless printing of high solid loading slurries into structures such as the "woodpile" structures used to fabricate dielectric photonic band gap crystals. In this work, tunable dielectric materials were developed and printed into woodpile structures via solid freefrom fabrication (SFF) toward demonstration of tunable photonic crystals. Barium strontium titanate ceramics possess interesting electrical properties including high permittivity, low loss, and high tunability. This paper discusses the processing route and dielectric characterization of $(Ba_xSr_{1-x}TiO_3)$:MgO ceramic composites, toward fabrication of tunable dielectric photonic band gap crystals.

INTRODUCTION

The material system of barium strontium titanate (BST) has been widely studied for low loss, tunable dielectric applications. Such applications include phased array antennas, photonic crystal waveguides, and photonic crystal filters. Phased array antennas enable beam sweeping without mechanically oscillating the antenna by altering the capacitance, and hence phase, of individual array elements and the vector of the array wavefront. Photonic crystal filters are 3D lattice structures that forbid the propagation of electromagnetic waves at distinct wavelengths or frequencies, thus creating a photonic band gap (PBG).[1,2] The unique ability of PBGs to create directions of zero effective photonic density of states enables waveguiding, switching, and filtering of a variety of electromagnetic radiation frequencies, from optical to GHz. Introduction of defects into these crystals enables photonic crystal waveguides, which allow propagation of light around 90° bends for the designed wavelength. To date, passive PBGs made of non-tunable materials have generally been produced, while introduction of tunable materials could enable high speed PBG switching and reconfigurable waveguide architectures. Developing a direct-write, tunable 3D PBG filter has been the focus of this research study, as a first step toward waveguides and more complicated devices.

Three methods were combined in this work: (1) fabrication of PBGs by the 3D SFF method of Robocasting[3-7], (2) modeling of PBG transmission and reflection as a function of dielectric permittivity and loss, and (3) development of novel tunable dielectric materials. The combination of these three efforts is aimed at enabling 3D fabrication of active photonic band gap structures, which would enable selective transmission or reflection of frequencies by

electrically tuning the PBG lattice. Examples of a static Al_2O_3 PBG lattice robocast by Smay et al. and its GHz transmission properties are shown in Figure 1.[4,5]

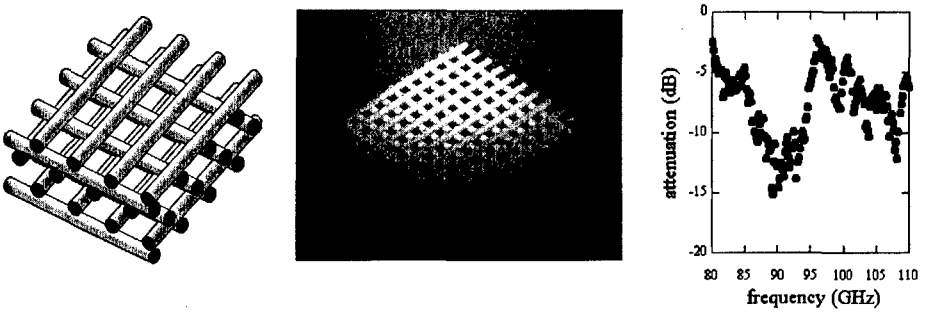

Figure 1. (left) Representation of a face centered tetragonal dielectric woodpile PBG structure, which mimics diamond cubic symmetry, (center) a robocast alumina PBG structure with 300μm rods, and (right) GHz transmission measurements of the robocast PBG structure. (Smay et al.[4,5])

While a large stop band is demonstrated for such Al_2O_3 PBG structures, the ability to selectively tune this behavior from fully transmitting to fully reflecting has not been developed. A means of tuning these materials is use of near-ferroelectric materials, which rearrange domains on application of a DC voltage. For single crystal barium titanate ($BaTiO_3$), the theoretical maximum tuning of relative permittivity is 97% ($\varepsilon_r = 4700 \rightarrow 130$). We are developing similar materials based on $(Ba_{1-x}Sr_x)TiO_3$ (BST), which show a high degree of AC permittivity tuning at low DC biases, as shown in Figure 2.

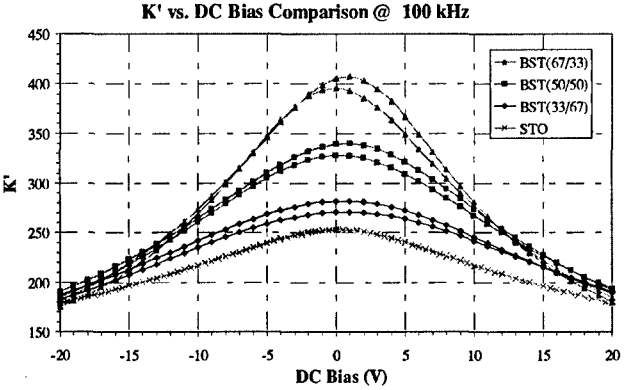

Figure 2. Dielectric constant vs. DC bias for $Ba_xSr_{1-x}TiO_3$ compositions from x = 0 to 0.67.

Materials choice for this application involves finding a compromise between high dielectric tunability and retaining a high Q (= $\varepsilon_r'/\varepsilon_r''$), ideally Q = 200-1000 in the 1-100 GHz range. Significant modeling of PBG structures was conducted with CFD Research Corporation (Huntsville, AL), to understand the influence of permittivity, dielectric loss, and PBG geometry on transmission gap width, depth, and stability. The CFDRD electromagnetic modeling data, acquired with their multiphysics ACE+ modeling software, demonstrated the importance of proper choice of dielectric constant and loss for applications. In brief, the modeling predicted very low loss materials ($\varepsilon''/\varepsilon' < 0.01$) with a permittivity $\varepsilon' < 100$ would be necessary for PBG applications. Materials with higher losses would be expected to be absorptive in the GHz range, while materials with higher permittivities would be expected to reflect, not transmit, GHz radiation outside the designed band gap region. In our present research, we have worked to counterbalance the desired low losses with the desired high dielectric constants (K) and high tunabilities of the material, where tunability is the percent change of the dielectric constant on application of a DC voltage bias (Figure 2). Again, this tunabilty is a means to shift the photonic band gap frequency, which would enable voltage-tunable filter and other active applications.

The objective of this materials research was to formulate, process, and fabricate a 3-D PBG lattice structure composed of BST mixed with a low permittivity, low loss nonferroelectric oxide, in this case magnesium oxide (MgO).[8] The first objective was to determine the desired ratio of barium titanate (BT) to strontium titanate (ST) to produce a low loss dielectric ($\varepsilon''/\varepsilon' < 0.01$) with a reasonable amount of tunability (3-15%). The $Ba_XSr_{1-X}TiO_3$ ratio selected was x = 33, BST 33/67. MgO was mixed in a mol ratio of 1:3 BST to MgO to correspond to unit cell matching. The corresponding material system of BST and MgO resulted in loss values less than 1% and tunability of approximately 5%. We are presently fabricating and testing 3D PBG structures of this material.

EXPERIMENTAL DETAILS

$Ba_XSr_{1-X}TiO_3$ powders were prepared by a solid state processing method. Commercial powders of $BaTiO_3$ and $SrTiO_3$ were milled together in ethanol with yttria stabilized zirconia (YSZ, diameter 10 mm) media for 24 hours on a U.S. Stoneware ball mill. The suspension was dried in an explosion-proof drying oven for 12 hours at 60°C. This powder was then dry milled for 4 hours to break up any agglomerates formed during the drying process, and calcined at 1100°C in air for 6 hours. After calcination, the BST powder was mixed with the MgO and ball milled in ethanol for an additional 24 hours. The suspension was again dried in an explosion proof oven for 12 hours at 60°C, and dry milled for an additional 4 hours. The BST-MgO powders were calcined at 1300°C in air for 6 hours. Upon completion of the final calcination step, the powders were sieved using a U.S. Standard Series No. 18 sieve.

The composite powders were uniaxially pressed at 100 MPa, then sintered at 1300°C in air for 6 hours. The sintered ceramic pellet dimensions were 13 mm in diameter and 1 mm or 3mm in thickness. The pellets were then polished and electroded by a DC sputtering unit. Dielectric constant, dielectric loss, and tunability measurements were carried out from 20 Hz to 1 MHz with an HP4284A Precision LCR meter. Dielectric measurements from 0.5-20 GHz were carried out on 7mm diameter, 3mm thickness cylindrical samples using an HP 8510 Network analyzer and HP 85071B software.

RESULTS AND DISCUSSION

Low frequency dielectric measurements, comparing BST pellets to BST-MgO pellets, indicated the addition of nonferroelectric MgO to BST significantly reduced the dielectric constant, as expected. A logarithmic dielectric mixing rule generally appeared appropriate for these composites. For example, BST 33/67 without MgO displayed a dielectric constant of 553, but when 3 moles of MgO were added for every 1 mol of BST, the dielectric constant decreased to 37 at 1 MHz. This addition of MgO allowed the dielectric constant to be tailored to near a goal of $\varepsilon' = 40$, as was modeled to be appropriate for PBG transmission.

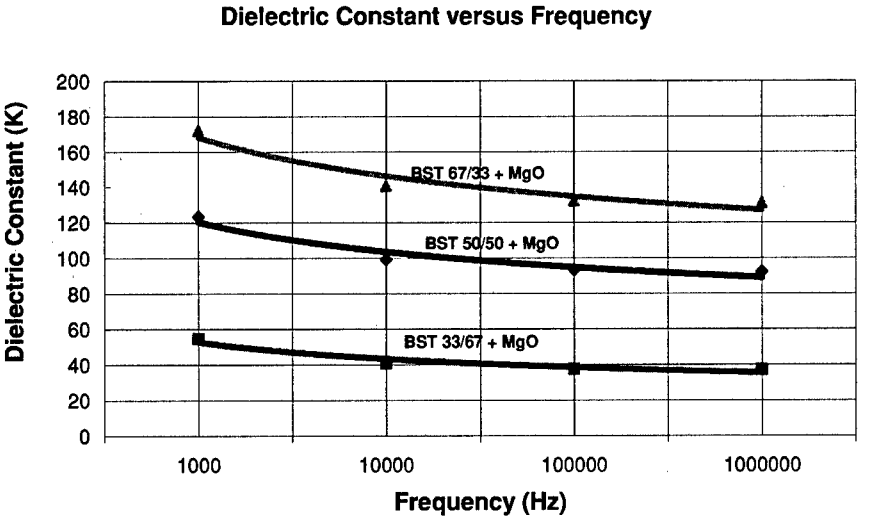

Figure 3. Variation of BST/MgO composite dielectric constants for different Ba:Sr ratios.

As one would expect, on increasing the barium content of the BST, the dielectric constant increased (Figures 2 and 3). This is attributed to the transition from paraelectric behavior to near-ferroelectric behavior as the overall Ba/Sr content nears 67/33. As can be seen in Figure 2, the capacitance-voltage hysteresis loops display an asymmetrical offset for samples of BST 50/50 and 67/33 composition, suggesting local polar regions undergoing domain switching. Such switching would have the effect of raising both permittivity and dielectric loss. For PBG applications, the dielectric loss has a crucial impact on the photonic band gap transmission. In particular, the PBG insertion loss (dB) increases, and the band gap sidewall slope (dB/GHz) and well depth (dB) decrease as dielectric loss increases. BST(33/67):MgO composites appear to display an acceptable combination of permittivity and low loss for tunable GHz applications. Q values above 500 were obtained for direct written composites, measured at 1 GHz (Figure 4).

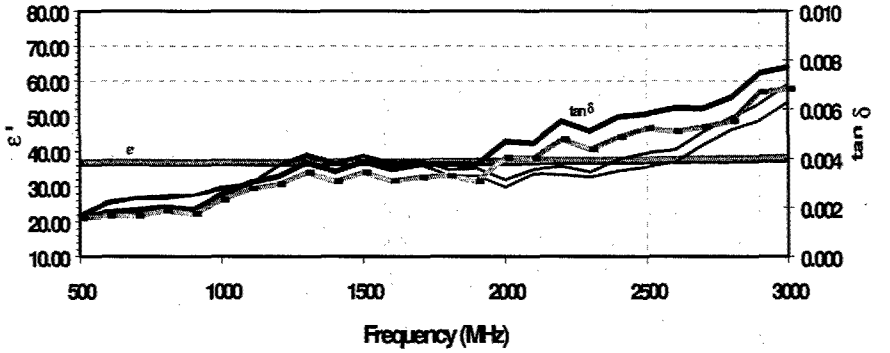

Figure 4. BST(33/67):MgO permittivity and tan δ versus frequency for four samples.

The ability to change permittivity and dielectric constant has been predicted by modeling to enable photonic band gap to shifts to different frequencies (Figure 5). Initial results show good correlation between measured Al_2O_3 PBG properties and CFDRC modeling results, and is being extended to BST PBG structures.

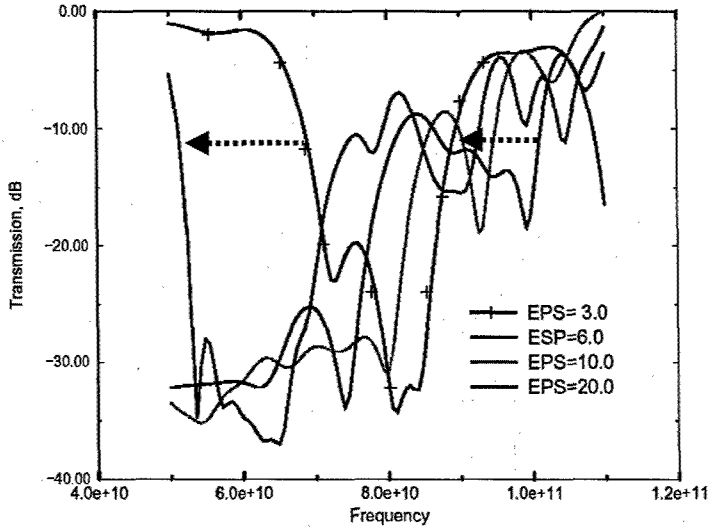

Figure 5. Effect of lattice permittivity on 40-120 GHz PBG transmission, for ε' (EPS) = 20 to 3.

CONCLUSION

In this work, we developed high Q, tunable dielectric compositions for direct write compatible, tunable PBG structures. Modeling results suggest a tunable dielectric with a $\varepsilon' = 40$ and $Q \sim 1000$ would be a suitable material for this application. From initial studies incorporating $(Ba,Sr)TiO_3$ with a non-ferroelectric phase, one strong candidate for such photonic band gap filters is BST33/67 + MgO (1:3 molar ratio). By adding the MgO in a 1 to 3 molar ratio, a low dielectric constant ($\varepsilon' = 37$) was achieved with low loss. BST 33/67 + MgO composites displayed lower loss values than BST 50/50 or 67/33 composites at high frequency (1 MHz - 100 GHz), which is our region of interest. From the GHZ testing, BST33/67 + MgO displayed a high enough permittivity in the GHz region to provide the necessary photonic band gap shift desired. Initial testing of robocast PBGs of BST/MgO composites are underway.

ACKNOWLEDGMENTS

This research was supported by DARPA-DSO under the Metamaterials program directed by Dr. Valerie Browning. Sandia is a multiprogram laboratory operated by Sandia Corporation, a Lockheed Martin Company, for the United States Department of Energy under contract DE-AC04-94AL85000.

REFERENCES

1. Special issue on Photonic Crystals, Advanced Materials **13**(6), 369-450, (2001).
2. K.M. Ho, C.T. Chan, C.M. Soukoulis, R. Biswas, M. Sigalas, Solid State Commun. **89**(5) 413 (1994).
3. J. Cesarano, R. Segalman, P. Calvert, Ceram. Ind. **148**(4), 94 (1998).
4. J.E. Smay, J. Cesarano, and J.A. Lewis, Langmuir **18**(14), 5429 (2002).
5. J.E. Smay, G.M. Gratson, R.F. Shepherd, J. Cesarano, and J.A. Lewis, Adv. Mater. **14**(18), 1279 (2002).
6. B.A. Tuttle, J.E. Smay, J. Cesarano, J.A. Voigt, T.W. Scofield, W.R. Olson, and J.A. Lewis, J. Am. Ceram. Soc. **84**(4) 872 (2001).
7. J.E. Smay, J. Cesarano, B.A. Tuttle, and J.A. Lewis, J. Appl. Phys. **92**(10), 6119 (2002).
8. L.C. Sengupta, E. Ngo, J. Synowczynski, Integrated Ferroelectrics **15**(1-4), 181 (1997).

Mat. Res. Soc. Symp. Proc. Vol. 758 © 2003 Materials Research Society LL1.8

Thermal and Residual Stress Modelling of the Selective Laser Sintering Process

Ameer K. Ibraheem, Brian Derby and Phillip J. Withers
Manchester Materials Science Centre, University of Manchester and UMIST, Grosvenor Street, Manchester M1 7HS, UK.

ABSTRACT

The production of functional tool steel components by selective laser sintering requires an understanding of the effects of the laser processing parameters on the microstructure evolution during the fabrication process. This would allow the production of tools that have predictable and reproducible microstructure, good mechanical properties and low residual stresses. In this paper, finite element modelling has been carried out to investigate the temperature distribution and residual stresses during laser sintering of hot-work tool steel powders. The effects of the laser power and scanning rate on the selective laser sintering process have been investigated. Thermal residual stresses accumulated during the process have been predicted and compared with strain measurements made using neutron diffraction.

INTRODUCTION

A suite of materials processing technologies has emerged capable of producing mechanical components directly from computer-aided design models, without the need for part-specific tooling. These technologies represent new processing capabilities known as rapid prototyping (RP). The basic feature of this fabrication approach is the repetitive deposition of material layers. In this process, the laser beam is focused onto a powder bed. A single layer of the part to be manufactured is melted, then the platform is lowered, powder is delivered on top of the previously processed layer, and the laser is scanned again to melt the second layer of the part on top of the first layer, and so on. This method offers the possibility of direct fabrication of metallic parts in a single step process. It's also, capable of producing functionally complex components on a reduced lead-time, and therefore, a significant reduction in production cost can be anticipated. This manufacturing style matches very well with the economically sensitive markets of today. This has been the main driver for investigating and developing these processes. However reliable manufacture can only be achieved if the process is developed to the degree that reproducible tools having satisfactory properties can be built. A better understanding of the effects of all parameters that influence the laser sintering process, such as laser power, scanning rate, scanning spacing, scanning pattern is needed. Only then can a tool that has a maximum strength and minimum residual stress be fabricated. Finite element modelling is useful in this respect for selecting operating parameters to minimize residual stresses in the manufactured components.

Other investigators have used finite element modelling for 1D, 2D and 3D thermal analysis to simulate the selective laser sintering process using a single material [1-2], or multiple materials [3]. These simulations have provided valuable insight into how thermal gradients and thermal residual stresses are developed in the manufactured components.

In the present study, the thermal analysis is carried out in such a manner that new elements are born during deposition. These then take part in the thermal analysis over successive time steps, dependant on the scanning rate of the laser beam. The dimensions of the elements are

selected from data that is determined experimentally depending on the laser power and scanning speed. Residual stresses in the manufactured parts are measured using neutron diffraction and compared with the predicted values.

THE MODEL

The model is described schematically in Figure 1. The analysis is carried out using a simple geometry, with the final size of the part being 20x20x9 mm^3. The numerical simulation is carried out using ANSYS code. The analytical solution uses the 3D thermal element SOLID70 to simulate the temperature field coupled with the 3D structural element SOLID45 to simulate the stress field. The nodal temperatures obtained from the thermal analysis act as the load. Initially all elements are removed using the command elements kill. The first element is generated on a mild steel substrate at a time step that depends on the scanning rate of the laser beam. Thermal analysis is then carried out and the second element is born in the following time step. This is repeated until the first track is completed. Then the second and further tracks are built up in the same manner, until the first layer is complete. The second layer is built up on top of the first layer and so on. The element is born as a solid before passing under the laser. It becomes liquid when its temperature exceeds its specified melting temperature (1427°C). Then solidifies when its temperature becomes below the melting point. The size of each element is determined by the melting depth and the track width of the fused powder. These are determined experimentally for a series of different laser powers and scanning rates from single track, thin wall and cube depositions. The selective laser processing was carried out using steel powders with a Nd-Yag laser at Liverpool University. The diameter of the laser beam is 100 μm. The material used was H13 hot work tool steel powder, (0.4% C, 0.4% Mn, 1% Si, 5.25% Cr, 1.35% Mo, 1% V), produced by Osprey Metals, UK.

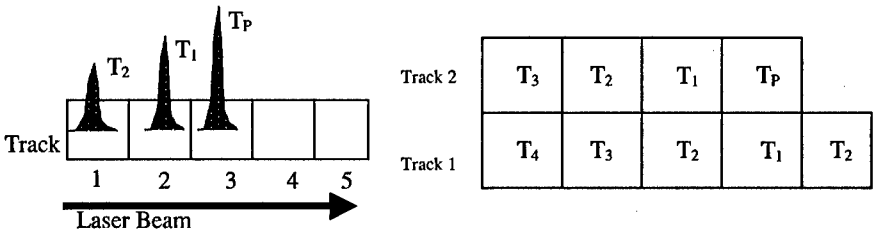

Figure 1. Elements are generated along a track in successive time steps, depending on the operating parameters. Each element reaches a peak temperature, when the laser beam passes over it. $T_P > T_1 > T_2 > T_3 > T_4$

The latent heat of fusion is not considered in the model and neither is convection from the liquid phase because of the small liquid pool size that is generated during laser sintering. The volume change associated with melting and solidification is also neglected. Heat loss is taken to be by conduction to the mild steel substrate and by convection to the air.

RESULTS AND DISCUSSION

The operating window, i.e. the laser power and frequency for melting the H13 powder was determined for the Nd-Yag laser, Figure 2. The track widths, Figure 3 were also determined for some laser power and scanning rates, these were used to determine the element size in the model for a given applied laser power.

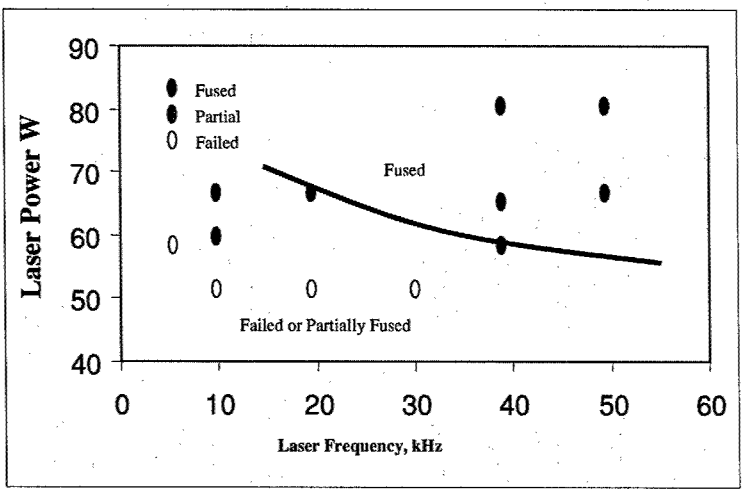

Figure 2. The effect of laser power and frequency on the fusion of steel powder.

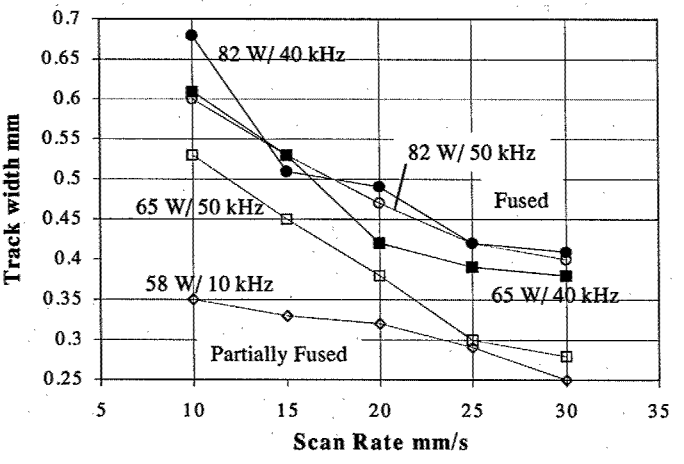

Figure 3. Track width decreases with the increasing scan rate, but it increases with increasing laser power for the same frequency.

Predictions of the transient temperature fields from the model are presented in Figure 4, for a laser power 80 W and scan speed of 500 mm/s. It can be seen that the size of the melting pool (>1427°C) is quite small and slightly larger than the diameter of the laser beam. Elements cool down rapidly (after 0.35 sec) and reheat again when the laser beam passes on top of them again. Therefore thermal residual stresses are expected to develop in the fused part after it cools down to room temperature.

Residual strains were measured in the fused part by neutron diffraction using the dedicated engineering instrument (ENGIN) on the PEARL beamline at the ISIS, the pulsed and muon source at the UK Rutherford Appleton Laboratory [4]. The strain in a material is

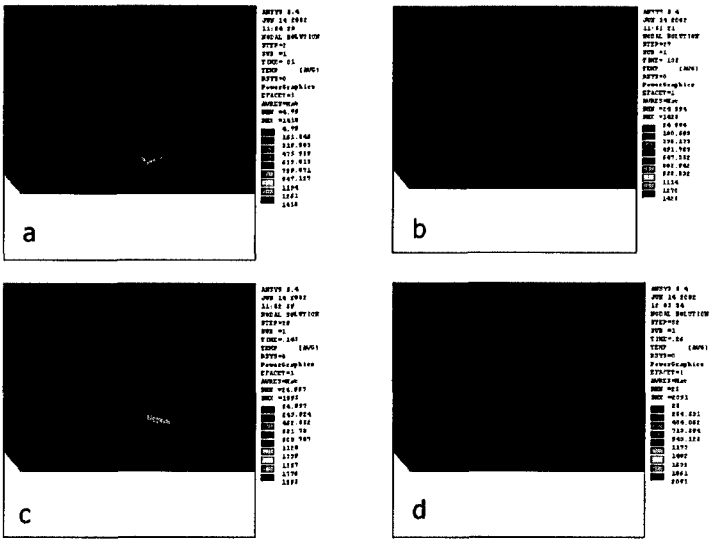

Figure 4. Transient temperature fields during the deposition process, at times (a): starting the first track, 0.01 sec, (b): after first layer, 0.135 sec, (c): starting the second layer, 0.145 sec and (d): two complete layers: 0.25 sec.

determined by the change in the atomic lattice planes relative to the lattice planes of the strain free material. The plane spacings of the strain free material were determined using H13 steel powder.

Neutron diffraction showed minimal residual strains in the fused blocks. Figure 5(a) shows an example of elastic strains in the laser scan direction through the thickness of the block. For comparison, the stress model also predicted low tensile residual stresses in the block. An example of the through thickness residual stresses field at the mid-plane of the block is shown in

Figure 5(b). Such a residual stress field is similar to that of a butt weld joint in which tensile stresses develop in the weld and compressive stresses develop in the base metal [5]. Although, the model predicts small tensile residual stresses, the residual strain measurement however is reasonable since these blocks are found to be only 85% dense, because of the presence of pores that are generated at the interface between adjacent tracks, Figure 6. This has probably allowed the thermal residual stresses to be relieved during processing. Porosity is thought to have an effect on the thermal and stress modelling and will be introduced into the model to determine how significant the effect is. Porosity makes the measurement of these already small residual stresses quite difficult.

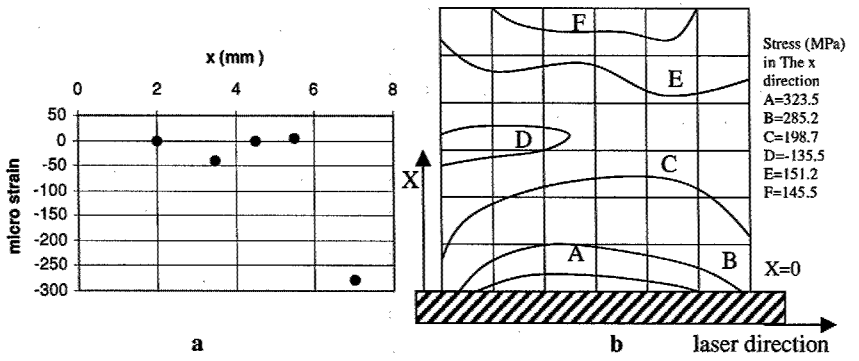

Figure 5. **(a)** Residual strains measured in the direction of the laser beam transverse through the sample thickness. **(b)** Predicted through thickness residual stress field at mid-plane of the block.

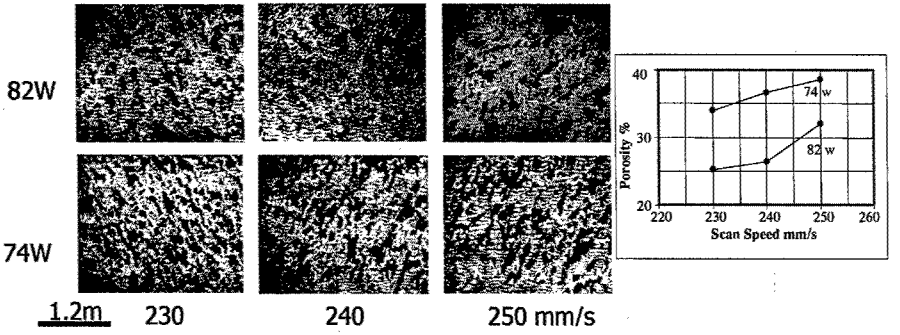

Figure 6. Presence of porosity in the fused samples, as a function of laser power an scan speed. Porosity increases with the increase of scan rate, and decreases with the increase of laser power.

CONCLUSIONS

Finite element modelling has been carried out to investigate the temperature distribution and residual stresses during laser sintering of hot-work tool steel powders. The effects of the laser power and scanning rate on the selective laser sintering process have been investigated. Thermal residual stresses accumulated during the process have been predicted to be quite small tensile stresses. Neutron diffraction showed minimal residual strain in the fused blocks probably due to the presence of pores that allowed stress to be relieved during processing.

REFERENCES

1. M. Kandis and T. L. Bergman, J. Manufact. Sci. Eng. **122**, 439, (2000).
2. T. H. C. Childs, C. Hauser, C. M. Taylor and A. E. Tontowi in *Proceeding of the 11th Annual SFF Symposium*, edited by D. L. Bourell, J. J. Beaman, R. H. Crawford, H. L. Marcus and J. W. Barlow, (The University of Texas, 2000) p100.
3. K. Dai and L. Shaw, Acta Mater. **49**, 4171 (2001).
4. M. Daymond, ISIS, Rutherford Appleton Laboratory, Chilton, Oxon, OX11 0QX, UK.
5. R. A. Owen, R. V. Preston, P. J. Withers, H. R. Shercliff and P. J. Webster, Mat. Sci. & Tech., In print (2002).

ACKNOWLEDGMENTS

The authors would like to thank Simon Pogson, Bill O'Neil and Peter Fox, Dept. of Engineering, The University of Liverpool for providing the fused samples and for many useful discussions. Thanks are also extended to Phill Dickens and Poonjolai Erasenthiran, Mechanical & Manufacturing Engineering, Loughborough University, Julian Evans and Shoufeng Yang, Department of Materials, Queen Mary, University of London for the many useful discussions. PJW acknowledges a Wolfson- Royal Society Merit Award. The research described here is supported by the Physical Sciences Research Council, under the INDEMAND programme, grant reference GR/N21697.

Mat. Res. Soc. Symp. Proc. Vol. 758 © 2003 Materials Research Society LL1.9

Surface Over-Melt During Laser Polishing of Indirect-SLS Metal Parts

J. A. Ramos†, D. L. Bourell, J. J. Beaman
Texas Materials Institute, Department of Mechanical Engineering, The University of Texas at Austin
†Department of Mechanical and Metallurgical Engineering, Pontificia Universidad Católica de Chile

ABSTRACT

Laser polishing of indirect-SLS parts made from 420 stainless powder infiltrated with bronze has been achieved using CO_2 and Nd:YAG lasers. Two mechanisms have been previously proposed for the reduction in surface roughness, namely: shallow surface melting (SMM) and surface over-melt (SOM). In SMM reflow of the molten surface minimizes the peak-valley height driven by capillary pressure and liquid curvature. On the other hand, during SOM the melting depth is such that the entire surface becomes liquid and formation of surface periodical structures dominates driven by a surface tension gradient. This surface morphology was identified by means of optical and scanning electron microscopy (SEM). The onset of this regime is dictated by the energy density (i.e., ratio of laser power to scan speed and beam diameter) as well as the initial roughness R_a value prior to laser surface polishing. In contrast with SMM, onset of the latter mechanism increases the roughness R_a with speed reduction. A thermo-physical model is presented, signaling good agreement with roughness R_a and characteristic surface wavelength results obtained for varying laser beam scan speeds. Understanding the surface over-melt mechanism is critical for determining the optimum polishing conditions that minimize roughness.

INTRODUCTION

Rapid Prototyping has proven to be a successful technique in shortening the manufacturing cycle for parts with complex geometry [1,2]. Selective Laser Sintering (SLS) is one such RP technology that benefits from the advantage of building up solid object from polymer, ceramic and metal-alloyed materials in powder form [1-3]. To build objects out of metal alloys, two variations of the SLS are currently available, namely, indirect and direct SLS. The former requires post-infiltration of a SLS formed green part (high melting point metal) by metal of low fusion point. The latter technique, as its name indicates, involves consolidation of metal powder by direct laser induced local fusion. However, the surface roughness achieved during the manufacture of rapid prototyping articles by these SLS techniques is still in the range of several microns [3]. At the same time, a sub-micron surface roughness R_a value is determinant when functional mechanical parts are to be built [3,4]. This is an issue yet to be solved along the path of rapid manufacturing evolution. An intermediate step in solving this problem is to employ the hardware available to the SLS process, specifically a high power laser unit and galvanometer scanner mirrors, to provide for laser polishing of the rapid prototyped object. Pursuing this objective, Ramos et al [5] were able to obtain decrements in R_a values up to 3 times the as-received values on indirect-SLS parts made from LaserForm ST-100, an alloy system commercialized by 3D Systems, Inc. This alloy consists of a 420 stainless steel matrix, 40 wt.% infiltrated with bronze (5 wt.% tin). For the operating window used (laser power 320 W and scan speed 692.7-101.3 mm/s), two surface modification regimes existed: shallow surface melting (SMM) and surface over-melt (SOM). In SMM reflow of the molten surface minimizes the peak-valley height driven by capillary pressure and liquid

curvature [6]. On the other hand, during SOM the extent of melting is such that the entire surface becomes liquid and low frequency high amplitude surface periodic formation dominates. These morphologies were identified by means of optical and scanning electron microscopy (SEM) [5,7]. The onset of each regime is dictated by the energy density (i.e., ratio of laser power to scan speed and beam diameter) as well as the initial roughness R_a value prior to laser surface polishing. For a fixed laser power, SMM shows a reduction in roughness R_a below the initial value with decreasing scanning speed up to a limiting value. Further decrease in scan speed causes onset of the SOM mechanism with increase in roughness R_a with speed reduction [5]. The present paper deals with the physical phenomena occurring during the laser surface polishing of indirect-SLS metallic parts, specifically the surface over-melt mechanism as reported in [5,7].

Since high power lasers have been used in materials processing research, observation of regularly spaced striations on metal surfaces after laser induced melting has already been reported [8-10]. The physical properties of the material as well as the laser process condition (i.e., power and speed) appear to determine the formation of such surface periodical structures. In some instances, these surface waves are attributed to an electrodynamic effect caused by the interaction of the laser radiation with surface electromagnetic waves causing modulation of the energy absorbed into the metal [8]. These resonant periodic structures have periods determined by the wavelength polarization and incident angle of the laser radiation [8]. However, experimental data reported in [9] showed that the typical length of these structures for carbon steels is of the order of 400 to 500 microns. Under these circumstances it has been concluded that it is most likely that these "large" wavelength features are not a consequence of the electrodynamic effect only, but are also impacted by the generation and relaxation of thermo-capillary oscillations on the molten surface layer by surface tension gradients induced during the motion of the laser beam. The periodic structures formed this way become frozen before relaxing completely as the cessation of the heat input from the energy source causes fast quenching of the melt [8-10].

A schematic drawing of the laser polishing process utilized to reduce the surface roughness of LaserForm ST-100 indirect SLS parts is illustrated in Figure 1. A focused laser beam of sufficient power to melt the surface of the object was raster-scanned at high speed a long a rectangular track. As shown in Figure 2 the motion of the beam caused the molten material underneath it to be pulled away towards the solidifying front, thus a ripple is formed.

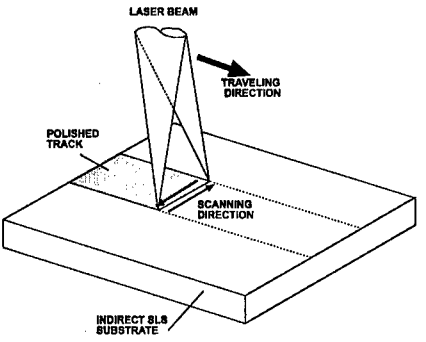

Figure 1. Schematic diagram of the laser polishing process.

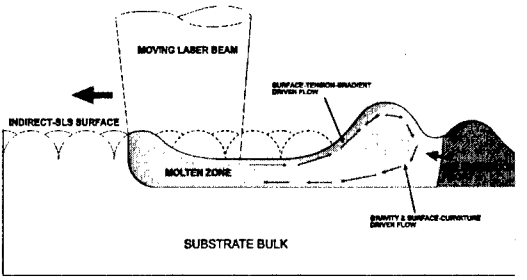

Figure 2. Schematic of a surface periodic structure formation during SOM mechanism.

This mass flow phenomenon is driven by the surface temperature difference between the laser beam and the solidifying zone caused by the motion of the laser beam [8]. This temperature difference creates a surface tension gradient of different sign that exerts a shear force on the liquid surface towards the solidifying front. Gravity and surface curvature effects counter this external shear force.

Once the thermal gradient vanishes, these forces will restore the surface height to the free level. However, viscous forces will delay this relaxation process. The periodic structure thus formed will only relax until the solidification front freezes it [9], assuming that the time for solidification is small relative to the time required for complete relaxation.

The thermo-physical model presented in this paper describes the amplitude behavior of the observed surface micro-relief and estimates the resulting surface roughness R_a. It is assumed that the surface relief formed acquires the shape of a sinusoid of fixed propagation vector, k and spatial phase ϕ. R_a values were measured from laser polished tracks that showed an increment in roughness with reducing scan speed above the as-received value, as well as the characteristic surface wavelength of each track λ. These measurements provided data to validate the model.

THEORY

Thermo-Physical modeling

Figure 3 illustrates a schematic diagram of the different variables that are involved in the formation of a surface relief Δh whenever a laser beam traverses the surface of the material causing a depth of melt h.

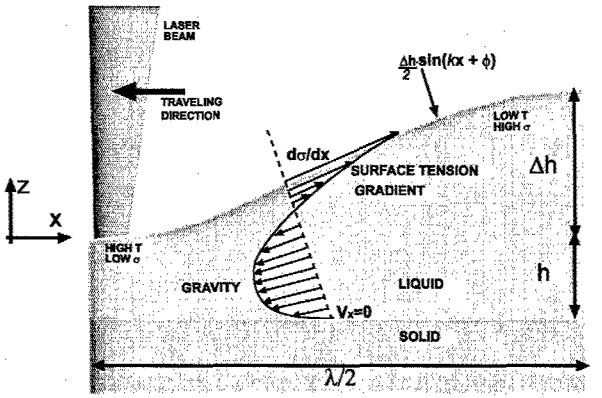

Figure 3. Schematic of the rippling phenomenon encountered in the SOM mechanism.

Anthony and Cline [8] modeled analytically this surface-rippling phenomenon observed during laser surface melting of metals. The steady-state form of the Navier-Stokes equation (i.e., Newton's Second law) for an incompressible fluid in two dimensions (x, z) over a horizontal surface was solved analytically together with the continuity equation, Eq. 1 and 2. Fluctuations in the fluid velocity v_x were considered only in the z direction.

$$-\frac{\partial p}{\partial x}+\frac{\partial}{\partial z}\left(\mu\frac{\partial v_x}{\partial z}\right)=0 \tag{1}$$

$$\int_{-h}^{\Delta h} v_x dz = 0 \tag{2}$$

Where p is the pressure tensor and μ is the dynamic viscosity of the fluid. The main assumption is that the only restoring force acting on the fluid comes from the hydrostatic pressure head difference along the x direction. In other words the effect of gravity g was accounted for as a pressure gradient due to the increase in surface height. This yields,

$$\frac{\partial p}{\partial x}=\rho g\frac{\partial z}{\partial x}\bigg|_{z=\Delta h} \tag{3}$$

Boundary conditions include the existence of a surface tension gradient at the surface of the fluid caused by the surface temperature difference at the laser beam center and where the solidification front is located. A zero velocity in the x direction is also assumed at the solid-liquid interface.

$$\text{at } z = \Delta h \qquad \frac{\partial \sigma}{\partial x}=\mu\frac{\partial v_x}{\partial z}=\frac{\partial \sigma}{\partial T}\frac{dT}{dx} \tag{4}$$

$$\text{at } z = -h \qquad v_x = 0 \tag{5}$$

Where T, σ and ρ are the surface temperature, surface tension and density, respectively. For most metals the surface tension of the liquid phase decreases with increasing temperature, this exerts a shear force that pulls the liquid away from the laser beam center (maximum temperature) towards the solidified zone (minimum temperature) thus forming a surface wave of maximum height, Δh. The expression for this maximum height as presented in [8] is,

$$\Delta h_{MAX}=\frac{3}{2}\cdot\frac{\Delta T}{\rho g h}\cdot\frac{d\sigma}{dT} \tag{6}$$

This expression determines the maximum surface height achieved. This height varies directly with the surface temperature change ΔT between the laser beam and solidification front (i.e., T_L-T_m) and surface tension temperature coefficient. It also varies inversely with the depth of melt h and the gravity term, ρg. There is no term that incorporates the effects of the surface curvature on the formation of the maximum height. We propose the following modification to Eq. 3 and 6, considering that the surface attains a sinusoidal shape having a characteristic wavelength λ. This is,

$$\frac{\partial p}{\partial x}=\left(\rho g\frac{\partial z}{\partial x}+\sigma\frac{\partial^3 z}{\partial x^3}\right)_{z=\Delta h} \tag{7}$$

$$\Delta h_{MAX}=\frac{3}{2}\cdot\frac{\Delta T}{(\rho g+\sigma\left(\frac{2\pi}{\lambda}\right)^2)h}\cdot\frac{d\sigma}{dT} \qquad (8)$$

In this situation gravity and surface curvature provide restoring forces that act against the effect of the surface tension gradient during the laser interaction. Once the laser beam has moved a considerable distance away (greater than λ 2), the surface thermal gradient vanishes and the established periodic surface wave commences to relax driven by these restoring forces (i.e., gravity and curvature). Opposing these forces is the deviatoric component of the pressure tensor of the fluid, namely the viscous force which is proportional to the dynamic viscosity μ of the fluid and the velocity gradient. An expression for the relaxation of the surface height as a function of time t, for times less than the local solidification time of the melt is given by,

$$\Delta h(t)=\Delta h_{MAX}\cdot\exp\left(-\frac{\mu}{\rho}\cdot\left(\frac{2\pi}{\lambda}\right)^2\cdot t\right) \qquad (9)$$

It can be readily shown that the decaying exponential term is typical of an over damped harmonic oscillatory system, and it has been also reported before in [9].

To determine the surface temperature change due to a moving laser beam we resort to the known steady-state analytical solution to the semi-infinite temperature field for a concentrated energy source moving with constant velocity [11]:

$$T(x,y,z)=\frac{P\cdot(1-\Re)}{2\pi\cdot K_{MOD}}\cdot\frac{1}{\sqrt{x^2+y^2+z^2}}\exp\left(-\frac{v_{SCAN}}{2\alpha}\cdot\left(\sqrt{x^2+y^2+z^2}+x\right)\right)+T_0 \qquad (10)$$

Where P, $\Re$, v_{scan}, α, and K_{MOD} have been defined in Table I. As it can be noticed, this expression becomes infinite when evaluated at x = y = z = 0, i.e. immediately below the laser beam. However, distances 1% of the laser beam diameter away from the center of the laser beam give a compromise for evaluating the surface temperature beneath the laser, T_L.

At the same time, Eq. 10 serves the purpose of estimating a value of the depth of melt, h. Although this expression does not consider the phase change from solid to liquid when the temperature field reaches the melting point, this effect can be approximated by modifying the heat conductivity, K, such that it includes the latent heat of fusion of the material [12].

Obtaining the maximum depth of melt means finding the coordinates (x_{max}, z_{max}) for y = 0 from Eq. 10. The maximum depth of melt , z_{max} = -h, occurs at half the length value of the major axis of the surface isothermal ellipse (i.e., at $T=T_m$). By making y = 0 and z = 0, and solving Eq. 10 for x, two values are found, and x_{max} is the average of the latter two roots. Then, z_{max} is found by solving Eq. 10 again this time evaluating it at y = 0 and x = x_{max}, and the negative root corresponds to h. Equation 10 also can provide a way to determine the solidification time, since the heat flow at the maximum depth of melt can be determined from it. This is obtained by taking the first derivative with respect to z, and evaluating it at (x_{max}, 0, z_{max}). The average solidification front velocity at the maximum depth of melt can be then obtained by using the Stefan condition [13], taking into account the specific latent heat of solidification of the alloy, L.

$$\bar{v}_{SOLIDIFICATION} = \frac{-K \left.\frac{\partial T}{\partial z}\right|_{z=-h}}{\rho L} \quad (11)$$

This velocity can then be used to estimate the average solidification time,

$$t_{SOLIDIFICATION} = \frac{2h}{\bar{v}_{SOLIDIFICATION}} \quad (12)$$

Finally, the estimation of the average arithmetic surface roughness R_a can be assessed simply by evaluating half of the maximum height after a relaxation time equal to $t_{SOLIDIFICATION}$, this is,

$$R_a = \frac{\Delta h(t_{SOLIDICATION})}{2} \quad (13)$$

RESULTS AND DISCUSSION

Optical and SEM observations

Figure 4 shows an optical macrograph of the surface of a laser polishing track created using a 320 W laser and a scanning speed of 128.9 mm/s, (620.6. J/cm^2). The average width of this track is 1930 μm. A periodic pattern of oblique linear features can be observed forming an angle of 30° with the horizontal axis (i.e., the laser beam scanning direction). From SEM observation at low magnification of the same sample surface, it can be seen more clearly that this periodic pattern is spaced in average every 360 μm approximately, Figure 5.

Figure 6 shows a higher magnification SEM image of the surface of the same laser track illustrating two consecutive pattern peaks which are spaced apart a magnitude λ = 300 μm and are clearly parallel to each other. Another feature seen on this image is the appearance of a second periodic pattern closely spaced making a 30° angle with the former. This pattern however, seems discontinuous by comparison.

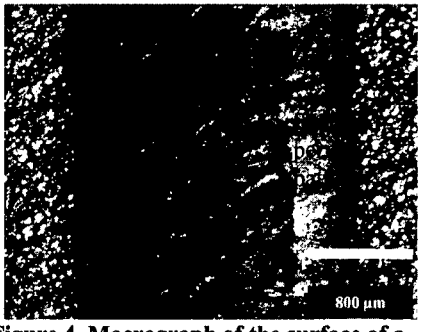

Figure 4. Macrograph of the surface of a SOM laser polished track, x25.

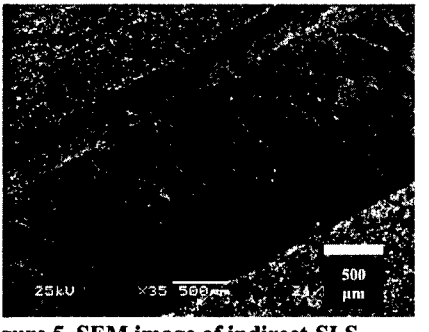

Figure 5. SEM image of indirect-SLS surface treated under SOM conditions, x35.

Closer examination of the surface in Figure 7 reveals that the second periodic pattern is dispersed, yet it has a shorter spacing of 10-20 μm. It is also perpendicular to the traveling direction of the laser beam thus parallel to the scanning direction. It consists of multiple agglomerated particles (1-5 μm in size), most likely oxides of Si, Al and Cr as determined previously [6].

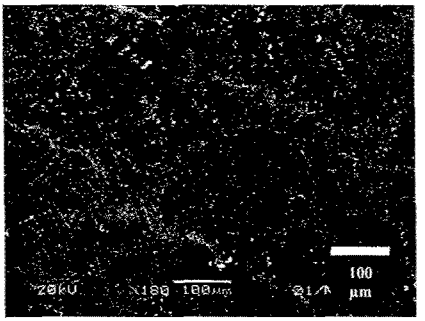

Figure 6. SEM image showing two consecutive periodic peaks, x180.

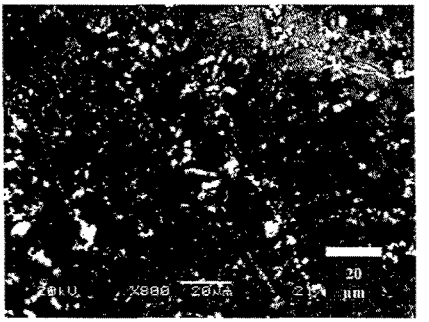

Figure 7. SEM image illustrating oxide particles along high frequency ripples, x800.

Thermo-Physical model results

The results of the thermo-physical model described previously are plotted in Figure 8 as surface roughness data together with experimental data measured from several laser polished tracks performed on LaserForm-ST100 specimens. The as-received R_a value of the surface was 2.98 μm. The laser power was kept fixed at 320 W and the scanning speed was varied from 692.7 to 101.3 mm/s. However, only the R_a results for speeds ranging from 177.2 to 101.3 mm/s are plotted below, as this is thought to be part of the SOM regime. Table I presents the variables included in the model as well as their values and units. Physical properties correspond to a 60 wt.% 420 stainless steel - 40 wt.% bronze (5 wt.% tin) alloy mixture.

Table I. Definition of variables.

Variable	Definition	Value
P	Laser power	320 W
R	Reflective and convective loses	0.725
ρ	Density of solid phase	8247 kg/m^3
α	Thermal diffusivity of solid phase	$4.985 \cdot 10^{-5}$ m^2/s
L	Specific latent heat of solidification	146500 J/kg
K	Heat conductivity of solid	172 W/m/K
K_{MOD}	Modified heat conductivity	216 W/m/K
v_{SCAN}	Laser beam scan speed	101-177 mm/s
T_M	Melting temperature	1347 °C
To	Initial temperature	25°C
μ	Viscosity of the liquid	5.45 mPa/s
σ	Surface tension of liquid-vapor	1.609 J/m^2
dσ/dT	Surface tension temperature coefficient	-26.1 mJ/m^2

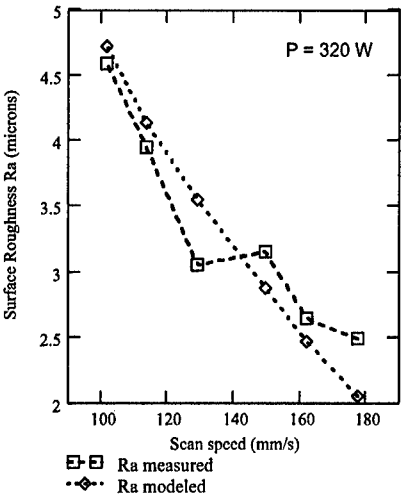

Figure 8. Plot of experimental and modeled surface roughness R_a data versus scan speed.

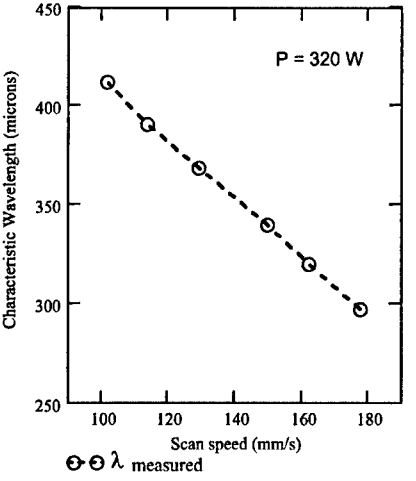

Figure 9. Plot of the measured average surface wavelength λ versus scan speed.

From the plot in Figure 8 it can be seen that the experimental data show an increment in the R_a value with decreasing scan speed. Only the data point corresponding to a scan speed of 128.9 mm/s seems to be lower compared to its predecessor. Nonetheless the difference in 0.10 μm falls within the standard deviation of the measurements (i.e., +-0.69 μm). The modeled R_a value shows the same trend as the measured values within the same order of magnitude. From the model, it can be inferred that as the scan speed is lowered the surface temperature immediately under the center of the laser beam increases, increasing the amplitude of the surface wave, but simultaneously the depth of melt is increased and so is the solidification time. These latter two variables tend to decrease the relief amplitude, however the effect of temperature overwhelms them. Moreover, the effect of adding a surface curvature term brings the amplitude down to a reasonable order of magnitude. The latter term and the viscous damping term depend on the characteristic wavelength of the surface periodic structure solidified. A plot of the measured average characteristic wavelength λ for each laser track is presented in Figure 9. Its trend is much the same as that of the modeled R_a values. We can infer that this parameter plays a significant role in the determination of the amplitude of the surface relief. As for the second periodic pattern observed under the SEM (Figs. 6 and 7), this model does not take into account its additive effect on the modeled surface roughness. However, it can be considered as part of the noise when measuring the R_a value of the treated surfaces experimentally.

CONCLUSIONS

Optical and SEM observation of the surface of the laser polished tracks under the SOM regime confirm the formation of two periodical structures, one of high frequency low amplitude and the other of low frequency high amplitude. Both contribute to the surface roughness

achieved after the laser polishing process, but the latter is thought to be more critical in increasing the R_a value above the as-received level.

A modified thermo-physical model based on previously reported models [8,9] is presented, signaling good agreement with roughness R_a and characteristic surface wavelength results obtained for a fixed laser power and varying laser beam scan speeds. Increment in roughness R_a value with decreasing scanning speed is predicted by the present model. The main contribution of the present model is the incorporation of the surface curvature effects as a restoring force aiding gravity to bring the amplitude of the surface wave down to zero. The main assumption here is that the surface relief behaves as it if were a sinusoid of fixed propagation vector.

ACKNOWLEDGEMENTS

The Laboratory for Freeform Fabrication gratefully acknowledges the support of the Office of Naval Research for funding the project "Surface Engineering for SFF Processes", Grant N°: N00014-00-1-0334. We would also like to thanks 3D Systems, Inc. (former DTM Corporation) for providing LaserForm™ ST-100 samples for testing.

REFERENCES

1. J.J.Beaman, J.W.Barlow, D.L.Bourell, and R.H.Crawford, *Solid Freeform Fabrication: A New Direction in Manufacturing,* (Kluwer Academic 1997).
2. J.A. McDonald, C.J. Ryall and D.I. Wimpenny, *Rapid Prototyping Casebook*, (Professional Engineering Publishing 2001).
3. L. Lü, J. Fuh and Y.S. Wong, *Laser Induced Materials and Processes for Rapid Prototyping*, (Kluwer Academic 2001).
4. J. Connolly, Direct Rapid Manufacturing – Is it Possible?, *Time Compression Technologies*, May (2001), pp. 46-47.
5. J.A.Ramos, J. Murphy, K.Wood, D.L. Bourell and J.J. Beaman, Surface Roughness Enhancement of Indirect-SLS Metal Parts by Laser Surface Polishing, *SFF Symposium Proc.*, 12 (2001).
6. J.A. Ramos and D.L. Bourell, in *Rapid Prototyping of Materials*, edited by F.D.S. Marquis and D.L. Bourell, (TMS, Warrendale PA, 2002), pp. 191-201.
7. J.A. Ramos, D.L. Bourell, and J.J. Beaman, Surface Characterization of Laser Polished Indirect-SLS Parts, *SFF Symposium Proc.*, 13 (2002).
8. A.M. Prokhorov, V.I.Konov, I. Ursu and I.N.Mihăilescu, *Laser Heating of Metals,* (Adam Hilger, 1990) pp.115-124.
9. T.R. Anthony and H.E. Cline, *J. Applied Physics*, Vol. 48, No 9, 3888-3894 (1977).
10. V.S. Avanesov and M.A. Zuev, "Investigation of surface topography after melting by laser beam", SPIE, Vol. 2713, 340-343.
11. D. Rosenthal, *Trans. ASME*, Vol. 68, 849-865 (1946).
12. Ø. Grong, N. Christensen, *J. Mater. Sci. and Tech.*, Vol. 2, 967-973 (1986).
13. W. Kurz, D.J. Fisher, *Fundamentals of Solidification,* 4th ed. (Trans Tech Publications, Zuerich, 1998) p. 164.

Solution and Spray Processing

Mat. Res. Soc. Symp. Proc. Vol. 758 © 2003 Materials Research Society LL2.5

Direct Fabrication of Patterned Functional Ceramic Films by Soft Solution Processing without Post-Firing

Masahiro Yoshimura, Tomoaki Watanabe, Takeshi Fujiwara, and Ryo Teranishi
Center for Materials Design, Materials and Structures Laboratory
Tokyo Institute of Technology
4259 Nagatsuta, Midori, Yokohama 226-8503, Japan

ABSTRACT

We are proposing an innovative concept and technology, Soft Solution Processing (SSP) for ceramics, which aims to achieve direct fabrication of shaped, sized, located, oriented ceramic materials from solutions without firing and/or sintering. We have successfully fabricated thin and thick films of $BaTiO_3$, $SrTiO_3$, $BaWO_4$, $SrMoO_4$, $LiCoO_2$, and $LiNiO_2$ by SSP in aqueous solutions from room temperature to 200 °C. In these experiments, interfacial reactions between a solid reactant (substrate) and component(s) in a solution have been designed and realized. By locally activating the reaction and moving the reaction point dynamically in these reactions, we can produce patterned ceramics directly in solution without masking, etching, pattern forming, or any post-heating such as firing or sintering. In this paper we present recent results for patterned ceramic films of PbS, CdS, and $LiCoO_2$. The processes used to produce these films are entirely new, and represent the first examples of successful direct patterning of ceramics from solutions. In previous reports, heating processes have been essential for synthesis and/or sintering of powders and precursors to obtain patterns in ceramic materials. Such processes inevitably cost environmentally and economically. In contrast, our method, where no firing is needed, provides an environmentally and economically less expensive alternative.

INTRODUCTION

The present human society is supported by the tremendous consumption of resources, energy and advanced materials. Thin and thick films of functional materials, including ceramics, have traditionally been fabricated by processes requiring huge amounts of energy and resources, some of which are wasted to the environment [1-3]. Such processes have caused the exhaustion of resources and environmental contamination. Recycling of waste materials is possible when we put more energy into the recycling process than into the production/fabrication processes, but this brings about further thermal contamination. In order to address this problem, we must aim to minimize the total energy consumption during the whole life cycle of products, from mining and up-grading of raw materials, through production/fabrication, transportation, usage, and disposal to recycling. Only then will processes become more environmentally friendly [1-3].

In this regard, we are proposing Soft Solution Processing (SSP) for production of advanced materials such as ceramics, semiconductors, composites etc (figure 1) [4]. SSP aims, based upon thermodynamic considerations, to fabricate shaped, sized and controlled advanced materials from aqueous solutions without excess heat and energy consumption and without using expensive equipment and precursors, preferably in a single step [1-3].

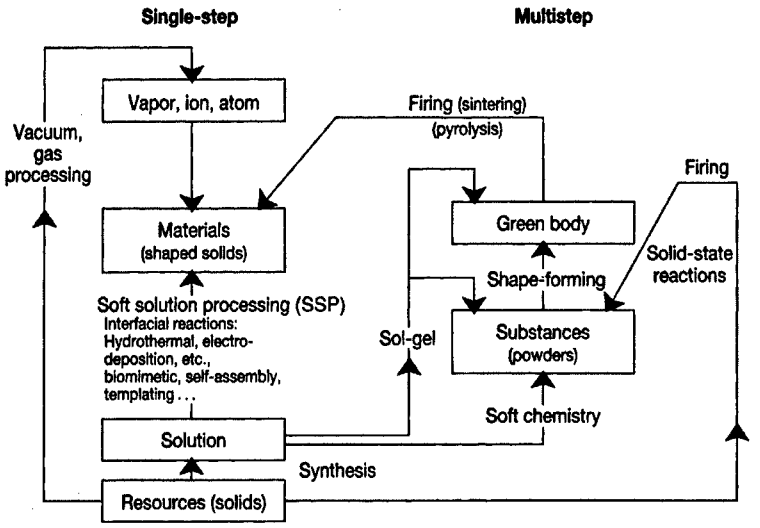

Figure 1. Schematic diagram of advanced materials processes showing the flow of single-step and multi-step processes. Soft Solution Process (SSP) aims to fabricate shaped materials, preferably in a single step, using solutions.

There has been considerable interest in processes where interfacial reactions, mostly at liquid/solid interfaces, are performed by self-assembling, templating, and/or self-organizing of species. Such processes are sometimes referred to as "Bio-mimetic". However, mimetic products cannot exceed the original products on which they are based; moreover bio-products are severely limited in terms of species, substances, and materials. For example, practically no metallic materials have been produced biologically, and biomineral species are limited in number to less than one hundred [2]. Although a huge range of organic substances can be synthesized, most common polymers and plastics, like polyethylene, polypropylene, vinyl, PET etc, have never been produced in bio systems. We, therefore, must learn about bio-processes, but not be limited by bio-products and/or bio-materials for the fabrication/production of advanced materials. Therefore, SSP, which should exceed the limitation of bio-processing and bio-products, might be bio-inspired but not be bio-mimetic. Figure 2 shows that Soft Processing (Soft Solution Processing) is the third area of production for advanced materials between bio-processing and industrial (so-called high technological or artificial) processing which is mostly used for semiconductors and inorganic materials, particularly for products with micro- and/or nano-sized features. In those industrial processing techniques, dry processes, such as CVD and PVD, using gas or vacuum systems, have been employed where highly energetic species like molecules, atoms, and/or ions are utilized for the production/fabrication of films. These dry processes consume huge amounts of energy compared to multi-step processes based upon solid state

reactions and wet process where solution precursors have been used as shown in figure 1. Without using such highly energetic species as dry process, or such high temperature heating as multi-step processes, SSP aims to fabricate directly shaped materials [1-3].

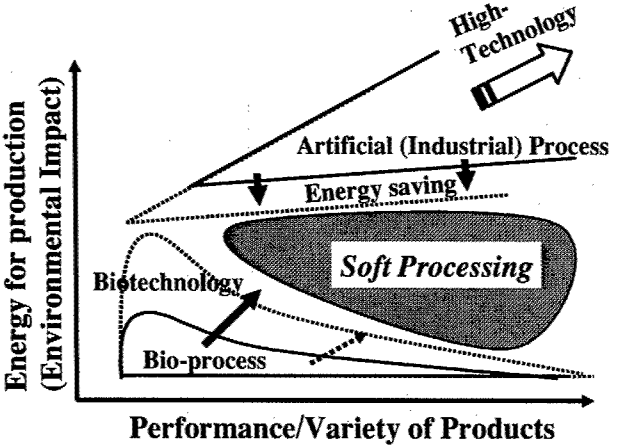

Figure 2. Energy vs. performance/variety in bio-processes and artificial processes. Soft Processing targets the production of high performance materials by environmentally benign methods.

We have reported the successful fabrication of various thin/thick crystalline films of double oxides such as $BaTiO_3$, $SrTiO_3$, AMO_4 (A=Ba, Sr, Ca, M=W, Mo), $LiMO_2$ (M=Co, Ni), YVO_4, etc., by SSP in aqueous solutions at 150°C or lower temperatures without any post-firing [1-7]. In these experiments, interfacial reactions between a solid reactant (substrate) and component(s) in a solution have been utilized as illustrated in figure 3, where ABO_x crystals are formed on the substrate **A** by the reaction with the species **B** and **O** from H_2O in the solution. These interfacial reactions must be activated, either chemically, thermally, electrochemically, photo chemically, sonochemically, mechanochemically, or by some other mechanism.

When we have activated/stimulated those reactions locally and/or moved the reaction point dynamically, we can get patterned ceramic films directly in solution without any post heating, masking or etching [6, 7]. Those direct patterning methods differ from previous patterning methods which consist of multi-step processes, for example: (1) synthesis of particles of compounds or precursors, (2) dispersion of the particles into a liquid ("ink"), (3) patterning of the particles on a substrate by printing of the "ink", (4) consolidation and/or fixing of the particles' pattern by heating. For example, some results for zirconia ceramics and PZT films fabricated by ink-jet printing have already been reported [8, 9]. However, in almost all the reports, jet printing has been used only as a method to give a pattern of solid particles on the substrate. The substrate with the pattern of solid particles must be fired at a high temperature to fix, sinter or solidify them. Otherwise, the substrate using a special binder to fix the solid

particles must be fired to remove that binder. In any case, these techniques are not fabricating a patterned film by reaction, but fabricating a pattern of particle that requires post-firing (figure 4).

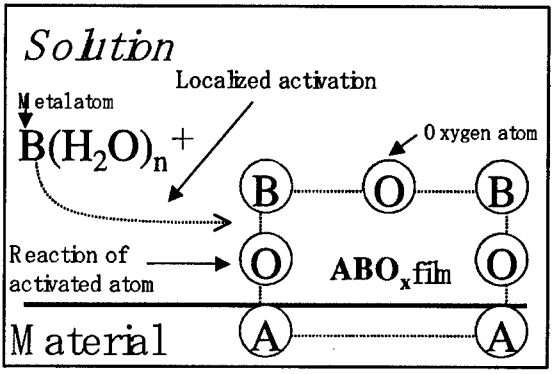

Figure 3. Concept of direct patterning by localized activation of interfacial reactions.

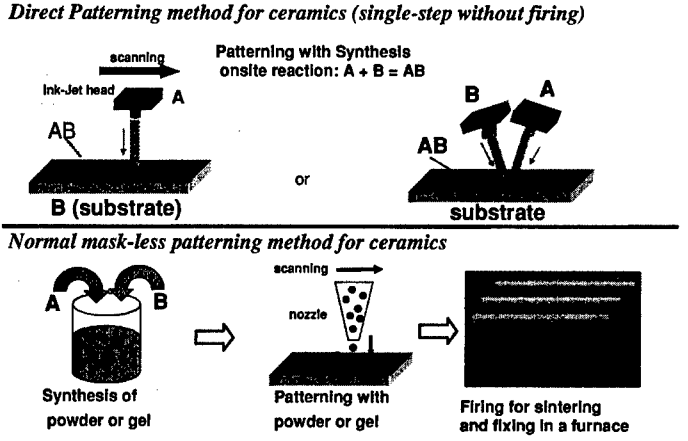

Figure 4. Comparison of "direct patterning" and "normal mask-less patterning" methods for ceramics.

The notable feature of direct patterning is that each reactant reacts directly on site, at the interface with the substrate. Therefore, the chemical driving force of the reaction, A+B = AB, can be utilized not only for synthesis but also for crystallization and/or consolidation of the compound AB. It is rather contrasting to general patterning methods where thermal driving force of post-firing is mostly used for the consolidation of the particles. The present technique has many merits as follows: (1) it needs simple equipment that is easy to control, (2) the process

is therefore very safe and harmless, (3) it allows direct patterning without masking, etching or complicated surface treatments, (4) it needs fewer reactants and lower energy and cost and (5) it is easy to recover the reactants.

Therefore, our direct patterning methods should be economically and environmentally friendly, avoiding excess consumption of energy and resources, and minimizing emission of waste, for example excess heat and gaseous by-products like CO_2 and H_2O.

DIRECT PATTERNING OF CdS AND PbS ON PAPER BY INK-JET REACTIONS [10]

Ink jet printing has been widely used for color printing on paper, where color particles are printed in a pattern. Ceramic particles can be similarly printed as a pattern on a substrate. However, they must be fired to fix and/or to consolidate the pattern on the substrate as mentioned above. We have recently developed a new method to fabricate ceramic patterns directly from solutions by the interfacial in situ reactions between two liquids, using an ink jet printer.

In the example of PbS, an aqueous solution of $Pb(NO_3)_2$ was soaked on a paper, then a solution of Na_2S was ink-jetted as a pattern at room temperature. A pattern of PbS was formed on the paper, which consisted of crystalline PbS particles as revealed in figure 5. These particles were less than 100 nm in size, but well crystallized and well embedded in the fibers of the paper (figure 6). Similarly, CdS was formed on paper from $CdCl_2$ and Na_2S solution. This material consisted of ≈30 nm size crystals with a band gap of 2.45 eV. Other ceramic patterns can be fabricated by similar methods.

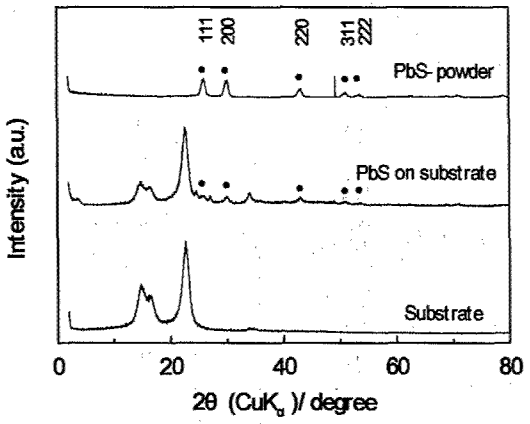

Figure 5. XRD patterns of PbS samples on paper prepared by ink jet reactions at room temperature. (a) Substrate, (b) PbS pattern on paper, (c) PbS powder synthesized in solution by ink jet reactions.

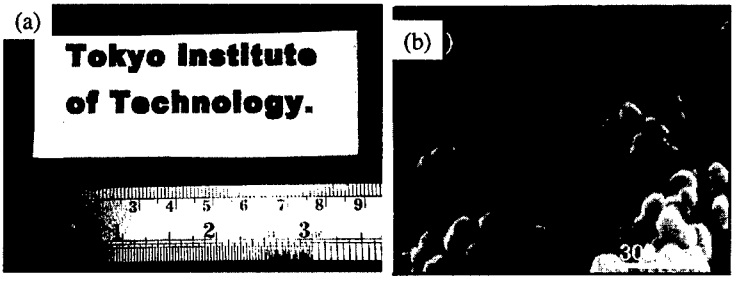

Figure 6. (a) Photograph of a PbS pattern on paper prepared by ink jet reactions at room temperature, (b) SEM photograph of the same sample.

DIRECT PATTERNING OF $LiCoO_2$ ON POROUS SUBSTRATES BY ELECTROCHEMICALLY ACTIVATED INTERFACIAL REACTIONS [11, 12]

Bio-minerals have been synthesized in aqueous solution by ion transfer reactions through a cell membrane. However, these biological processes can produce only a limited range of materials like amorphous silica, calcium carbonate, calcium phosphate, calcium sulfate and iron oxide, but not others like $LiCoO_2$, $BaTiO_3$ [1-2]. We propose electrochemically activated interfacial reactions for film fabrication by "Artificial Biomineralization" [11], where the interfacial reactions between solutions separated by membranes are used with the assistance of electrochemical reactions to fabricate crystallized $LiCoO_2$ films directly on paper at low temperatures (figure 7).

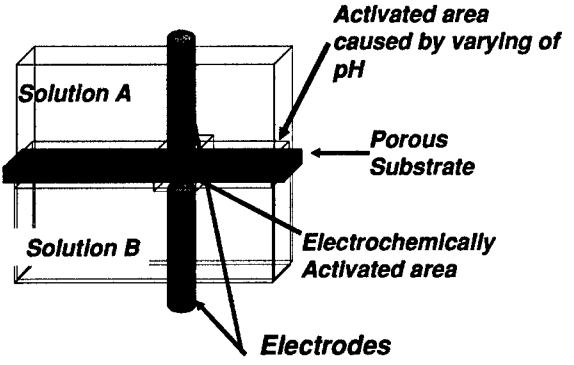

Figure 7. Schematic diagram of an electrochemically activated interfacial reaction method.

A $LiCoO_2$ film can be synthesized by the reaction between Li^+ and CoO_2^- ions in a solution. CoO_2^- ions can be produced by chemical or electrochemical oxidation of $HCoO_2^-$ or Co^{2+} ions. Therefore electrochemical dissolution of a Co anode or electrochemical oxidation of

$HCoO_2^-$ ions near a carbon anode can give a CoO_2^- flux to a porous substrate like paper in the shape of the anode. This can give a $LiCoO_2$ crystalline film in the pattern of the anode on the paper (figure 8). Typically this consists of plate-like crystals a few μm in size. However the phases, shapes and sizes of the crystals produced by this method can be controlled by the flow of solution(s), electrical current, and/or geometry of electrodes and substrates.

Other direct patterning methods using laser activation or localized electrochemical activation have been under development in our group. These are demonstrating that the fabrication of patterned ceramics can be realized in solutions at low temperatures below 150°C, or even at room temperature, without any post-firing, masking and etching, which have been regarded as essential processing in conventional patterning of ceramics.

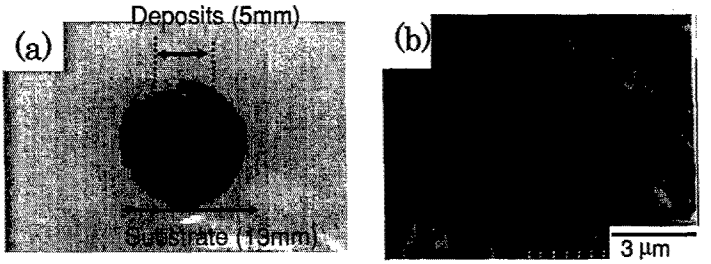

Figure 8. (a) Photograph of a patterned $LiCoO_2$ sample prepared electrochemically by interfacial reaction on paper at 120 °C, (b) SEM photograph of the same sample.

ACKNOWLEDGEMENTS

The authors are thankful for JSPS (Japan Society for the Promotion of Science), particularly No. 69 Committees for the financial support, 96R06901, and also to members in our group for their cooperation and contribution in the research.

REFERENCES

1. M. Yoshimura, *J. Mater. Res.*, **13**, 796 (1998).
2. M. Yoshimura and J. Livage, *MRS Bull.*, 25, 12 (2000) .
3. M. Yoshimura, W. Suchanek, and K-S. Han, *J. Mater. Cham.*, **9**, 77 (1999).
4. M. Yoshimura, W. Suchanek, and K. Byrappa, *MRS Bull.*, **25** , 17 (2000).
5. T. Watanabe, H. Uono, S-W. Song, K-S. Han, and M. Yoshimura, *J. Solid State Chem.*, 162, 364 (2001).
6. S-W Song, H. Fujita, and M. Yoshimura, *Adv. Mater.*, **14**, 268 (2002).
7. T. Watanabe, W-S. Cho, W. L. Suchanek, M. Endo, Y. Ikuma, and M. Yoshimura, Solid State Science, **3**, 183 (2001).
8. M. Mott, J.H. Song, J.G. Evans, *J. Am. Ceram. Soc.* **82**, 1653 (1999).
9. H. Adachi, Y. Kuroda, T. Imahashi, K. Yanagisawa, *Jpn. J. Appl. Phys.* **36**, 1159 (1997).
10. R. Teranishi, T. Fujiwara, T. Watanabe, and M. Yoshimura, *Solid State Ionics*, **151**, 97 (2002).

11. T. Fujiwara, Y. Nakagawa, T. Nakaue, S-W. Song, T. Watanabe, R. Teranishi, and M. Yoshimura, *Chem. Phys. Lett.*, **365**, 369 (2002).
12. T. Fujiwara and M. Yoshimura, *J. Electroanal. Chem.*, (*in press*).

Mat. Res. Soc. Symp. Proc. Vol. 758 © 2003 Materials Research Society LL2.6

Cold Gas Dynamic Manufacturing – A new approach to Near-Net Shape Metal Component Fabrication

R. H. Morgan, C. J. Sutcliffe, J. Pattison, M. Murphy, C. Gallagher,
A. Papworth, P. Fox, W. O'Neill
Manufacturing Science and Engineering Research Centre, Department of Engineering
The University of Liverpool, L69 3GH, UK. r.morgan@liverpool.ac.uk

ABSTRACT

Cold Gas Dynamic Manufacturing (CGDM) is a high-rate, direct deposition process capable of combining many dissimilar materials in the production of a single component. The process is based on Cold Gas Dynamic Spraying (CGDS) – a surface coating technology in which small, un-heated particles are accelerated to high velocities (typically above 500 m/s) in a supersonic gas jet and directed towards a substrate material. The process does not use a heat source (as with similar plasma and HVOF spray technologies), but rather employs the high kinetic energy of the particles to effect bonding through plastic deformation upon impact with the substrate or previously deposited layer. As a consequence it lends itself to the processing of temperature sensitive material systems such as oxidising, phase-sensitive or nano-structured materials. To achieve metallic bonding incident particles require velocities greater than a certain material-specific threshold value, such that thin surface films are ruptured, generating a direct interface. This bonding mechanism has been compared to explosive welding.

This paper discusses the further development of the CGDS technique from surface coating technology into the basis for a novel Additive Fabrication process. The description of the apparatus is presented in addition to the basic processing conditions for the deposition of aluminium material. Particular attention is paid to the morphology of the deposited material, the microstructure and the interfacial boundary between splats.

CURRENT TECHNOLOGY AND LIMITATIONS

Current trends in the area of Rapid Prototyping (RP) and Manufacturing have led to the development of processes which provide end users with metal components which are not simply form and fit prototypes, but allow functional load-bearing testing or actual in-service use.

The enabling technologies such as Laser Engineered Net Shaping (LENS) [1] and Direct Metal Laser Re-Melting (DMLR) [2] use a laser to melt and fuse high strength, high temperature metallic powder particles into a net or neat-net shape solid form on a layer-by-layer basis. The problems associated with such fabrication processes include the high thermally induced stresses generated in the component and also the requirement of high purity inert environments to prevent oxidation during processing [3]. Furthermore, detrimental microstructure and phase changes may occur. Such metallurgic transformations introduce further complications in the fabrication of Functionally Graded Material (FGM) components or the utilisation of novel nanocrystalline powders.

A new fabrication technology currently under development at the University of Liverpool, UK, is Cold Gas Dynamic Manufacturing. This process will enable the fabrication of near-net shape multiple material components at room temperature, with little or no melting, thus preventing many of the problems that are associated with laser based technologies.

The CGDM technique uses a supersonic gas jet to accelerate small diameter (10-50 μm) particles to high velocities in the range 500-1000 ms^{-1}. The particles are directed towards a target surface and upon impact undergo plastic deformation. It is thought that the kinetic energy of the particles is sufficiently high to effect rupture of surface oxide films, resulting in metal-to-metal bonding with a mechanism considered similar to that of explosive welding [4].

Historical perspective

CGDM is an evolutionary progression from Cold Gas Dynamic Spraying (CGDS) or Cold Spray. The origins of Cold Spray date back to the turn of the twentieth century, introduced by Samuel Thurston in 1902 [5]. The process was subsequently re-discovered and a developed into a material coating technology at The Russian Academy of Sciences, Novosibirsk in the 1980s [6]. Scientists conducting supersonic wind tunnel tests observed that above a certain material-specific critical velocity, particles entrained in the fluid stream adhered to a body obstructing the flow. Table I shows the threshold velocities for deposition of a variety of engineering materials.

Material	Critical Deposition Velocity (ms^{-1})
Copper	560-580
Nickel	620-640
Iron	620-640
Aluminium	680-700

Table I. Critical velocities for deposition for various materials.

The potential advantages of the process were quickly realised and steps were undertaken to develop the phenomenon into a material coating process to compete with coating technologies such as thermal spray [7]. Since then, a variety of research institutions and universities have been investigating cold spray, its underlying physical principles and the materials formed. To date, a variety of materials including copper, aluminium, titanium, silver, nickel-based superalloys, metal matrix composites and nanostructured materials have been successfully deposited [8].

The CGDM process takes the principles of Cold Spray and uses it to create discrete features by xy movement of a CNC controlled deposition nozzle above a substrate. Following the deposition of a layer, a high-speed machining spindle is employed to remove excess material deposited by the diverging spray from the nozzle. Subsequent layers are built up using these process steps until the component is complete. This paper details the preliminary results of the work carried out on CGDM.

EXPERIMENTAL ARRANGEMENT

The experimental arrangement for CGDM comprises of the following components: gas delivery; process chamber; gas recovery. These will be discussed in turn:

Gas delivery

In order for the sprayed particles to attain sufficient kinetic energy to undergo plastic deformation upon impact they must be accelerated to very high velocities by the gas jet. Typical process gasses can be air or nitrogen, however low molecular weight gasses such as helium are preferred, as they will achieve higher velocities [9]. The high-pressure gas (15-30 bar) is delivered through a convergent-divergent nozzle, such as that shown in figure 1, to achieve supersonic velocity. The design of such a nozzle is briefly described below.

Nozzle design

Using quasi one-dimensional flow theory, assuming adiabatic, inviscid gas, the flow can be described as isentropic and hence any change in pressure will be accompanied by a change in density. Under this assumption, the area-velocity relation can be achieved [10]. When applying this relation to subsonic flow (M<1), a decrease in area will result in an increase in velocity (and vice versa), whereas in supersonic flow (M>1), an increase in velocity is associated with an increase in area.

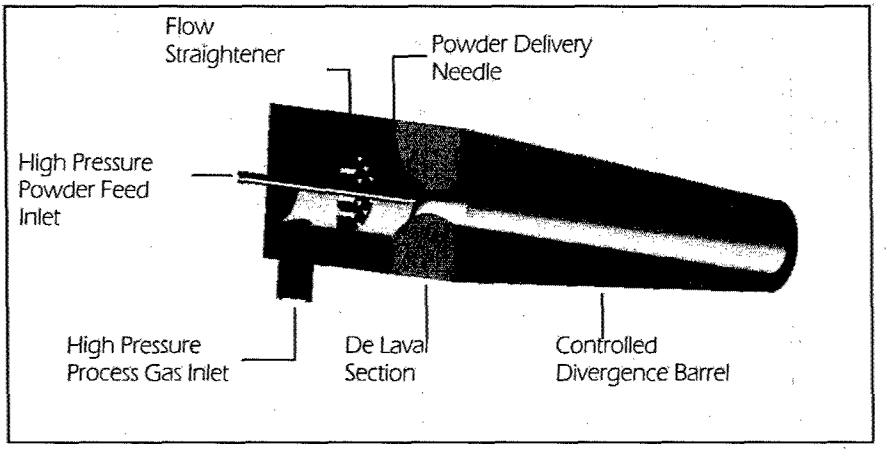

Figure 1. Illustration of nozzle used in Cold Gas Dynamic Manufacturing process.

In the convergent subsonic flow section of a De Laval nozzle, the velocity increases up to the throat, at which point the flow becomes choked (M=1). Immediately after the throat, as the nozzle diverges, the expansion of the gas accelerates the flow to supersonic velocity. Using the Mach number relation through a variable area duct [10], the nozzle exit area can be determined for a particular throat diameter and desired Mach number at a given input pressure and temperature for a particular gas or gas mix. By this method, an axi-symmetric De Laval section has been designed for an output Mach number of 2.4 with helium as the process gas at an input stagnation pressure of 15 bar.

This approach, however, will lead only to the gas velocity and not the more important particle velocity. The particles entrained in the gas jet are much more massive than the gas

molecules and therefore have too much inertia to keep up with the sudden gas acceleration [11]. The particles do accelerate, due to the drag force imposed upon them by the high velocity gas. The drag force on a particle accelerating through the nozzle is given by the equation:

$$F = C_d.A.(\frac{1}{2}\rho.V_{rel}^{\ 2}) \quad (1)$$

where C_d is the skin friction drag coefficient, A is the cross sectional area of a particle and $1/2\rho V_{rel}^2$ is the dynamic pressure of gas stream relative to the particle

In order for the particles to achieve to their critical velocity, the longer time they spend in the high-speed gas stream the faster their ultimate velocity. Therefore, the divergence length of the nozzle must be optimised to achieve maximum acceleration of the particles. If the divergence length is too short, the particles will not reach their critical velocity. If the nozzle length is too long however, increasing boundary layer effects of the nozzle wall will slow down the gas stream [12].

To optimise the length of the divergence, a series of numerical simulations utilising an industry standard CFD package with a state of the art discrete phase modeller was undertaken. The results of the CFD predictions of the centre-line Mach number can be seen in figure 2. From the throat (x = 0.00), gas velocity is rapidly accelerated to a maximum, maintaining a high velocity just below 1400m/s along the length of the divergence until the nozzle exit is reached. Upon exiting the nozzle, the gas again expands slightly resulting in an increase in velocity. Once the jet is in the atmosphere, viscous forces rapidly entrain atmospheric air, dissipating energy and

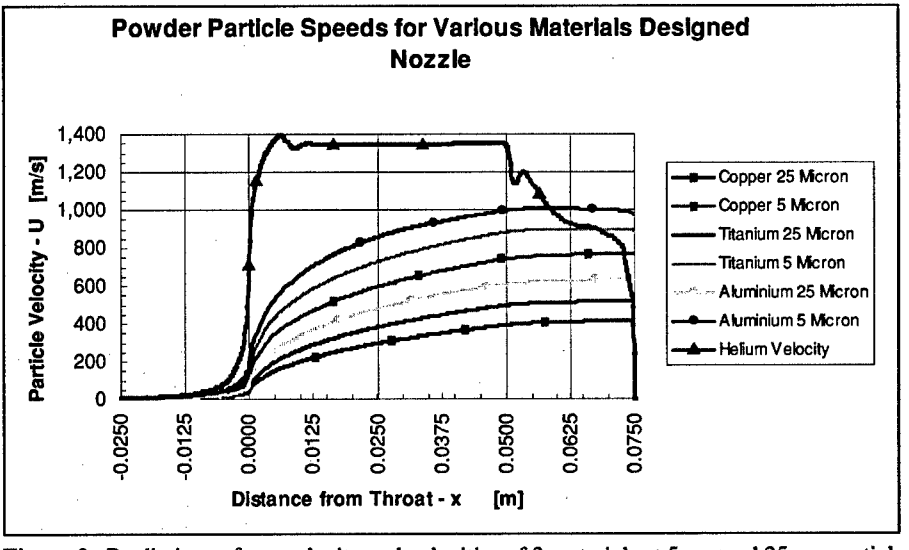

Figure 2. Predictions of gas velocity and velocities of 3 materials at 5 μm and 25 μm particle size.

abruptly reducing the gas velocity. Finally, the jet impacts the substrate plate and is decelerated to almost zero velocity in the axial direction. Particles entrained in the high velocity flow are accelerated steadily along the nozzle length. In fact, the particles continue to accelerate outside the nozzle exit as they still occupy a region in the flow where the relative gas velocity continues to have an impact on the drag force as described by equation 1.

Figure 2 clearly shows the influence of particle size on velocity. In general, small particles with low mass will achieve higher velocities. However, there are limitations to the size of particles; small particles are highly explosive due to their high surface energy, they also tend to agglomerate to form larger particle groups and their surface oxide to volume ratio is increased. Furthermore, the effect of "bow shock" will decelerate smaller, lighter particles. As the gas jet impinges on the substrate surface, a shock wave is formed directly opposing the flow, resulting in a region of stagnation. The decelerating effect of the bow shock on the smaller, lighter Al particles can be seen in figure 2 as they near the substrate.

Process chamber and gas recovery

Powder is fed into the nozzle via a high-pressure gravity feeder (Praxair 1264HP). A perforated spinning disk within the feeder is rotated at a particular speed to set powder mass flow rate. The powder is delivered into the high-pressure convergent section of the nozzle via a tube. The small diameter powders are extremely explosive if exposed to an oxidising atmosphere, therefore, the process chamber is kept inert and the gas and any un-adhered powder are collected. The Initial design for this collection system is shown in figure 3. A clear PU cylinder with a flexible PTFE seal around its base allow the nozzle and chamber to slide as one along a ground base plate

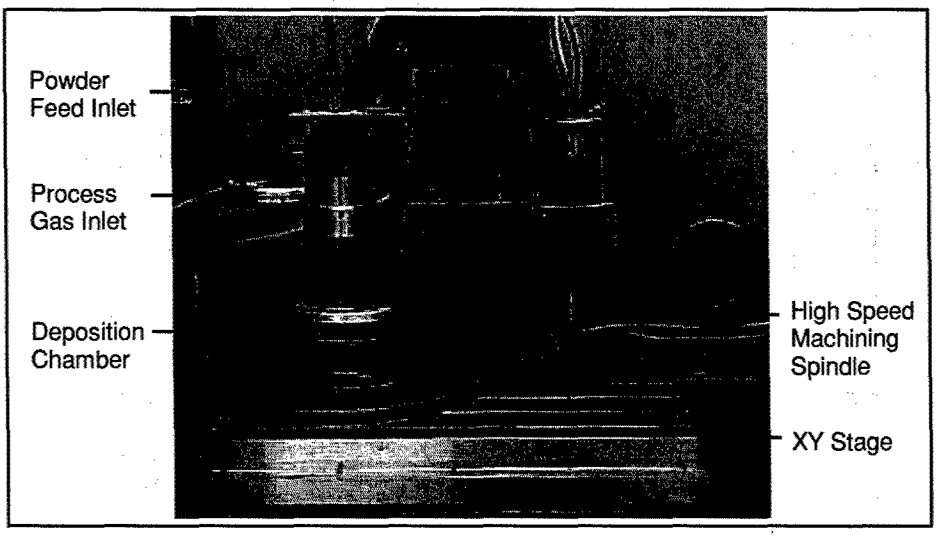

Figure 3. Experimental arrangement incorporating process control chamber and high speed machining spindle.

effectively providing a moveable inert chamber. The chamber exhausts into a scrubbing system consisting of various cyclone and membrane filters, which remove the particles before the gas is exhausted to atmosphere outside the laboratory. Due to the high gas consumption, gas recovery will become an important issue for Cold Spray processes. Work is currently being carried out in this field by industrial collaborators BOC Gases.

RESULTS

Material deposition

The material used in this study is, gas atomised, spherical, pure (industrial grade) aluminium powder supplied by Aluminium Power Company, UK. The powder size is specified as –10 + 45 μm. From table I, the critical deposition velocity of aluminium is 680-700 m/s. Though this is a particularly high threshold velocity, the low material density of aluminium (2.7 g/cm^3) results in its low inertia and hence ease of acceleration.

The main process variables of pressure, nozzle standoff distance, traverse speed and powder mass flow rate were analysed for optimisation of material deposition; table II lists the variable ranges. Figure 4 shows a typical series of deposit tracks on an Al substrate.

Process Parameter	Variable Range
Process Gas Pressure	11 – 22.5 bar
Nozzle Stand Of Distance	10 – 50 mm
Powder mass flow rate	12.5 – 52.5 g/min
Nozzle traverse rate	50 – 400 mm/min

Table II. Process parameters investigated in CGDM deposition trials.

The results of the deposition trials are extensive and beyond the general nature of this paper. However, the effects of the process variables can be generalised as follows:

Input Gas pressure: Deposition was achieved throughout all input stagnation pressures suggesting critical velocity was achieved. Particles in the centre of the gas stream reach higher velocities than those on the outer edges resulting in a central peak along the length of the deposits, as can be seen in figure 4. Track width increases with pressure as the velocity distribution of the gas jet outside the nozzle is increased, resulting in particles at the extremities of the spray achieving the critical deposition velocity.

Stand Off Distance: Stand off distance contributes greatly to the width of a deposit due to the increase in divergence of the spray. Similarly, the diverging spray also leads to a reduction in deposition height as the deposited powder is spread over a larger area. There is a maximum stand off distance of 50mm beyond which deposition falls off dramatically. This is due to continued deceleration of the particles over a greater length outside the nozzle.

Powder mass flow rate: As powder mass flow rate is increased, the deposition track height increases. At first this occurs rapidly, then reaching a maximum at 45 g/min. Beyond this mass flow rate, excess powder loading within the nozzle causes chocking at the throat and acceleration is less efficient resulting in a limited deposition.

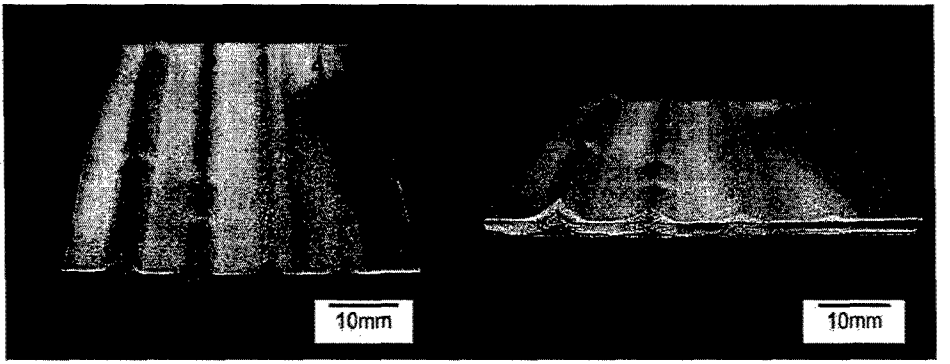

Figure 4. Typical experimental array of single-pass tracks deposited by CGDM:
Constants: Pressure (P) =14 bar, Standoff (h) = 40 mm, Powder mass flow rate (m) = 15 g/min.
Traverse speed (L-R): 1 = 50 mm/min, 2 = 100 mm/min, 3 = 250 mm/min, 4 = 500 mm/min.

Traverse Speed: Figure 4 is an example of the effects of traverse speed. As is expected, the deposition height is a function of the powder deposited per unit length, and therefore an increase in traverse speed leads to a decrease in deposition thickness.

These simple analyses of deposition are important to the development of a near-net shape manufacturing system. As can be seen, the peaked profile of the deposits will result in poor edge definition and optimisation of spray overlap is under investigation. Also, the development of 2D profile nozzles is under investigation to provide flatter deposit profile. However, of overriding importance to the successful production of components by this route is the structural integrity and material characteristics of the deposit.

Microstructural analysis of deposits

Samples were prepared using standard metallographic techniques and etched with 1% NaO_3 solution. Figure 5a shows the typical microstructure. The image reveals splat morphologies significantly different from the shape of the feedstock; the aspect ratio of the impacted particles being substantially higher than that of the spherical, gas atomised powders. This suggests that the material is undergoing significant deformation upon impaction. The amount of deformation results in low porosity in the deposit. However, dark interfacial lines between the splats are apparent. This suggests that metallic bonding is not occurring and that oxide films still exist.

Figure 5b shows the same deposit etched for a greater length of time to emphasise the interfaces between splats. There is little evidence throughout the samples of interfacial bonding taking place. The boundaries between splats have grown significantly, further supporting evidence of poor bonding.

Figure 6 shows SEM images of single particle impacts. Here, significant deformation of the spherical particles can be seen. Evidence of jetting can be seen around the edges of particles. Crater formation of the substrate is also visible in some instances.

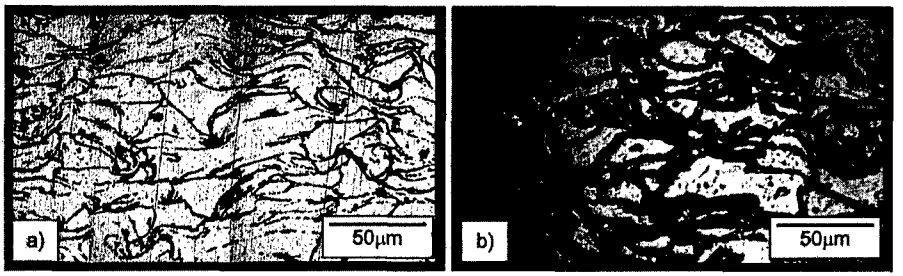

Figure 5. Microstructure of Al deposit – a) Splat morphology shows particles have undergone significant deformation; b) Interfaces between splats have enlarged suggesting no metallic bonding has occurred.

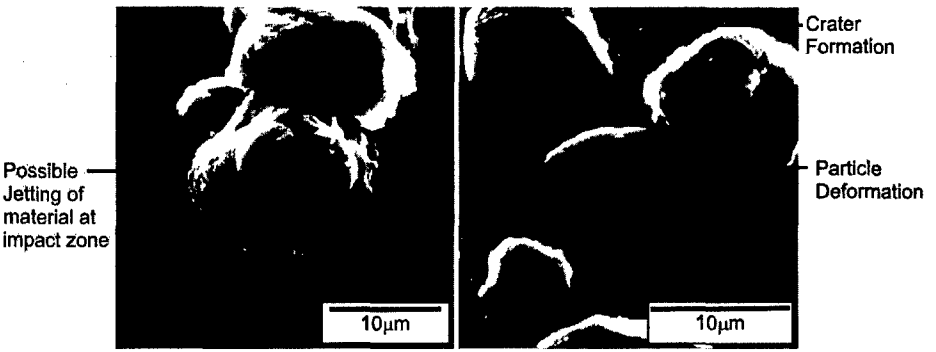

Figure 6. SEM image of Al particles impacted on polished steel substrate. Particle deformation and possible jetting is evident. The formation of an impact crater is also visible in the right hand image.

Auger Electron Spectroscopy (AES) analysis of a deposit sample fractured under high vacuum reveals high oxygen content across the fracture surface, as shown in figure 7. Here, the peaks of C, O_2 and Al are clear. Figure 8 shows the same sample surface after ion beam milling. The milling rate was 7 Å/min. After 45 minutes, the oxygen and carbon spectra are almost completely removed, inferring an oxide thickness of 31 nm (Figure 8).

Discussion

The initial deposition trials have provided a means of identifying the important process parameters for CGDM in terms of deposition rate and deposition thickness. There are, however, a number of issues that need addressing before the technique can be successfully applied to manufacturing.

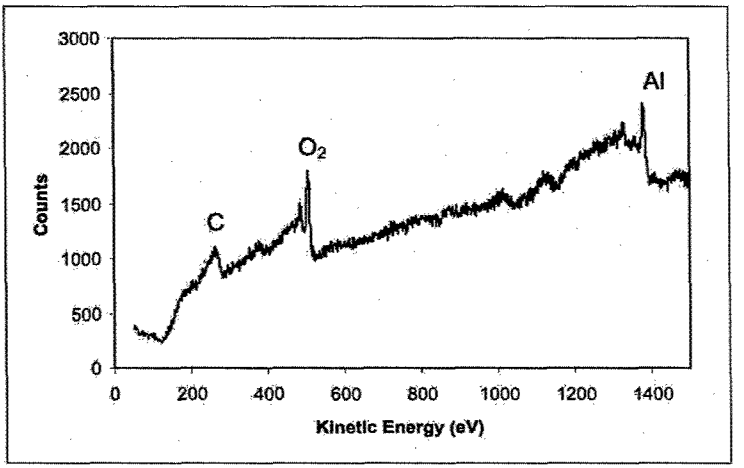

Figure 7. Auger Electron Spectroscopy of CGDM fractured surface. Fractured under vacuum, the sample exhibits carbon, oxygen and aluminium spectra from the surface.

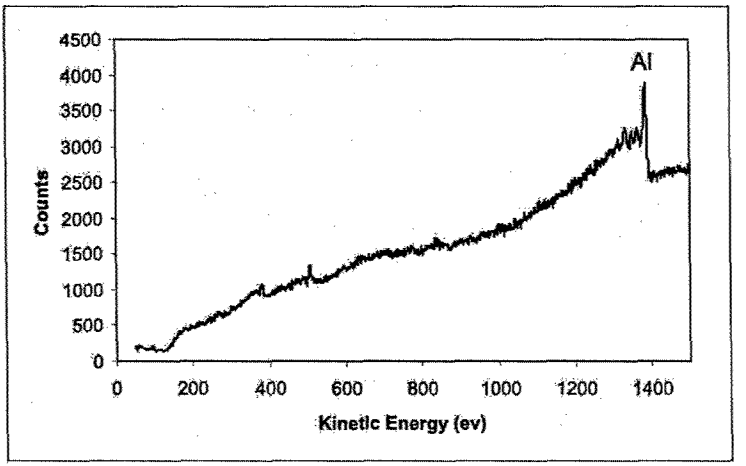

Figure 8. Auger Electron Spectroscopy of CGDM fractured surface. Fractured under vacuum, the sample surface is ion-beam milled for 45 min at a rate of 7 Å/min. The carbon and oxygen contaminants have been removed from the sample surface.

The shape characteristics of the deposit will be an important factor in determining the performance of the process. The peaked shape of the deposits will inevitably lead to poor edge definition and will consequently have an impact on minimum feature size and shape in component fabrication, because of this, a certain degree of back machining of the deposit will be

required. The ratio of material removal to deposited material will also have an impact on the viability of the process, as will the effect of the machining process on the material properties.

A more fundamental issue to be addressed is the properties of the deposited material. The mechanisms of adhesion in cold spray deposition are still not fully understood. Van Steenkiste *et al* identify three possible candidate mechanisms for bonding [13]. If the velocity of the particles is sufficient to exceed yield stress upon collision, then adhesion through plastic deformation will occur. Figure 5 shows the structure of the material exhibits substantial deformation of the particles upon impact, while SEM analysis supports this with evidence of particle deformation and crater formation of the substrate.

The second mechanism for adhesion may be through partial melting and fusion of the material upon impact. The occurrence of jetting may indicate that the material undergoes a kinetic to thermal energy transition leading to softening or partial melting. This has been observed by other researchers and has also been predicted by modelling of the impact zone with temperatures in excess of 900 K, of the order of the melt temperature of aluminium [14, 15].

The third mechanism for particle-particle/substrate adhesion is through fracture of the oxide such that metal-metal bonding can occur. The particles would require a further increase in velocity for this bonding mechanism to take place [13].

In the work reported here, it is clear that particles are undergoing deformation. However, the analysis of the microstructure suggests that interfacial bonding is not being achieved; rather, there is conformal deformation of the particles with the pre-deposited material and mechanical interlocking is taking place. Auger spectroscopy supports this through the detection of carbon and oxygen spectra from the fracture surface. Also, the ion-beam milling of the surface results in removal of these peaks after 31 nm. This depth corresponds with the typical oxide thickness for commercial, passivated powders (20-40 nm). From this, it can be surmised that the particles are not achieving the critical velocity to effect metallic bonding through rupture of the oxide film.

Higher particle velocities can be achieved through an increase in gas velocity. Increasing gas pressure will do this, but at the expense of increased gas consumption and rapidly diminishing returns. A more effective method is to raise the gas temperature. The local sonic velocity in the throat of the nozzle is related to the specific gas properties according to the relationship:

$$V_g = \sqrt{\gamma R T_g} \qquad (2)$$

where γ is the ratio of specific heats, R is the specific gas constant and T is the gas temperature in the throat. Thus an increase in gas temperature will bring about a proportional increase in gas and hence particle velocities. To this end, the CGDM apparatus is undergoing modification for the inclusion of gas heating.

The adhesion mechanism in cold spray is still not fully understood. It appears that bonding involves the compaction, deformation, re-orientation and plastic flow of particles under high pressure to break through surface oxides and generate metallic bonds. However, there are many questions still unanswered; how often does metallic bonding occur throughout a cold spray material? What becomes of the pre-existing oxide that resides on the surfaces of the feedstock material? How does this affect the bulk properties of the fabricated material? Can highly oxide-sensitive material be processed successfully for the fabrication of load bearing components? Many other issues also need addressing; the high-energy multiple impacts cold work the material [13], how does this affect the bulk properties? What of the residual stresses in the deposit? For

spray coatings, these issues may not have the same importance as for freeform fabrication, however, it is clear there is a need for a greater understanding of the materials science of cold gas dynamic spraying. To this end work is in progress, both experimentally and theoretically, to provide further insight into the physical mechanisms that take place in order to develop this coating technology as a means of net-shape component fabrication.

CONCLUSIONS

The CGDM process has been shown to hold significant promise for the controlled build up of near net shape components. The process holds significant advantages over thermal based freeform fabrication technologies. This initial study has sought to establish the effect of the main processing variables (Pressure, particle mass flow rate, traverse-speed, nozzle standoff distance) on the resulting deposit shape and structure. Microstructural and SEM analysis of the deposit reveals significant deformation of impacted material. However, further analysis by Auger Electron Spectroscopy has revealed the presence of oxygen across interfacial boundaries suggesting insufficient particle velocities to achieve metallic bonding upon impact. Further experimental and theoretical work is in progress to develop the technology into a freeform net-shape manufacturing technology.

ACKNOWLEGMENTS

The authors would like to thank Lawrence Bailey and Richard Arnold, engineers at the Manufacturing Science and Engineering Research Centre involved in this research and industrial collaborators BOC Gases for their continued support. This project is funded by the EPSRC through the establishment of the Innovative Manufacturing Research Centres.

REFERENCES

1. M.L. Griffith, M.E. Schlienger, L.D. Harwell, M.S. Oliver, M.D. Baldwin, M.T. Ensz, M. Essien, J. Brooks, C.V. Robino, J.E. Smugeresky, W.H. Hofmeister, M.J. Wert, D.V Nelson, Materials and Design, **20** (2) 1999.
2. R.H. Morgan, A.J. Papworth, C.J. Sutcliffe, P. Fox, W. O'Neill, Journal of Materials Science, **37** (15) 2002
3. C. Hauser, T.H.C. Childs, K.W. Dalgarno, Proc Solid Freeform Fabrication Symposium, University of Texas at Austin, TX. **10** 1999
4. M.F. Smith, J.E. Brockman, R.C. Dykhuzien, D.L. Gilmore, R.A. Neiser, T.J. Roemer, Mat. Res. Soc. Symp. Proc. 542. 1999.
5. News Article, IOM^3 Materials World, **10** (9) 2002
6. A. Papyrin, Adv Mat and Proc. 159 (9) 2001
7. A.P. Alkhimov, A.N. Papyrin, V. F. Kosarev, N.I. Nesterovich, M.M. Shushpanov. US Patent. No 5,302,414 1994
8. J. Karithkeyan, Proc. TSS Cold Spray Conf 2002.
9. D.L. Gilmore, R.C. Dykhuzien, R.A. Neiser, T.J. Roemer, M.F. Smith, Journ Thermal Spray Tech **8** (4) 1999

10. B.S. Massey, Mechanics of Fluids. Van Nostrand Reinhold Publishers. London 1970
11. G.S. Settles, S.T. Geppert. Journ Protective Coatings and Linings, **13** (10) 1996
12. B.R. Munson, D.F. Young, T.H. Okiishi. Fundamentals of Fluid Mechanics. Wiley Publications 1990
13. T.H. Van Steenkiste, J.R. Smith, R.E. Teets, J.J. Moleski, D.W. Gorkiwicz, R.P. Tipson, D.R. Marantz, K.A. Kowalsky, W.L. Riggs II, P.H. Zajchowski, B. Pilsner, R.C. McCune, K.J. Barnett. Surface and Coatings Technology **111** (1) 1999
14. R.C. Dykhuzien, M.F. Smith, D.L. Gilmore, R.A. Neiser, X. Jiang, S. Sampath, Journ Thermal Spray Tech **8** (4) 1999
15. A.N. Papyrin, V.F. Kosarev, S.V. Klinkov, A.P. Alkhimov. Proc Int. Thermal Spray Conf 2002

Mat. Res. Soc. Symp. Proc. Vol. 758 © 2003 Materials Research Society LL2.7

Interfacial Layer Effects in $Ba_{1-x}Sr_xTiO_3$ Thick Films prepared by Plasma Spray

Kipyung Ahn[1], Bruce W. Wessels[1], and Sanjay Sampath[2]

[1] Department of Materials Science and Engineering, Northwestern University, Evanston, IL 60208
[2] Department of Materials Science and Engineering, SUNY-Stony Brook, Stony Brook, NY 11794

ABSTRACT

The dielectric properties of high k dielectric thick films prepared by thermal spray were investigated. $BaTiO_3$ and $Ba_{0.68}Sr_{0.32}TiO_3$ thick films were deposited using plasma spray on Ag·Pd screen-printed alumina substrates. The sprayed films were predominantly polycrystalline but contained an amorphous second phase. The dielectric constants of the films decreased with decreasing film thickness in 10 ~ 60 μm range. This was attributed to the presence of an interfacial layer between the film and the substrate as determined by capacitance measurements. The capacitance density of the interfacial layer was determined to be ~ 2.7 nF/cm^2. The capacitance density of the interfacial layer increased to 12 nF/cm^2 after post heat treatment at 500 °C for 20 hours.

INTRODUCTION

Direct writing of passive components including capacitors, resistors, and inductors is being actively considered to simplify the fabrication process and provide greater flexibility compared to conventional processes such as tape casting, screen printing, and lamination [1,2]. Thermal spray is under development as one possible approach. Thermal spray is a continuous and directed spray process in which melted particles are accelerated to high velocities and impinge on a substrate, where thin splats are formed by rapid solidification. The successive impingement of the molten particles results in the formation of thick films.

Various electronic materials have been deposited using thermal spray for electronic applications including conductors, resistors, insulators, inductors, capacitors, and sensors [3,4]. Structural and dielectric properties of thermal spray deposited high k dielectrics such as $BaTiO_3$ and $Ba_{0.68}Sr_{0.32}TiO_3$ were investigated for capacitor applications [5,6]. The dielectric constant of the as-deposited films was lower than the bulk ceramics. The reduced dielectric constants in thermal spray deposited high k dielectric films have been attributed to the presence of an amorphous phase, porosity, and fine grain size.

In this study, the dielectric properties of the high k dielectric films were investigated as a function of film thickness. The presence of a low dielectric constant interfacial layer between the film and the substrate was shown from the thickness dependence of the dielectric constants. The effect of the interfacial layer on the dielectric constant was examined using a series capacitance model. The thermal stability of the interfacial layer was determined by post heat treatment.

Table 1. Sample list used in this study.

Sample	Composition	Thickness (μm)
BT1	$BaTiO_3$	60
BT2	$BaTiO_3$	50
BST	$Ba_{0.68}Sr_{0.32}TiO_3$	40

EXPERIMENTAL DETAILS

$BaTiO_3$ and $Ba_{0.68}Sr_{0.32}TiO_3$ (BST) powders used in this study were purchased from Trans Tech Inc and the feed powder size was –325 mesh (<44 μm). $BaTiO_3$ and BST thick films were deposited using a Plasma Technik F4 plasma spray torch onto Ag·Pd (70/30) screen-printed alumina substrates. The thick films used in this study are listed in Table I . Phase purity and crystallinity were determined by θ - 2θ X-ray diffraction scans with a Scintag four circle diffractometer (XDS 2000) using Cu Kα radiation.

To measure the dielectric properties, silver top electrodes were applied on the films, forming parallel plate capacitor structures. The screen-printed Ag·Pd layer on Al_2O_3 substrate was used as the bottom electrode. A schematic of the capacitor structure is shown in Figure 1. The dielectric properties were measured with an HP 4192A impedance analyzer. The thickness dependence of the dielectric constant was examined using a successive polishing method. The film thickness at each polishing step was measured with a micrometer and a Tencor P-10 profilometer.

RESULTS AND DISCUSSION

X-ray diffraction patterns of the $BaTiO_3$ and BST thick films are shown in Figure 2. The as-deposited films contained an amorphous phase, evidenced by a highly diffuse peak in the range of 22 ~ 34 °. The amorphous phase in thermal spray deposited films is believed to be formed by rapid thermal quenching of sprayed molten powders during deposition. Besides the amorphous phase, no other secondary phases were observed. After post heat treatment at 500 °C for 20 hours in air, the amorphous peak disappeared, indicating crystallization of the amorphous phase during the heat treatment.

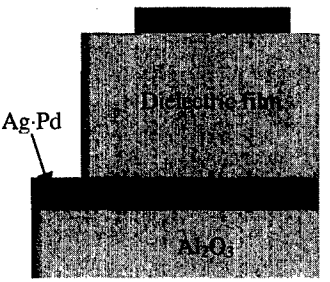

Figure 1. Schematic of the capacitor structure.

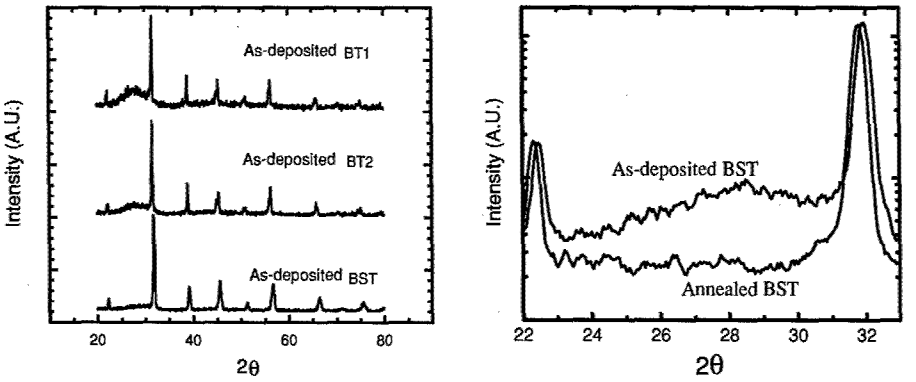

Figure 2. X-ray diffraction patterns of the as-deposited and annealed films.

The dielectric constant of the film was measured as a function of the film thickness and the results are shown in Figure 3. The dielectric constant decreased with the reduction of the film thickness for all samples. X-ray diffraction patterns obtained at various thicknesses showed that the crystallinity did not change with the film thickness. This suggests that the decrease in dielectric constants results from the presence of a low dielectric constant interfacial layer between the film and the substrate. In this case, the film and the interfacial layer are in series and the overall dielectric constant is affected by the low dielectric constant layer. The total capacitance density of the film can be expressed using a series capacitance model [7];

$$\frac{A}{C_{tot}} = \frac{A}{C_i} + \frac{A}{C_B} = \frac{t_i}{\varepsilon_i \varepsilon_0} + \frac{(t - t_i)}{\varepsilon_B \varepsilon_0} \qquad (1)$$

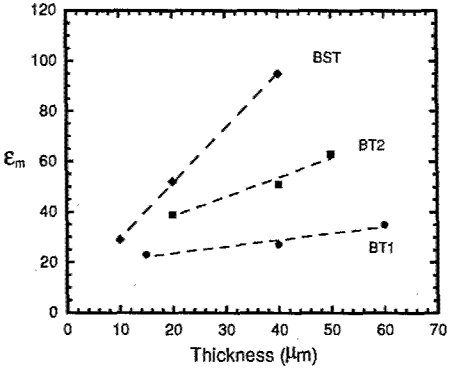

Figure 3. Dielectric constants at various thicknesses.

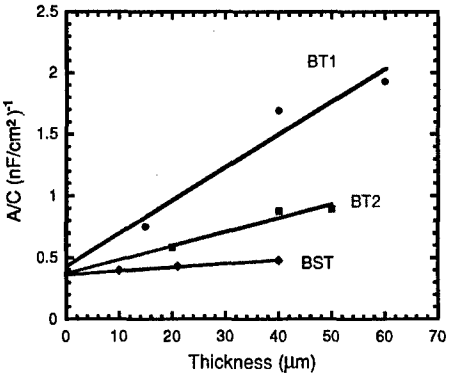

Figure 4. $(C/A)^{-1}$ vs. film thickness in as-deposited films.

where A is the area, C_{tot} is the total capacitance, C_B is the bulk film capacitance, C_i is the capacitance of the interfacial layer, ε_i is the permittivity of the interfacial layer, ε_0 is the permittivity of vacuum, ε_B is the permittivity of the bulk film, t_i is the interfacial layer thickness, and t is the total film thickness.

To investigate the effect of the interfacial layer on the dielectric constant of the film, the inverse of the capacitance densities, $(C/A)^{-1}$, was plotted as a function of the film thickness in Figure 4. In all samples, non-zero intercepts were obtained. The positive non-zero intercepts indicate the existence of a low dielectric constant interfacial layer. Using equation (1), when t is much larger than t_i, the capacitance density of the interfacial layer and the dielectric constant of the bulk film can be obtained from the intercept on the $(C/A)^{-1}$ axis and the slope of the plot, respectively.

From Figure 4, the bulk dielectric constant and the capacitance density of the interfacial layer were calculated. The results are presented with the measured dielectric constants in Table II. Differences in the bulk dielectric constants of the films are believed to be attributed to differences in the crystallinity of the films, as shown in Figure 2. In all films, the measured dielectric constant, ε_m, was lower than the bulk dielectric constant, ε_B, due to the presence of the low dielectric constant interfacial layer. The capacitance densities of interfacial layers were comparable in all samples, showing the interfacial layer thicknesses are similar in magnitude.

Table 2. Bulk dielectric constants and capacitance densities of the interfacial layer calculated from Figure 4, and the measured dielectric constants, ε_m.

Sample	ε_B	C_i/A (nF/cm^2)	ε_m
BT1	42	2.3	35
BT2	100	2.6	63
BST	420	2.7	95

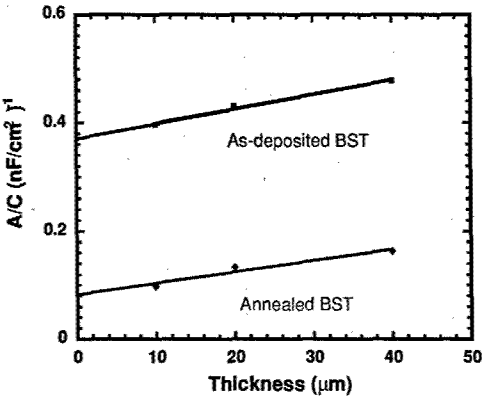

Figure 5. Inverse of capacitance density $(C/A)^{-1}$ vs. film thickness in as-deposited and annealed BST.

To determine the thermal stability of the interfacial layer, BST films were annealed at 500 °C for 20 hours in air. Dielectric properties of the annealed film were measured as a function of the thickness with the polishing procedure described above. The inverse of the capacitance densities of the as-deposited and annealed BST films are shown as a function of the film thickness in Figure 5. The bulk dielectric constant and the capacitance density of the interfacial layer were obtained using equation (1) and the results are presented in Table III. Note that the capacitance density of the interfacial layer, C_i/A, increased by one order of magnitude after annealing. From this, it is believed that the interfacial layer is an amorphous layer [8]. The increase in C_i/A implies the dielectric constant of interfacial layer increases presumably due to crystallization of the interfacial layer.

The bulk dielectric constant also increased after annealing, which was attributed to crystallization of the amorphous phase within the bulk film, as shown in Figure 2. It should be noted that the difference between ε_m and ε_B was significant for the as-deposited film. Moreover, the increase in ε_m is much larger than that in ε_B after annealing. This implies the measured dielectric constant is strongly influenced by the dielectric properties of the interfacial layer and the increase in the dielectric constant for the annealed film is mainly attributed to property changes in the interfacial layer.

Table 3. Bulk dielectric constants and capacitance densities of the interfacial layer calculated from Figure 5, and the measured dielectric constants.

Sample	ε_B	C_i/A (nF/cm^2)	ε_m
As-deposited BST	420	2.7	95
Annealed BST	540	12	280

CONCLUSIONS

$BaTiO_3$ and $Ba_{0.68}Sr_{0.32}TiO_3$ dielectric thick films were prepared by plasma spray. Dielectric properties of the films were investigated as a function of film thickness over the range of 10 ~ 60 μm. The dielectric constant decreased with decreasing film thickness, which was attributed to the presence of a low dielectric constant interfacial layer between the film and the substrate. The capacitance density of the interfacial layer in the as-deposited films was ~ 2.7 nF/cm^2, as determined using a series capacitance model. The interfacial layer was affected by post heat treatment at 500 °C and the capacitance density of the interfacial layer increased to 12 nF/cm^2 after the heat treatment. The increase of the dielectric constant in the annealed film is mainly attributed to changes in the capacitance density of the interfacial layer.

ACKNOWLEDGEMENTS

This research was supported by DARPA/ONR award N000140010654. This work made use of the central facilities of the Materials Research Center at Northwestern University supported by the MRSEC program under a NSF grant (DMR-0076097).

REFERENCES

1. K. H. Church, C. Fore, T. Feeley, in *Materials Development for Direct Write technologies*, edited by D. B. Chrisey, D. R. Gamota, H. Helvajian, and D. P. Taylor, (Mater. Res. Soc. Proc. **624**, San Francisco, CA, 2000) pp3-8
2. W. L. Warren, in *Direct-Write Technologies for Rapid Prototyping Applications*, edited by A. Piqué and D. B. Chrisey, (Academic Press, 2002), pp17-31
3. S. Sampath, H. Herman, A. Patel, R. Gambino, R. Greenlaw, and E. Tormey, in *Materials Development for Direct Write technologies*, edited by D. B. Chrisey, D. R. Gamota, H. Helvajian, and D. P. Taylor, (Mater. Res. Soc. Proc. **624**, San Francisco, CA, 2000) pp181 - 188
4. P. Ctibor and J. Sedlacek, J. Eur. Ceram. Soc. **21**, 1685 (2001)
5. A. H. Dent, A. Patel, J. Gutleber, E. Tormey, S. Sampath, H. Herman, Mater. Sci. Eng. B **87**, 23 (2001)
6. K. Ahn, B. W. Wessels, R. Greenlaw, and S. Sampath, in *Electroactive Polymers and Rapid Prototyping*, edited by Y. B. Cohen, (Mater. Res. Soc. Proc. **698**, Boston, MA, 2001)
7. T. M. Shaw, S. Trolier-McKinstry, and P. C. McIntyre, Annu. Rev. Mater. Sci. **30**, 263 (2000)
8. E. J. Young, E. Mateeva, J. J. Moore, B. Mishra, and M. Loch, Thin Solid Films **377-378**, 788 (2000)

Direct-Write of Microelectronics

Mat. Res. Soc. Symp. Proc. Vol. 758 © 2003 Materials Research Society LL3.5

Direct-Write Process for UV-Curable Epoxy Materials by Inkjet Technology

W. Voit [a,b], K.V. Rao [b] and W. Zapka [a]
[a] XaarJet AB, SE-175 26 Järfälla, Sweden
[b] Engineering Materials Physics Division, Royal Institute of Technology (KTH), SE-100 44 Stockholm, Sweden

ABSTRACT

We demonstrate drop-on-demand inkjet printing technique to be a high throughput method for the patterned deposition of UV-curable epoxy materials. Different multi-nozzle printheads have been used to produce epoxy droplets with controlled volume in the range from 15 to 180 pl, and to apply the droplets with high placement accuracy. For a large dot grid pattern, which was printed by addressing 126 individual ink channels, standard deviations of $\sigma_x = 2.3$ µm and $\sigma_y = 2.6$ µm have been achieved for the error in dot placement. The deposited epoxy dots were found to form planar convex lenses with a focal length of 142 µm. In addition, we have successfully printed magnetic nanoparticles in a carrier fluid with the drop-on-demand printheads, as a step towards the production of composites.

INTRODUCTION

The ability of inkjet techniques to deposit a large variety of different materials, including polymers, material-precursors or dispersions of nanoparticles in fluidic media, makes it a highly flexible process for direct-write applications. The inkjet process is an additive non-contact method, and can be applied even on surfaces with pronounced topography. In particular multi-nozzle drop-on-demand inkjet printheads enable the deposition of patterned layers at a rate of several tens of cm^2 per second.

The versatility of this technique has been demonstrated for the production of different structures and devices in ceramic, electronic and MEMS applications [1-3]. Epoxy materials have been deposited before for applications in MEMS packaging and optics, but by using inkjet devices that are based on a single channel actuation [4]. We have recently reported the dispensing of epoxy materials for bonding applications using a multi-nozzle piezoelectric inkjet printhead [5].

In this paper we describe the dot diameters achievable for epoxy materials with the present day inkjet printing capabilities, their placement accuracy and their surface profiles. In addition, we present attempts to print geometric patterns with magnetic inks, indicating the potential of drop-on-demand inkjet printing for future applications in micro-manufacturing, specifically the printing of nanosized solid particles of ceramic, electrically conductive or magnetic materials for the production of complex hybrid devices.

EXPERIMENTAL DETAILS OF THE INKJET DEPOSITION METHOD

Piezoelectric drop-on-demand inkjet printheads from Xaar have been used in the experimental work presented herein to deposit epoxy materials onto different substrates. The mode of operation of these printheads is based on the generation of an acoustic wave within a small actuator channel due to an appropriate movement of the channel walls. This acoustic wave

creates the ejection of a single ink droplet through a well-defined nozzle at the end of the actuator channel [6, 7]. Xaar's different models of inkjet printheads comprise 126, 128 or 500 ink-channels in a linear arrangement. For most of the experiments described in this work an XJ126 printhead model with 126 channels was used (shown in Fig. 1). This printhead type delivers drop volumes of 50 pl or 80 pl for standard printheads, or variable drop volumes between 15 pl and 60 pl for a greyscale model. The drop repetition frequency for each channel is up to 7.5 kHz. Prototype printhead models with drop volumes down to 3-5 pl and as large as 180 pl are under development. The physical channel pitch of 137 µm results in a printing resolution of 185 dpi (dots per inch) with the printhead oriented at 90 degrees against the scanning direction, whereas higher resolutions, like 360 dpi, can be achieved by inclining the printhead appropriately, or by multiple printing while displacing the printhead for a fraction of its channel pitch.

Since the mechanism of drop formation is non-thermal, the stresses on both the printheads and the fluids are largely reduced in comparison with thermal inkjet techniques. Thus, a large variety of fluids and thermally sensitive liquids can be used, and high lifetimes of the printhead are guaranteed. Additionally, the XJ126 type printheads offer the possibility to adjust driving voltage levels and waveforms, to enable the drop ejection with different types of fluidic media. For the printheads used in this work, an additional passivation layer on the channel and electrode surface has been introduced, to avoid corrosion of these surfaces when aggressive fluids are used.

The XJ126 inkjet printhead is integrated into a custom-built computer-controlled flatbed printing set-up to be used for the deposition experiments. An xy-axis system based on linear motor drives is mounted on top of a heavy, vibration-damped granite table to ensure high printing accuracy and reliability. The x-axis, which holds the printhead on a height-adjustable fixture, is equipped with an *LW7* linear motor stage from Anorad Corporation. During printing, this x-axis drive scans the printhead at a constant linear speed above the substrate surface, while a printhead controller addresses the appropriate channels of the printhead. The substrate is placed onto a vacuum table on the y-axis stage, which is driven by an Anorad *LW10* drive. The usage of linear xy-drives allows for a high maximum velocity of 1.2 m/s, with an encoder resolution of 1 µm for the x-axis and 0.5 µm for the y-axis. The sample table can hold substrates up to 0.6 × 0.84 m in size. A Peltier element is integrated in the head mount fixture to be able to heat both the printhead and the ink supply, to extend the operation range of the printhead for liquids with higher viscosity. A slight vacuum is applied to the ink supply container, as the inkjet printhead needs a negative ink pressure in its channels during operation.

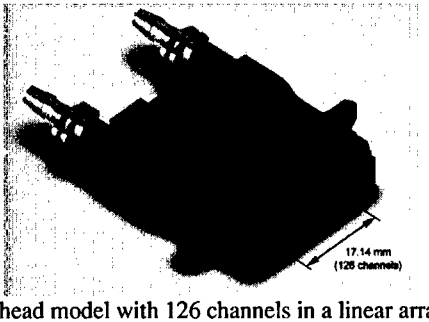

Figure 1. The XJ126 printhead model with 126 channels in a linear arrangement.

SELECTION AND CHARACTERIZATION OF EPOXY MATERIALS

A variety of single component, UV-curable epoxy materials with different viscosities and surface tensions have been characterized and tested for the deposition experiments with the Xaar inkjet printhead. The chosen materials were suited for optical and bonding applications.

Table I summarizes the relevant rheological parameters and the curing mechanism of the tested epoxy materials. The viscosity values were measured with a *StressTech* Rheometer from Reologica Instruments, and the static surface tension was obtained using the Du-Nouy ring method. Epoxy X1, X3 and X4 were only curable by UV-light, and required a radiation of 100 mW/cm^2 for 1-2 minutes at a wavelength of 300-400 nm for the curing process. Epoxy X2 was additionally curable at temperatures above 130 °C.

An important parameter for the ability to eject droplets with a piezoelectric inkjet printhead is the low viscosity of the fluidic materials, since the printhead design with its narrow channels restricts the flow of highly viscous liquids significantly. A reduction of the viscosity of the epoxy materials could be achieved by elevating the temperature, as shown in table I. Furthermore, epoxy materials with different values for the static surface tension were selected. This parameter influences the ability of the epoxy to wet a given substrate, but it has to be in a defined range for the use in an inkjet printhead.

The epoxy materials from table I were studied regarding the drop formation in an XJ126 inkjet printhead. A custom-built microscopic setup with stroboscopic illumination was used for this investigation, which allowed the visualization of ink droplets in flight. With Epoxy X1 a regular drop formation at frequencies up to 5 kHz was possible at 25 °C, but with strong tendency for the ink-jet to break into a number of smaller satellite drops. Epoxy X2 allowed a stable drop formation up to frequencies of 3 kHz at 25 °C, and with increased reliability and higher maximum frequencies up to 5 kHz at a temperature of 40 °C. With samples X3 and X4 drop ejection was only possible at lower frequencies and at temperatures exceeding 40 °C and 60°C, respectively. No clogging of the actuator channels and nozzles was observed with any of the tested epoxies, even for longer idling periods up to several days. This indicates that pre-curing of the epoxy materials inside the printhead was absent. As a result of these investigations Epoxy X2 was chosen for the further deposition experiments.

Table I. UV-curable epoxy materials tested for printing with the inkjet printheads.

Sample	*Viscosity [mPa·s] at 25°C*	*Viscosity [mPa·s] at 40°C*	*Surface tension [mN/m] at RT*	*Curing*
Epoxy X1	15	10	41.9	UV
Epoxy X2	85	45	42.5	UV + heat (>130°C)
Epoxy X3	120	60	28.0	UV
Epoxy X4	205	95	40.0	UV

RESULTS AND DISCUSSION OF INKJET DEPOSITION EXPERIMENTS

An example of an array of deposited and cured epoxy dots on a silicon substrate is shown in Fig. 2. An optical micrograph of patterns with higher complexity can be seen in Fig. 3. All structures and dot patterns have been directly printed onto the substrate in one printing sweep while individually addressing the 126 channels of the inkjet printhead. In the case of the pattern in Fig. 2 only every 3rd channel was firing at a time, resulting in a dot array spacing of 411 µm.

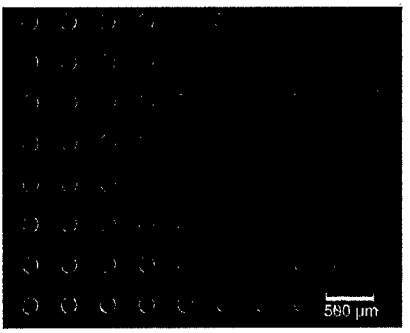

Figure 2. Array of cured epoxy dots with a spacing of 411 µm (printed with Epoxy X2 onto a silicon substrate).

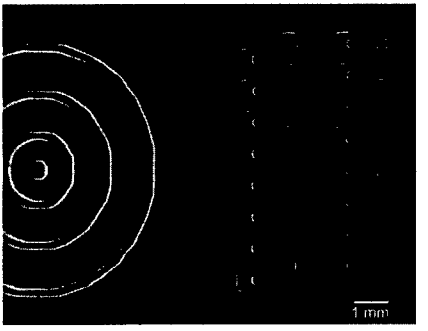

Figure 3. Examples of inkjet printed epoxy pattern (silicon substrate).

In order to evaluate the dot placement accuracy and repeatability when addressing 126 individual printhead channels, a dot array of more than 1×10^4 dots was printed onto a silicon substrate, cured and analysed optically using a Mitutoyo *Quick Vision* system. The pattern was deposited at a linear printing speed of 0.1 m/s, which corresponds to a drop repetition frequency of 730 Hz. The printhead-to-surface distance was kept constant at 1mm during printing.

A normal distributed error in dot placement was found (shown graphically in Fig. 4 for the x-direction). The placement error had standard deviations of $\sigma_x = 2.3$ µm and $\sigma_y = 2.6$ µm along the x- and y-direction, respectively. The mean dot diameter was 146 µm with $\sigma = 1.8$ µm, and the average error in circularity of the dots was found to be less than 1 µm. These results were achieved using an XJ126-300 printhead model, which delivers drop volumes of about 50 pl.

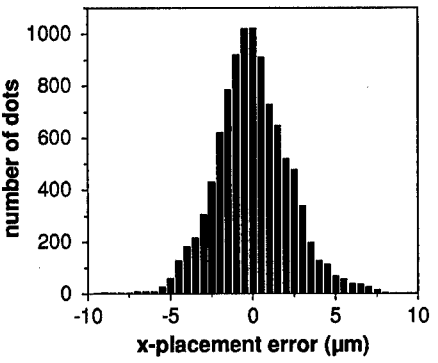

Figure 4. Dot placement error in x-direction (printing direction) for a pattern with 10^4 dots, $\sigma_x = 2.3$ µm.

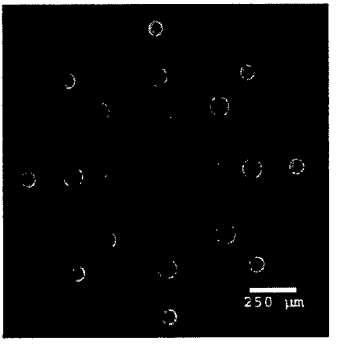

Figure 5. Dot pattern utilizing variable droplet volumes from a greyscale printhead, deposited in one printhead sweep (Epoxy X2 onto silicon).

A specific goal of this work was to produce different structure dimensions by varying the deposited droplet volumes. For this purpose a greyscale printhead was used, which is able to produce droplets in 4 different volume levels of 15, 30, 45 or 60 pl from each of its printhead channels. Fig. 5 shows a pattern of cured epoxy dots printed onto a silicon substrate, which was achieved within one single printing pass by using all 4 different levels of the greyscale printhead. The resulting dot diameters were between 85 µm for 15 pl drop volumes and 140 µm for the 60 pl drops. The height of the epoxy dots was found to be of the order of 4.5 µm for 15 pl drop volumes and 8 µm for 60 pl drop volumes. Smaller structure dimensions could be achieved when printing onto substrates with reduced wetting behavior, such as glass substrates. In this case the dot size was decreased to a range between 55 µm and 110 µm for the different volume levels between 15 pl and 60 pl.

With a large-drop printhead model, producing epoxy drop volumes of 180 pl, the resulting dot sizes were nearly 200 µm on silicon and 150µm on glass substrates.

The process of using a printhead with a large number of printhead nozzles for the deposition of epoxy materials allows high deposition rates. With an XJ126-300 printhead that delivers epoxy drop volumes of 50 pl from each of its 126 channels at maximum drop repetition frequencies of 5 kHz, a continuous layer of around 8 µm thickness could be deposited at a rate of 42 cm^2 per second. Thicker layers can be achieved by applying a multi-pass printing approach and intermediate UV-curing steps. However, our investigations have shown that it is difficult to maintain a good structural control for thicker layers above 50 µm when printing with Epoxy X2.

A common problem for the dispensing process of fluidic media is the occurrence of overfill at areas of crossing line patterns, which results in an undesired flow-out of the liquid into the edge area (see Fig. 6a). Suitable compensation pattern could correct this and produce sharp edges at the crossing lines, as shown in Fig. 6b. This compensation was accomplished by reducing the number of deposited epoxy droplets at the area of the crossing lines. Further compensation to produce an undercut at the corners of the crossing lines was possible, as shown in Fig. 6c.

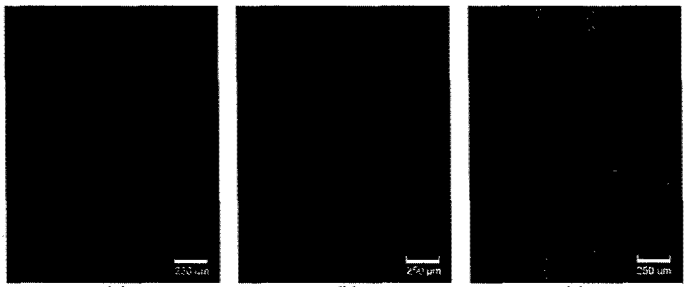

Figure 6. Optical micrographs of epoxy pattern at a crossing line pattern on a silicon substrate, (a) without compensation, (b) compensated for sharp edges, and (c) compensated for an undercut at the corners.

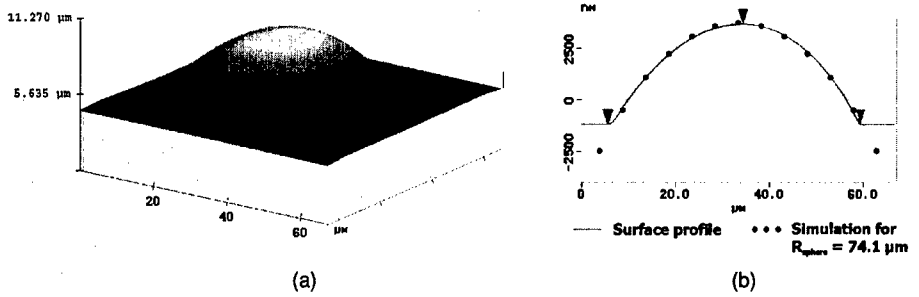

Figure 7. AFM image of a microlens deposited by direct inkjet printing, (a) topography image, (b) surface profile observed from the AFM measurement, together with a spherical fit.

Applications of this direct-write process for UV-curable epoxy materials would be in the fabrication and assembly of micro-fluidic biochips and MEMS devices. We have also applied this inkjet method for the production of micro-optical devices, specifically for the deposition of microlenses. Fig. 7a shows a topographic Atomic Force Microscope (AFM) image of such a microlens deposited onto a glass substrate, printed with a 15 pl droplet from the greyscale printhead. The AFM measurement yielded a diameter of 53 µm and a height of 5 µm for this lens.

Fig. 7b shows that the surface of the dot could be well fitted by a sphere with radius R_s = 74.1µm, so that the dots represent planar convex lenses. With the focal length of a thin planar convex lens given by $f = R_s/(n-1)$, and the refractive index of n = 1.522 for Epoxy X2, a value of f = 142 µm can be calculated for the deposited microlenses. A focal length in this range is for example particularly suited for optical fibre to device coupling applications.

In another experiment the deposition of composites consisting of magnetic materials in a polymeric matrix was investigated. These composites are intended for low- and medium density storage applications on disposable substrates, and for magnetic character recognition. In Fig. 8a such an inkjet printed magnetic pattern is shown.

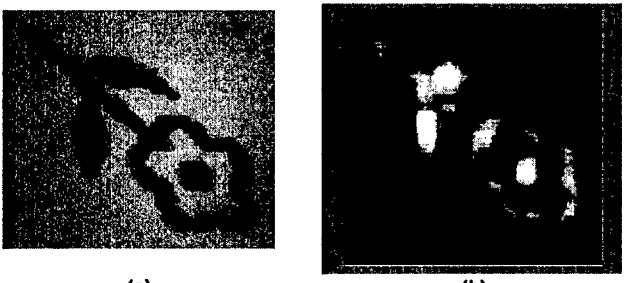

Figure 8. (a) Optical image and (b) map of the local AC-susceptibility of a magnetic test pattern inkjet printed with magnetic ink; brighter colors in the magnetic scan visualize larger magnitudes of the susceptibility (scan area was 3.25×3.25 mm).

The magnetic material consisted in this case of nanosized γ-Fe_2O_3 particles. The magnetic nanoparticles were surface coated with polystyrene and dispersed in an organic carrier liquid. After drying of the printed structures the pattern was detectable by magnetic imaging. This detection was performed utilizing a novel 'in-plane' magnetic susceptibility imaging method developed recently [8]. Fig. 8b shows a mapping of the local distribution of the 'in-plane' susceptibility, measured for the inkjet printed pattern shown in Fig. 8a.

Further experiments to disperse magnetic nanoparticles in the UV-curable epoxy materials are currently in progress.

CONCLUSIONS

We have demonstrated in this work that a direct-write process of UV-curable epoxy materials could be achieved with high accuracy and high deposition rates using a multi-nozzle inkjet printhead. With this technique it was possible to produce dot array patterns and complex structure shapes in one printing sweep, addressing all 126 channels of the printhead individually. The epoxy dots can be deposited with a standard deviation of 2.3 µm and 2.6 µm in x- and y-direction. The control of the structure sizes of the deposited epoxy pattern was possible by variation of the droplet volumes.

The inkjet deposition technique could be used for the production of optical microlenses of almost perfect planar-convex shape. With a focal length of 142 µm these lenses appear suitable for micro-optical devices. Another promising application area of the direct-write process with inkjet printheads is the deposition of magnetic materials in a polymeric matrix for the production of magnetic information carriers.

ACKNOWLEDGEMENTS

This work was funded by the Swedish Agency for Innovation Systems (VINNOVA). The authors would like to thank Magnus Alsered from MA Kapslingsteknik, Sweden, for the consulting and characterization on epoxy materials, and Prof. S. Margel, Bar-Ilan University (RA), Israel, for the preparation of the magnetic nanoparticles.

REFERENCES

1. X. Zhao, J.R.G. Evans, M.J. Edirisinghe and J.H. Song, J. Mater. Sci. **37**, 1987 (2002).
2. Hong, C.M., and Wagner, S.: 'Inkjet printed copper source/drain metallization for amorphous silicon thin-film transistors', IEEE Electron Device Lett., 2000, 21 (8) pp. 384-386
3. S.B. Fuller, E.J. Wilhelm and J.M. Jacobson, J. Microelectromech. Syst. **11** (1), 54 (2002).
4. W.R. Cox and T. Chen, Optics & Photonics News **12** (6), 32 (2001).
5. W. Voit, M. Zimmermann, M. Alsered, K.V. Rao and W. Zapka, The IMAPS Nordic Conference 2002, Stockholm, Sweden, pp. 64-70 (2002).
6. G. Beurer and J. Kretschmer, Proc. IS&T's NIP **13**, 621 (1997).
7. H.J. Manning and R.A. Harvey, R.A., Proc. IS&T's NIP **15**, 35 (1999).
8. V. Ström and K.V. Rao, J. Vac. Sci. Technol. A **16** (4) 2687 (1998).

Mat. Res. Soc. Symp. Proc. Vol. 758 © 2003 Materials Research Society

Fabrication Of Mesoscale Energy Storage Systems By Laser Direct-Write

Craig B. Arnold[1], Ryan C. Wartena[2], Karen E. Swider-Lyons[2], Alberto Piqué[1]
[1]Code 6372 and [2]Code 6171
Naval Research Laboratory
Washington, DC. 20375, USA

ABSTRACT

Over the last two decades, there has been a trend towards the development of smaller and more autonomous electronic devices, yet the question of how to power these microdevices with correspondingly small power sources remains. To address this problem, we employ a laser forward-transfer process in combination with ultraviolet laser micromachining, to fabricate mesoscale electrochemical power sources, such as microbatteries and micro-ultracapacitors. This direct-write laser-engineering approach enables the deposition of battery materials (hydrous ruthenium oxide, manganese oxide, lithium cobalt oxide, etc.) under ambient temperature and atmospheric conditions, resulting in films with the desired morphological and electrochemical properties. Planar and stacked cell configurations are produced and tested for their energy storage and power delivery capabilities and exhibit favorable performance in comparison to current battery technology.

INTRODUCTION

Current trends for developing advanced electronic systems place emphasis in achieving sizes and weights generally associated with integrated circuits. This requires further miniaturization, while enhancing the functionality and reliability of existing components. It also requires new strategies to eliminate the long lead times required for the fabrication of prototypes and evaluation of new materials and designs. In particular, for micro-power sources development, the trend is toward the fabrication of sub-millimeter-scale devices which can be incorporated into any type of platform [1,2].

The small size of these power sources introduces new challenges, in particular for the fabrication and packaging of these devices. Traditional approaches for the manufacturing of power sources, such as rolling or pressing powders into metal cans, are not practical when applied to mesoscale systems. Thus, new fabrication techniques are required to develop small power sources that can be integrated with other microelectronic devices.

This paper describes the use of a laser-based direct-write approach, developed at the Naval Research Laboratory, to rapidly deposit and/or process various types of micro-power sources and their associated components. The laser direct-write process has been used successfully for the fabrication of mesocale energy storage systems, such as micro-ultracapacitors, and microbatteries [3,4].

The first type of micro-power source described in this paper is the hydrous ruthenium oxide micro-ultracapacitor system. This system has a very high specific

capacitance (capacitance per unit mass) and is therefore ideal for small system sizes [5]. These rechargeable devices can be discharged quickly at high power and are thus suitable for circuits with pulsed power requirements, such as for data transmission.

The second system comprises two alkaline chemistry microbatteries, zinc-maganese oxide and zinc-silver oxide. These two common systems are used for numerous applications at the commercial level and have well-established chemistries. They are environmentally friendly and relatively insensitive to ambient conditions. They can be produced in both primary and secondary forms, meaning they can be disposable or rechargeable, although for the purposes of this work, the focus has been on primary cells.

Finally, we have begun work on high-energy, rechargeable lithium-ion microbatteries having lithium cobalt oxide positive electrodes (cathode) and carbon negative electrodes (anode) [6]. These materials have the potential for providing a higher energy and power density than the alkaline system in a rechargeable cell. However, these types of microbatteries are the most challenging since they are sensitive to environmental issues, such as air or water contamination. Ultimately, our goal is to optimize each of these systems to meet the desired power generation requirements for microelectronic applications.

BACKGROUND

Direct-write techniques, which do not require photolithographic processing steps, provide an alternative for the development and fabrication of micro-power sources. Examples of direct-write technologies for fabricating or modifying metallic interconnects and/or other electronic passive elements include ink jet printing [7], direct-write of ceramic slurries (Micropen©) [8], and laser chemical vapor deposition (LCVD) [9]. These techniques excel in certain applications for which lithographic processes are not compatible, i.e., for those applications requiring rapid turnaround and/or pattern iteration, conformal patterning, or patterning onto and over existing components [1]. However, none of the above techniques is capable of operating in air and at room temperature while maintaining near 10-μm resolution and without requiring *ex-situ* processing. Furthermore, more than one technique must be used to deposit and process the range of materials employed for the fabrication of mesoscopic power sources.

Laser direct-write is a promising approach for the manufacture of integrated micro-power sources since it is compatible with the broad array of materials required to fabricate microbatteries or micro-ultracapacitors. In addition, the laser direct-write system can be used for laser micromachining substrates, current collectors, electrodes and interfaces between materials. This approach offers the ability to prototype custom power sources/systems with optimum power/energy profiles for a particular microelectronic device. Finally the laser direct-write technique allows for the fabrication of micropower sources under ambient conditions, which means that it can accommodate temperature- and vacuum-sensitive battery materials and electrolytes.

The use of laser direct-write to fabricate the next generation of micro-power sources is attractive because it has the potential to satisfy the three requirements of a truly integrated micro-power system. First, it is possible to improve the specific energy and power (energy/power per unit mass) within a system by integrating the power supply directly onto the substrate. This will enable a drastic reduction in the weight of non-

power components in the system. For instance, for a small 5 mm diameter commercial button cell, almost 1/3 of the total mass is due to the stainless steel can used for packaging the active material. If the same battery were to be scaled down to 1mm, the relative mass of the can would now account for over ¾ of the total mass of the reduced battery.

Second, it is possible to enhance the overall system efficiency by distributing the power to where it is needed. Instead of having one main battery that is fed to multiple devices, a battery at the point of use would eliminate long interconnects and leads from the microsystem. This would reduce ohmic losses, decrease the weight and volume of the total system, plus lower the electromagnetic interference.

Third, and perhaps most important, the power requirements of a micro power source may be met more efficiently if different types of power sources are combined. This is the concept of a hybrid power generating system [2,10]. Such a system may include the ability to deliver energy at various power levels, provide power conditioning and also be capable to harvest energy to enable the energy storage components to be recharged when needed. In this system low power and high energy is delivered by batteries, while high power is supplied by ultracapacitors, and solar cells could be used to harvest energy and recharge the electrochemical power sources.

Batteries

Fundamentally, a mesoscale microbattery is no different from a large scale battery as energy stored as chemical energy is converted to electrical energy through oxidation and reduction reactions. The construction of all electrochemical energy conversion cells consist of 3 major components: anode (negative), cathode (positive), and electrolyte/separator. The electrons for the external load circuit are generated by the oxidation of the active material in the anode. For example, in the case of a Ag_2O-Zn alkaline battery, the Zn metal is oxidized into Zn hydroxide. The resulting electrons go through the load and reduce the active material in the cathode, i.e. the silver oxide is reduced to silver metal. The ions liberated in the process diffuse through the electrolyte/separator towards either the anode or cathode thus completing the circuit. The direction of the ions depend on their charge state. In alkaline cells, negative hydroxide ions move toward the anode while in lithium-ion cells, the positive lithium ions diffuse toward the cathode. The separator prevents the anode and cathode from an electrical short, thereby forcing electrons through the external load. Of course, in order to connect the cell to the outside world, metal current collectors are needed at both the anode and cathode.

To improve battery performance, small amounts of additives are combined with the active material. For instance, since silver oxide is not a very good electron conductor, carbon is added to improve the electronic conductivity. Other additives decrease the formation of gases or self-discharge of the battery. See for example Vincent and Scrosati for an overview of different battery chemistries [11]. Figure 1 shows a simple schematic of a typical battery.

There has been much effort to develop small microbatteries for various primary and secondary chemistries. In one successful approach, the anode, cathode, and solid-state electrolyte are all deposited using standard physical vapor deposition techniques in

vacuum with subsequent patterning through photolithography in order to generate each individual cell [12,13].

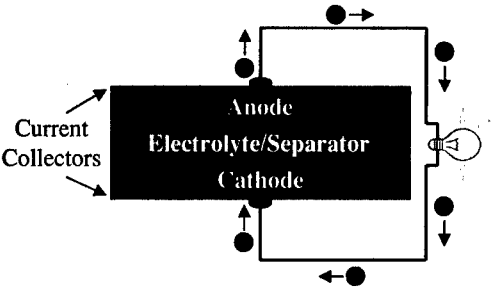

Figure 1. Schematic of a battery cell connected to a load.

Ultracapacitors

An ultracapacitor has properties similar to both batteries and capacitors but lies somewhere in between on the spectrum of energy storage devices. Ultracapacitor cells are constructed by sandwiching an ionically conductive electrolyte between two electrically conductive electrodes. Charge may be stored in a double layer at the interface between the electrodes and electrolyte or in oxidation-reduction reactions at the electrode. There are still an anode and cathode, but in the case of a symmetric device, both of these are the same material.

Like a capacitor, an ultracapacitor has the ability to very rapidly discharge its energy leading to a high power density. However like a battery, it has the ability to store a large amount of energy in the charged state of the active materials. So in the most basic manner, an ultracapacitor can be seen as a battery with a high discharge rate. These devices are typically used for load leveling and applications where short bursts of power are needed. Ultracapacitors go by other aliases such as electrochemical capacitors, supercapacitors, or pseudocapacitors. An excellent discussion on the fundamentals and applications of ultracapacitors is provided by Conway [14].

Laser Direct-Write

Laser direct-write involves the forward transfer of materials from a UV-transparent support to a receiving substrate. The transfers are performed by mixing the active, or sensitive material in a liquid vehicle to form an "ink", which is applied to the UV-transparent support to form the "ribbon" as shown in Figure 2. The specifics of the laser transfer process have been discussed elsewhere [15,16]. A focused UV laser pulse is directed through the backside of the ribbon so that the laser energy interacts with the ink at the support interface. Because the UV laser pulse is strongly absorbed by the ink, only a very shallow volume of ink at the support interface evaporates due to localized heating from the laser-material interaction. This vaporization forward transfers the

remaining ink by uniformly propelling it away from the support towards the receiving substrate.

By removing the ribbon, the laser pulse can interact directly with the substrate in order to micromachine channels and through vias into polymer, semiconductor, and metal surfaces, as well as trim deposited structures to meet design specifications. All micromachining and material transfer can be controlled by computer (CAD/CAM), which allows the rapid fabrication of complex structures without the aid of masks or moulds. This technique has the potential to generate, by a single tool, complete prototype systems on a substrate including all the components required for a mesoscale energy storage system.

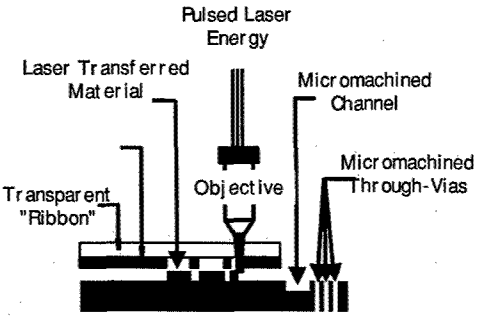

Figure 2. Schematic diagram of the laser direct-write system.

EXPERIMENTAL

Preparation of Ribbons for Laser Direct-Write

Borosilicate glass discs, double side polished, 5.0 cm diameter × 3mm thick are used as ribbon supports. For the fabrication of the micro-ultracapacitors, commercially available hydrous ruthenium oxide powder (Alfa-Aesar, $RuO_2 \cdot 2.5H_2O$) is oven heated to 150 °C for 18 hours to yield a material with the desired water content of 0.5 mol of H_2O per mol of RuO_2 for optimal charge storage [5]. The dry powder is combined with 5 M sulfuric acid to form a hydrous ruthenium oxide ink. For the fabrication of the alkaline microbattery cathodes, powders of electrolytic MnO_2 (< 425 mesh, JEC) and Ag_2O (< 325 mesh, Alfa) are each mixed with 5 –10 wt% graphite (Erachem Super P). The resulting powders are mixed with a solution comprised of PVDF-HFP binder in propylene carbonate until forming a uniform paste to make the MnO_2 and Ag_2O inks respectively. The ink for the anodes is made by mixing, Zn powders (3 μm dia., GoodFellow), in a similar solution of binder in propylene carbonate until forming a uniform paste. Inks for the Li-ion electrodes comprise lithium cobalt oxide, KS6 carbon and an organic binder (PVDF) for the cathode and MCMB 2528 carbon with PVDF for the anode. Both powder mixtures are made into a slurry with 1-methyl-2-

pyrrolidinone(NMP) solvent and mixed until a uniform paste is formed. All the inks are then applied to one side of the borosilicate glass discs using a wire-coater (#6 Gardner) to create a 5 to 10-μm-thick ink layer.

The coated side of the ribbons is kept at a distance of 100–200 μm from the substrate with a spacer. Both the substrate and the ribbon are held in place using a vacuum chuck over the X–Y substrate translation stage. The third harmonic emission of a Nd:YVO_4 laser, $\lambda = 355$ nm (Spectra Physics), is directed through a circular aperture and a 10× objective lens, resulting in a 85 μm diameter spot at the ribbon. The laser fluence is varied between 0.1 – 0.5 J/cm^2 depending on the material being transferred, and is estimated by averaging the total energy of the incident beam over the irradiated area. The mass of the transferred materials is measured using a microbalance (Sartorious M2P).

Fabrication and Testing of Planar Ultracapacitors and Stacked and Planar Microbatteries

RuO_xH_y Ultracapacitors

Planar micro-ultracapacitor electrodes and cells are deposited on 1-cm × 1-cm gold-coated quartz substrates. Details on the fabrication and testing of these devices are provided elsewhere [3,17]. For the micro-ultracapacitor cells, four current collector pads in the form of a "window pane" are first electrically isolated by UV laser micromachining 20-μm grooves in the surface of the gold-coated substrates. Hydrous ruthenium oxide films, approximately 1-mm × 2-mm × 15-μm thick, are then deposited across the machined grooves in the gold-coated quartz and laser micromachined into two identical 0.5-mm × 2-mm × 15-μm electrodes. A Nafion film is drop cast on top of the micro-ultracapacitor cell and allowed to air dry to prevent electrode delamination during testing.

The hydrous ruthenium oxide samples are electrochemically evaluated through cyclic voltammetry (CV) and chronopotentiometry (CP) carried out using an EG&G PAR potentiostat (Model 263). For CV, single electrodes deposited on graphite foil are submerged in a solution of 0.5 M H_2SO_4 in a standard 3 electrode configuration using platinum mesh as a counter electrode and a Pd/H reference electrode that is comparable to a normal hydrogen electrode (NHE). For CP, Nafion-coated planar micro-ultracapacitor cells on the gold-coated quartz substrates are submerged under a droplet of 0.5 M H_2SO_4 and the cell is connected to the potentiostat through a probe station. Data is acquired at specified currents for potentials between 0 and 1 V in this two-electrode configuration.

Alkaline Microbatteries

For the stacked alkaline microbatteries, separate MnO_2 and Ag_2O cathode pads, 3 mm × 3 mm in area and 40-μm thick, are laser transferred onto 1-cm^2 gold-coated glass substrates. The pads are heated to 150 °C in an oven for 5 to 10 minutes to remove the propylene carbonate solvent and to bind the powders to the substrate. Then a 4-mm × 4-mm × 10-μm thick porous insulating layer is laser transferred over each of the MnO_2 and Ag_2O pads to serve as the separator between the metal oxide cathode and the Zn anode. A Zn layer is laser transferred onto the separator in the form of a 2.5-mm × 2.5-mm × 20-μm thick pad. At this point, the resulting MnO_2/separator/Zn and Ag_2O/separator/Zn structures are ready for evaluation. For the planar alkaline microbatteries, a four finger

interdigitated structure, 5-mm long by 2-mm wide is formed by depositing interdigitated pads for the Ag_2O cathode and Zn anode onto a laser micromachined Pt-coated alumina substrate, oven drying the pads and then laser micromachining the gap between the pads to remove any debris that could cause a short between the pads.

To characterize the discharge behavior of the zinc/MnO_2 and zinc/Ag_2O alkaline microbatteries, a droplet of 9 N KOH is placed on top of the cells. Then, CP measurements are performed using a probe station connected to the potentiostat. Additional information on the characterization and results of alkaline microbattery cells made by laser direct-write appears elsewhere in this proceedings volume [18].

Li-ion microbatteries

The Li-ion electrodes are fabricated onto separate substrates as pads 3-mm × 3-mm × 40-μm thick. Composites of $LiCoO_2$, carbon, and PVDF are transferred onto aluminum foil substrates/current collectors while the carbon/PVDF composite is transferred onto copper foil to serve as the positive and negative electrodes, respectively. After laser transfer, the electrodes are dried in a vacuum oven for 12 hours at 110 °C. The electrodes are transferred to an Ar atmosphere and submerged in a 1 M $LiClO_4$/propylene carbonate electrolyte solution for at least 12 h prior to electrochemical evaluation.

Single electrodes are evaluated in half-cell measurements by CV at 0.1 mV/sec using the potentiostat and CP using a battery tester (Maccor model 2300). These three-electrode half-cells utilize a Li-foil (Li/Li^+) reference electrode and Li-foil counter electrode that are aligned with 1 cm of the $LiClO_4$/propylene carbonate between them [6]. The C negative electrodes are cycled between 1 and 0.05 V vs. Li/Li^+ and the $LiCoO_2$ positive electrodes are cycled between 3 and 4.2 V vs. Li/Li^+ at various charging and discharging rates. CP is also carried out on full cells where the positive and negative electrodes are also referenced to a (Li/Li^+) reference electrode and aligned with 1 cm of electrolyte between them. There are no rest periods between the multiple charge and discharge cycles.

RESULTS AND DISCUSSION

The layers of the various materials for micro-power sources deposited by the laser direct-write process show similar morphological and electrochemical properties when compared to layers deposited by stenciling. Figure 3 shows scanning electron microscopy (SEM) images of the surfaces of laser transferred films comprising $RuO_2 \cdot 0.5H_2O$, Ag_2O + C and $LiCoO_2$ + C. It is apparent from these images that the laser transfer process does not result in any obvious changes to the morphology of each of these systems, as there are no indications of melted or fractured material on these length scales.

The hydrous ruthenium oxide pad from a laser transferred micro-ultracapacitor has a uniform mesoporous structure that enables the electrolyte to reach all the way into the bulk of the electrode layers, thus allowing a more effective use of the active material (Fig 3a). Figure 3(b) belongs to a silver oxide + carbon layer from one of the alkaline microbatteries. Here again, a porous structure can be observed, together with micron and submicron-sized particles corresponding to the Ag_2O powders. The nanometer scale structures are the porous carbon material, which is evenly distributed through out the pad.

This carbon provides the high electronic conductivity not present in the silver oxide. In addition, it allows electrolyte penetration into the cathode allowing more efficient use of the electrode material. Finally, figure 3(c) shows a $LiCoO_2$ layer from one of the Li-ion microbatteries. In this case, the high porosity carbon regions can be seen, while the dense material belonging to the $LiCoO_2$ powders shows a flattened plate structure. This lithium cobalt oxide powder structure facilitates the intercalation of lithium into the lattice leading to higher capacities. These images demonstrate that the laser direct-write

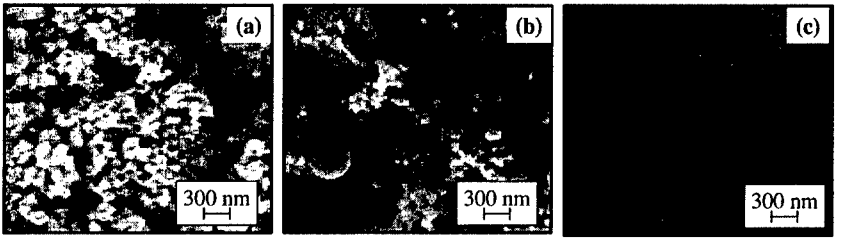

Figure 3. SEM micrographs from the surface of (a) $RuO_2 \cdot 2.5H_2O$,(b) Ag_2O + C and (c) $LiCoO_2$ + C laser transferred films.

technique allows for the deposition of high-surface area, structurally defective and porous materials, which are ideally suited for electrochemical systems.

Planar Micro-Ultracapacitors

Figure 4(a) shows an optical micrograph of a pair of laser transferred planar micro-ultracapacitors. The volume of each cell is 2 x 10^{-5} ml and the mass is less than 0.1 mg per cell, which is less than the mass of a human hair. The charge and discharge behavior of these micro-ultracapacitors has been evaluated for single cells and for pairs of cell connected in series and in parallel. Figure 4(b) shows the CP plots for charge and discharge at currents of 50 and 10 μA respectively for a single cell, and for series and

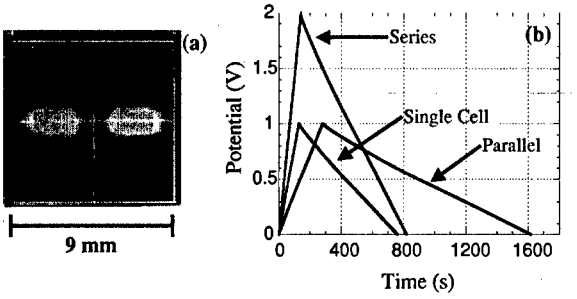

Figure 4. (a) Optical micrograph of a planar micro-ultracapacitor on a gold-coated substrate fabricated by laser direct-write. (b) Chronopotentiometry data from a single cell and from a pair of ultracapacitors connected in series and in parallel, all charged at 50 μA and discharged at 10 μA.

parallel configurations of two cells. The single cell and the pair connected in parallel are charged to 1 volt, while the series configuration is charged to 2 volts. In all cases the discharge behavior remains nearly linear. The discharge times are over 10 minutes at this current. For the single ultracapacitor, the capacitance calculated from this plot, is 6.5 mF. This corresponds to a specific capacitance of ~80 F/g when normalized by the measured mass of the laser transferred material (active material plus electrolyte). Furthermore, the capacitance of the series and parallel combinations measured from the plot are in agreement with the appropriate addition of single cell capacitances.

Stacked and Planar Alkaline Microbatteries

Figure 5(a) shows a schematic for the cross-section of a stacked alkaline microbattery cell made by laser direct-write. Figure 5(b), shows a set of optical micrographs illustrating each of the laser transferred layers resulting in a zinc/MnO_2 alkaline microbattery made on top of a gold-coated glass substrate. After the zinc pad is laser deposited, a graphite foil current collector is placed on top of the zinc and the microbatteries are ready to be tested. The stacked zinc/MnO_2 alkaline microbatteries all showed open circuit potentials of ~1.3 V, which are lower than the expected value of 1.5 V.

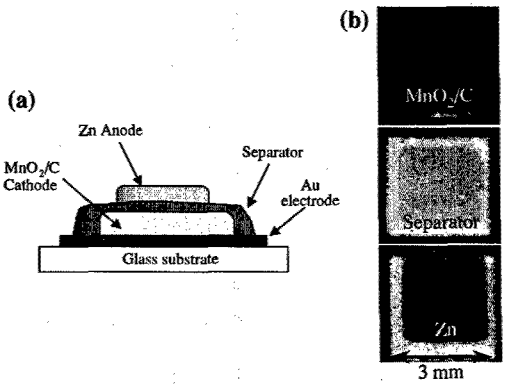

Figure 5. (a) Cross section schematic of a stacked alkaline microbattery made by laser direct-write. (b) Optical micrographs showing each of the layers present in a Zn/MnO_2 alkaline microbattery.

Figure 6(a) shows an optical micrograph of an interdigitated planar zinc/Ag_2O microbattery made by laser direct-write. The open circuit potential for the planar cells is 1.55 V, which is to be expected for the silver-oxide/zinc system. Figure 6(b) shows the discharge behavior for the same interdigitated planar cell at a discharge current of 25 μA. The data shows that the planar alkaline microbattery made by laser direct-write has discharge characteristics similar to those from an ideal zinc/Ag_2O battery. However, the actual capacity for the cell is lower than would be expected from the theoretical capacities of the materials used. After post discharge analysis of the cell, it was

determined that the failure of the cell was due to delamination of the Zn anode. It should be pointed out that none of the alkaline microbattery cells fabricated for this work were packaged and thus the KOH electrolyte solution would evaporate with time. Future work will focus in increasing the specific energy of these alkaline microbatteries, and in developing and testing various packaging approaches.

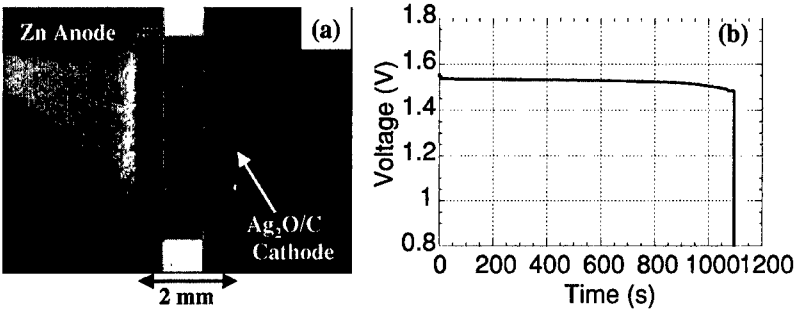

Figure 6. (a) Optical micrograph of a planar interdigitated Zn/Ag_2O microbattery fabricated by laser direct-write on a Pt-coated alumina substrate. (b) Discharge behavior at 25 μA from this microbattery. The sudden drop at ~1100 seconds is due to delamination of the Zn anode.

Li-ion Microbatteries

The electrodes fabricated using the laser direct-write system for a Li-ion microbattery are shown in Figure 7. The Cu and Al foil current collectors are laser micromachined to the required shape, while the carbon anode and $LiCoO_2$ cathode are laser deposited in 3 mm × 3 mm pads. Each of these electrodes show excellent capacities in half-cell measurements [6]. Adhesion of the active materials to the current collectors appears to have a large impact on the measured capacities.

Under full cell measurements, a specific discharge capacity of 40 mAh per gram of $LiCoO_2$ is measured when cycled between 3 and 4.2 V. The capacity continuously increases over the duration of the experiment (after 325 hours of operation and 57 cycles, the capacity is still increasing). The capacity of the cell is lower than the expected 125 mAh/g presumably due to water contamination in the dry box. Future work will focus on eliminating water contamination in the test environment, plus optimizing various packaging schemes.

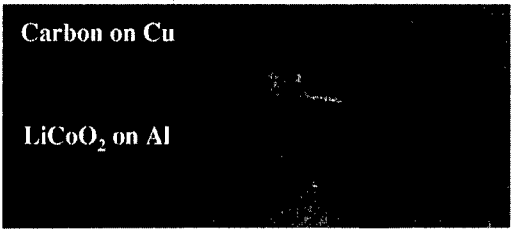

Figure 7. Optical micrograph of a $LiCoO_2$ cathode pad and a C anode pad laser forward transferred onto Al and Cu current collectors respectively.

SUMMARY AND OUTLOOK

We are applying a direct-write laser engineering technique to the production of integrated and distributed hybrid micropower sources that include planar micro-ultracapacitors, planar and stacked microbatteries and in the future, energy harvesting components. Using laser direct-write in combination with ultraviolet laser micromachining, we have successfully fabricated hydrous ruthenium oxide micro-ultracapacitor cells, primary alkaline manganese-oxide/zinc and silver-oxide/zinc microbatteries in planar and stacked configurations, and secondary Li-ion microbattery electrodes. In most cases, the prototype systems tested for this work showed the expected open circuit potentials and exhibited uniform discharge behavior under constant loads. Several challenges remain such as further increasing the capacity and longevity of these mesoscopic power sources. Future work will focus in addressing these issues plus optimizing the packaging of these devices.

ACKNOWLEDGEMENTS

The authors thank B. Pratap and E. Coakley for assistance in materials characterization, and Dr. Aimee Curtright for helpful discussions. We are grateful to the Office of Naval Research for financial support. CBA and RCW are post-doctoral fellows with the National Research Council and American Society for Engineering Education, respectively.

REFERENCES

1. A. Piqué and D.B. Chrisey, editors, *Direct-Write Technologies for Rapid Prototyping* Applications, (Academic Press, San Diego CA, 2002).
2. K.E. Swider-Lyons, A. Piqué , C.B. Arnold and R.C. Wartena, in *The Encyclopedia of Materials Science and Technology*, edited by K.H.J. Bushcow, R.W. Cahn, M.C. Flemings, B. Ilschner, E.J. Kramer, and S. Mahajan, (Elsevier, New York, 2002).
3. C.B. Arnold, R.C. Wartena, K.E. Swider-Lyons, and A. Piqué, *J. Electrochem. Soc.*, in press (2003).
4. A. Piqué, C.B. Arnold, R.C. Wartena, D.W. Weir, B. Pratap, K.E. Swider-Lyons, R.A. Kant, and D.B. Chrisey, in Third International Symposium on Laser Precision Microfabrication, Osaka, Japan, 2002 (SPIE, Bellingham, WA, in press).
5. J.P. Zheng, P.J. Cygan, and T. R. Jow, *J. Electrochem. Soc.*, **142**, 2699 (1995).
6. R.C. Wartena, C.B. Arnold, A. Piqué, and K.E. Swider-Lyons, *Micropower for Microdevieces*, Proceedings of the Electrochemical Society Meeting, Salt Lake City, UT, 2002, (Electrochemical Society, Pennington, NJ in press).
7. D.J. Hayes and D.B. Wallace, SPIE Proceedings, **2920**, 296, (1996).
8. D. Dimos and P. Yang, Proc. of 48th Electronic Components and Technology Conf., Seattle, Washington, p. 225 (IEEE, New York, 1998).
9. D.J. Ehrlich and J.Y. Tsao, editors, *Laser Microfabrication: Thin Film Processes and Lithography*, (Academic Press, Boston, 1989).
10. R.P. Rafaelle, A.F. Hepp, G.A. Landis and D.J. Hoffman, *Prog. In Photovolt: Res. Appl.*, **10**, 391 (2002).

11. C.A. Vincent and B. Scrosati, *Modern Batteries: An Introduction to Electrochemical Power Sources*, 2nd ed. (John Wiley & Sons, New York, 1997).
12. J.B. Bates, N.J. Dudney, D.C. Lubben, G.R. Gruzalski, B.S. Kwak, X.Yu, and R.A. Zuhr, *J. Power Sources,* **54**, 58 (1995).
13. J.B. Bates, N.J. Dudney, B. Neudecker, A. Ueda, and C.D. Evans, *Solid State Ionics,* **135**, 33 (2000).
14. B.E. Conway, *Electrochemical Capacitors*, (Kluwer-Academic, New York, 1999).
15. A. Piqué, D.B. Chrisey, R.C.Y. Auyeung, J. Fitz-Gerald, H.D. Wu, R.A. McGill, S. Lakeou, P.K. Wu, V. Nguyen, and M. Duignan, *Appl. Phys. A*, **69**, 279 (1999).
16. D. Young, R.C.Y. Auyeung, A. Piqué, D.B. Chrisey, and D.D. Dlott, *Applied Surface Science*, **197-198**, 181, (2002).
17. C.B. Arnold, R.C. Wartena, B. Pratap, K.E. Swider-Lyons, and A. Piqué, in *Electroactive Polymers and Rapid Prototyping*, edited by D.B. Chrisey and S.C. Danforth, (Materials Research Society, Pittsburgh, PA, 2002), Vol. **689**, pp. 275–280.
18. C.B. Arnold and A. Piqué, Proceedings of the Materials Research Society Meeting, Boston, MA, 2002, (Materials Research Society, Pittsburgh, PA, 2003, in press).

Mat. Res. Soc. Symp. Proc. Vol. 758 © 2003 Materials Research Society LL3.7

Development of PZT Suspensions for Ceramic Ink-Jet Printing

B. Derby, D.H. Lee, T. Wang and D. Hall
Manchester Materials Science Centre, UMIST and the University of Manchester,
Grosvenor St., Manchester, M1 7HS, UK

ABSTRACT

The direct ink-jet printing of ceramic powders requires the development of highly fluid suspensions of ceramic particles with viscosity < 40 mPas. Here we describe the development of two such ceramic suspensions, which contain up to 30% by volume of PZT particles in either an azeotropic mixture of MEK and ethanol or in an alkane wax at 120 °C. The influence of various processing parameters on fluid rheology are investigated and trial fluids have been passed through an ink-jet printing head.

INTRODUCTION

Ink-jet printing is now a mature technology and has widespread applications in the fields of printing, product marking and microdosing. Initial work combining ink-jet printing and layered manufacturing for the production of ceramic parts was undertaken by Sachs and co-workers, using a process of selectively printing binders onto powder beds [1]. Evans and co-workers extended this concept by pioneering the direct printing of ceramic suspensions using ink-jet printers [2-4]. Direct ink-jet printing is a very attractive route for the freeform fabrication of ceramics as fabrication of an object by droplet deposition allows the composition of each voxel of a design to be individually determined. This extends the fabrication method to components requiring multiple materials or materials of graded composition.

Initial studies of direct ink-jet printing used commercial ink-jet printers optimised for text printing, and thus the volume of ceramic powder available in suspension was relatively low (< 10 volume%). This was because the viscosity of the suspensions had to be low to allow printing using the unmodified printers available. Evans' work used ceramic suspensions in aqueous or alcohol-based media. The liquid carrier or solvent is removed by evaporation from the deposit after printing. Solid objects can be fabricated by overprinting, however the combination of low solid volume, and the need to remove the solvent before deposition of subsequent layers, resulted in a relatively low rate of growth in the direction normal to the printed plane.

Our earlier work on ceramic ink-jet printing used alumina powders suspended in low melting point alkane (paraffin) waxes [5,6]. These suspensions solidify on impact and build up a thickness more rapidly than do deposits that solidify by evaporation. Both these methods have their advantages and disadvantages. Suspending fluids that evaporate allow dilute, low viscosity ceramic particle suspensions to be used. However solid distribution during drying is affected by Marangoni convection and the resulting deposit may show an irregular packing density. Phase-change fluids that solidify on impact result in more uniform particle distributions but now the solidified fluid must be removed from the object by an additional processing step prior to firing. Whichever route is used to prepare printable fluids, it is desirable to obtain the maximum fraction of particles in stable suspension while maintaining a fluid viscosity sufficiently low to allow droplet formation in an ink-jet printing device. Using the ink-jet printing systems available at

Manchester this viscosity limit is 40 mPas at the printing temperature. With alumina powders it is possible to achieve stable suspensions with up to 40% solids fraction with viscosity sufficiently low for ink-jet printing [6].

In this article we describe methods to produce printable suspensions of the piezoelectric ceramic lead ziconate titanate (PZT) in wax and other solvents.

MATERIALS AND EXPERIMENTAL PROCEDURE

PZT powder, of grade PC5H (a soft piezoelectric material), was provided by Morgan Electroceramics (Wrexham, UK). Two solvent systems have been investigated using either a paraffin (alkane) wax of melting temperature 57 °C (Aldrich, Poole, UK) or an azeotropic mixture of 67% methyl ethyl ketone and 33% absolute ethanol (MEK/EtOH) (Aldrich, Poole, UK). Two dispersant systems have been used: a commercial polyester dispersant (Hypermer LP1, Uniqema, Everberg, Belgium) — combined with Octadecylamine (Aldrich, Poole, UK) and a phosphate ester based dispersant (Phospholan PE182, Akros Chemicals, Manchester, UK).

The PZT powder was calcined for 5 hours at 650 °C to remove a polymeric binder on the as-received powder. The calcined powder was either ball milled for 72 hours or attrition milled for 6 hours in alcohol to remove any agglomeration that occurred during calcining. The dried powders were mixed with the appropriate medium and dispersant before ball milling for up to 24 hours at 10 – 20 rpm. The mixing/milling process was conducted at room temperature with the MEK/EtOH solvent. The temperature of mixing for the wax-based suspension was 120 °C, which is the operating temperature of the high temperature ink jet head.

Suspension viscosity was measured using a concentric cylinder rheometer (Brookfield, Middleboro, MA, USA). Suspension stability was assessed by leaving suspensions in measuring cylinders at the appropriate temperature and investigating particle distribution after periods of time. In order to assess the printability of the suspensions they were passed through a single ink-jet printing head. For the MEK/EtOH solvent system a room temperature printhead was used (Microfab, Plano, TX, USA), while for the wax based system a system optimised for printing at 120°C was used (Sanders Design International, Wilton NH, USA).

RESULTS AND DISCUSSION

For the initial trials the phosphate ester dispersant system was used. This gave reasonably stable suspensions in both MEK/EtOH and wax solvents. Suspension viscosity was found to be strongly affected by ball milling with longer milling times giving lower viscosity up to some optimum time above which viscosity increased again. This increase in viscosity is believed to indicate the thermomechanical degradation of the dispersant molecules during milling. This behaviour is clearly seen in figure 1 where the optimum milling time for a 20% by volume dispersion of PZT in the MEK/EtOH solvent is 18 hours, and for the wax solvent 4hours. The shorter time before degradation found with the wax-based materials is believed to be because this material is milled at 120 °C.

Suspension viscosity was also found to depend strongly on the amount of dispersant used. The behaviour in figure 2 also shows an optimum result at 1% by weight of the phosphate ester for both solvent media when 20 vol% PZT is in suspension. The optimum value indicates site saturation on the PZT particle surface. Any dispersant in addition to this value remains in solution and increases viscosity without further improving particle dispersion. Figure 3 shows the

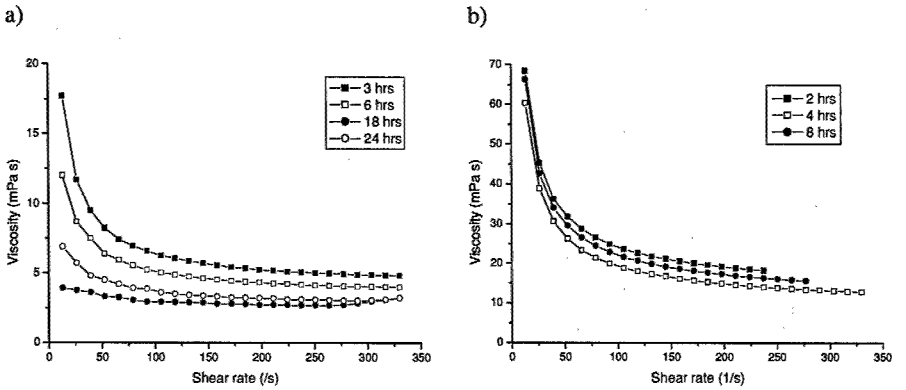

Figure 1. Viscosity of 20 vol% PZT suspensions, with 1 wt% PE182 dispersant, as a function of shear rate after various ball milling times: a) MEK/EtOH solvent at room temperature, b) wax solvent at 120 °C.

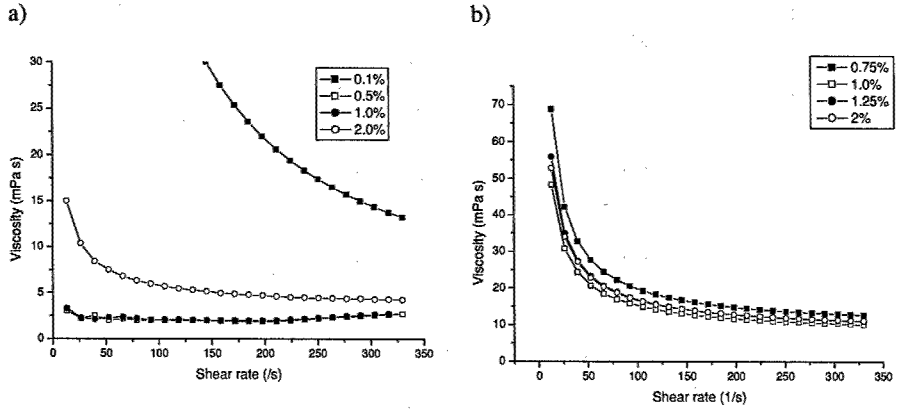

Figure 2. Effect of varying the content of phosphate ester dispersant on the viscosity of the 20 vol% PZT suspensions : a) MEK/EtOH solvent at room temperature, b) wax solvent at 120 °C.

effect of increasing particle volume in suspension. With the MEK/EtOH solvent the suspension viscosity is sufficiently low to allow printing at 30 vol% PZT. However, the viscosity of the wax based material is too high.

There are a number of potential applications for components fabricated from PZT where the higher aspect ratio deposit available through printing wax based suspensions would be an advantage. Hence a different dispersant system based on a commercial polyester was studied. Previous work on alumina had identified the Hypermer series of dispersants as being particularly effective with alumina [5,6] and these were explored for use with PZT.

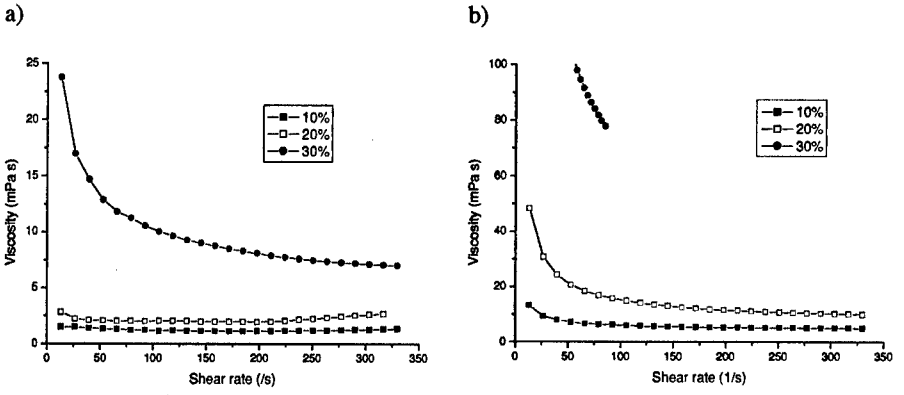

Figure 3. The influence of the volume fraction of PZT particles in suspension on fluid viscosity : a) MEK/EtOH solvent at room temperature, b) wax solvent at 120 °C.

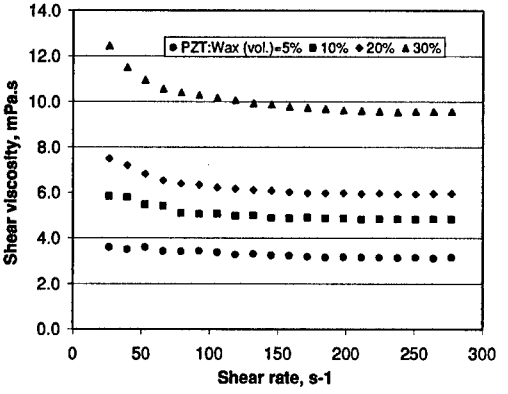

Figure 4. Viscosity of PZT suspensions in wax as a function of volume solids, measured at 120 °C with Hypermer LP1 dispersant.

It is well known that a combination of long chain and short chain surfactant molecules can be particularly effective in dispersing ceramics particles [7]. Earlier work had shown that Hypermer LP1 can be used with octadecanoic acid (stearic acid) and octadecylamine to produce suspensions of alumina in wax with very low viscosity [5, 6]

Suspensions of PZT in wax were prepared containing 1 wt% Hypermer LP1 and 0.5 wt% octadecylamine and a range of PZT powder concentrations. These were ball milled for 6 hours at 120 °C to ensure adequate dispersion. The viscosity of this range of materials was measured and the results given in figure 4. On comparing figure 4 with figure 3b it is clear that the Hypermer LP1 dispersant system gives significantly lower viscosities than the phosphate ester system.

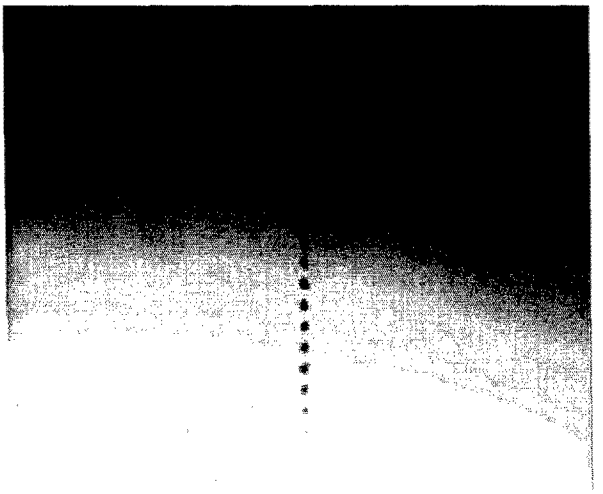

Figure 5. Ink-jet printed droplets of 30 vol% PZT suspension in MEK/EtOH.

Both the phosphate ester dispersed MEK/EtOH and the Hypermer dispersed wax based system have suffiently low viscosity at 30 vol% PZT to be printable. Preliminary trials have been successful (figure 5) with the fluids having been successfully printed through the test station.

CONCLUSIONS

It is possible to prepare PZT suspensions of high solid loading that can be successfully used for ink-jet printing. A phosphate ester dispersant has been used with MEK/EtOH azeotropic solvents while a combination of a polyester and a short chain amine terminated alkane produces the best result with wax as a solvent.

ACKNOWLEDGEMENTS

We would like to acknowledge the support of the EPSRC and Ministry of Defence through project grant reference GR/N16969. We also acknowledge the support of Morgan Electroceramics who provided the PZT powder.

REFERENCES

1. E. Sachs, M. Cima, P. Williams, D. Brancazio, and J. Cornie, J. Eng. Industry - Trans. ASME **114**, 481 (1992).
2. P. F. Blazdell and J. R. G. Evans, J. Mater. Process. Tech. **99**, 94 (2000).
3. C. E. Slade and J. R. G. Evans, J. Mater. Sci. Lett. **17**, 1669 (1998).

4. Q. F. Xiang, J. R. G. Evans, M. J. Edirisinghe, and P. F. Blazdell, Proc. Inst. Mech. Eng. B – J. Eng. Manuf. **211**, 211 (1997)
5. K. A. M. Seerden, N. Reis, J. R. G. Evans, P. S. Grant, J. W. Halloran, and B. Derby, Journal of the American Ceramic Society, **84**, (2001) 2514-2420.
6. C. Ainsley, N. Reis and B. Derby, J. Mater. Sci. **35**, 3155 (2002).
7. J.H. Song and J.R.G. Evans, J. Rheol. **40**, 131-152 (1996).

Mat. Res. Soc. Symp. Proc. Vol. 758 © 2003 Materials Research Society LL3.8

Laser Direct-Write Of Alkaline Microbatteries

Craig B. Arnold and Alberto Piqué
Materials Science and Technology Division
Naval Research Laboratory, Washington, DC 20375, USA

ABSTRACT

We are developing a laser engineering approach to fabricate and optimize various types of alkaline microbatteries. Microbattery cells are produced using a laser forward transfer process that is compatible with the materials required to make the anode, cathode, separator and current collectors. The use of an ultraviolet transfer laser (wavelength = 355 nm, 30 ns FWHM) enables other operations such as surface processing, trimming and micromachining of the transferred materials and substrate and is performed in situ. Such multi-capability for adding, removing and processing material is unique to this direct-write technique and provides the ability to laser pattern complicated structures needed for fabricating complete microbattery assemblies. In this paper, we demonstrate the production of planar zinc-silver oxide alkaline cell by laser direct-write under ambient conditions. The microbattery cells exhibit 1.5-1.6 V open circuit potentials, as expected for the battery chemistry and show flat discharge behavior under constant current loads.

INTRODUCTION

Over the last two decades, there has been a continuing trend toward smaller and more autonomous micro-electronic sensing and microelectromechanical devices and systems. As this miniaturization pushes forward, the classical concept of an independent, monolithic power source is no longer sufficient to meet the demands of these advanced devices [1, 2, 3]. In these cases, one of the main concerns is the necessary reduction in both area and thickness of the power source to meet the geometric requirements for integration with the microdevices.

There has been much effort to develop small microbatteries for various primary and secondary chemistries. One successful approach for the lithium based system uses solid state electrolytes in a stacked configuration [4, 5]. In this case, the anode, cathode, and solid-state electrolyte are deposited using standard physical vapor deposition techniques in vacuum with patterning through photolithography. In other experiments, alkaline microbatteries have been produced in a planar configuration where the anode and cathode are located adjacent to each other on the substrate [6, 7]. In this case, materials are deposited through electrochemical and vacuum techniques while the patterning is accomplished through photolithography.

An alternative approach to the production of microbattery cells is through laser engineering [8, 9]. In this technique, we use laser direct-write to directly deposit material where needed [10, 11, 12]. Subsequent laser processing such as annealing or machining is performed *in situ* without the need to remove the substrate. Under this approach, there is no need for expensive vacuum or lithographic processing as all stages of cell construction are performed under atmospheric conditions. Furthermore, our technique does not require re-engineering of fabricated microdevices since we can add material, on location, directly to preexisting circuit boards. We have successfully applied this technique to the production of planar, symmetric hydrous

ruthenium oxide electrochemical capacitors [13, 14] as well as stacked alkaline microbattery structures [15].

In this paper we demonstrate the use of a laser engineering approach to the production of planar alkaline microbattery cells. We use laser direct-write to deposit Zn anodes and Ag_2O cathodes in planar configurations and use laser micromachining to ultimately shape the deposited materials into microbattery cells. Our cells exhibit the appropriate open circuit potential as well as the expected flat discharge behavior under constant current.

EXPERIMENT

Zinc and monovalent silver oxide (Ag_2O) are deposited using a patented laser direct-write technique developed at the Naval Research Laboratory [10, 11, 12]. Figure 1a shows a schematic of the general technique. Commercially available powders are combined with a liquid transfer vehicle to form a suspension or ink. This ink is spread on a borosilicate glass plate using a wire-coater (# 6 Garner) to form a coating approximately 5 μm thick. A frequency-tripled Nd:YVO_4 laser (λ=355 nm) irradiates the ink through the back of the glass plate to induce a forward transfer of material to a substrate $\sim$100 μm below the ribbon. The mass of the transferred material is accurately measured using a microbalance (Sartorius M2P) with μg resolution.

The microbattery cell is constructed by first preparing the substrate, then depositing the cathode followed by the anode. We use platinum coated alumina substrates that have been diced into 1 cm x 1 cm squares. The cell geometry is planar (anode adjacent to cathode) with the circular shape of diameter 2500 μm shown in figure 2a. Substrates are prepared by preliminary solvent cleaning using acetone and isopropanol, followed by UV laser micromachining to electrically isolate the anode current collector from the cathode current collector and establish alignment marks (white lines in figure 2a).

In order to improve the conductivity of the Ag_2O cathode material, the powder is mixed with 5 wt.% graphite (Erachem Super P). The powder mixture is combined with a solution of PVDF-HFP binder in propylene carbonate to form the cathode ink. The cathode is deposited in a "C" shape with outer diameter 2500 μm and inner diameter 1250 μm. Following deposition of the cathode, the substrate is baked at 150 °C for 5-10 minutes to remove the propylene carbonate solvent and to bind the cathode to the substrate.

The anode ink used in this experiment is pure Zn mixed with a similar solution of binder and propylene carbonate. This ink is deposited in a circular region of diameter 800 μm and subsequently baked at 150 °C for 5-10 minutes. Finally, after deposition and processing of cathode and anode, the separation gap between them is UV laser micromachined to remove any additional materials that could cause shorting of the cells (figure 1b). The typical weight of transferred material is 200 μg.

Electrochemical evaluation of cell voltage and discharge behavior is carried out using a potentiostat (EG&G PAR Model 263) connected to a probe station. A droplet of 9N KOH is placed on top of both anode and cathode, spanning across the gap to activate the cell. Chronopotentiometry is used to discharge the cells at various currents between the open circuit potential and 0.8 V in a two-electrode configuration.

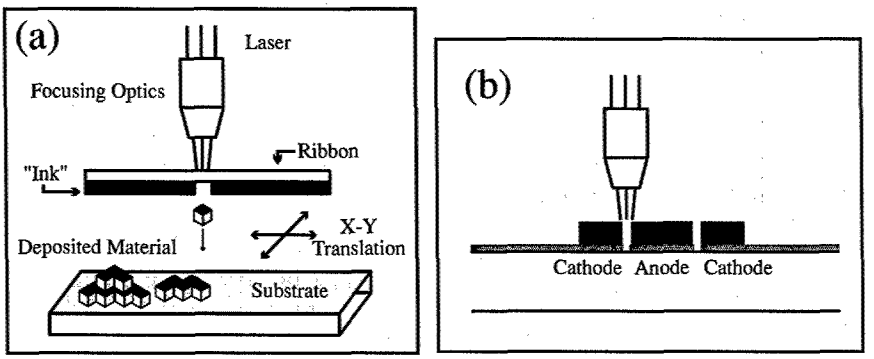

Figure 1. (a) Cartoon of laser direct-write process. (b) Cross sectional view of micromachining between anode and cathode.

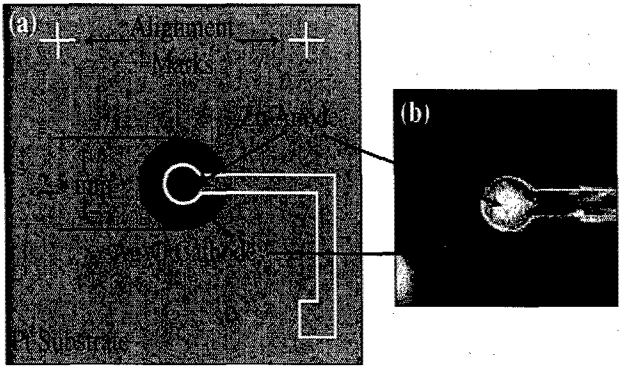

Figure 2. (a) Cartoon of planar battery configuration. (b) Picture of laser deposited planar microbattery.

RESULTS

Figure 2b shows an optical micrograph of an actual microbattery cell. The separation between the central anode and annular cathode can be clearly seen by the appearance of the white alumina below the substrate surface. The microstructure of the deposited material is shown in figure 3. The cathode shows the appearance of micron sized particles of Ag_2O interspersed in a mesh of threadlike carbon. Such a structure enables good electron conductivity in the cathode through the carbon network, while leaving a relatively large surface area of Ag_2O exposed to the

electrolyte for charge transfer. The anode structure is quite different, exhibiting isolated and clustered particles of Zn approximately 3 μm in diameter. This structure enables a high surface area in contact with the electrolyte.

Upon connecting the microbattery cells to the potentiostat, the open circuit potential is measured for each cell. We find the open circuit potentials range from 1.5-1.6 V as expected for the zinc-Ag_2O chemistry. This suggests that our laser engineering procedure of ink formulation, laser transfer, and subsequent drying does not modify the chemical properties of either anode or cathode material.

A typical constant current discharge curve for a single cell is shown in figure 4 for a current of 10 μA. This particular cell has a cathode mass of 110 μg ($\sim$105 μg Ag_2O) and anode mass of of 80 μg. Based on these masses, the cell is cathode limited with a theoretical capacity of 23.5 μA·Hr. The open circuit potential for this cell is measured to be 1.55 V. Upon discharge, there is an initial drop of $\sim$10 mV to 1.54 V followed by the characteristically flat behavior that is expected for the Zn-Ag_2O system [16]. This initial potential drop is due to internal resistance in the cell which is greater for a planar geometry in comparison to a stacked structure.

After approximately 900 seconds of discharge, the potential in the cell has a sharp drop by 10 mV followed by a flat discharge for a while before exhibiting a second drop of 15 mV and subsequent failure shortly thereafter. Based on optical microscopy of the cell during the experiment, we conclude that sharp decreases in potential are due to partial delamination of the anode with ultimate failure due to complete delamination. Similar failure occurred for all other cells using the same ink formulation and geometry. We have achieved improved adhesion results when using more binder in our formulation, but over time we still have delamination problems. As figure 3b demonstrates, the Zn particles are spherical in shape and large amounts of polymer binder would be necessary to maintain adhesion between them. However, too much binder increases the electron resistance of the anode and therefore increases the loss in the cell and

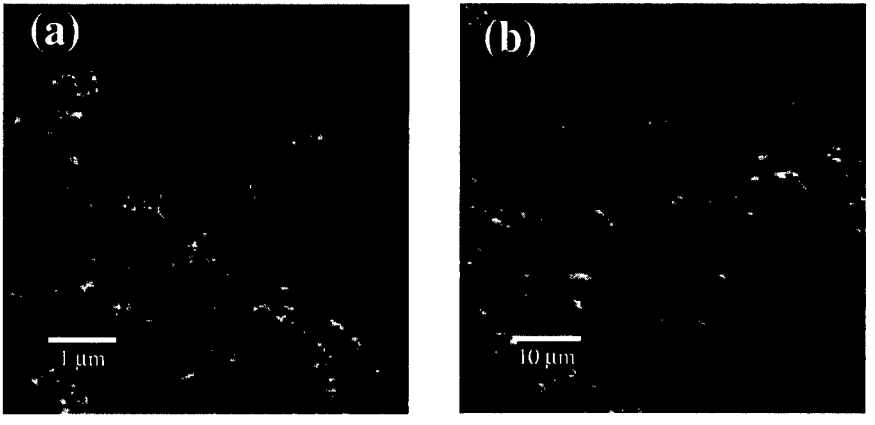

Figure 3. SEM micrographs of (a) cathode and (b) anode. Note different scale bars in the two images.

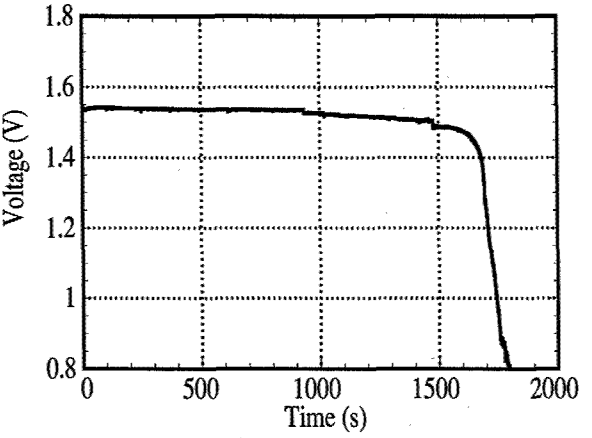

Figure 4. Discharge behavior of alkaline microbattery at 10 μA.

decreases the ability to be discharged at higher currents.

The experimental capacity as well as energy and power of the cell are obtained from the discharge curve of figure 4. The measured capacity of this cell at 10 μA discharge current is 5 μA·Hr, with an energy and power of 7.3 μW·Hr and 14.7 μW respectively. This capacity is less than the theoretical capacity by a factor of approximately 5. As discussed previously, the poor adhesion of the anode is predominantly responsible for the decrease in capacity.

SUMMARY

Laser engineering provides a new approach to making alkaline microbattery cells. We have shown the ability to laser deposit anode and cathode material to construct a working cell in a planar configuration with a total mass of transferred material less than 200 μg. The cell exhibits the expected open circuit potential of the zinc-silver oxide system of 1.5-1.6 V. Under constant current discharge conditions of 10 μA, the cell is able to maintain its potential for almost 30 minutes before cell failure. The open circuit potential and flat discharge behavior observed for our cells indicate that laser engineering is a viable approach for producing alkaline microbatteries in planar geometries. One of the key advantages of this technique is the ability to both deposit and remove material from the substrate *in situ*. The actual capacity and energy of this system are lower than would be expected from theoretical calculation based on the materials used. From visual observations during discharge, it is determined that failure of the cell is not due to complete discharge, but rather due to catastrophic delamination of the Zn anode.

ACKNOWLEDGEMENTS

The authors thank B. Pratap and E. Coakley for assistance in materials characterization and Dr. K.E. Swider-Lyons for helpful discussion. This research was supported in part by the Office of Naval Research. CBA acknowledges the support of the National Research Council postdoctoral associate program.

REFERENCES

1. J. N. Harb, R. M. LaFollette, R. H. Selfridge, and L. L. Howell, J. Power Sources **104**, 46 (2002).
2. P. B. Koeneman, I. J. Busch-Vishniac, and K. L. Wood, J. Microelectromech. Sys. **6**, 355 (1997).
3. M. Balkanski, Sol. Energy Mater. Sol. Cells **62**, 21 (2000).
4. J. B. Bates, N. J. Dudney, D. C. Lubben, G. R. Gruzalski, B. S. Kwak, X. Yu, and R. A. Zuhr, J. Power Sources **54**, 58 (1995).
5. J. B. Bates, N. J. Dudney, B. Neudecker, A. Ueda, and C. D. Evans, Solid State Ionics **135**, 33 (2000).
6. P. H. Humble, J. N. Harb, and R. LaFollette, J. Electrochem. Soc. **148**, A1357 (2001).
7. R. M. LaFollette, J. N. Harb, and P. Humble, in *The Sixteenth Annual Battery Conference on Applications and Advances*, IEEE, edited by R. S. L. Das and H. Frank (IEEE, Piscataway, NJ, 2001), pp. 349–354.
8. K. E. Swider-Lyons, A. Piqué, C. B. Arnold, and R. C. Wartena, in *Electroactive Polymers and Rapid Prototyping*, edited by D. B. Chrisey and S. C. Danforth (Materials Research Society, Pittsburgh, PA, 2002), Vol. 689, pp. 265–275.
9. K. E. Swider-Lyons, A. Piqué, C. B. Arnold, and R. C. Wartena, in *The Encyclopedia of Materials Science and Technology*, edited by K. H. J. Bushcow, R. W. Cahn, M. C. Flemings, B. Ilschner, E. J. Kramer, and S. Mahajan (Pergamon, New York, 2002).
10. D. B. Chrisey, R. A. McGill, and A. Piqué, U.S. Patent No. 6,177,151 (1999).
11. A. Piqué, D. B. Chrisey, J. M. Fitz-Gerald, R. A. McGill, R. C. Y. Auyeung, H. D. Wu, S. Lakeou, V. Nguyen, R. Chung, and M. Duignan, J. Mater. Res. **15**, 1872 (2000).
12. D. B. Chrisey, A. Piqué, J. Fitz-Gerald, R. C. Y. Auyeung, R. A. McGill, H. D. Wu, and M. Duignan, Appl. Surf. Sci. **154-155**, 593 (2000).
13. C. B. Arnold, R. C. Wartena, K. E. Swider-Lyons, and A. Piqué, J. Electrochem. Soc. (*in press*).
14. C. B. Arnold, R. C. Wartena, B. Pratap, K. E. Swider-Lyons, and A. Piqué, in *Electroactive Polymers and Rapid Prototyping*, edited by D. B. Chrisey and S. C. Danforth (Materials Research Society, Pittsburgh, PA, 2002), Vol. 689, pp. 275–280.
15. A. Piqué, C. B. Arnold, R. C. Wartena, D. W. Weir, B. Pratap, K. E. Swider-Lyons, R. A. Kant, and D. B. Chrisey, in *Third International Symposium on Laser Precision Microfabrication* (SPIE, Bellingham, WA, *In Press*).
16. S. A. Megahed, J. Passaniti, and J. C. Springstead, in *Handbook of Batteries*, edited by D. Linden and T. B. Reddy (McGraw-Hill, New York, 2002), Chap. 12, pp. 12.1–12.17.

Nanoscale Rapid Prototyping

Mat. Res. Soc. Symp. Proc. Vol. 758 © 2003 Materials Research Society

Programmable Technologies for Micro- and Nano-Scale Pattern and Material Transfer and Possible Applications for Control of Self-Assembly

David J. Nagel
Department of Electrical and Computer Engineering, The George Washington University
2033 K Street NW (Suite 340J), Washington DC 20052, U. S. A.

ABSTRACT

Programmable methods for transferring materials to surfaces in patterns can produce structures with micrometer and nanometer scale features. All such technologies involve combinations of information, materials and energy. The materials in additive technologies can originate in the vapor phase, as liquids or suspensions, or as solids. The energy can come from laser, electron or ion beams, or the pressures used in writing, dispensing, jetting or flow methods. Many of the programmable techniques do not require high temperatures, so they can be used to make fine-scale structures of organic and bio-materials, and even live biologicals. Quantitative comparisons of both additive and subtractive programmable methods show that only a few, based on electron or ion beams, or on proximal probes, are capable of making nanometer-scale structures. Assembly methods, notably self- and directed-assembly, should prove to be central to the realization of manufacturable nanotechnology. Programmable deposition technologies may be used to supply materials for, and otherwise control self-assembly processes. The four sets of technologies, namely masked lithography, direct-write techniques, self-assembly and directed-assembly, provide a versatile and powerful toolbox for making micro-and nano-meter scale devices and systems.

INTRODUCTION

Many programmable, data-driven, so-called "direct-write", technologies for producing fine-scale lines on work pieces have been developed in the past decade. The person designing a process flow for the production of some device or system containing micro- or nano-scale features now has many tools at their disposal. These tools are widely applicable for the production of micro-electronics, -magnetics, -optics and -mechanics (MEMS). A recent book provides a convenient summary of direct-write methods and their characteristics [1].

It is worthwhile to compare the direct-write techniques with the conventional methods that have been used with increasing precision for decades to produce integrated circuits. Three types of processes are used by the semiconductor industry, as indicated by the boxes in figure 1. They necessarily involve the transfer of a pattern *onto* the work piece in order to achieve some desired form in a thin layer of material. This is usually done with fixed masks. However, programmable electro-optical or micro-mechanical masks are now being used in some cases, where the best resolution is not required. Two types of material transfer steps are also employed, namely material addition (deposition) or material removal (etching). In the programmable technologies of interest here, the pattern transfer step is accomplished simultaneously with the material transfer process, as shown by the ovals in figure 1.

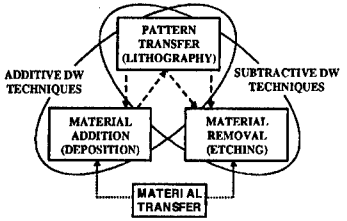

Figure 1. The three processes (boxes) used in conventional lithographic processing, which are employed in pairs (ovals) for direct write (DW) processes.

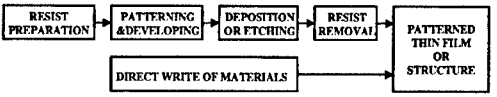

Figure 2. Comparison of the conventional lithographic method of producing patterned thin films (top) with the steps used in data-driven direct-write technologies, which do not involve masks or photoresists.

Another way to appreciate the differences between conventional, masked production of small structures and direct-write techniques is given in figure 2. There it is shown that the conventional approach requires resist preparation and removal steps, in addition to the patterning and material transfer steps. Photoresists require deposition (usually by spinning), baking and development, besides their final removal. The production of complex modern integrated circuits involves the use of over two dozen masks and over 200 process steps.

The programmable technologies, which do not require expensive masks and the use of photoresists, are attractive due to their relative simplicity. Not only do they require substantially fewer process steps, but also their programmability dramatically shortens the time required for the implementation of design changes. Direct-write methods can employ a wide variety of materials and a great diversity of substrates. Often, they are low temperature processes. This expands the variety of materials that can be handled. In particular, it enables the use of organic materials (such as electronic polymers), bio-materials (for example, proteins) and live biological entities (notably viable cells). The low temperatures also make it possible to avoid undesirable processes, such as grain growth. Further, while conventional processing is generally limited to the production of patterned *thin* films, the programmable technologies can produce thick, essentially-3D structures in some cases and fully 3D structures in other instances.

There are limitations to the results that can be obtained with direct-write methods. Inevitably, they are relatively slow because of their serial character. Line widths are limited to sizes greater than one micrometer in most, but, importantly, not all cases. The quality of the patterned materials is less than desired in some cases. For example, if almost fully dense materials are needed, post processing is often required. This adds time to the overall production of a device or system, degrading the advantage gained by the absence of the mask design, production and use steps. In short, programmable processes for pattern and material transfer offer a set of advantages and disadvantages, as is the case with almost all technologies.

This paper provides a survey of some of the salient characteristics of direct-write processes for additive and subtractive production of micro- and nano-scale structures. A review by this author written about a year ago describes the techniques, but does not give a quantitative comparison [2]. Such comparisons for three classes of additive programmable methodologies are given after two introductory sections, one on the three factors involved in all these methods, and a second on characteristics for describing and comparing the technologies. Then, the subtractive techniques are compared. We are concerned both with technologies to make things

in place, which includes conventional approaches and the direct-write methods, and also with techniques in which parts are made separately and then moved into place. Hence, the plethora of assembly processes will be reviewed. The penultimate section deals with the many opportunities to make micro- and nano-structures that are enabled by the relentless development of new materials and new forms of old materials. The conclusion features the techniques that have the ability to produce structures on the nanometer scale. Techniques from each major class of tools (conventional lithography, direct-write and self- or directed-assembly) are likely to be used to make advanced components and systems for both research and commercial production.

BASIC ELEMENTS OF DIRECT-WRITE PROCESSES

There is a triad of requirements for all direct-write techniques. Information dictates the pattern in which the material is put onto the work piece, and energy is needed to effect the transfer of the material. Energy is further required for post processing steps that may possibly be needed. Any of these three factors can limit the rate at which a programmable technique produces the desired structures. The three requirements can be used in a wide variety of sequences, as illustrated in figure 3. It is possible that all three are brought together at once, with ink jetting being an example. Many of the direct-write techniques involve such simultaneous interactions. In laser sintering, a layer of material is put down first and then the pattern and energy are applied in the form of a moving laser beam. In xerography, the pattern is impressed on a drum with electrostatic energy, and then the material (toner) is applied. In self-assembly, the material contains the information for assembly, which is enabled by the application of thermal, vibratory or other forms of energy. Given the many combinations for information and material transfer, the several sources of energy and the wide variety of possible sequences, it is likely that new direct-write methods will be demonstrated in the future.

CHARACTERISTICS OF DIRECT-WRITE PROCESSES

Many characteristics are needed to describe any one direct-write technology, and to compare alternative techniques for a production of a desired device or system. For all methods, additive or subtractive, the source of the information and energy are key considerations. For additive techniques, the source of the material is also critical. For subtractive methods, the disposition of the removed material is sometimes a consideration.

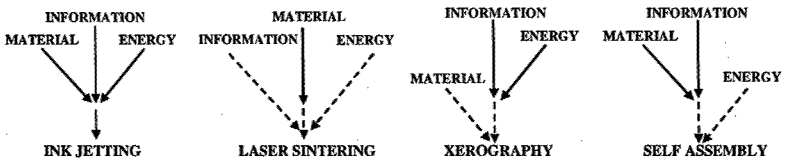

Figure 3. Examples of the ways in which information, material and energy can be transferred to a substrate by direct-write technologies. The solid lines indicate the initial steps and the dashed lines are for subsequent steps in the overall processes.

Several geometrical factors are important. They include the shape, size and orientation of the resolution element, or voxel, employed in a pulsed technique. The minimum and maximum

lateral resolution (line width), and the length and thickness or depth of the voxel are important. The rate of voxel transfer, along with their geometry, size and orientation, determines the linear writing rate for both additive and subtractive methods. The ability to deposit materials on top of each other in multiple passes obviously determines the attainable thickness of the final structure, just as multiple passes in an etching process will determine the depth of a written structure. The precision with which the voxels can be placed on the substrate, or on top of each other, are other significant geometrical (positional) considerations.

Material factors are also central to the description and comparison of additive technologies. Which materials can be transferred, and their state (properties) after transfer, are both critical. The compatibility of particular transferred materials with specific substrates, especially regarding adhesion, is also important for the applicability of a technique. The adhesion of the transferred material to itself can be a consideration. Volumetric rates for vapor deposition methods are critical, as is the range of materials that can be deposited from vapors. Such rates are also important for the many laser-driven methods in which the transferred material starts out in the liquid or solid phase. For writing and dispensing methods, the cross sectional geometries of the fluid stream, both as applied and after relaxation, are of interest. Linear and volumetric rates of writing and dispensing are certainly critical, as are shrinkage, cracking and delamination after deposition. Drop or stream formation, and coherence after impact with the work piece, are significant factors, as is the shape of the transferred material after its deposition. Materials factors are also germane to subtractive processes. For example, particular lasers will etch some materials much more efficiently and cleanly than others.

With so many characteristics of interest for a particular programmable technology, it is clear that a thorough comparison of techniques would be both complex and lengthy. Development and employment of "measures of goodness" or "figures of merit" for comparison of techniques would be challenging. Comparisons of the electrical, magnetic, optical, mechanical and other properties of structures made by the diverse data-driven methods are also complex. In this paper, we will focus on an intermediate level of detail. The source of material and energy will be used to organize the various additive direct-write technologies. This is done in figure 4 for techniques that are described in references [1] and [2]. Then, we will compare three classes of additive methods, outlined by the boxes in that figure, before making a similar comparison for subtractive technologies. We will limit the comparisons to the resolution, thickness or depth of the structures produced and the production rate. Some comments will be made on the variety of materials that can be handled by any class of techniques.

Figure 4 is an imperfect, but useful, way to group the additive technologies. Methods in which the transferred material starts in the vapor phase, and is made in place, have much in common with each other. They constitute a first group, and will be compared in the next section. Techniques in which focused laser beams influence materials that begin as liquids (including suspensions) or as solids (thin films or particles), and are then put in place, make up a second group, which is the subject of the following section. Then, methods in a third group, including various writing, dispensing, jetting and flow methods, are compared in yet another section. It is noted in passing that, for technologies involving focused beams, those beams can be employed for imaging and characterization, as well as the production of fine-scale structures.

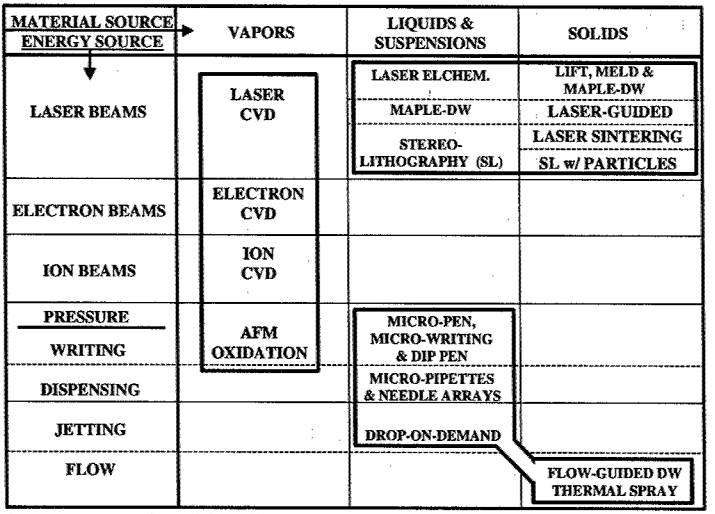

Figure 4. Arrangement of additive direct-write technologies according to the source of the material transferred to a substrate and the source of energy to effect the transfer.

CHEMICAL VAPOR DEPOSITION BY LASER, ELECTRON OR ION BEAMS

The direct writing of materials by the use of focused beams of photons, electrons or ions, or by employing proximal probes, to decompose vapor molecules has two major advantages. A wide variety of materials can be deposited by such means, and truly three-dimensional structures can be made using beams of quanta under computer control. Figure 5 summarizes the characteristics of these processes. It is seen that laser-induced chemical vapor deposition (CVD) offers the ability to make structures over one millimeter in size, but is limited in resolution to about one micrometer. 3D laser deposition from vapors has been demonstrated for refractory materials, such as metallic tungsten and alumina (sapphire). As shown in figure 5, nanometer-scale structures can be made by ion-induced CVD and by oxidation induced on the surface of a silicon wafer by passage of the probe in an Atomic Force Microscope (AFM). However, deposition rates are quite slow. Multiple beams and probes can speed CVD writing.

	RESOLUTION μm	HEIGHT μm	RATE mm/sec	MATERIALS
LASER CVD	~0.1-1	>1000	1	MANY
ELECTRON CVD	0.1	10		MANY
ION CVD	0.01	10	*	MANY
AFM OXIDATION	0.02	~0.001		SiO_2

* 2-30 ATOMS PER INCIDENT GALLIUM ATOM

Figure 5. Major characteristics of beam and proximal probe methods for direct-write CVD of structures. Ovals highlight the ability to produce nanometer-scale features.

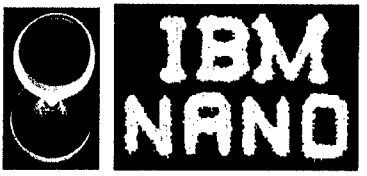

Figure 6. Micro-goblet 2.75 μm in diameter made by ion-induced CVD of carbon [3] and an AFM image of 20 nm wide lines formed by oxidation of Si using a biased AFM [4].

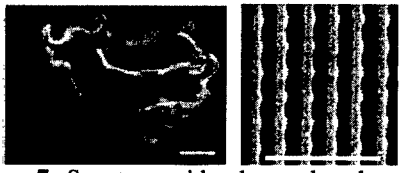

Figure 7. Structures with sub-wavelength features. Plastic bull about the size of a red blood cell formed by two-photon stereo-lithography [5]. Photonic crystal made by use of a femtosecond laser [6]. The bars are 2 μm.

LASER CONTROL OF LIQUIDS AND SOLIDS

Laser control of deposition from vapors was cited in the last section. Lasers are also used for direct writing of materials that begin in the liquid or solid phases, or as suspensions. In general, the several methods in this category are limited to micrometer resolution by diffraction. However, the use of two-photon or very intense femtosecond (fsec) pulses can produce sub-micrometer and sub-wavelength features, as shown in figure 7. Characteristics of laser-guided direct-write processes for materials that start as liquids or solids are given in figure 8.

	RESOLUTION μm	THICKNESS μm	RATE	MATERIALS
LASER TWO-PHOTON	0.12	Few	μm^3/min	POLYMERS
FSEC LASER	0.1	Few		POLYMERS
LASER RAPID PROTOTYPING	~1	~10 μm per layer	Few mm per hour	POLYMERS & OTHERS
LASER FORWARD TRANSFER	1-200	0.1-10	1 m/sec	MANY
LASER GUIDED DIRECT WRITE	2	~1	$10^{-4} mm^3$/sec	MANY
SELECTIVE LASER SINTERING	200	~125		POLYMERS & OTHERS
LASER PRINTING	10	~1	6 cm^2/sec	SEVERAL

Figure 8. Spatial and other characteristics of direct-write processes in which lasers control the deposition of materials from liquids, including suspensions, or from solids.

WRITING, DISPENSING, JETTING AND FLOW PROCESSES

A wide range of direct-write processes involves the mechanical or other transfer of materials onto a work piece in a pattern, often by using pressure or capillarity as the driving force. Their primary features are summarized in Figure 9. Of these, only the dip pen method offers nanometer-scale resolution in the produced patterns. It employs a proximal probe in an AFM to guide the placement of a liquid onto a surface. As is the case for other nanometer-capable methods, the dip pen writing rate is relatively slow.

	RESOLUTION μm	THICKNESS μm	RATE mm/sec	MATERIALS
MICRO-DISPENSING	1-300	< 1-100	>1000	MANY
MICRO-PEN™	50	250	750	MANY
MICRO-WRITING	10	0.005		LIQUIDS
DIP PEN	0.015	0.005	0.001	SEVERAL
NEEDLE ARRAYS	0.1-5 nL	~1	~100 Hz	LIQUIDS
JETTING	40-200	~100	500	MANY
ELECTROCAPILLARITY	Not Used Yet for Direct-Writing			CONDUCTING LIQUIDS
GAS DYNAMIC	1000	8000	5-50 cm/sec	MANY
FLOW-GUIDED	25	Few	0.25mm³/sec	MANY
THERMAL SPRAY	>500	~50	5-50 cm/sec	MANY
PLASMA SPRAY	>500	>5		MANY

Figure 9. Characteristics of processes for patterned writing, dispensing, jetting and flow transfer onto a work piece of materials from liquids, suspensions or other particles.

SUBTRACTIVE PROCESSES

The additive processes noted above are complimented by a collection of direct-write techniques that can etch material from a work piece, as summarized in Figure 10. It is possible that AFM guided etching will produce nanometer-scale lines, as do the ion beam processes.

		RESOLUTION μm	DEPTH μm	RATE	MATERIALS
LASER ABLATION	EXCIM. (248&193 nm)	~1	CAN BE > 1 mm	CAN BE > 100 mm per sec	MANY, ESP. POLYMERS
	Nd (1060 & 533nm)	~1			MANY, ESP. METALS
	CO_2 (10.6 μm)	FEW			MANY, ESP. CERAMICS
LASER PHOTO CHEMICAL ETCHING		FEW	>200	CAN BE >10μm/sec	MANY
ELECTRON BEAM CHEMICAL ETCHING		~1	~mm	10^5 μm³ per sec	SILICON & OTHERS
ION BEAM MILLING		0.05	>10	*	MANY
ION BEAM CHEMICAL ETCHING		0.05	>10	10 X	MANY
MICRO-ABRASION		10	CAN BE > 1 mm		MANY

* 1 μm³/sec/nA Ga BEAM

Figure 10. Characteristics of technologies for programmable removable of materials from substrates.

SELF AND DIRECTED PROGRAMMABLE ASSEMBLY PROCESSES

The hallmark of all functional engineering systems on any scale is their heterogeneity. Homogeneous materials do find many uses based on diverse properties, including electrical (conductors), magnetic (rotors in motors), optical (lenses) and mechanical (strength for structures). However, the devices and systems that characterize the modern world, ranging from integrated circuits to complex electro-mechanical systems, such as video recorders, to communications satellites, all get their abilities by dint of having many different components consisting of diverse materials that are made by numerous different processes.

The abilities to both make components and to assemble them characterized the industrial revolution of the 19th century. Assembly on fine scales, such as watch movements and surgical devices, was greatly advanced in the 20th century. Stepwise fabrication of many devices in parallel, notably for production of integrated circuits, was one of the new and characteristic technologies of the last century. It is widely predicted that self-assembly of nanometer-scale structures will be very important in making leading edge technologies in the 21st century. Such structures will still contain large numbers of atoms, which translates to long fabrication times for slow direct-write methods. Self-assembly may be fast enough to be practical for production of nanostructures in heterogeneous devices and systems, if it can be properly controlled. That is, a combination of self-assembly and direct writing may be commercially viable.

The need for heterogeneity in functional devices and systems seems to clash with the fundamental character of self-assembly, namely its operation independent of external inputs. However, there are three ways in which self-assembly can be controlled. First, if the elements that are assembling are made appropriately, then they will assemble in the desired fashion. Second, the operation of self-assembly requires not only the proper materials, but also the appropriate media and conditions. Finally, limiting the number of elements that can assemble serves to control the size of the resulting structure. Each of these approaches has some advantageous features and some limitations.

Current abilities to produce complex molecules with desired shapes and surface energies enable control of the sub-micrometer and larger structures into which they will self assemble. Whitesides and his colleagues have made geometrical units, with sizes as large as millimeters, which have functionalized surfaces [7]. When put in liquid media and agitated, the units will assemble according to the dictates of the designed surface energies. They term this strategy "programmable" self-assembly, because they control the geometry and surface characteristics in ways that will result in desired structures.

The fact that self-assembly requires the proper conditions, as well as the right material units, can also be used for its control. Here, direct-write technologies might play an important role in controlling what happens on the nanometer-scale. If the pH of the aqueous medium in which self-assembly is occurring is critical to its operation, then jetting or other direct means of delivering acidic or basic solutions could start, speed, slow or stop self-assembly. If the self-assembly process is light sensitive, then the programmable employment of focused laser beams could provide control. In a similar fashion, beams of light could be used to increase the temperature of the medium and hence the rates of self-assembly.

Finally, limiting the number of units available for self-assembly is another means for control of what results. Putting picoliter droplets of dilute suspensions of the units of interest in the correct position at the right time during the production of a device or system might be

possible using jetting technologies. Laser "tweezers" might also be used to control what is put in which location prior to a self-assembly event.

In short, self-assembly must be directed, modulated or other wise controlled to achieve functional components and systems, which are always inhomogeneous. The required control can be exerted in three possible ways: (a) at the unit level by proper design, (b) by control of conditions or (c) by limiting the number of units that can assemble. It can be asserted that all three of these means of controlling self-assembly are "programmable" because each of them can be flexibly sequenced to produce the structure of interest. Which means of control will prove to be useful and robust for specific units and particular target structures remains to be determined from future experiments and simulations.

The inevitable feature of any method involving self-assembly is that the size of the structures within the units will determine the finest achievable structures. Millimeter-sized units with micrometer-scale features will result in assembled components having features only as fine as micrometers. However, there is an aspect of this approach that might lead to finer features. Employment of very thin patterned surface films, which would have both the appropriate overall energies for the self-assembly operation and also in-plane functionality, could yield structures on the nanometer-scale in at least one dimension.

Hopes for production of three-dimensional nano-structures follow from the fact that natural proteins and other complex organic molecules, which have nanometer-scale structures, both self assemble into their characteristic shapes (by complex folding) and then assemble with each other (by aggregation or crystallization). Hence, designer proteins, possibly made by living organisms on the basis of man-made DNA instructions, offer the possibility of making heterogeneous structures on the nanometer scale. DNA has been used to direct the assembly of nanoparticles [8]. Living cells are already being co-opted for the production of drugs and even inorganic materials [9] It seems likely that biological production of designer proteins and other molecular units will be common place in the coming years.

It must be noted that *directed-assembly* of structures into more complex devices and systems, as has been done for most systems over history, is being extended to ever smaller scales. The company Zyvex is developing small-scale versions of pick-and-place machines to make structures of parts with micrometer-scale dimensions, with many assemblers working in parallel [10]. Molecular pick and place devices have been envisioned by Drexler [11]. Proximal probes have been used to move atoms and molecules on surfaces and to cut long organic molecules. Another start-up company, Alien Technologies, is using a fluidic self-assembly approach for putting active electro-optical components into surfaces [12]. Micro-fluidic means of controllably delivering units to a work piece are being developed [13]. They can employ laminar flow to precisely control both the locations on a "growing" assembly at which the new units arrive and their dwell times. Figure 11 is a sketch of a micro-fluidic system for controllable mixing and jetting of nano-particles and -structures from reservoirs onto a work piece. Such a system could also be used for programmed delivery of fluids without suspended particles or parts. Which of these extensions of classic assembly will prove to be commercially viable remains to be determined. It is probably necessary to find some niche uses for each approach in order to sustain the companies developing them while the range of applications for a particular approach is broadened.

The alternative to putting pre-existing parts in place by any means is to grow them in place. Carbon nanotubes were initially made separately, and have been maneuvered into position to form transistors and other devices. Later, it was learned that they could be grown in

specified positions. Growth in place can be viewed as a form of directed-assembly. It is expected that the two approaches to the positioning of nanometer-scale structures will each find wide application.

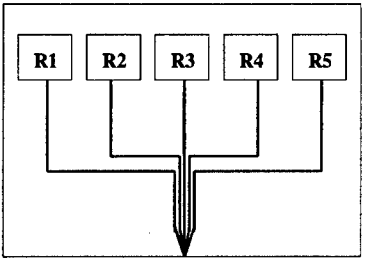

Figure 11. Layout of a micro-fluidic chip for programmable mixing and jetting of fluids from the reservoirs labeled R 1-5. The fluids might be neat or else contain suspended particles or parts for subsequent self-assembly on the surface of a work piece.

Sequential or hierarchical self- and directed- assembly, in combination with lithographically-directed (templated) processes, are likely to be important for the production of complex nano-devices and -systems. It is possible that the major challenge of connecting the micrometer-scale world to nanometer-scale devices will be overcome by using combinations of these many tools.

NEW MATERIALS

The availability of new materials, and new forms of old materials, will have a great impact on the employment of direct-write technologies. This has already been demonstrated by the recent availability of micrometer and nanometer scale particles of materials that can be put onto work pieces in suspensions or by flow methods. Suspensions of quantum dots with remarkable optical properties are now commercially available for use in direct-write processes.

New materials and units will influence assembly processes, as well as processes that do not involve inter-particle forces and self-assembly. Many examples of the production of units could be given. One of them from a recent paper is in figure 12 [14]. It shows particles of silver with regular geometric shapes and closely similar sizes. These were grown by a chemical process, which occurred in the presence of a polymer. Possibly, their surfaces can be functionalized, just as has been done for quantum dots (to avoid agglomeration) and for millimeter-sized units (for self-assembly).

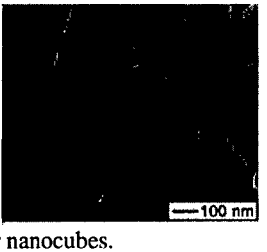

Figure 12. SEM images of silver nanocubes.

It is not clear now whether the capabilities of programmable technologies for making structures will advance more by the development of new processes, by the refinement of existing processes, or by the availability of new or modified materials for use in any of the processes. Probably, important advances will be made in each of these arenas.

CONCLUSION

The collection of programmable, direct-write technologies for production of fine-scale structures is relatively new. However, the methods already show significant practical promise. More important, there are several clear avenues open for their growth in capabilities and applications. Some of them could involve new ways to bring together the information, material and energy that are inevitably required for direct writing of patterns and structures. The employment of new materials and units was just noted. That alone is very significant. So also is the fact that many of the direct-write methods involve only relatively low processing temperatures. This enables structures to be made of organic materials, bio-materials and living cells. It is expected that the production of devices made of organic electronic materials by a combination of direct-write and printing technologies will be significant commercially.

In reviewing the capabilities of the various additive and subtractive direct-write processes, it is seen that only a few operate directly on the nanometer scale in two or more dimensions. Most of the direct-write methods, especially the flow technologies, are not extensible to the nanometer range. It is not surprising that only those beam methods in which the beam can be focused to spots well under a micrometer in diameter qualify for making nano-structures. This generally excludes lasers because of the diffraction limit of light, despite their convenience of operating in air, except for some two-photon and high intensity operations. Electron and ion beams do produce nanometer-scale lines and structures at the expense of working in a vacuum. In general, the technologies that can produce nanometer-scale lines are slow, that is, their linear speeds are low. It is possible to use micro-machining technologies to make systems that have many parallel beams of electrons or ions, so that multiple patterns can be written, or multiple structures produced in parallel.

Proximal probes, especially atomic force microscopes, which intrinsically function on the nanometer scale, are also among the tools for programmable writing with dimensions well under one micrometer. The emergence of devices having many such probes, so that numerous lines can be written in parallel, is an important current development. This will ameliorate the intrinsically slow character of direct-write methods using proximal probes. Examples are given in figure 13 for lithography, dip pen nano writing and data storage.

There is great interest in assembly of units with dimensions on or smaller than the micrometer scale. This is basically due to the requirement that devices and systems have the right materials in the right places to achieve the desired performance. Self-assembly is expected to permit the proper location of large numbers of moieties, with sizes ranging from atoms to millimeter-scale parts. However, it is fundamentally necessary to control self-assembly, if designed and functional structures are to be realized. Happily, there are three basic and broad approaches to the control of self-assembly. Direct-write technologies might be useful for two of the classes of control mechanisms, namely the determination of assembly conditions or the dispensing of limited numbers of units for self-assembly. Meanwhile, new means of classic

"directed" assembly are being developed for fine-scale parts. Hierarchical self- and directed-assembly offer a diverse set of tools for the production of micro- and nano-scale structures.

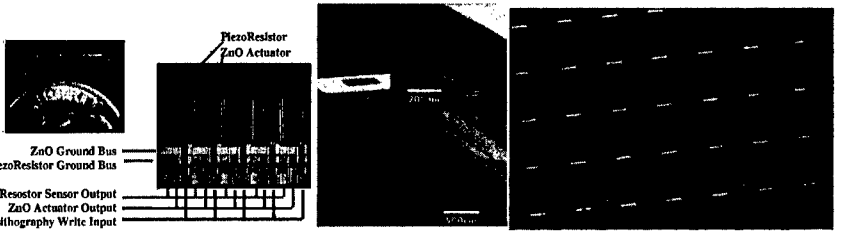

Figure 13. Left: Photograph of 50 piezoelectrically-actuated and piezoresistivally-sensed proximal probes for lithography, and an enlargement of five of them [15]. Center: A 32 probe array (top) and an eight probe array for dip pen lithography [16]. Right: Optical micrograph of some of the 1024 proximal probes in the "Millipede" data storage technology being developed by IBM [17]. An array of 10,000 independently-controlled proximal probe tips was reported recently [18].

In the larger view, there are four classes of methods for producing structures on the micro-and nano-meter scales. They are (a) conventional lithography, with its associated deposition and etching processes, (b) some programmable direct-write techniques, (c) self-assembly methodologies, in which the material units contain instructions for their arrangement, if conditions are proper, and (d) directed or programmed assembly. It seems certain that tools from each of these sets will be used as needed to make increasingly complex and capable devices on the micro- and nano-scales for both research and for commercial purposes.

ACKNOWLEDGMENT

Alberto Pique suggested this paper. His gracious impetus was welcome and is appreciated.

REFERENCES

1. "Direct-Write Technologies for Rapid Prototyping Applications", ed. A. Pique and D. B. Chrisey (Academic Press, 2002)
2. D. J. Nagel, "Technologies for Micrometer and Nanometer Pattern and Material Transfer" in Reference 1, pp. 577-701
3. "Ion Beam Forms Nanoscale Objects", Laser Focus World, March 2001, pp56-59
4. P. Avouris et al, Applied Physics A, **66** S659 (1998)
5. S. Kawata et al, Nature, **412**, 697 - 698, (2001) and http://optics.org/article/news/7/8/15
6. "Femtosecond Pulses Generate Microstructures", http://optics.org/articles/ole/7/12/3/1
7. G. M. Whitesides et al., J. Am. Chem. Soc., **120**, 8267-8268 (1998)
8. C. A. Mirkin et al, Nature, **382**, 607-609 (1996)
9. D. E. Morse, http://www.lifesci.ucsb.edu/mcdb/faculty/morse/research/research.html
10. http://www.zyvex.com/
11. E. Drexler, "Engines of Creation", (Anchor, 1987)
12. http://www.alientechnology.com/technology/overview.html

13. R. T. Howe, unpublished, http://www-bsac.eecs.berkeley.edu/~howe/
14. Y. Sun and Y. Xia, Science, **298**, 2176-9 (2002)
15. C. F. Quate, http://www.stanford.edu/group/quate_group/Home/HomePages/Presentations/
16. M. Zhang et al, Nanotechnology **13** 212-217 (2002)
17. P. Vettiger et al, http://domino.research.ibm.com/Comm/bios.nsf/pages/millipede.html/$FILE/pv7201-preprint.pdf
18. C. A. Mirkin, Materials Research Society Fall Conference, Boston MA, December 2002

Mat. Res. Soc. Symp. Proc. Vol. 758 © 2003 Materials Research Society LL4.2

Development of Parallel Dip Pen Nanolithography Probe Arrays for High Throughput Nanolithography

David A. Bullen[1], Xuefeng Wang[1], Jun Zou[1], Sung-Wook Chung[2], Chang Liu[1], and Chad A. Mirkin[2]
[1]Micro and Nanotechnology Laboratory, University of Illinois at Urbana-Champaign, Urbana, IL, 61801
[2]Department of Chemistry, Northwestern University, Chicago, IL

ABSTRACT

Dip Pen Nanolithography (DPN) is a lithographic technique that allows direct deposition of chemicals, metals, biological macromolecules, and other molecular "inks" with nanometer dimensions and precision. This paper addresses recent developments in the design and demonstration of high-density multiprobe DPN arrays. High-density arrays increase the process throughput over individual atomic force microscope (AFM) probes and are easier to use than arrays of undiced commercial probes. We have demonstrated passive arrays made of silicon (8 probes, 310 μm tip-to-tip spacing) and silicon nitride (32 probes, 100 μm tip-to-tip spacing). We have also demonstrated silicon nitride "active" arrays (10 probes, 100 μm tip-to-tip spacing) that have embedded thermal actuators for individual probe control. An optimization model for these devices, based on a generalized multilayer thermal actuator, is also described.

INTRODUCTION

Dip Pen Nanolithography (DPN) is a recently introduced [1] method of scanning probe lithography that offers significant advantages over other lithographic processes. In this method, chemicals are adsorbed onto an AFM probe then deposited on a surface by diffusion from the tip while scanning in contact mode. The most common probe is a silicon nitride AFM tip that has been coated by dipping it in a chemical solution or by evaporation from a heated source.

DPN has been successfully applied to a wide variety of patterning tasks. It has been used to pattern biological macromolecules such as thiol-modified ssDNA [2], collagen (via direct patterning) [3], and rabbit immunoglobulin G (via selective adsorption onto 16-mercaptohexadecanoic acid patterns) [4]. The meniscus that forms between the probe tip and substrate in air has been used as a nanoscale chemical reactor to pattern sol-gel precursors [5], a variety of metals [6,7], and conducting polymers [8]. Surface binding in the these demonstrations ranges from strong covalent bonds, as in the thiol-gold [1] and silane-oxide [9] systems, to weaker electrostatic, van der Waals, hydrophobic, and hydrogen bonds [10]. In some cases, the covalent chemistries have been shown strong enough to act as masks in various substrate etching applications [11,14].

The wide variety of tasks for which DPN has been used is an indicator of its potential for commercialization, but success will require more than just robust chemistry systems. The real power of DPN can only be unlocked with pattern generation capabilities that far exceed those of single probe systems. The first attempt at multiprobe patterning [12] used a 1-D array of undiced commercial probes. Although this method works, the arrays are so wide (~1.5mm per probe) that array-to-surface misalignment limits the array size with little gain in pattern density. We have

developed a variety of high-density, one-dimensional, passive and active probe arrays that satisfy the need for true high-density pattern generation.

PASSIVE PROBE ARRAYS

We have demonstrated passive high-density probe arrays [13] with tip-to-tip spacing that is more than an order of magnitude better than what is achievable using commercial probes. The arrays are easier to align with the substrate and function in a wide variety of AFMs. SEM micrographs of the devices are shown in Figure 1. One design consists of silicon nitride probes that are 375 μm long (base to probe tip), 50 μm wide, 600nm thick, and have a tip-to-tip spacing of 100 μm. The probes have an analytically estimated spring constant of 0.018 N/m and have been used for lithography and topographic imaging [13]. Another design uses silicon probes with beams that are 15 μm wide and 5 μm thick. The tip-to-tip spacing is 310μm. The suspension is folded to increase the beam's effective length and lower its spring constant to an FEA estimated value of 0.315 N/m. They have been used in lithography and tapping mode imaging applications [13]. Figure 2 shows examples of imaging and lithographic results from both designs. All lithography was performed using 1-octadecanethiol (ODT) on a gold substrate.

The fabrication of these devices has been previously described [14] and is summarized here. The probe tips are first formed by anisotropicly etching the surface of a <100> silicon wafer, followed by oxidation sharpening [15]. For silicon nitride probes, the wafer is coated with low

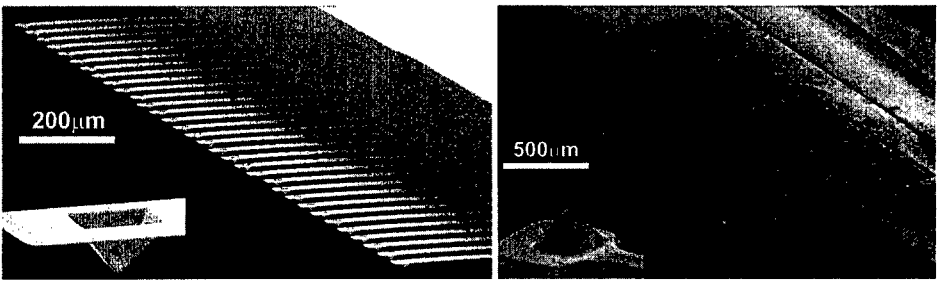

Figure 1. (Left) A passive array of 32 rectangular silicon nitride DPN probes. **(Right)** A passive array of eight folded-beam silicon DPN probes.

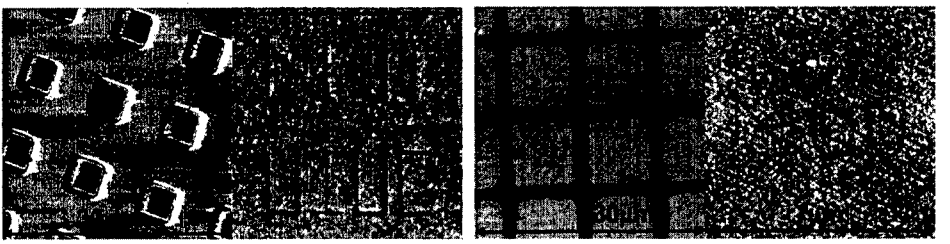

Figure 2. (Left two images) A contact mode calibration grating image and ODT pattern from a passive silicon nitride DPN probe. The ODT characters are 5 μm tall and the line width is 260nm **(Right two images)** A tapping mode calibration grating image and ODT pattern from a passive silicon DPN probe. The ODT characters are 1.5 μm tall and the line width is 60 nm.

pressure chemical vapor deposited (LPCVD) silicon nitride and the beams are etched out using reactive ion etching. The beams are then released by anisotropic wet etching from the front side of the wafer. For silicon devices, the beams are etched out of an implanted boron etch stop layer and the remaining silicon is removed by anisotropic wet etching.

ACTIVE PROBE ARRAYS

Active probe arrays contain actuators within each probe to lift individual tips off the surface. This allows different patterns to be written by different probes when all probes travel the same path. For our case, thermal actuation was chosen for its large deflection, fabrication simplicity, and robust operation. The active probe arrays consist of a linear array of cantilever beams, each having its own joule heater, silicon nitride/gold bimetallic thermal actuator, and tip. An SEM micrograph of an array is shown in Figure 3 along with an illustration of its operating principle. When the heater is energized, the probes are hot and the tips are lifted from the surface to suspend lithography. When the heater is de-energized, the probe is cool, the tips are pressed against the surface, and lithography is performed in contact mode. The fabrication process for these devices is an extension of the process used to make the devices in Figure 1. The only difference is the addition of steps to evaporate and pattern a chrome/gold layer before the final release etch. This layer forms the heater, power leads, and actuator.

N-layer thermal actuator modeling

Although these devices are referred to as bimetallic thermal actuators, they are actually three layer devices due to the need for an adhesion layer. Many deflection models have been published on the bimetallic case [16-22] but we have found that approximating multilayer (>2 layers) devices as bilayer devices can lead to significant error when estimating tip deflection. Most practical devices need additional layers for promoting adhesion or electrical isolation. As a result of this deficiency, we have created a more general model that characterizes cantilevers with an arbitrary number of layers, each having its own width, thickness, modulus of elasticity, thermal expansion coefficient, and intrinsic stress state. The beam radius of curvature is calculated by summation across some or all of the layers of the structure and may be applied to uses beyond

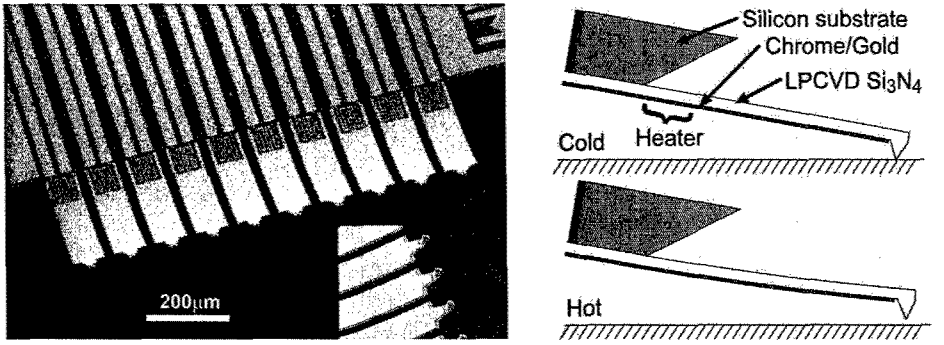

Figure 3. (Left) An array of ten 295 μm long, thermally actuated DPN probes.**(Right)** Thermally actuated DPN probe operation. Heated probes deflect away from the surface.

this particular situation. An abbreviated derivation follows.

Given a beam with n material layers, numbered i=1 to n, the first task is to find the location of the neutral axis using the effective width technique [23]. After canceling the elastic modulus of the reference material, the distance between the neutral axis and the bottom of the beam is given by

$$\bar{y} = \frac{\sum_{i=1}^{n} E_i w_i t_i \left(\frac{t_i}{2} + \sum_{j=1}^{i-1} t_j \right)}{\sum_{i=1}^{n} E_i w_i t_i}, \tag{1}$$

where E is the modulus of elasticity, w is the width, and t is the thickness of the ith layer. The outer summation (i) is applied over all layers while the inner summation (j) is over the layers below layer i. The term in parenthesis is the distance from the bottom of the beam to the middle of the ith layer. The flexural stiffness of the beam is found using the effective width technique and the parallel axis theorem and is given by

$$I_{eff} E_o = \sum_{i=1}^{n} \left[\frac{E_i w_i t_i^3}{12} + E_i w_i t_i \left(\left(\frac{t_i}{2} + \sum_{j=1}^{i-1} t_j \right) - \bar{y} \right)^2 \right], \tag{2}$$

where E_o is an arbitrary reference modulus.

The radius of curvature of the operating actuator results from four sequential processes: (1) layer deposition with a preexisting stress, (2) patterning of all layers to a uniform length, (3) relaxation following release from the substrate, and (4) heating or cooling to the operating temperature. The stress state in each layer is the sum of a uniform component and an assumed linear gradient and is, in general, unrelated to the stress in the other layers. The total strain in a given layer i can be found by superimposing the strain due to uniform intrinsic stress, thermal expansion, and the change in beam length

$$\varepsilon_i = \frac{\sigma_{i,unif} (1 - \nu_i)}{E_i} - \alpha_i \Delta T + \ln \left(\frac{L_{beam}}{L_{patterned}} \right), \tag{3}$$

where ν is the poisson's ratio, $\sigma_{i,unif}$ is the biaxial hydrostatic stress, α is the thermal expansion coefficient, ΔT is the change in temperature of the entire beam, $L_{patterned}$ is the patterned length of the beam before release from the substrate, and L_{beam} is the final length of the beam after release and heating. Since the cantilever beam carries no axial load, the force exerted by each layer due to internal stresses is given by P=$Ewt\varepsilon$ and must sum to zero giving

$$\sum_{i=1}^{n} P_i = \ln \left(\frac{L_{beam}}{L_{patterned}} \right) \sum_{i=1}^{n} E_i w_i t_i + \sum_{i=1}^{n} \left(w_i t_i \sigma_{i,unif} (1 - \nu_i) - E_i w_i t_i \alpha_i \Delta T \right) = 0. \tag{4}$$

Equation (4) can be solved for the strain due to the change in beam length, given by $ln(L_{beam}/L_{patterned})$. Substituting this result into (3) yields the total strain in layer *i*. The total strain is then used to find the force and moment exerted by each layer on the beam. Summing these moments gives the total moment within the beam due to thermal stress and uniform intrinsic stresses,

$$M_{uni} = \sum_{i=1}^{n}\left[E_i w_i t_i\left(\frac{\sigma_{i,unif}(1-\nu_i)}{E_i} - \alpha_i \Delta T - \frac{\sum_{i=1}^{n} w_i t_i\left(\sigma_{i,unif}(1-\nu_i) - E_i \alpha_i \Delta T\right)}{\sum_{i=1}^{n} E_i w_i t_i}\right)\left(\frac{t_i}{2} + \sum_{j=1}^{i-1} t_j\right)\right]. \quad (5)$$

A stress gradient may also be present in each layer resulting from changes in the film growth conditions during deposition. Assuming that this stress gradient is linear and uniform in the plane of the film, the total moment exerted on the beam by layer stress gradients is given by summing the individual moments exerted by each gradient

$$M_{grad} = \frac{1}{6}\sum_{i=1}^{n} w_i t_i^2 \sigma_{i,grad}(1-\nu_i), \quad (6)$$

where $\sigma_{i,grad}$ is the maximum value of the gradient stress. Thus, the radius of curvature, from which the deflection can be calculated, is found from

$$R = \frac{I_{eff} E_o}{M_{unif} + M_{grad}}. \quad (7)$$

Equations (1,2,5,6, and 7) constitute a system that allows for the calculation of the radius of curvature of a heated composite beam consisting of any number of layers, each with its own material properties, geometry, and intrinsic stress.

This n-layer model has been compared with FEA simulations of uniformly heated cantilevers having up to seven layers. The parameters used in the simulations are listed in Table I and the results have been plotted in Figure 4. Case 1 and 2 represent a simple thermal actuator layout and only differ by the addition of a 150Å chromium adhesion layer. The effect of this addition is to increase the tip deflection by 12%. This illustrates how significant errors can result from the bimetallic approximation. Case 3 is an arbitrary 5-layer design that the n-layer model estimates with less than 4.5% error from the FEA solution. Case 4 and 5 represent a 7-layer design that clearly cannot be approximated as a bimetallic actuator. The two cases only differ in that the first assumes no intrinsic stresses while second includes the stresses. The intrinsic stresses result in a negative tip deflection at ΔT=0. The analytical solution is within 4% of the FEA solution in both cases.

Array feasibility modeling

The task of modeling thermally actuated DPN probes does not end with the estimation of tip deflection. In real applications, several additional issues must be accommodated to produce

Table I. Geometry and properties of five test beams used in FEA simulations.

Layer	t (Å)	w (μm)	Material	E (GPa)	α (*10^{-6}/°C)	$\sigma_{i,unif}$ (MPa)
Case 1: 400μm long, ν = .3						
1	3000	50	Si_3N_4	200	2.8	0
2	300	50	Au	80	14.3	0
Case 2: 400μm long, ν = .3						
1	3000	50	Si_3N_4	200	2.8	0
2	150	50	Cr	90	6.0	0
3	300	50	Au	80	14.3	0
Case 3: 1000μm long, ν = .33						
1	5200	100	Si	190	2.6	0
2	2300	90	Au	80	14.3	0
3	6100	130	SiO_2	67	.35	0
4	4800	120	Ti	110	8.6	.0
5	8900	110	SiO_2	67	.35	0
Case 4(without stress) and 5(with stress): 1000μm long, ν = .3						
1	6500	45	Au	80	14.3	40
2	500	45	Ti	110	8.6	0
3	5000	50	SiO_2	67	.35	-20
4	30000	50	Si	190	2.6	0
5	2000	40	SiO_2	67	.35	-52
6	500	25	Cr	90	6.0	0
7	5000	25	W	344	4.5	-30

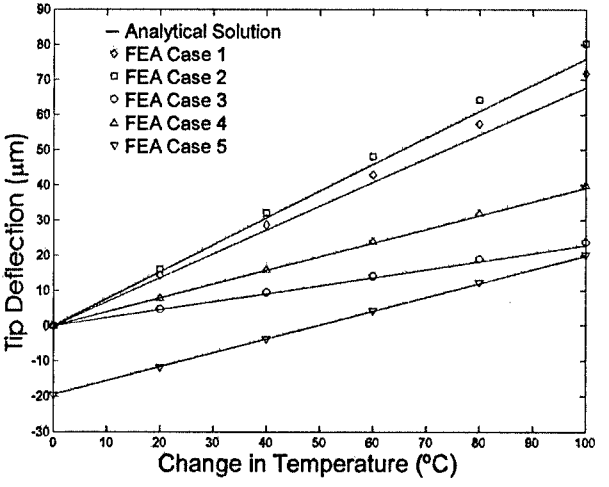

Figure 4. Comparison of probe deflections found using the analytical model, equations (1,2,5,6, and 7), and FEA deflection results. Each case represents a layout as defined in Table I. In all cases, the analytical result differed from the FEA result by less than 6%.

functional devices that will not damage the substrate surface. In most DPN applications, there are at least four ways an array may fail to produce the desired result. The probe may be stiff enough, or the tip sharp enough, to scratch the surface. The intrinsic stresses may be large enough to excessively curl the beam after release. The actuator may not generate enough force to overcome tip-to-surface adhesion. Or finally, the actuator may not generate enough deflection to overcome the array overdrive. Overdrive is defined as the additional distance downward, beyond the point of first contact with the substrate, that the array must be pressed to overcome array-to-surface misalignment and irregularities in the tip-to-tip height.

To prevent these failures, the probe geometry and operating parameters can be changed. Unfortunately, many changes will have an opposite impact on the various constraints. For example, increasing the probe stiffness will increase the force it can generate but will also increase the risk of scratching the substrate. The simplicity gained by eliminating the need for individual probe feedback control is offset by the need to carefully evaluate designs before fabrication.

To resolve these conflicting design issues, the n-layer beam model was combined with simple relationships that describe Hertz contact mechanics and capillary adhesion [24] to create an array design simulator [25]. The simulation iterates through a predetermined set of geometries and calculates the probe shape, spring constant, actuator deflection, actuator force, tip adhesion force, and maximum allowable tip down force. This information is used to estimate whether the probe will fail any of above criteria. Designs that pass are plotted against their geometrical parameters to graphically show the relationships between successful layouts.

The results of an example simulation are plotted in Figure 5. The box represents the range of examined actuator designs (approximately 61,000 geometries that differ by length and actuator layer thickness). Designs that pass all the selection criteria (in this case 3,549 or 5.8%) are considered successful and plotted. Failing layouts can also be plotted to show their interrelationships. The plots give a clear visual description of the performance of every design in the design space and allow for a rapid visual evaluation of several optimization schemes.

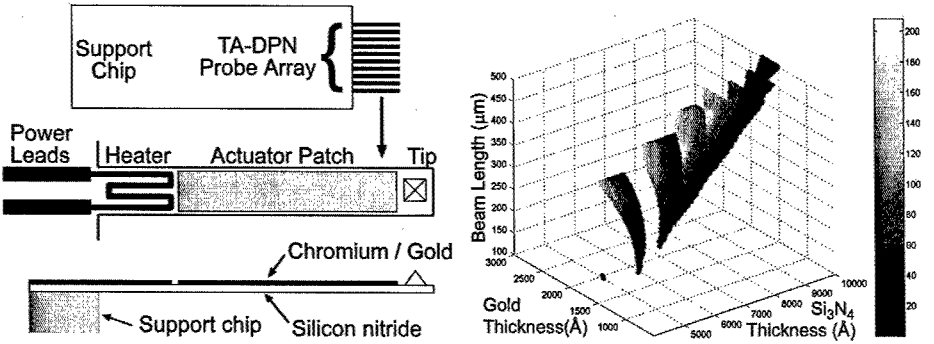

Figure 5. (Left) The simplified layout used in the example feasibility simulation. **(Right)** A 3-D plot of the successful designs based on the probe layout. Every geometry in the box was simulated and the successful designs were indicated with a shaded dot. The shading indicates the actuator force in percent excess of the minimum necessary to overcome tip-to-surface adhesion. The plot clearly shows the relationship between successful designs and the probe geometry.

Devices

The devices in Figure 3 represent a design that has been optimized across several criteria. The maximum length was fixed at 300 μm to prevent wet release stiction problems. The maximum allowable temperature was limited to 60°C to prevent oxidation of the ODT "ink". Probe stiffness was limited to prevent scratching a gold substrate with a maximum allowable tip-to-substrate angular misalignment of 1 degree. The final design parameters were adjusted to give the greatest chance of a successful design despite minor process variations. To meet these criteria, the devices in Figure 3 have a silicon nitride thickness of 9300 Å and gold thickness of 3650 Å. The probes are 80 μm wide, 295 μm long, and have a tip-to-tip spacing of 100 μm. The analytically estimated spring constant is 0.154 N/m. The heater films have the same thickness as the actuator films.

The thermal performance of the thermally actuated DPN probe is plotted in Figure 6. The typical operating power is approximately 2.5 mW, corresponding to a tip deflection of 10 μm during operation. Analytical modeling indicates that, at this power, the probes reach an average temperature of ~28°C above ambient, which is supported by uniform temperature testing. For chemical inks that are sensitive to heat, the environment can be cooled to allow thermal actuation without excessive temperatures. In our experiments, the binding and friction characteristics of ODT were unaffected by these temperature regimes.

A demonstration of the use of an active probe is shown in Figure 7. In this figure, an active DPN probe was passed through an identical figure-8 pattern several times. The actuator was used to lift the probe from the surface, thus altering the resulting pattern during each run.

A final note concerns tip sharpness. In most AFM applications, tip sharpness is an important issue. During fabrication of our devices, silicon "forms" are coated with silicon nitride to form the tips, thus the tip radius is approximately equal to the nitride film thickness. This can affect the minimum line width and would appear to be a major disadvantage, but we have found that there are several benefits to consider. The overcoat method makes possible a simple and robust fabrication procedure that does not require wafer bonding. The large tip radius also increases the availability of ink near the contact point and greatly reduces the risk of scratching the substrate.

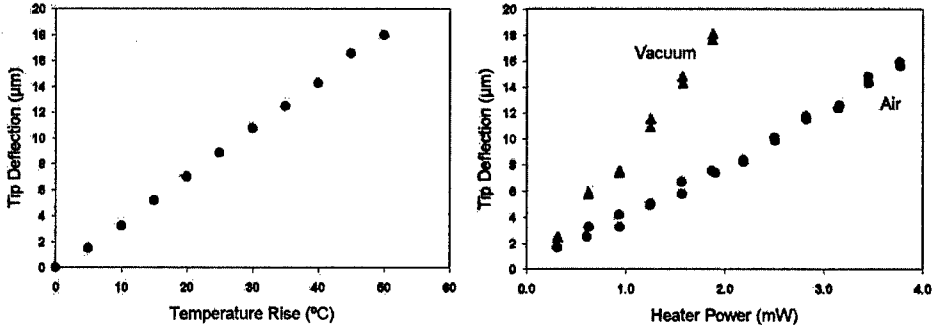

Figure 6. Tip deflection vs. uniform temperature rise and heater power for the devices in Figure 3. Results from two probes are shown in the deflection vs. power plot. The large difference between the vacuum deflection (<300mTorr) and deflection in air illustrates the impact of convection heat transfer on probe performance.

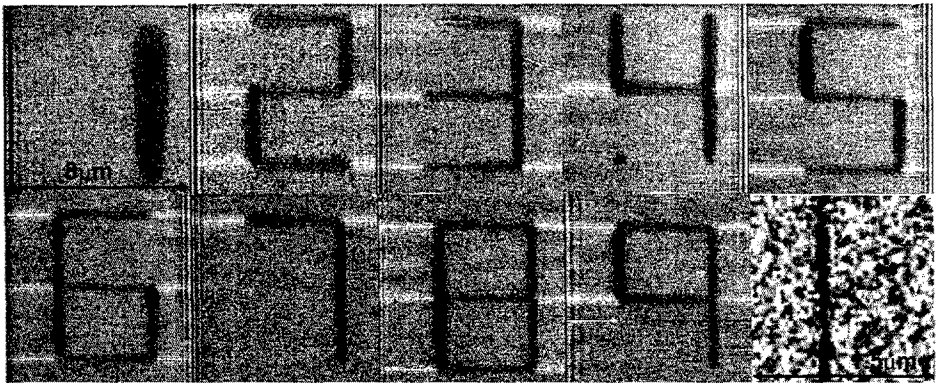

Figure 7. (1-9) 6 μm x 4 μm patterns generated by a single thermally actuated DPN probe. Each number was generated by passing the probe through the same figure-8 path and using the thermal actuator to lift the tip as necessary to create the desired pattern. The ODT patterns are written on gold at .3 μm/sec and imaged using lateral force microscopy with a commercial probe. **(Lower right)** An LFM image of an 80 nm wide ODT line drawn on a gold substrate by an active probe design at 20 μm/sec.

This, in turn, allows the system to tolerate greater tip-to-substrate misalignment. The line width issue can be partially remedied by increasing the write speed. In our early testing, as shown in Figure 7, we have achieved a minimum line width of 80 nm at a write speed of 20 μm/sec. New designs that combine these advantages with sharper tips are under development.

CONCLUSIONS

We have developed high-density passive and active probe arrays for performing dip pen nanolithography. The probes are produced using a simple and robust fabrication processes, and are capable of producing patters with sub-100 nm dimensions. The active probes operate by lifting the probe tip off the surface when their thermal actuators are heated. A performance simulator was created, based on a new n-layer thermal actuator model, to optimize probe designs for the lithography conditions. The resulting designs operate with a power of 2.5 mW per probe, leading to an average temperature rise of approximately 28°C and a tip deflection of 10 μm. A demonstration of pattern variation using a thermally actuated probe was also given.

ACKNOWLEDGEMENTS

This work was performed under the Advanced Lithography Program of the Defense Advanced Research Projects Agency (DARPA) (grant DAAD19-00-1-0414). The authors also wish to acknowledge financial support from the Air Force Office of Scientific Research and the Nanoscale Science and Engineering Initiative of the National Science Foundation under NSF Award Number EEC-0118025.

REFERENCES

1. R. Piner, J. Zhu, F. Xu, S. Hong, and C. Mirkin, *Science*, **283**, 661, (1999)
2. L. Demers, D. Ginger, S. Park, Z. Li, S. Chung, C. Mirkin, *Science*, **296**, 1836, (2002)
3. D. Wilson, R. Martin, S. Hong, M. Cronin-Golomb, C. Mirkin, and D. Kaplan, *Proc. Nat. Acad. Sci.*, **98**(24), 13660, (2001).
4. K. Lee, S. Park, C. Mirkin, J. Smith, M. Mrksich, *Science*, **295**, 1702, (2002)
5. M. Su, X. Liu, S. Li, V. P. Dravid, and C. Mirkin, *J. Am. Chem. Soc.*, **124**(8), 1560, (2002).
6. B. Maynor, Y. Li, and J. Liu, *Langmuir*, **17**, 2575, (2001)
7. Y. Li, B. Maynor, and J. Liu, *J. Am. Chem. Soc.*, **123**, 2105, (2001)
8. B. Maynor, S. Filocamo, M. Grinstaff, and J. Liu, *J. Am. Chem. Soc.*, **124**(4), 522, (2002).
9. Ivanisevic and C. Mirkin, *J. Am. Chem. Soc.*, 123, 7887, (2001)
10. M. Su and V. Dravid, *Appl. Phys. Lett.*, **80**(23), 4434, (2002)
11. D. Weinberger, S. Hong, C. Mirkin, B. Wessels, and T. Higgins, *Adv. Mater.*, **12**(21), 1600, (2000)
12. Hong and C. Mirkin, *Science*, **288**, 1808, (2000)
13. M. Zhang, D. Bullen, and C. Liu, *Proc. of the 2001 1st IEEE Conf. on Nanotechnology*, 27, (2001)
14. M. Zhang, D. Bullen, S. Chung, S. Hong, K. Ryu, Z. Fan, C. Mirkin and C. Liu, *Nanotechnology*, **13**, 212, (2002)
15. C. Liu, R. Gamble, *Sensors Actuators A*, **71**, 233, (1998).
16. S.P. Timoshenko, *J. Opt. Soc. Am.*, **11**, 233, (1925)
17. W-H. Chu, M. Mehregany, R. Mullen, *J. Micromech. Microeng.*, **3**, 4, (1993)
18. Y. Zhang, Y. Zhang, R.B. Marcus, *J. Micromech. Microeng.*, **8**, 43, (1999)
19. V. Pamula, A. Jog, R. Fair, *Tech. Proc. of the MSM 2001 International Conf. on Modeling and Simulation of Microsystems Conf.*, 410, (2001)
20. Y. Min, Y. Kim, *J. Micromech. Microeng.*, **10**, 314, (2000)
21. W. Fang, *J. Micromech. Microeng.*, **9**, 230, (1999)
22. J. Gorrell, P. Holloway, K. Shannon, *Proc. of the Solid State Sensor and Actuator Workshop*, 300, (1998)
23. R.J. Roark, *Roark's Formulas for Stress and Strain*, 6th ed., 117, McGraw-Hill, New York, (1989)
24. B. Bhushan, *Principles and Applications of Tribology*, John Wiley, New York, (1999)
25. D. Bullen, C. Liu, *Proc. SPIE, Smart Electronics, MEMS, and Nanotechnology, SPIE's 9th Annual International Symposium on Smart Structures and Materials*, **4700**, 288, (2002)

Mat. Res. Soc. Symp. Proc. Vol. 758 © 2003 Materials Research Society LL4.4

MTU Laser-Based Direct-Write Techniques: Recent Development and Nanoparticles Patterning Results

Edward M. Nadgorny[1], Changgong Zhou[1], Jaroslaw Drelich[2, 3], and Randy Zahn[2]
[1]Department of Physics, [2]Department of Materials Science and Engineering, and [3]Engineering Research Center for Wireless Integrated Microsystems, Michigan Technological University, 1400 Townsend Drive, Houghton, MI 49931, U.S.A.

ABSTRACT

Two laser-based direct-write techniques to guide particles from a mist source to a target substrate by laser beams were recently developed at Michigan Tech. The laser-guided direct-write (LGDW) technique uses a hollow optical fiber, while the laser-guided microsensor patterning (LGMP) technique uses a micrometer-sized aperture. The techniques are suggested to be utilized for patterning microstructures made of nanoparticles that are either crystallized from liquid precursors or directly deposited from nanoparticle-in-liquid suspensions. The computational results based on the paraxial Fraunhofer approximation of a Gaussian beam diffracted by a circular aperture and experimental measurements of corresponding deposition rate under different conditions suggest several factors for setup optimization of LGMP. The results indicate that among the most important factors are the aperture size relative to the laser beam-waist size and the divergence of the beam near the aperture. Examples of gold-thiolate, protein-coated polystyrene, and carbon-polymer composites deposition are presented.

INTRODUCTION

Laser-based guidance of nanoparticles is one of many techniques in the new emerging field of direct-write technologies allowing effective and advanced patterning of various materials for the fabrication of sensors and electronics (see an extensive review [1] for more details). Two laser-based techniques have recently been developed at MTU, LGDW and LGMP [2-6]. Both of the techniques use laser-induced optical forces to transport particles from a supply source and deposit them on a substrate mounted on a translation stage. They are differentiated mainly by the method of focusing the particles before depositing on the substrate: LGDW uses a hollow optical fiber while LGMP an aperture and lens-controlled narrow laser beam. These techniques are quite general and enable one to deposit almost any material that can be atomized to produce micron or submicron-sized carriers, i.e. liquid droplets. Such droplets may be in the form of liquid precursors, single-phase liquid solutions or colloidal suspensions of solid particles. Complex structures can be patterned by repeatedly depositing individual particles on the translated substrate. The techniques can operate over a wide range of particles sizes, from several nm to about one micron. So far, a variety of structures have been constructed on different substrates using metals, dielectrics, semiconductors, piezoelectric and ionic crystals, as well as living cells and proteins [2-7].

Unlike well-known optical trapping techniques, the laser-based direct-write techniques utilize optical transverse gradient forces to confine particles inside weakly focused laser beams and take advantage of radiation pressure and absorption force to move particles axially. An optical trap, on the other hand, sometimes referred to as an optical tweezer, see [8] for review, makes use of a strongly focused laser beam with a very strong axial gradient to allow axial trapping. This difference also illustrates the main advantage of the direct-write techniques over

optical tweezers: their ability to transport particles from various particle sources onto substrates to "write" on them. This paper briefly describes the setup and features of the MTU LGDW and LGMP techniques and shows some recent examples of their applications in deposition of nanomaterials.

MTU TECHNOLOGIES

The principal setup of the laser-based direct-write techniques is shown schematically in Figure 1. It consists of a mist chamber (MC), source chamber (SC), process chamber (PC), and a laser system. The mist chamber includes an atomizer and delivery system to make a mist of sub-micron sized liquid droplets that are precursors for the deposited material. The source chamber is connected to a process chamber by a micron-sized hollow optical fiber (LGDW) or aperture (LGMP). Typical fiber and aperture sizes are about 20 μm, and the droplets must be much smaller than the fiber or aperture sizes, typically being of the order of a micron or less. The laser beam is coupled into a fiber or aperture by an optical lens of low numerical aperture to allow particle guidance to a substrate that is mounted on a translational stage. The supply chamber provides an environment suitable for the deposition process and shields the particles from convection currents that can deflect particles out of laser's confinement. More details can be found in [2-4, 7] for LGDW and in [5, 6] for LGMP. The main difference between the two versions is that LGDW utilizes the guiding optical fields in a grazing-incidence mode inside the hollow fiber, while the guidance in LGMP is achieved by diffracted laser radiation.

As mentioned, the guidance efficiency depends strongly on the optical transverse gradient force and, therefore, on the optical axial intensity. The intensity inside a hollow fiber decreases exponentially with the distance, and the decay is usually characterized by a parameter z_0 or the decay length. For a typical fiber of the inner diameter $2a = 20$ μm, $z_0 \approx 8$ mm, and it is size and wavelength dependent, $z_0 \propto a^3/\lambda^2$ [3]. The equivalent circular-aperture parameter is the Rayleigh range z_R, or the border between the near-field diffraction region (at $z < z_R$) and the

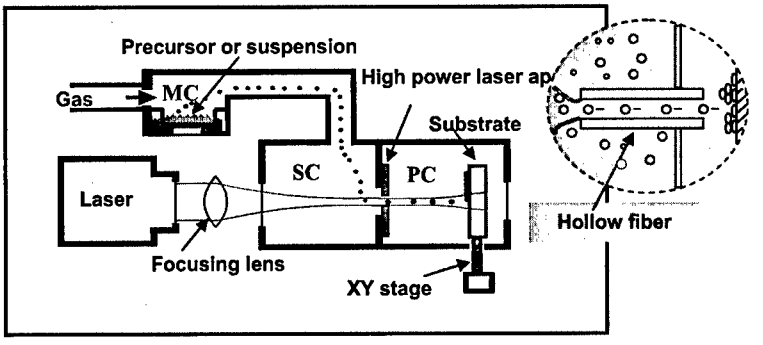

Figure 1. Schematic of laser-based direct-write techniques: source of droplets/particles (atomizer, carrier gas supply and the mist chamber MC); laser system (laser and focusing lens); supply (SC) and process (PC) chambers linked by either the high-power laser aperture (LGMP) or hollow optical fiber (LGDW, shown in the offset); movable substrate on a translational stage.

far-filed diffraction region (at $z > z_R$). The Rayleigh range scales approximately as $z_R \propto a^2/\lambda$, being typically shorter than z_0 [9]; for instance, $z_R \approx 1$ mm for the 25-μm aperture. Unlike the hollow fiber case, the intensity in the near-field region might be even higher than the incident light intensity, decreasing only at $z > z_0$. Additionally, LGMP practically excludes particles clogging and allows lower laser intensity; it also free from attenuation limits of LGDW due to smaller hollow fiber size. On the other hand, LGMP is more sensitive to axial gradient forces, especially for such nanoparticles as gold with a higher polarizability [10] and requires a better optical design to avoid the inverse radiation pressure.

The computational results based on the paraxial Fraunhofer approximation of a gaussian beam diffracted by a circular aperture [9, 11] suggest several factors for setup optimization of LGMP. The calculations and experimental comparison of the diffraction patterns with the best particle flux through the 25-μm aperture have shown that one of the most important factors is the aperture radius a relative to the gaussian beam-waist radius w_0. It was found that the ratio a/w_0 should be at least equal to or larger than 1.7. This number is larger than an optimum aperture ratio of 1.125 (to obtain the maximum axial intensity in the far-field range) but closer to 1.57 for ≥ 99% power transmission [12]. The other important factor is the divergence of the beam ahead of the aperture. A large divergence in the region near the beam waist (as utilized in the optical tweezers [8]) can lead to reverse radiation pressure, especially for small particles $<< \lambda$ [10]. Experiments with a setup (100-nm polystyrene spheres, 25-μm circular aperture and 30-mm focusing lens) have shown that guidance exists at as low laser power as ≤ 100 mW.

High accuracy is essential for direct write applications. Since it is determined by many factors, systematic studies are required to estimate their contributions. Preliminary experiments with five different materials [13] have shown that the deposition accuracy is inversely proportional to the transport distance; it also strongly depends on the material properties of the transported particles, such the refractive index and absorption, and relatively weakly on the laser power when measured inside a low-power range.

RESULTS AND DISCUSSION

All experiments discussed below were performed using a cw frequency doubled Nd:YVO_4 laser (Millennia II, Spectra-Physics, $\lambda = 532$ nm, 2.0 W, TEM_{00} mode) for deposition and an AFM (Dimension 3000) for characterization. Glass substrates were cleaned using a standard procedure (Alconox powder cleaner and ultrasonic bath). Some substrates were additionally silanized.

Deposition of gold-thiolate nanoparticles

Synthesis of new materials, including nanomaterials, can take advantage of the laser heating of droplets during their transportation and deposition. The techniques allow us in-situ melting of deposited gold particles to form microelectrodes at the ends of nanoparticle depositions; additionally, porous microstructures can result from evaporation of the deposited nanoparticle-in-liquid droplets [5, 6]. Porous and relatively uniform microstructures can be fabricated using as small nanoparticles as a few nm. Figure 2a shows spheres made of 7-nm hydrophobic gold particles. The size of these spheres varies from about 200 nm to one micron, and the diameter of the spheres is a direct consequence of the size distribution of the nanoparticle-in-liquid droplets

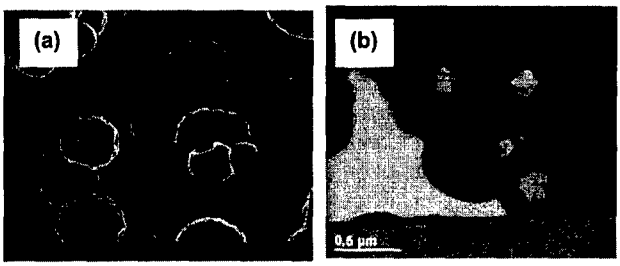

Figure 2. Structures formed by 7-nm Au-S$(CH_2)_7CH_3$ particles deposited by at a laser power of 200 mW on glass: (a) scanning electron micrograph of microspheres; (b) transmission electron micrograph of the partially sectioned microspheres.

generated by the atomizer and, to a lesser degree, the nanoparticle concentration in the droplets. The hydrophobic gold nanoparticles pack together producing stable microstructures as a result of the inter-particle van der Waals forces.

The transmission electron micrograph in Figure 2b reveals that the spheres are empty inside as indicated by a bright area of the sectioned spheres. Such an inhomogeneity reduces the strength of fabricated microstructures and causes a partial collapse of the shells. As a result, small undulations are formed, as can be seen in Figure 2a. The formation of such shells is assumed to be a result of combined effects of liquid evaporation and capillarity phenomena. Indeed, when the laser beam heats liquid droplets, evaporation progresses easily through the outer surface of the droplets. It is also initiated on the nanoparticle surfaces inside the droplets via nucleation and growth of nanobubbles. As long as the density of nanoparticles in the droplet is small, the bubbles can easily escape to the droplet surface. This is not the case, however, when a dense structure of nanoparticles is created producing fine porosity through particle-to-particle alignment. In this situation, a dense monolayer of hydrophobic gold nanoparticles has probably already been formed on the surface of each toluene droplet at an early stage of the fabrication experiment, soon after droplet generation. Gaseous bubbles cannot pass through such a dense configuration of nanoparticles without disrupting its structure due to high capillary pressure opposing this process. An estimate by the simplified Young-Laplace equation $\Delta P = 2\gamma / R$, where γ is the surface tension of liquid and R is the radius of capillary opening, shows that a pressure of about 280 atm is required to force the gaseous-toluene interface to move through a capillary opening of 4 nm in diameter.

It remains to be seen if the hollow microspheres made of gold and other nanoparticles synthesized in our laboratory can found new application, such as capsules for the controlled release of drugs and production of new catalysts with controlled porosity and specific surface area.

Deposition of polystyrene nanospheres

Spherical polystyrene nanoparticles are attractive for patterning due to their availability in a variety of sizes and their well-known surface properties. They are also commonly used as carriers for proteins in biosensor fabrication. When deposited from water suspensions, both polystyrene nanoparticles and polystyrene nanoparticles coated with avidin proteins form spherical well-ordered structures. Additionally, avidin proteins remain active on the surface of the carrier polystyrene particles after their deposition with LGMP [5]. Two examples of such cluster-like structures made of 100-nm protein-coated and uncoated polystyrene particles (Duke Scientific) by 200-mW power deposition are shown in Figure 3. Small irregularities of several nm in width were observed only on avidin-coated polystyrene. They are assumed to be formed due to incomplete coating of the polystyrene particles with protein layer(s). Proteins adsorb on the hydrophobic surface of polystyrene from solution and can also be deposited through the

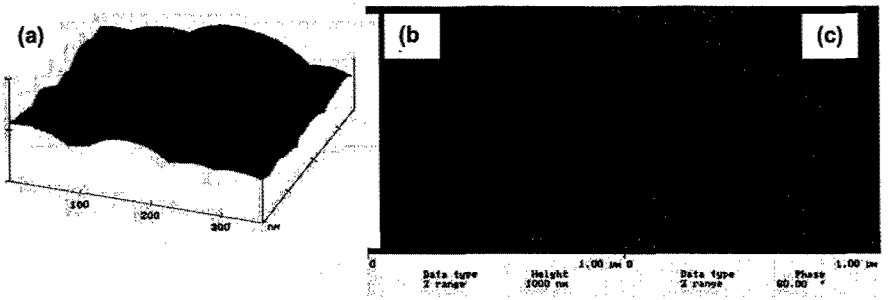

Figure 3. (a) AFM 3-D topographic image of clusters of 100-nm avidin-coated polystyrene particles deposited on silanized glass. (b) AFM topographic image of 100-nm uncoated polystyrene particles deposited on untreated glass. (c) AFM phase image of the same particles.

liquid-solid-air three-phase line during its retraction when the volume of liquid decreases.

As our experiments indicated, LGMP opens an option to control the size and the shape of the deposited clusters. At a higher evaporation rate (particles with strong absorption and/or a higher laser power), the deposited particles carry no or little water, forming spherical clusters similar to those shown in Figure 2. At a lower evaporation rate (particles with weak absorption and/or lower laser power), deposited droplets are still liquid and spread polystyrene spheres to form lens-like clusters, such as shown in Figure 3c. Thus, the shape and size of formed clusters can be controlled by changing the substrate wetting properties (hydrophilic/hydrophobic).

Deposition of carbon-polymer composite

The resistivity of polymers is commonly changed by incorporating conductive particles, such as carbon and metals, into the polymeric matrix. Such composites constitute an attractive basis for sensing devices based on the absorption of organic pollutants by the polymeric matrix. Contaminants absorption causes the polymer to swell, which increases the distance between conductive particles and changes the conductivity of the composites. Chemical stability of such composites combined with their good adhesion to many substrates are additional attractive features in patterning of this type of materials over many other systems of weakly interacting particles.

Fabrication of microstrips of carbon-polymer composites is currently explored in our research using LGMP. Commercially available carbon nanoparticles of irregular shape (from 30 to 100 nm) are suspended in polyvinyl acetate-toluene solutions for atomization and deposition. Our goal is to investigate the stability and controlled melting of such a composite under the laser beam, as well as the phase segregation inside the deposited matrix. As an example, Figure 4 shows a cluster of carbon-polyvinyl acetate deposited on glass. Carbon nanoparticles (300 mg) were dispersed in a solution of 3.2 g polyvinyl acetate in 50 ml toluene. Both AFM phase and 3-D images reveal locations of a few carbon particles on the surface of polymeric cluster visible as small dark and regular areas. They can also be distinguished from irregularities of the cluster surface of 3D topographic image. Note that the body of each carbon particle remains immersed in the polymeric matrix. The accumulation of carbon particles at the surface of a polymeric droplet is a rare phenomenon since the carbon particles have a tendency to remain dispersed in the polymeric matrix. This is the result of strong interactions between polyvinyl acetate and carbon particles used in this study.

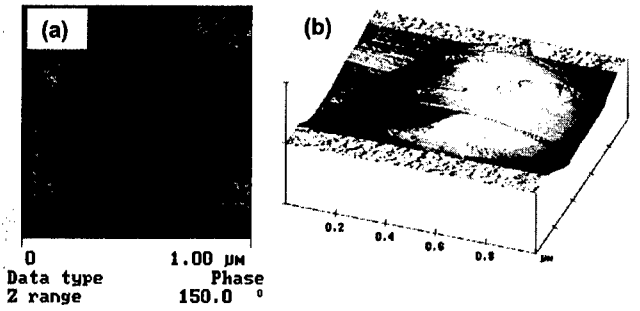

Figure 4. A cluster of carbon-polyvinyl acetate of about 1 µm in diameter and 0.5 µm in height deposited on glass at a laser power of 0.3 W: (a) AFM phase image; (b) AFM 3D topographic image.

ACKNOWLEDGEMENTS

The authors would like to express their appreciation to Elvin Beach and Steve Rozeveld of Dow Chemical Company for their help on scanning electron microscopy and transmission electron microscopy images and to Juntao Xu for deposition of gold-thiolate nanoparticles. The gold-thiolate nanoparticles were received from E.T. Zellers of the University of Michigan.

REFERENCES

1. A. Pique and D.B. Chrisey (editors), *Direct-Write Technologies for Rapid Prototyping Applications* (Academic Press, 2002).
2. M. J. Renn and R. Pastel, *J. Vac. Sci Technol.* **B16**, 3859 (1998).
3. M. J. Renn, R. Pastel, and H. J. Lewandowski, *Phys. Rev. Lett.* **82**, 1574 (1999).
4. E.M. Nadgorny, R.L. Pastel, A.A. Struthers, and A. Miner in *Mass and Charge Transport in Inorganic Materials - Fundamentals to Devices, Part B*, edited by P. Vincenzini and V. Buscaglia (Intl. Conf. Proceedings, Italy, Techna, Faenza, 2000), pp 1107-14.
5. J. Xu, Ch. Zhou, Sh. Grant, E. Nadgorny, and J. Drelich in *Functional Nanostructured Materials Through Multiscale Assembly and Novel Patterning Techniques* (Mater. Res. Soc. Proc. **728**, Pittsburgh, PA, 2002), pp. S7.6.1-6.6.
6. J. Drelich, E.M. Nadgorny, E.T. Zellers, J. Xu, Ch. Zhou, C.L. White, and W.M. Cross in *Functional Fillers and Nanoscale Minerals*, edited by J.J. Kellar, M.A. Herpfer, and B.M. Moudgil (Proc. of Intl Symp., SME, Littleton, OH, 2003), pp. 85-94.
7. M.J. Renn, G. Marquez, B.H. King, M. Essien, and W.D. Miller in [1], pp. 475-92.
8. A. Ashkin, *Optical Trapping and manipulation of neutral particles using lasers* (World Scientific, 2002).
9. A. Siegman, *Lasers* (University Science Book, 1986), p. 729.
10. K. Svoboda and S. M. Block, *Opt. Lett.* **19**, 930 (1994).
11. J.P. Campbell and L.G. DeShazer, *J.Opt. Soc. Am.* **59**, 1427 (1969).
12. Ref. [11], pp. 666 and 734.
13. R. Pastel, P. Geiser, A. Strutheres, E. Nadgorny (2000), unpublished results.

Mat. Res. Soc. Symp. Proc. Vol. 758 © 2003 Materials Research Society LL4.5

Versatile Nanodeposition of Dielectrics and Metals by Non-contact Direct-Write Technology

H.D. Wanzenboeck[1], H. Langfischer[1], S. Harasek[1], B. Basnar[1], H. Hutter[2], E. Bertagnolli[1]
Vienna University of Technology
[1]Institute for Solid State Electronics, Floragasse 7- E362; 1040 Vienna, AUSTRIA
[2]Institute for Analytical Chemistry; Getreidemarkt 9 - E 151; 1060 Vienna, AUSTRIA

ABSTRACT

Direct-write techniques allow processing in the nanometer range and have become powerful methods for rapid prototyping of microelectronic circuits and micro-electro-mechanical systems (MEMS). Chemical reactions are initiated by a focused beam leading to deposition of solid material on literally any surface. We have used this method to deposit metals such as tungsten and dielectrics such as silicon oxide using a focused ion beam (FIB) with 10 to 50 kV acceleration voltage. Controlled guidance of the beam allows deposition of both metallic and dielectric material with features in the 100 nm range. The deposition of separate structures of metallic and dielectric material deposited next to each other is shown on samples of different roughness. 3-dimensional exemplary prototypes in the sub-µm range and multilayer structures demonstrate the versatility of this method for prototyping and mix-and-match approaches with commercial semiconductor devices. A characterization of the deposited material was performed to clarify chemical composition and surface morphology of deposited structures. The deposition parameters were found to influence the chemical composition and electronic properties of the material. Direct-write deposition of dielectrics and metals by FIB allows fabrication of 3-dimensional prototypes with custom-tailored material properties.

INTRODUCTION

Direct-write techniques have become increasingly important for rapid prototyping of microelectronic circuits and MEMS as these direct-write methods allow access to the nanometer range [1,2]. These non-contact techniques typically use energetic focused beams to facilitate processing on a locally confined space down to nanometer range. The focused beam makes it possible to initiate chemical reactions leading to deposition of solid material on literally any surface. In this work a focused ion beam (FIB) is used to deposit metals such as tungsten or dielectrics such as silicon oxide enabling the generation of prototypes for microelectronic applications. With deliberate control of the beam position a point-by-point deposition of both metallic and dielectric material is achieved [3]. The smallest features obtained with this direct-write method were below 100 nm.

The advantage of the direct write technique is that it is a mask-less approach. Therefore, prototypes can be realized quickly and cost-effectively. Unlike optical projection lithography no photomask needs to be produced and changes of the layout can be implemented quickly. This provides the long sought flexibility to device development. Furthermore, the feasibility to fabricate

spatial structures extends the application range towards creation of 3-dimensional devices. With beam-induced direct-write techniques the deposition of material is feasible regardless of the roughness or prior structure of the sample and the suitability of these methods for mix-and-match techniques is demonstrated in this work by direct-write deposition on commercial microchips.

With FIB-CVD individual structures of metallic and dielectric material may be deposited next to each other. Several exemplary prototypes such as functional MIM (metal-insulator-metal) capacitor structures and geometrical modifications of 3-dimensional substrates such as AFM (atomic force microscope) cantilevers demonstrate the feasibility of this method for the generation of functional multimaterial structures in the sub-µm range. The deposition parameters have a strong influence on the chemical composition and electronic properties of the material. Therefore, a chemical and physical characterization of the materials is performed. These material attributes will impact the final performance of both electronic and mechanical devices. Direct-write deposition allows for custom tailoring and fine-tuning of material properties. These direct-write techniques show a future potential for prototyping of 2- and 3-dimensional components [4, 5].

EXPERIMENTAL DETAILS

Direct-write deposition of layers and 3-dimensional structures of silicon oxide and tungsten was performed by chemical vapor deposition (CVD). The CVD process was locally induced by a focused ion beam (FIB). The silicon oxide deposition was obtained by decomposition and reaction of a binary precursor gas mixture of siloxane and oxygen while the metal deposition was achieved by local decomposition of tungstenhexacarbonyl precursor. The deposition chamber had a base pressure of 10E-7 Torr. Introduction of precursor gases increased the total pressure to the 10E-6 to 10E-5 Torr regime. Gaseous tetramethylcyclotetrasiloxane (TMCTS) and molecular oxygen were coadsorbed at the substrate surface. The surface reaction leading to deposition of dielectric material on the substrate surface was locally induced by an impinging Ga+ beam. Thus, the deposited material is confined to a restricted area from 0.01 μm^2 up to 1 mm^2. Direct-write techniques allow for arbitrary geometry relying only on the guidance of the focused beam. The ion beam could be focused down to a diameter of 5 nm. Smallest features deposited were in the 100 nm range due to overspray effects by sputtering and redeposition of previously deposited material.

The Ga ions were generated by a liquid metal ion source accelerated with 50 kV. An electrostatic lens system for focusing and a deflection system for scanning the beam provided a focused beam with an ion current adjustable between 4 pA and 2 nA. The pixel spacing during scanning could be adjusted in the nm to the µm range. For deposition the ion beam was directed perpendicular to the sample surface. Commercial Microchips or semiconductor materials such as Si (100) or GaAs were used as substrates.

Topology of the deposited structures was investigated by atomic force microscopy (AFM) using a Digital Instruments 3100 in tapping mode. The chemical composition of deposited materials was determined by secondary ion mass spectroscopy (SIMS) using a CAMECA IMS 3f sector field system. The SIMS-tool was operated in depth profiling mode to determine changes of chemical composition with varying layer thickness. A 15 nA Cs+ ion beam was focused on a 60 µm diameter spot of the 150x150 sample area. The recorded signal, as counts/min account for the concentration in the deposited material.

DISCUSSION

Direct-Write Deposition with a focused ion beam was evaluated for its appropriateness for practical applications. Therefore, the homogeny of the deposited material and the reproducibility of the process were examined. For numerous applications the morphology of the deposited material is essential so that the surface roughness of directly deposited material was investigated. To display the suitability for practical applications prototypes for multilayered and 3-dimensional structures were fabricated by FIB-Direct Write Deposition.

Chemical Composition

The chemical composition of silicon oxide deposited by FIB-CVD was investigated by secondary ion mass spectroscopy (SIMS). A depth profile of two individually deposited samples shows the composition of the material with the proceeding deposition (Fig. 1).

The SIMS-spectra prove a homogeneous chemical composition of the FIB-deposited material. This indicates a stable, robust process for the direct-write deposition of silicon oxide However, previous studies have shown that, at the substrate interface, an intermixing layer is formed under highly energetic ion bombardment [6]. During SIMS sputtering Si and O are the dominant species and also SiO ions are found signifying the existence of silicon oxide bonds. Furthermore, contaminations of C and Ga originating from the ion beam are observed. However, the logarithmic scale of the ion counts suggests silicon and oxide as the main components of the deposited material.

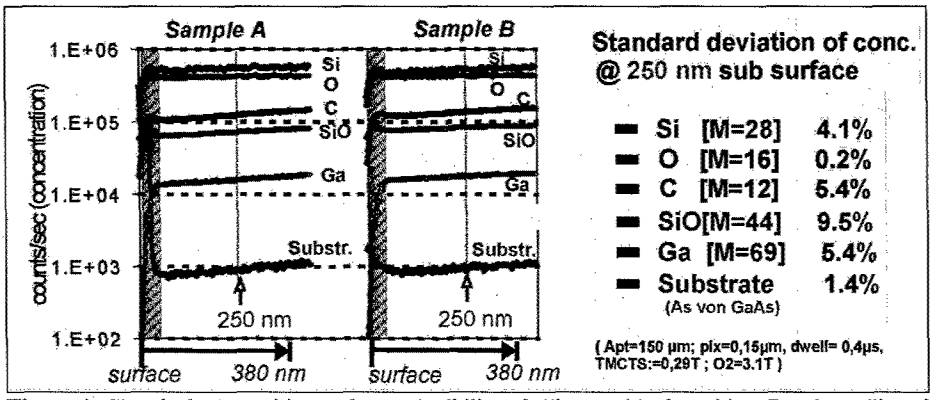

Figure 1. Chemical composition and reproducibility of silicon oxide deposition. Depth profiles of 2 silicon oxide structures fabricated separately but with identical process parameters were measured- the composition of the FIB-deposited material was analyzed by SIMS. The concentration variations of single species were calculated for the material composition at 250 nm sputter depth.

The comparison of the two individually processed samples renders the FIB-CVD direct-write deposition a highly reproducible process. The concentrations of all species are highly comparable

between both samples. The ion counts of different species were compared for 250 nm sputter depth. The standard deviation of most detected species is below 5% and signifies an excellent repeatability. This allows employing direct-write deposition also for applications where a constant material quality is demanded. However, the variation of process parameters allows to change the chemical composition and to tailor material properties accordingly to meet specific requirements [7].

Surface Roughness

For mechanical applications the surface morphology is a central characteristic. The surface roughness of silicon oxide deposited by FIB-CVD was investigated by atomic force microscopy (Fig.2). The selection of the pixel spacing was found to have a significant influence on the surface roughness of the deposited material. All other process parameters such as total ion dose, dwell time per pixel and composition of the gas atmosphere were maintained invariable so that only the spacing between beam spot positions during a scan is responsible for the observed changes. With a small pixel spacing a very smooth surface with a RMS roughness in the 3 nm range was obtained (Fig. 2 left). With pixels positioned so close that neighboring beam profiles are overlapping a very a homogeneous deposition over the entire surface was obtained. Large pixel spacing resulted in a rough surface with a RMS roughness exceeding 10 nm. The large distance between neighboring beam spots led to a locally inhomogeneous ion exposure facilitating slightly different deposition rates in the sub-µm range.

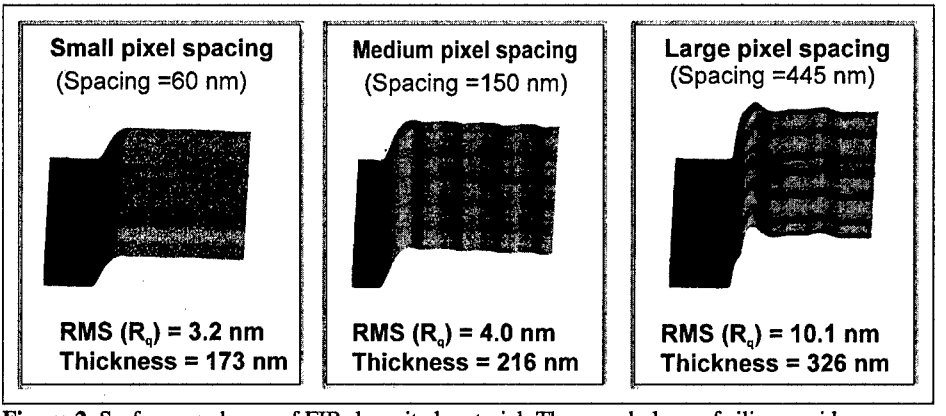

Figure 2. Surface roughness of FIB-deposited material. The morphology of silicon oxide fabricated by FIB-CVD was recorded by AFM. The process parameter pixel spacing - the distance between beam spots during the scan operation - was varied.

The different thickness of deposited material obtained with an identical ion dose in all cases has to be noted (Fig. 2). With ion induced deposition the resulting deposition rate is always in equilibrium between depositing new material by the FIB-induced CVD reaction and removing material again by ion sputtering. Large pixel spacing facilitates a more effective utilization of ions for deposition while the negative consequences of sputtering are diminished. By widening the

pixel spacing the deposition rate could almost be doubled. This indicates a higher efficiency of the deposition process with large pixel spacing, but at the cost of a higher surface roughness. Chemical analysis by Auger electron spectroscopy showed lower Ga-concentrations with large pixel spacing, while the amount of Ga implanted in the deposited material was higher with a small pixel spacing.

3-dimensional Structures

Direct-write deposition is a versatile tool for fabrication of 3-dimensional structures. An experimental multilayer structure for interconnect modification of commercial microchips displays the capability to rewire an integrated circuit using three additional interconnect layers (Fig 3). With the multilayer interconnect metal lines were deposited by FIB-CVD to lay conductive paths. The metallic features are separated by silicon oxide, that was deposited by FIB direct-write deposition acting as interline and interlayer dielectric. Imaging by FIB allows aligning the structure to be deposited on the substrate surface. Positioning of individual metal interconnects can be performed in-situ during the fabrication process and without any necessity for a previously fabricated mask.

Direct-write deposition is also a powerful method for prototyping of 3-dimensional devices down to the sub-µm range. A structure with several pillars of 1x1 µm cross section was deposited (Fig. 4). An aspect ratio height to side length of 30 could be achieved with the shown structures. Also curved pillars were fabricated - a design that is not accessible with standard lithography techniques. This versatility in the design renders FIB direct-write deposition an excellent tool for development of new MEMS prototypes.

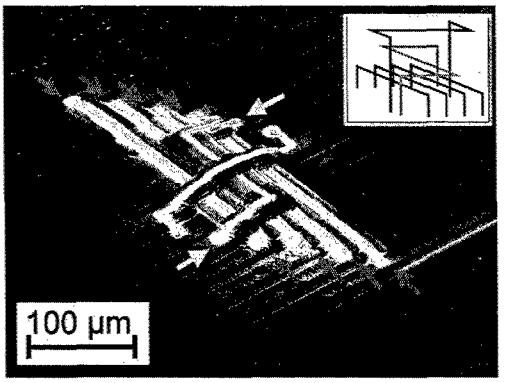

Figure 3. Multilevel interconnect prototype. On the surface of the commercial microchip a 3-layer interconnect structure was fabricated by FIB-CVD of tungsten (bright lines) and silicon oxide (thicker dark lines). The conductive metal lines are well separated by dielectric material.

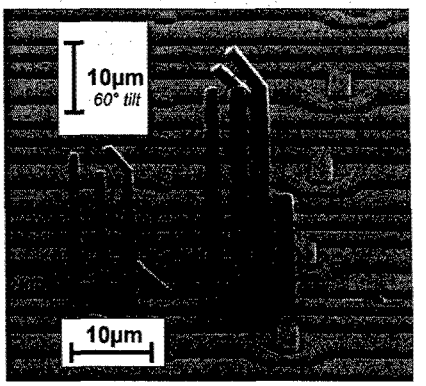

Figure 4. Two 3-dimensional structures fabricated by direct-write deposition of silicon oxide. The single pillars have a 1x1 µm cross section and are up to 30 µm high and are positioned on preselected spots.

CONCLUSIONS

We have shown that the direct-write deposition utilizing a focused ion beam is a versatile process that allows depositing metals and dielectric materials. The deposition process can be influenced in manifold ways by adjusting the process parameters in order to tailor the material properties such as chemical composition or surface roughness. The FIB-CVD process was shown to be highly reproducible and provides material of a homogeneous chemical composition. The capability to deposit conductive and insulating material renders direct-write deposition an ideal prototyping technique for microelectronics. The feasibility to directly deposit 3-dimensional structures of arbitrary shape down below 1µm feature size gives this method a high potential as development tool of future MEMS prototypes.

ACKNOWLEDGEMENT

The Austrian Society for Microelectronics (Gesellschaft für Mikroelektronik) is acknowledged for financial support. We thank Prof. E. Gornik for providing the clean room of the microstructure center for this work. H. Hutter and M. Gritsch are acknowledged for SIMS analysis of the samples.

REFERENCES

1. Daniel J.H., Moore D.F., Walker J.F., "Focused ion beams for microfabrication", *Engineering Science and Education Journal* **1998(4)**, 53 (1998).
2. Murguia J.E., Musil C.R., Shepard M.I., Lezec H., Antoniadis D.A., Melngailis J., "Merging focused ion beam patterning and optical lithography in device and circuit fabrication", *Journal of Vacuum Science & Technology B* **8**(6), 1374 (1990).
3. Iliadis A.A., Andronescu S.N., Yang W., Vispute R.D., Stanishevsky A., Orloff J.H., Sharma R.P., Venkatesan T., Wood M.C., Jones K.A., "Pt and W Ohmic contacts to p-6H-SiC by focused ion beam direct-write deposition", *Journal of Electronic Materials* **28**(3); 136 (1999).
4. Stanishevsky A., Aggarwal A.S., Prakash A.S., Melngailis J., Ramesh R., "Focused ion-beam patterning of nanoscale ferroelectric capacitors", *Journal of Vacuum Science & Technology B* **16**(6), 3899 (1998).
5. Yutani N., Suzuki K., Enomoto Y., "High-Tc Josephson Junctions on Micro V-shape groove prepared by focused ion beam", *IEEE Trans. Appl. Superconductivity* **9**(2), 2878 (1999).
6. Wanzenboeck H.D., Langfischer H., Lugstein A., Bertagnolli E., Grabner U., Pongratz P., Basnar B., Smoliner J., Gornik E., "Effects of Ga-irradiation on properties of materials processed by a focused ion beam (FIB)", in *Ion Beam Synthesis and Processing of Advanced Materials*, Materials Research Society Symposium Proceedings Vol., 2001, O6.6.1-9.
7. Wanzenboeck H.D., Lugstein A., Langfischer H., Bertagnolli E., Gritsch M., Hutter H., "Ion beam induced deposition of dielectric nanostructures", Eighth International Conference on Dielectric Materials, Measurements and Applications (DMMA), Conf. Publ. No. 473, 2000, p. 485.

Mat. Res. Soc. Symp. Proc. Vol. 758 © 2003 Materials Research Society LL4.6

Two-Photon Laser Micro-Nano Fabrication; Understanding from Single-Voxel Level

Satoshi Kawata[1] and Hong-Bo Sun[2]
Department of Applied Physics, Osaka University, Suita, Osaka, 565-0871, Japan
[1]The Institute of Physical and Chemical Research (RIKEN), Hirosawa, Wako, Saitama 351-0198, Japan
[2]PRESTO, Japan Science and Technology Corporation (JST)

ABSTRACT

For laser nanofabrication using two-photon photopolymerization, a deep understanding of the nature of focal spots that are related to two-photon excitation is essential for achieving a high spatial resolution in three dimensions. Here we report the use of a technology we call ascending scan for characterizing the three-dimensional size and shape of single polymerization elements (voxels), and introduce several features of voxels that have not been fully noticed before. These findings are important for tailoring nanofeatures according to design.

INTRODUCTION

Two-photon photopolymerization [1-7] has been recognized as an important technology for nanofabrication. The current research effort is mainly devoted to the synthesis of high efficiency photo initiators and sensitizers [4, 10]. However, as a new technology, a lot of work has been done to establish it as a nanotechnology. Examples include the achievement of sub-diffraction-limit spatial resolution by the radical quenching effect [8, 9], improvement of fabrication efficiency by using 3D vector scanning [9], 3D micro-diagnosis by fluorescent dye labeling and two-photon confocal scanning [11], micro-device functionalization [12], and so forth. Different from conventional laser rapid prototyping, depicting micro-objects with SDL features needs a deep understanding of characteristics of two-photon excitation related focal spots. This work has not been done before. In this paper, we will introduce a 3D focal spot imaging technology, ascending scan [13], and an investigation by using this technology on how basic laser parameters influence the focal spot size and shape, and therefore the nanofabrication.

EXPERIMENTAL SYSTEM

The experimental system was the same as we used before [12, 13]. A Ti: Sapphire laser that was operated at mode-lock and delivered 100 fs pulses at a repetition rate of 80 MHz was

employed as an exposure source (MaiTai, Spectra Physics). The laser wavelength was tuned to 780 nm. The laser beam was focused by a high-numerical-aperture (NA~1.4) objective lens into a sample. A Galvano mirror set was used for moving the focal spot in two horizontal dimensions and a piezo stage for up-down scanning, both synchronized and controlled with a computer. A urethane acrylate resin, SCR 500 (from Japan Synthetic Rubber, JSR) was used for two-photon-absorption (TPA) photopolymerization, of which the absorption peaks at UV and extends to the visible range to 530 nm. The entire fabrication process was monitored *in-situ* with a CCD camera. After fabrication, samples were developed in methanol so that unsolidified liquid was removed. Finally samples were dried and imaged with a scanning electron beam microscope.

THREE-DIMENSIONAL FOCAL SPOT CHARACTERIZATION

The 3D spatial resolution was conventionally characterized from a resin spot or line that was polymerized on the surface of a substrate. By atomic force microscope (AFM) or scanning electron microscope (SEM) measurement, the width and height of the spot were considered as the lateral and longitudinal dimensions of a voxel, in other words, the lateral and longitudinal spatial resolutions, respectively. Due to a truncation effect, the substrate surface recorded spot is actually only a part of an entire voxel. The above simple measurement scheme brought a lot of misleading conclusions. To get reliable spatial resolution information, a complete and isolated voxel is needed. To reach this end, we scan the laser focal point from inside the substrate to an above surface height, residing at a series of positions for exposure [Fig. 1(a)]. The left-side voxels are truncated, and are utilized in conventional AFM or SEM observations. In the rightmost region, voxels form but float away during developing. Only if the residing spot number is reasonably large, there are always some voxels formed at the immediate substrate surface that are not truncated and are weakly attached. After developing, these voxels remain where they were polymerized and fall down [Fig. 1(b)]. From these voxels, both lateral and longitudinal spatial resolutions are attained [Fig. 1 (c)].

VOXELS INFLUENCED BY LASER PULSE ENERGY, EXPOSURE TIME, NUMERICAL APERTURE, AND POLARIZATION

Laser beams are described by their spatial, temporal, spectral and polarization distributions in addition to coherence properties. As fundamental limits the beams can be diffraction and bandwidth limited, linearly polarized and coherent. Usually these limits are not satisfied or even required in applications.

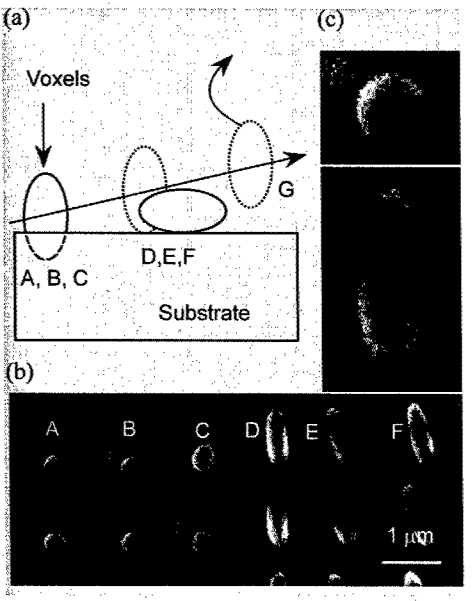

Figure 1. The ascending scan method for observation of the 3 dimensions of a voxel. (a) The principle of the technology; (b) SEM image of the truncated (A, B, C) and overturned (D, E, F) voxels; and (c) magnified images of a voxel.

In the current research, a 780-nm-wavelength laser with a 100-fs pulse width at a repetition rate of 80 MHz possesses a spectral full width at half maximum (FWHM) of approximately 10 nm, implying a time-bandwidth product of $\Delta t \cdot \Delta \omega = 0.493$, near the transform limit of 0.441 of a Gaussian pulse shape. A short pulse width (< 1 ps) is essential to provide a high transient power in time domain to launch nonlinear optical processes and exclude thermal effects, which are difficult to localize. The broad laser spectrum associated with the ultrashort pulse width brings about the chromatic aberration, which has been overcome by use of apochromats. Also due to the wide spectrum, the coherence length (l_c) of femtosecond lasers becomes short, e.g. around 40 μm in the current system as estimated by $\lambda_c = 0.624\ \lambda / \Delta\lambda_{FWHM}$, which is the major hindrance of large-volume holographic applications. For single-color and single-beam focusing geometry as we used in this research, the coherence condition for forming a virtual energy level that is needed by two-photon absorption (TPA) is naturally satisfied.

Comparing with the roles of temporal, spectral and coherence performances discussed above, laser energy distribution and beam polarization directly determine the spatial resolution of fabrication. By using the ascending method, we investigated how some basic laser parameters influence voxels, including exposure time, laser pulse energy, NA and polarization. This information is important because for tailoring nanostructures, not only the focal spot size, but also its shape determine the accuracy and dimensions of target objects.

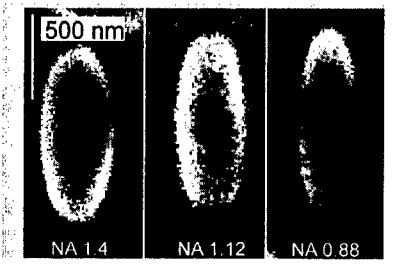

Figure 2. Side-view SEM images of voxels formed under different NA focusing.

Figure 2 shows the side-view SEM image of voxels formed under the same laser power exposure but beams focused with lens of different NAs. The longitudinal size increases as NA is reduced within expectation. However, it is found the lateral size obtained at high NA is no smaller than that at low NA. This contradicts theoretical results, but could be understood by considering the threshold effect of TPA polymerization. In case of low-NA focusing, the laser power is distributed to a larger volume, and the solidified front demarcated by the threshold camber is vertically expanded and laterally shrunk. Therefore low-NA gives smaller lateral voxel size. The gradient of light intensity distribution in high-NA focused light field is steeper and energy is more concentrated to the center of focal spot, which facilitates pinpoint exposure at smaller volume. Therefore smallest visible voxels by 1.4 and 0.8 NA are 120 nm and 260 nm, respectively. Hence, for high-accuracy nanofabrication, a high NA objective is preferable. Further research shows that near-threshold exposure condition, increasing exposure time and increasing laser pulse energy causes different exposure dose-dependent voxel size. The former is basically a logarithmic function that reflects the radical diffusion process, while the latter dependence is from an enhanced two-photon absorption effect.

We also tested how polarization influences the voxel shape. We found that the voxel cross-section perpendicular to the optical axis direction was not circular as expected, but an ellipse with axis ratio of roughly 1.1. This is shown in Fig. 3.

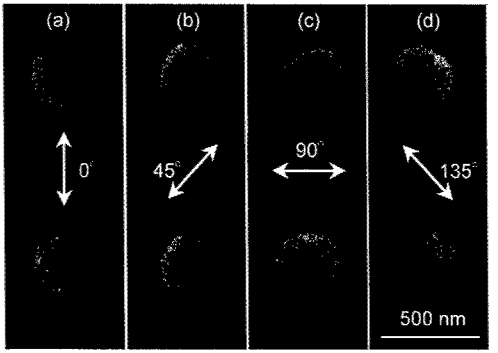

Figure 3. Top-view SEM images of voxels produced with lasers of different linear polarization directions.

The above phenomenon was explained by a depolarization effect that was predicted by electromagnetic focusing theory. It is already known that, when the beam incident angle α is small, the focal field (E_x, E_y, E_z) is sufficiently described by a cylindrically symmetric function [$E(r)$, 0,0] with $r=\sqrt{(x^2+y^2)}$, where the input beam is assumed to propagate in the z-direction and be polarized along the x-direction. Nevertheless, when $\alpha > 40^\circ$ (NA > 0.7), the symmetry is broken and the field with significant E_y and E_z component appears. More precisely, the electric field can be expressed as:

$$E(r_2,\phi,z_2)=\frac{\pi i}{\lambda}\{[I_0+\cos(2\phi)I_2]\mathbf{i}+\sin(2\phi)I_2\mathbf{j}+2i\cos\phi I_1\mathbf{k}\}$$

where **i**, **j** and **k** are the unit vectors in the x, y and z directions, respectively, variables r_2, z_2 and ϕ are cylindrical coordinates of an observation point. I_0, I_1 and I_2 are non-zero variables [see definitions in Ref.15]. Hence, it is clear that the electric field at the focal region is depolarized. The calculated result is shown in Fig. 4. The fact that the orientation of voxels changes corresponding to the polarization direction provides solid evidence for the origin of the ellipse cross-section.

CONCLUSION

We propose an ascending scan method for imaging single voxels in three dimensions. By using this technology we studied how basic laser parameters influence the shape and size of voxels. This technology and our findings are important for understanding the two-photon

photopolymerization nanofabrication technology. Also it can be utilized for evaluating newly synthesized photopolymers to test their usability in 3D laser nanofabrication.

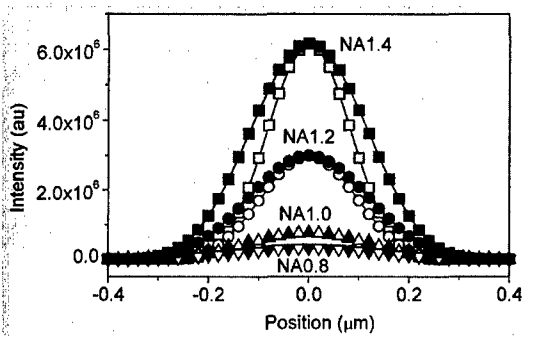

Figure 4. Two-photon point spread functions at focal plane. The open symbols denote the direction perpendicular to polarization (y axis) and solid symbols are within the polarization plane (x axis).

REFERENCES

1. S. Maruo, O. Nakamura and S. Kawata, Opt. Lett. **22**, 132 (1997).
2. S. Maruo and S. Kawata, J. IEEE MEMS **7**, 411 (1998).
3. H. –B. Sun, S. Matsuo and H. Misawa, Appl. Phys. Lett. **74**, 86 (1999).
4. B. H. Cumpston, S. P. Ananthavel, S. Barlow, D. L. Dyer, J. E. Ehrlich, L. L. Erskine, Ahmed A. Heikal, S. M. Kuebuler, I. -Y. Sandy Lee, D. M. Maugon, J. Qin, H. Rokel, M. Rumi, X. Wu, S. R. Marder and J. W. Perry, Nature 398, 51 (1999).
5. H. -B. Sun, T. Kawakami, Y. Xu, J.-Y. Ye, S. Matuso, H. Misawa, M. Miwa, and R. Kaneko, Opt. Lett. **25**, 1110 (2000).
6. H. -B. Sun, Y. Xu, S. Juodkazis, K. Sun, M. Watanabe, J. Nishii, S. Matsuo and H. Misawa, Opt. Lett. **26**, 325 (2001).
7. H. –B. Sun, V. Mizeikis, Y. Xu, S. Juodkazis, J. –Y. Ye, S. Matsuo and H. Misawa, Appl. Phys. Lett. 79, 1 (2001).
8. S. Kawata, H. –B. Sun, T. Tanaka and K. Takada, Nature 412, 667 (2001)
9. T. Tanaka, H. –B. Sun and S. Kawata, Appl. Phys. Lett. 80, 312 (2002).
10. K. D. Belfield, K. J. Schafer, Y. U. Liu, J. Liu, X. B. Ren and E. W. Van Stryland, J. Phys. Org. Chem, 13, 837 (2000).
11. H. –B. Sun, T. Tanaka, K. Takada and S. Kawata, Appl. Phys. Lett. 79, 1411 (2001).
12. H. –B. Sun, K. Takada and S. Kawata, Appl. Phys. Lett. 79, 3173 (2001).
13. H. -B. Sun, T. Tanaka and S. Kawata, Appl. Phys. Lett. 80, 3673 (2002)
14. H. –B. Sun, M. Maeda, K. Takada, J. Chon, M. Gu and S. Kawata, submitted.
15. M. Gu, Advanced Optical Imaging Theory (Springer, Heide lberg, 1999).

Tissue Engineering and Biomedical Applications

Mat. Res. Soc. Symp. Proc. Vol. 758 © 2003 Materials Research Society LL5.1

Bone Tissue Scaffold Technologies Based on RP Adopted Droplet Assembly[1]

Renji Zhang, Yongnian Yan and Feng Lin
Dept. of Mechanical Engineering, Tsinghua University, Beijing 100084, P. R. China
[1] Supported by the Hi-Tech Research and Development Program of China, No. 715-009-0160.

ABSTRACT

Tissue engineering tries to grow replacement tissues to repair damaged bones. In this paper, the fabrication technology of Multi-nozzle Deposition Manufacturing (MDM) was adopted to fabricate scaffolds of a tissue engineered bone at low temperature. The composite of poly(L-lactic acid) and tri-calcium phosphate (TCP) was chosen to form bone tissue engineering scaffolds. The new computer aided manufacturing process can make porous PLLA/TCP scaffolds. A new surface processing technology of apatite coating on bone tissue engineered scaffolds was also adopted. This digital forming technology was based on rapid prototyping (RP), in which a digital droplets assembly technology was introduced. The MDM technology of 4 nozzles was developed based on the layer-by-layer manufacturing principle of Solid Freeform Fabrication (SFF) in our laboratory. The bone scaffolds made by the multi-nozzle deposition process in the MDM system have good biocompatibility and bone conductive properties as a molecular scaffold for bone morphogenic protein (BMP) in the implantation experiment of repairing segment defects in rabbits' and dogs' radiuses.

INTRODUCTION

Tissue Engineering has been developed and applied widely recently for the ability to provide medical implantations which repair, maintain and promote the function and morphology of injured tissues or organs. As one of the keystrokes of tissue engineering, scaffolds are important for the following functions: directing the growth of cells migrating from surrounding tissue or of cells seeded within the porous scaffold and providing a substrate for cell attachment, proliferation, differentiated function and, in certain cases, cell migration; for an article cartilage/bone transplant, the scaffold must have the proper mechanical properties to support the normal physiological functions. Research on scaffolds has been a hot arena[1-5]. The structure of human bone is built up with multi-phase composites of cells. There are three kinds of main structural elements: cells which constitute functional units, the extra-cellular matrix (ECM) and bone scaffolds. Traditional materials such as metals, ceramics, polymers and composites are always exotic materials in the human body. Implants with these materials could only replace functions partially.

Traditional scaffold manufacturing technologies include fiber bonding, solvent casting, particulate leasing, membrane lamination, melt molding and emulsion freeze drying. These can hardly make customized scaffolds for different patients with specially designed functional

gradient structure including gradient material structure and gradient morphology structure. Those features of bone scaffolds are important for the regeneration of the structural tissue. After careful consideration, this paper presents PLLA/apatite/Collagen as a materials system for Rapid Prototyping and manufacturing of bone tissue engineering scaffolds[6-8]. This system has the ability to manufacture scaffolds with good bio-compatibility, bioactivity, higher strength and workability. Chemical reaction methods are put forward to deposit apatite coating on scaffolds. The hybrid structure of bone tissue engineering scaffolds was used in the PLLA/apatite/Collagen system, and this structure was made by rapid prototyping and manufacturing for bone tissue engineering scaffolds. Two kinds of collagen-apatite composites have been prepared with alkali reaction and mechanical mixing methods. Collagen has been coated on the surface of PLLA/TCP tissue engineering scaffolds through the vac-sorb method, and then apatite has been deposited on scaffolds with an unbalanced reaction method, thus a hybrid structure of PLLA/apatite/Collagen has been prepared. SEM observation shows that collagen sponges are adhered on the pores of the scaffolds and apatite is deposited on the collagen sponge. Tests show that the hybrid structure has good bio-compatibility.

In this paper, the rapid prototyping manufacturing (RPM) technology based on droplet assembly has been adopted. There are two important characteristics for this RPM technology: one is that bio-materials were deposited at low-temperature, and the other is that bio-materials were deposited droplet by droplet precisely[9-12]. This kind of bio-manufacturing method could be used in some other fields, and there are some other researches and applications[13-16]. We introduce different RP technologies in different applied fields of bio-manufacturing.

MATERIALS SYSTEM FOR BONE TISSUE ENGINEERING SCAFFOLDS AND ITS PREPARATION

Materials system

Fig. 1 is a list of some Materials of Bone Tissue Engineering Scaffolds. A scaffold should exhibit the following characteristics [1]: 1) three-dimensional and highly porous structure with an interconnected pore network for cell growth and flow transport of nutrients and metabolic waste; 2) biocompatibility and bioresorbability with a controllable degradation and resorption rate to match cell/tissue growth in vitro and /or in vivo; 3) suitable surface chemistry for cell attachment, proliferation, and differentiation; 4) mechanical properties to match those of the tissues at the site of implantation; and 5) ease of processing to form a variety of shapes and sizes.

Biodegradable biomaterials, poly(L-lactic acid) (PLLA), tricalcium phosphate (TCP) and their composites, have already been used to fabricate bone tissue engineering scaffolds by many different fabrication technologies including fiber bonding, solvent casting, particulate leaching, membrane lamination, melt molding, etc. PLLA grains with an average molecular weight of approximately 53,000 were kindly offered by Institute of Chemistry, Chinese Academy of Science. TCP powder was purchased from Forth Reagent Factory of Shanghai, China. Fig. 2 shows a Scaffold of large bone tissue engineering using rapid prototyping technology. Left is the

Carrier scaffold of PLLA/TCP with multi-pores on 3-D orthogonal directions (×30), and right is the Carrier scaffold of PLLA/TCP for dog radio-bone (×5).

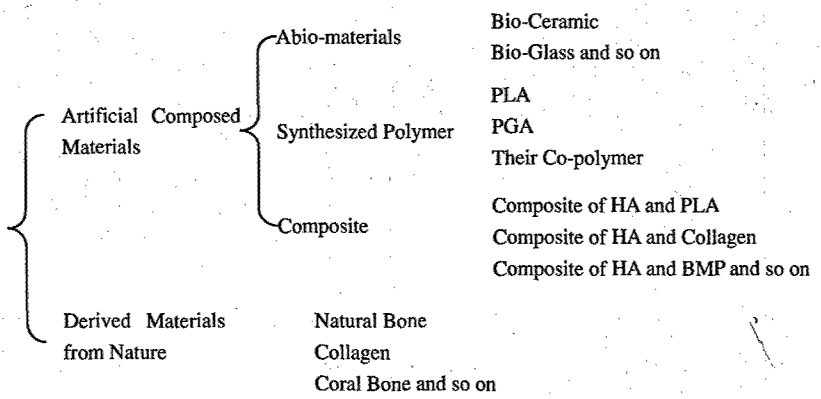

Figure 1. Materials of bone tissue engineering scaffolds.

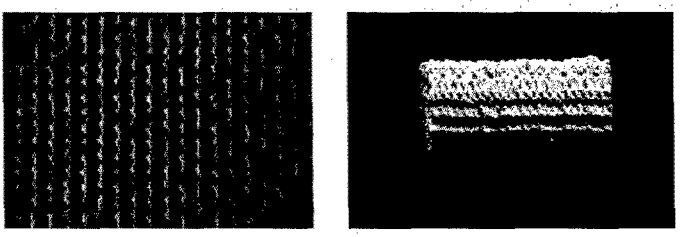

(a) (b)

Figure 2. Scaffold of large bone tissue engineering using rapid prototyping technology. (a) Carrier scaffold of PLLA/TCP with multi-pores on 3-D orthogonal directions (×30). (b) Carrier scaffold of PLLA/TCP for dog radial-bone (×5).

Surface coating processing

There are two methods of surface coating with tricalcium phosphate. In the first, PLLA is put into simulated body fluid (SBF), and then TCP is deposited onto its surface. This is a near-equilibrium chemical deposition process. In the second method, a film of scaffold material PLLA is made and put into solutions of TCP, where deposition occurs by means of non-equilibrium reaction (Fig. 3). The porous morphology of the scaffolds was studied by scanning electron microscopy at 20 kV. The dimension of macro pores is about 300~500 μm. There is micro porous structure around the macro pores. The average dimension of the micro pores is about 5 μm. It is shown that the minute TCP particles are embedded in the PLLA walls and can be distinguished.

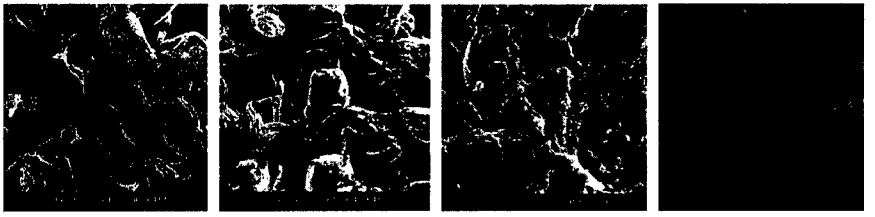

(a) (b) (c) (d)

Figure 3. Multi-pore structure of PLLA tissue engineering scaffold and the surfaces of the scaffold after dipping in solutions of TCP. (a) Horizontal section of the scaffold (×50). (b) Perpendicular section of the scaffold (×50). (c) Scaffold surface after 3 Days (×2500). (d) Scaffold surface after 10 days (×2500).

The PLLA film was cut into strips of 3 mm. Then, three kinds of solutions were obtained with $CaCl_2$ and $K_2HPO_4 \cdot 3H_2O$. Solution A was of 1.12M $CaCl_2$, solution B was of 0.56M K_2HPO_4, and solution C was of 0.28M K_2HPO_4. KOH was put into solutions B and C, so that the pH was about 14. A strip of PLLA was put into solution B for about 20 min, with the ratio of solid against liquid being 1:30 (w/v). Then, it was put into solution A with a ratio of solid against liquid of 1:50 (w/v) at 37 °C for a reaction time of 3 min, 5 min, 10 min, 15 min, 30 min, 1 h or 2 h respectively. The sample was then washed with de-ionised water. This is the so called Process B+A. Processes C+A and A+C were similar to this process. Three samples were obtained for each time. Fig. 4 shows SEM photos of processes B+A. The morphologies of this composite in different times for process B+A were as follows: there is no deposition in 3 min; there are some island-like depositions on the PLLA surface in 10 min; the surface is almost covered by deposition material in 2 h and the size of the deposited particles is about 1 μm. Fig. 5 is the evolution of the mole ratio of Ca/P in the mineralization processes for processes C+A and B+A. The difference is mainly in the first 1 h. Fig. 6 shows the morphology of the surfaces for process of B+A for 10 min. It is known that a pre-process of isopropanol is suitable for deposition of TCP.

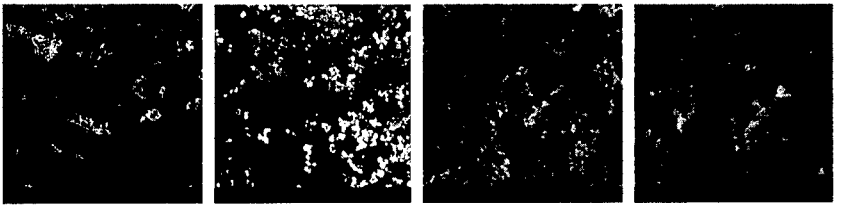

(a) (b) (c) (d)

Figure 4. Processes of B+A for: (a) 3 min (×3000); (b) 10 min (×3000); (c)2 h (×3000); (d) 2 h (×3000).

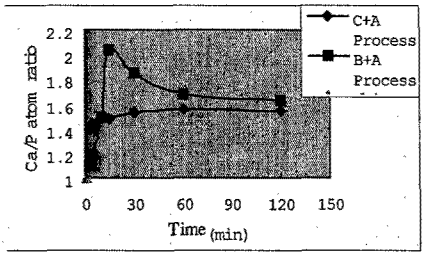

Figure 5. Evolution of mole ratio of Ca/P in the mineralization process.

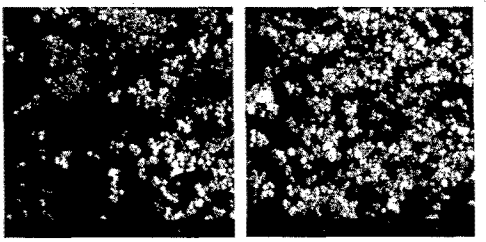

(a) (b)

Figure 6. Process of B+A for 10 min, (a) without pre-process of isopropanol (×3000), and (b) with pre-process of isopropanol (×3000).

FABRICATION BASED ON RP ADOPTED DROPLET ASSEMBLY

Introduction to manufacturing systems for bio-manufacturing

Four kinds of bio-manufacturing systems are built up in the Center of Laser Rapid Forming, Tsinghua university (Fig. 7). The fabrication methods for these four systems are based on RP adopted droplet assembly. There are a lot of different bio-materials for each bio-manufacturing system. Fig 7(a) is a platform for bio-manufacturing, and a lot of experimental results were obtained from this platform. For example, the particles of bio-materials could be deposited with their droplets transformed from solid state to liquid state based on a spraying technology. Fig 7(b) is the MedForm equipment. It is for repair a skull defects with polymers by means of melted extrusion modeling technology using bio-compatible materials. Fig. 7(c) is a desktop RP machine. It is for bio-manufacturing of ear bone for microtia patients. Microtia should be corrected or reconstructed with biomaterials, such as ultra-high molecular weight polyethylene, which is similar to the cartilage of ear. There are four nozzles on the TissForm system in Fig. 7(d). Droplets solidify and assemble at room temperature or low-temperature one by one. Three kinds of materials for bone tissue engineering scaffolds mentioned in this paper are provided and came from three nozzles.

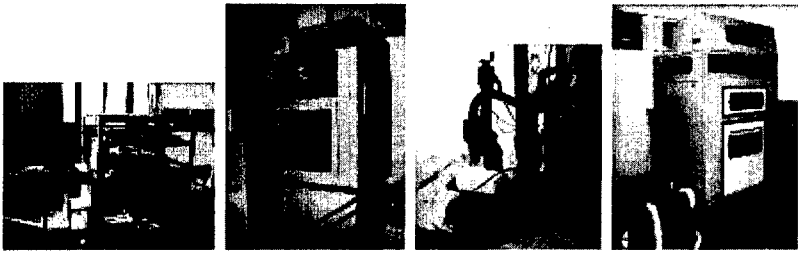

(a) (b) (c) (d)

Figure 7. Four kinds of bio-manufacturing systems in CLRF, Tsinghua: (a) Bio-manufacturing platform; (b) MedForm system for materials with biocompatibility; (c) Open bio-manufacturing system; (d) TissForm system for tissue engineering materials.

Bone tissue engineering process

The material slurry was formed into frozen scaffolds in a low-temperature deposition manufacturing (LDM) system. Fig. 8 shows the structure of the LDM system. First, the material slurry was fed into the material supply that has a soft pipe connected to a screw pump nozzle. The diameter of the outlet of the nozzle is 0.3 mm. The LDM system built scaffolds layer by layer, directly computer-driven by 3-dimensional digital models. This was accomplished in low temperature environment under 0 °C in the refrigerator. The computer controlled the nozzle to move in the X-Y plane, extrude the material slurry out and deposit it onto the platform in the area defined by the digital models. The layer of deposited materials was frozen on the platform. Also under the control of the computer, the platform moved down 0.15 mm in the Z direction after the forming process of each layer. In this manner, the frozen scaffold was stacked up layer by layer. To ensure the forming of the pores of the vertical cross section, the extruded material was deposited into a series of parallel lines along the Y direction from the 1st to the 3rd layer while moving parallel to the X direction from the 4th to 6th layer; the scanning direction of the nozzle alternated every 3 layers as shown in Fig. 9. By changing the number of layers between changes of scanning direction, and the distance between the parallel lines in each layer, the pore dimensions can be adjusted. After the forming process, the frozen scaffolds made by the LDM system were freeze-dried in an ALPHA1-2 Freeze dryer for 38 hours to remove the solvent. After treatment by freeze drying, the scaffolds are in the solid state in normal atmospheric temperature.

Cells culture

The porous matrices were placed in 96-well tissue culture plates 5 mm in diameter and 2 mm high. After being sterilized in 70% alcohol overnight, the matrices were rinsed extensively with distilled water and washed by PBS and Dulbecco's Modified Eagle Medium (DMEM) medium twice separately. L929 cell suspension was supplied by Jishuitan Hospital of Beijing. 100 µl L929 cell suspension at a density of cells 5×10^5 /ml DMEM medium was dropped into each well.

Then it was incubated in a humidified atmosphere with 37 °C, 5% CO_2. The culture medium was changed after 1.5 days. After 2.5 days incubation, the matrices were fixed with 2.5% glutaraldehyde in phosphate-buffered saline (PBS) overnight at 4 °C.

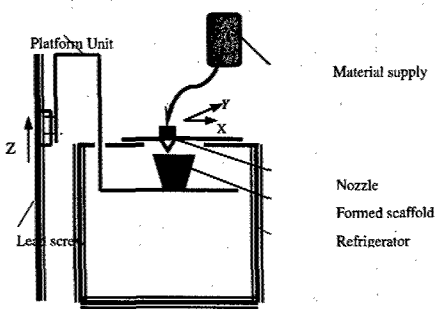

Figure 8. Schematic illustration of LDM.

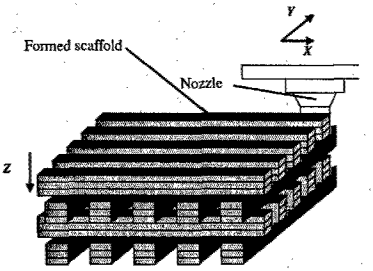

Figure 9. Illustration of the forming process of scaffolds in the LDM system.

After thoroughly washing with PBS, the cells were dehydrated by graded ethanol and critical point dried and examined by scanning electron microscopy (SEM). Table I shows the results of this experiment. The densities of different kinds of cells are almost the same. The densities of samples No. 3 and 4 are smaller a little, but the density for sample No. 2 is somewhat higher. The morphologies of cells growing on the surfaces of different materials were observed by microscopy. It is known that the growing conditions are good enough on surfaces of sample No. 1-5. It is concluded that these bio-materials have no toxicity. The adhesion and propagation of cells on the surfaces of materials are also good enough for samples of No. 1-5. But for the sample of pure PLLA (No. 6), the situation is different completely. There is no adhesion of cells on the surface of the material. This result shows that the bio-properties are improved for our material system.

Table I. Serial Numbers of Materials, Processing Methods and Cell Density

Number of Materials	1#	2#	3#	4#	5#	6#
Processing Method	No pre-processing, deposition in A for 15 min	No pre-processing, deposition in A for 80 min	No pre-processing, deposition in A for 12 h	Pre-processing in water, deposition in A for 10 min	Pre-processing with isopropanol, deposition in A for 50min	On pure PLA coating
Cell Density	5.6×10^5	6.0×10^5	3.9×10^5	3.2×10^5	5.0×10^5	4.9×10^5

CONCLUSIONS

Bone tissue scaffold technologies based on RP adopted droplet assembly were studied in this paper. In summary:

1. A new bio-material system was given for bone tissue scaffolds. This is the porous PLLA/TCP composite with BMP.
2. The fabrication technology of Multi-nozzle Deposition Manufacturing (MDM) was adopted to fabricate bone tissue engineered scaffolds in low temperature.
3. The cell culture experiments show that the bone scaffolds made by us have good bio-compatibility and bone conductive property as a molecular scaffold. It also gave good results in the implantation experiments for repairing segment defects in rabbits' and dogs' radiuses[11-12].

REFERENCES

1. Yongnian Yan, Renji Zhang, Fuzhai Cui and Qingping Lu, Jetting forming technology for tissue engineering materials of artificial human bone, China Mechanical Engineering, 2000, 11(10): 1116-1119.
2. Zhuo Xiong, Yongnian Yan and Renji Zhang, Rapid prototyping of bone tissue engineering scaffolds, in Proceedings of the 2nd national conference on tissue engineering of China, 2000, Guangzhou, p205.
3. Yongnian Yan, Fuzhai Cui, Renji Zhang and Yunyu Hu, Rapid Prototyping Manufacturing for artificial human bone, Materials Review, 2000, 14(2): 11-13.
4. Li Wang, Zhuo Xiong, Yongnian Yan and Renji Zhang, Analysis and realization of rapid prototyping for materials of bone tissue engineering, Materials Review, 2001, 15(11): 49—51.
5. Weiguo Zheng, Renji Zhang, Yongnian Yan, A Novel Method for Designing Gradient Tissue Engineering Scaffolds with Heterogeneous Materials, in Proceedings on 2002 International Bone Research Instructional Course & Hands-on Workshop, Hong Kong, Oct. 17-19, 2002.
6. Li Wang, Yongnian Yan, Renji Zhang, and Zhaolin Zhan, The research of the description and analysis way of materials in rapid prototyping process, J. Kunmin University of Science and Technology, 2001, 26(4): 55-58.
7. Hongyi Yang, Zhuo Xiong, Yongnian Yan and Renji Zhang. *The Structure and Properties of Porous Scaffolds for Bone Tissue Engineering Fabricated via Low-Temperature Deposition,* Progress in Rapid Prototyping and Rapid Manufacturing, in Proceedings of the 2nd International Conference on Rapid Prototyping Manufacturing, Beijing '2002, ed. Yongnian Yan, August 19-20, Beijing, p537-542.
8. Li Wang, Yongnian Yan, Renji Zhang, and Zhaolin Zhan, The research of the description and analysis way of materials in rapid prototyping peocess, J. Kunmin University of Science and Technology, 2001, 26(4): 55-58.
9. Zhuo Xiong, Yongnian Yan, Lifeng Chen and Renji Zhang, Two new rapid prototyping

technology for cell delivery scaffolds of bone tissue engineering, China Mechanical Engineering, 2001, 12(5): 515-518.

10. Zhuo Xiong, Yongnian Yan, Y. Yunyu Hu and Renji Zhang, *Layered Manufacturing of Tissue engineering Scaffolds via Multi-nozzle Deposition.* in Proceedings of the 1st Sino-Korean Conference on Advanced Manufacturing Technology, Eds. H. F. Shen and S. M. Xiong, Nov. 5-9, 2001, Beijing, China, pp148-154.
11. Zhuo Xiong, Yongnian Yan, Renji Zhang and Lei Sun, Fabrication of porous poly(L-lactic acid) scaffolds for bone tissue engineering via extrusion, Scripta Materialia, 2001, 45: 773-779.
12. Zhuo Xiong, Yongnian Yan, Shengguo Wang, Renji Zhang and Chao Zhang, Fabrication of porous scaffolds for bone tissue engineering via low-temperature deposition, Scripta Materialia, 2002, 46: 771-776.
13. Peng Qi, Hongtao Gao, Renji Zhang, Yongnian Yan, and Qingping Lu. *Data Processing in Rapid Prototyping of Medical Model*, Progress in Rapid Prototyping and Rapid Manufacturing, in Proceedings of the 2nd International Conference on Rapid Prototyping Manufacturing, Beijing '2002, ed. Yongnian Yan, August 19-20, Beijing, p559-562.
14. Li Wang, Yongnian Yan, Renji Zhang, and Zhaolin Zhan, The research of the description and analysis way of materials in rapid prototyping peocess, J. Kunmin University of Science and Technology, 2001, 26(4): 55-58.
15. Guangxin Tang, Renji Zhang and Yongnian Yan, *The MEM Forming Technology in Bio-medical Application*, Frontiers of Design and Manufacturing, Proceedings of the 5th International Conference on Frontiers of Design and Manufacturing (ICFDM 2002), Eds. Dongming Guo, 10-12, July 2002, Dalian, vol.2, pp301-304.
16. Tingchun Shi, Da Yuan, Renji Zhang, Yongnian Yan, and Qingping Lu. *Customized Rapid Manufacturing Bio-Functional Parts-Scaffold of Auricular Cartilage for Macrotia*, Progress in Rapid Prototyping and Rapid Manufacturing, in Proceedings of the 2nd International Conference on Rapid Prototyping Manufacturing, Beijing '2002, ed. Yongnian Yan, August 19-20, Beijing, p551-554.

Mat. Res. Soc. Symp. Proc. Vol. 758 © 2003 Materials Research Society LL5.2

Characterisation of Collagen Scaffolds using X-ray Microtomography

Patrick J. Smith, Eleftherios Sachlos[1], Samuel McDonald, Nuno Reis, Brian Derby, Paul M. Mummery and Jan T. Czernuszka[1]
Manchester Materials Science Centre, UMIST and University of Manchester, Grosvenor Street, Manchester, M1 7HS, England.
[1] Department of Materials, University of Oxford, Parks Road, Oxford, OX1 3PH, England.

ABSTRACT

Collagen scaffolds have been produced that incorporate predefined internal channels. The scaffolds were obtained with the aid of sacrificial moulds that have been manufactured using a rapid prototyping technique. A computer aided design file of the mould was created and then realised using an ink-jet printer. A dispersion of collagen was then cast into the mould and frozen. Ethanol was used to dissolve the mould leaving the collagen, which was then freeze dried to produce the final product. The scaffold was then analysed using X-ray microtomography (XMT) to determine whether the desired internal structure was obtained. It was found necessary to add saturated potassium iodide (KI) solution to the scaffold in order to analyse it satisfactorily by XMT. The resultant images indicate that the desired internal structure was obtained.

INTRODUCTION

The new multidisciplinary field of Tissue Engineering has arisen to satisfy the demand for biological substitutes to repair living tissue [1]. Tissue engineering involves the growth of relevant biological material into the required organ or tissue. However, unaided cells do not grow into the required orientations and therefore the resulting tissues are not of the correct shape. A solution is provided by the use of three-dimensional (3D) scaffolds acting as guides for cellular growth. Tissue engineered scaffolds are porous structures usually made from bioresorbable material containing appropriate factors to induce cell adhesion and growth. This allows the attached cells to migrate and colonise the whole scaffold. During the scaffold degradation, cells proliferate and occupy newly liberated spaces to create a viable tissue replacement [2].

Biodegradable and bioresorbable polymers and ceramics have been used to make 3D scaffolds [3 - 5]. Both synthetic and natural polymers have been used. The material used in this investigation is the natural polymer, collagen. Collagen is an abundant protein present in the connective tissue (and extra-cellular matrix in bone) of mammals.

Existing methods for scaffold fabrication are dependant on the generation of pores within the matrix; typical pore generators are salt particles and ice crystals. The distribution of pores however cannot be controlled precisely. As a consequence, current techniques cannot produce complicated internal features, e.g. channels that could act as an artificial vascular system. This internal system is desirable because it allows the flow of a blood-like medium throughout the construct, which supplies oxygen and nutrients to cells migrating deep into the scaffold.

Solid Freeform Fabrication (SFF), an outgrowth of Rapid Prototyping (RP), can have a great impact on tissue engineering by producing scaffolds with tailored architectures. SFF processes can deliver complex shapes with intricate internal features directly from computer-generated models [6]. In this paper, an inkjet printing technique has been used to produce a 3D

mould, which is the negative shape of the desired scaffold. The collagen scaffolds were then made by freezing an aqueous dispersion of collagen inside the sacrificial mould. This results in the nucleation of ice crystals, which grow and force the collagen into the interstitial spaces, thereby aggregating the collagen. The ice crystals are removed by sublimation using a conventional freeze-drying technique.

As-produced collagen scaffolds have been analysed using X-ray microtomography [7-9]. This technique is favourable as it is non-destructive and also enables 3D analysis from a set of cross-sections. Techniques such as scanning electron microscopy and mercury porosimetry are destructive and only provide two-dimensional information that may not be representative of the whole construct. This paper reports the results of using X-ray microtomography to analyse 3D collagen scaffolds.

EXPERIMENTAL

The preparation of the collagen scaffolds used in this study is described in greater detail elsewhere [2]. Briefly, moulds with the required negative-shape, were designed using commercial CAD software and manufactured using the commercial SFF system, Model-Maker II (Solidscape Inc. Merrimack, NH, USA). Figures 1 and 2 show the mould design used to make the collagen scaffolds and relevant cross-sectional areas of the mould respectively.

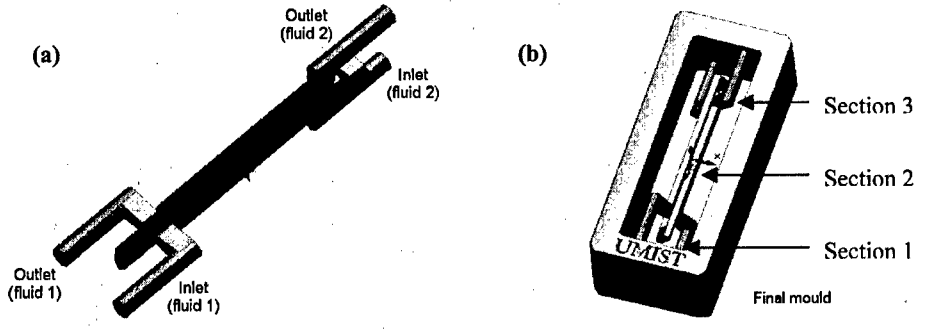

Figure 1. The mould design used to make the collagen scaffolds, (a) shows the internal channel structure and (b) the final mould indicating cross-sections of interest; these are shown in diagrammatical form in Figure 2.

The build material used in the mould was a proprietary low molecular weight polar material (ProtoBuild, Solidscape Inc.). A collagen dispersion was then cast into the mould and frozen at about –20 °C. The mould was then immersed in ethanol, which dissolved the mould and the ice crystals. The collagen scaffold was then dried after solvent exchange with liquid carbon dioxide. Figure 3 shows a typical mould and the collagen scaffold produced. Subsequent moulds produced for this study were doped with KI and methylene blue dye. The collagen scaffolds were also doped with an aqueous saturated potassium iodide (KI) solution.

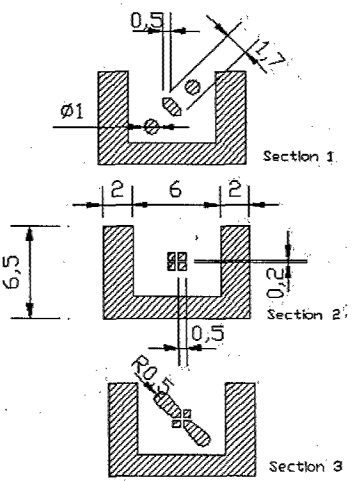

Figure 2. Cross sections of the mould design, which provides details of the desired internal structure. (All dimensions are in millimetres.)

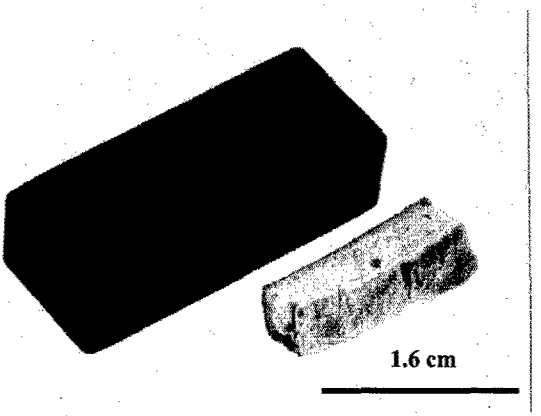

Figure 3. A typical Model Maker II produced mould next to a typical collagen scaffold.

The X-ray microtomographic system (XMT) used in this study was a HMX-225 radiography platform (X-Tek, Tring, UK) run under Tomahawk tomography software (AEA Technology, Harwell, UK). The XMT works by placing a specimen in the path of X-rays. The specimen can be rotated and also translated perpendicularly to the X-ray beam. In tomographic imaging, a number of absorption profiles of the specimen are captured using a cone projection for a complete rotation of the sample. Typically, a radiograph is taken every 0.5°. From these data, the 3D image can be reconstructed using a standard filtered back-projection algorithm [7]. The system allows the X-ray voltage and current to be varied independently.

RESULTS AND DISCUSSION

Initial observations of collagen scaffolds using XMT were disappointing due to poor contrast because of collagen's low X-ray absorption. Subsequently a doping regime was employed to enable the scaffolds to be detected using XMT. This involved applying a few drops of a saturated KI solution onto a collagen scaffold, which caused the scaffold to reduce in volume by approximately 50%. The necessary addition of the KI solution introduced surface tension forces that caused the collapse of the fragile pore structure. Figure 4 shows the images of slices taken in the *xy* direction of the KI doped collagen scaffold. When these two images are compared with the diagram in Figure 2 it can be clearly seen that Figure 4a corresponds with Section 3 in the diagram and Figure 4b corresponds with Section 1. That is to say that the scaffold has the desired internal structure.

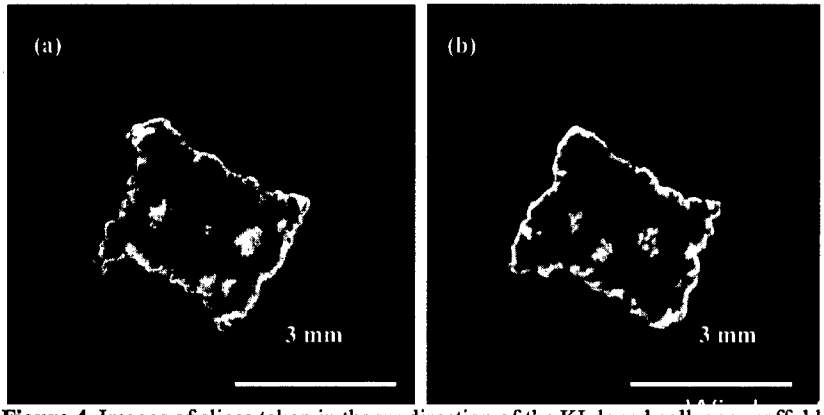

Figure 4. Images of slices taken in the xy direction of the KI doped collagen scaffold; (a) corresponds to section 3 and (b) corresponds to section 1 in Figure 1 respectively.

These images are encouraging; however further examination of Figure 4a and the design for Section 3 in Figure 2 shows a small mismatch. Section 3 consists of four discrete channels, whereas Figure 4a suggests that the channels have collapsed in on one another. It is thought that this apparent "merger" of channels is an effect of the KI doping. In the preparation of the collagen scaffolds great care is taken to protect the scaffolds from water. This is because the surface tension of the water would cause the collapse of the delicate porous structure [2]. However, in order to obtain XMT images it was necessary to add an aqueous solution of KI. Therefore, the above images actually show the dispersal of KI throughout the collagen matrix. Looking again at the diagram of Section 3 in Figure 2, it can be seen that the collagen separating the four chambers is very thin. It is thought that this area of the matrix has not absorbed any KI and therefore has not been detected by XMT. This is coupled with the collapse of porosity and the reduction in volume of the collagen scaffold. Figure 5 shows images taken in the *xy* direction of the scaffold corresponding to Section 2.

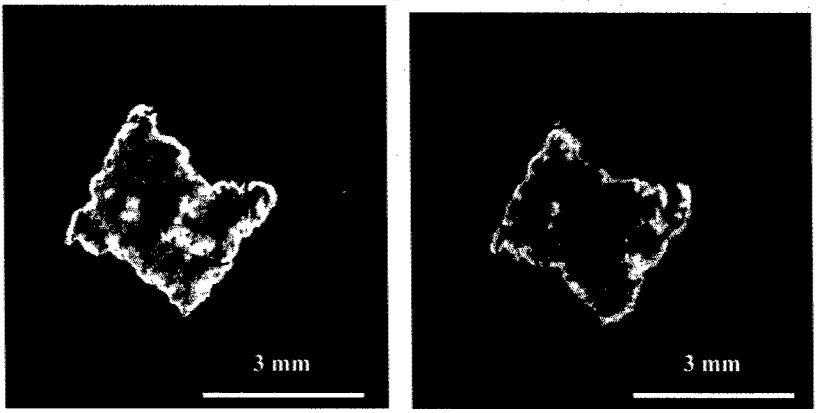

Figure 5. Images of slices taken in the *xy* direction of the KI doped collagen scaffold corresponding to section 2 in Figure 2.

It can be seen that the internal structure observed is a reasonable approximation to that expected. There is a lack of segregation between the four channels observed and it is thought this is due to the reasons stated.

Figure 6 show images of slices taken in the *xz* plane. It can be clearly seen that the desired internal structure has been obtained.

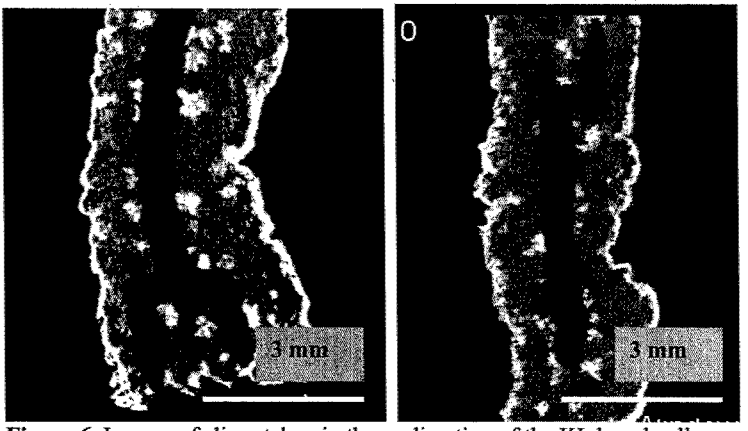

Figure 6. Images of slices taken in the *xz* direction of the KI doped collagen scaffold corresponding to section 2 in Figure 1.

This analysis shows that the collagen scaffolds do have the internal structure that has been designed for them. However, the necessary addition of KI solution has made those scaffolds that were analysed unusable. Various dopants were added in the preparation stage in order to remove the destructive step of aqueous KI solution addition, including KI itself. However, none of these dopants were detected by XMT.

CONCLUSION

Collagen scaffolds have been prepared using SFF produced moulds. The moulds incorporated a complex internal network of channels, which are necessary to the final function of the collagen structure. The scaffolds were analysed using XMT to determine whether the desired internal structure had been produced. Initially the scaffolds could not be imaged using XMT. This necessitated the addition of saturated KI solution. This enabled the scaffolds to be imaged. It could clearly be seen that the collagen scaffold has the internal structure that was designed.

ACKNOWLEDGEMENTS

The authors would like to thank EPSRC for provision of the XMT facility.

REFERENCES

1. R. Langer and J.P. Vacanti, *Science*, **260**, 920 (1993)
2. E.Sachlos, N. Reis, C. Ainsley, B. Derby and J.T. Czernuszka, *Biomaterials* (Accepted for publication)
3. B. Muller, F. Beckmann, M. Huser, F. Maspero, G. Szekely, K. Ruffieux, P. Thurner and E. Wintermantel, *Biomolecular Engineering*, **19**, 73 (2002)
4. J.L.C. van Susante, J. Pieper, P. Buma, T.H. van Keppevelt, H. van Beuningen, P.M. van der Kraan, J.H. Veerkamp, W.B. van den Berg and R.P.H. Veth, *Biomaterials*, **22**, 2359 (2001)
5. R. Landers, U. Hubner, R. Schmelzeisen and R. Mulhaupt, *Biomaterials*, **23**, 4437 (2002)
6. C. Ainsley, N. Reis, and B. Derby, *Seventh European Ceramics Conference Proceedings*, pg 297 (2001)
7. P.M. Mummery, B. Derby, P. Anderson, G.R. Davies and J.C. Elliott, *Journal of Microscopy*, **177**, 399 (1995)
8. R.C. Barroso, R.T. Lopes, E.F.O. de Jesus and L.F. Oliveira, *Nuclear Instruments & Methods in Physics Research A*, **471**, 75 (2001)
9. J.C Elliot, P. Anderson, G. Davies, S.D. Dover, S.R. Stock, T.M. Breunig, A. Guvenilir and S.D. Antolovich, *Journal of X-ray science and technology*, **2**, 249 (1990)

Mat. Res. Soc. Symp. Proc. Vol. 758 © 2003 Materials Research Society LL5.3

A Process to Make Collagen Scaffolds with an Artificial Circulatory System using Rapid Prototyping

Eleftherios Sachlos[1], Nuno Reis[1,2], Chris Ainsley[2], Brian Derby[2] and Jan T. Czernuszka[1]
[1]Department of Materials, University of Oxford,
Parks Road, Oxford, OX1 3PH, U.K.
[2]Manchester Materials Science Centre, University of Manchester and UMIST,
Grosvenor St, Manchester, M1 7HS, U.K.

ABSTRACT

Tissue engineering aims to produce biological substitutes to restore or repair damaged human tissues or organs. The principle strategy behind tissue engineering involves seeding relevant cell(s) onto porous 3D biodegradable scaffolds. The scaffold acts as a temporary substrate where the cells can attach and then proliferate and differentiate. Collagen is the major protein constituent of the extracellular matrix in the human body and therefore an attractive scaffold material. Current collagen scaffolds are foams which limit the mass transport of oxygen and nutrients deep into the scaffold, and consequently cannot support the growth of thick-cross sections of tissue (greater than 500 μm). We have developed a novel process to make collagen and collagen-hydroxyapatite scaffolds containing an internal artificial circulatory system in the form of branching channels using a sacrificial mould, casting and critical point drying technique. The mould is made using a commercial rapid prototyping system, the Model-Maker II, and is designed to possess a series of connected shafts. The mould is dissolved away and the solvent itself removed by critical point drying with liquid carbon dioxide. Processed hydroxyapatite has been characterised by XRD and FTIR analysis. Tissue engineering with collagen scaffolds possessing controlled internal microarchitecture may be the key to growing thick cross-sections of human tissue.

INTRODUCTION

Tissue engineering has the potential to significantly improve clinical treatment of damaged human tissue, currently based on organ transplantation and biomaterial implantation, by producing an unlimited supply of immunologically-tolerant 'biological substitutes' that can repair or replace the defect site and grow with the patient. One of the strategies employed involves the expansion of human cells in vitro on biodegradable porous scaffolds. This serves as a substrate for cellular attachment and defines the macroscopic shape of the engineered tissue [1]. Proliferating cells are expected to occupy the freed space created during scaffold degradation and eventually produce a completely natural tissue.

Most scaffolds used for tissue engineering are open-cell foam structures which have resulted in the growth of thin cross-sections of tissue. For example, bone has been grown in vitro to a thickness of 370-500μm [2, 3]. The small cellular penetration depth of scaffolds may be due to the lack of nutrient and oxygen diffusion deep into the interior of the scaffold; cell colonisation of the scaffold's periphery can become a barrier, or limit, to the diffusion of these essential components. Thus cell migration and survival deep inside the scaffold is hindered.

Rapid prototyping (RP) can impact on tissue engineering by producing scaffolds with an internal artificial circulatory system which can overcome the diffusion constraints of the foam-

structured scaffolds. 3D Printing has been used to prepare poly(glycolic-co-lactic) acid scaffolds with interconnected networks of channels allowing the dynamic culturing of hepatocytes [4]. Polycaprolactone has been extruded using fused deposition modelling and produced honeycomb-like scaffolds used for the culture of bone and cartilage [5]. Similar structures have been manufactured with the 3D Bioplotter™ using alginate and fibrin to create hydrogel scaffolds [6]. Hydroxyapatite (HA) scaffolds with a series of radial and orthogonal interconnected channels have been made directly with stereolithography, using HA-loaded photocurable resin [7], or indirectly by casting HA-acrylate suspension into moulds made with stereolithography [8]. However, collagen scaffolds have yet to be made using RP technology.

Collagen is the major protein constituent of the human extracellular matrix and possesses a surface that favours attachment [9], morphology, migration and in certain cases the differentiation of cells [10]. We report a novel process to create collagen scaffolds with an artificial circulatory system which is defined by RP technology. Collagen and collagen-HA composite scaffolds have been manufactured.

EXPERIMENTAL DETAILS

Dispersion formulation

Collagen type I from bovine Achilles tendon (Sigma-Aldrich) was added to 0.05M acetic acid aqueous solution, with pH adjusted to 3.2 by the dropwise addition of 0.5M sodium hydroxide, to yield a 1%w/v concentration. The dispersion was homogenised on ice for 90s using a conventional blender, and then exposed to a vacuum of 1mbar at room temperature for 20min using a vacuum oven (Vacuum Oven, Gallenkamp). The dispersion was stored at 4°C in a refrigerator (ER7610C, Electrolux) until required. HA particles (Captal® 60-1, Plasma Biotal) were added to the collagen dispersion and mixed to uniformly distribute the particles.

The process

Sacrificial moulds, designed using commercial CAD software, were printed with the Model-Maker II (Solidscape Inc). The proprietary materials, ProtoBuild™ and ProtoSupport™, were used to create the mould and support structures, respectively. The support material was removed by immersion in the proprietary solvent, BioAct™, for 30min at 50°C aided by gentle stirring. The moulds were then washed with water and air-dried.

Collagen or collagen-HA dispersion was then cast into the mould and submitted to -20°C in a freezer (EU7120C, Electrolux) for 24h. The samples were then immersed in ethanol for 3h and transferred to a critical point drier (E100, Polaron). There, the ethanol was exchanged with liquid carbon dioxide (CO_2) at 15-18°C and a pressure of 50bar for 3h before the temperature was increased to 33-36°C, which turned the liquid CO_2 into gaseous CO_2 that was then slowly released from the chamber.

Internal scaffold morphology

Moulds containing frozen collagen and collagen-HA were immersed in liquid nitrogen for several seconds and sectioned with a sharp razor blade to reveal the interior. Samples were then dehydrated in ethanol for 3h and critical point dried for 3h. The sections were then gold-sputter

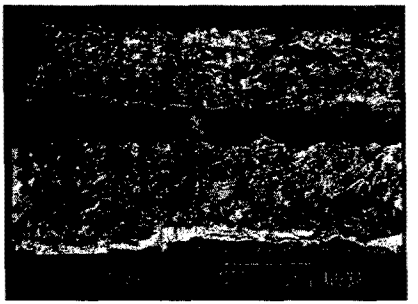

Figure 1. Secondary electron image of processed collagen scaffold with channel running horizontally.

coated (E5400, Biorad, Polaron Division) for 180s. A SEM (JSM-840F, JEOL) operated at 2.5kV was used to image the sectioned surface.

HA characterisation

HA powder (Captal® 60-1, Plasma Biotal) was immersed in ethanol for 3h and critical point dried for 3h. The powder was analysed before and after processing with X-ray diffraction and Fourier transform infrared spectroscopy. The X-ray diffractometer (PW1710, Philips) was operated at 35kV and a current of 50mA. Samples were scanned from 15-60° (2θ) at a step size of 0.02° (2θ) and time per step of 1s. HA samples for FTIR analysis were mixed with ground potassium bromide powder and pressed into 13mm discs. Samples were analysed in transmission using a FTIR spectrometer (Spectrum 2000 Explorer, Perkin-Elmer) at a resolution of $2cm^{-1}$ and 64 scans.

RESULTS

Figure 1 shows a secondary electron SEM image of a collagen scaffold after processing. The channel running through the full length of the scaffold is approximately 400μm in width.

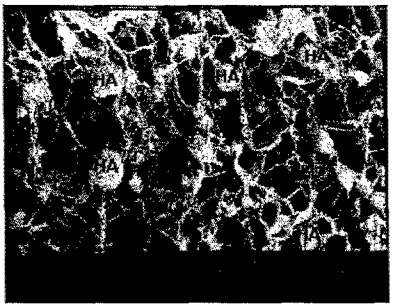

Figure 2. Secondary electron image of scaffold showing interconnecting porosity of collagen matrix and hydroxyapatite (HA) particles.

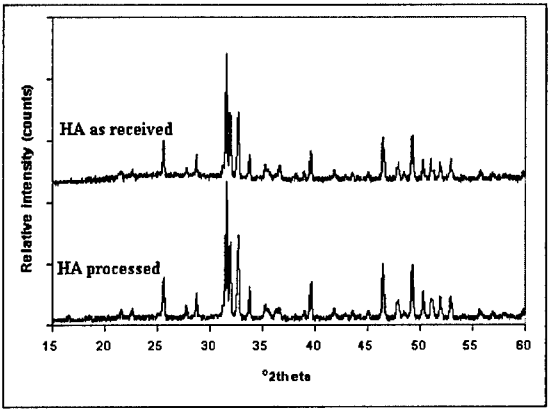

Figure 3. XRD spectra of hydroxyapatite as received and after processing. The same HA peaks are evident in both spectra.

The collagen is organised into an open-cell pore structure as shown in figure 2. Furthermore, HA particles added to the collagen dispersion are also present after processing and randomly distributed throughout the scaffold. XRD analysis of processed HA particles exhibited no change in the spectrum compared to the material as received from the manufacturer as shown in figure 3. Furthermore, FTIR analysis of processed HA particles revealed the phosphate v_1, v_2, v_3, v_4 and hydroxyl stretching peaks of HA are present and at their characteristic wavenumbers as shown in figure 4. A CO_2 peak at 2300-2400cm^{-1}, absent in the spectrum of HA as received, is evident in the spectrum of processed HA.

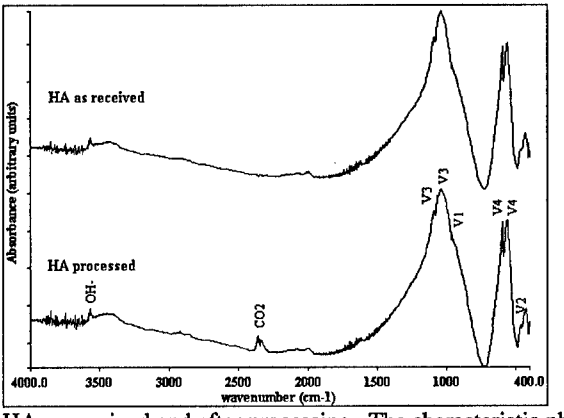

Figure 4. FTIR of HA as received and after processing. The characteristic phosphate v1, v2, v3, v4 peaks of HA are labelled accordingly. Processed HA reveals a CO_2 peak at 2300-2400cm^{-1}.

DISCUSSION

The process, presented in this paper, is able to create collagen scaffolds with controlled internal channels as shown in figure 1. The channels are intended to act as an artificial circulatory system by permitting the flow of nutrient-rich medium and supporting the migration and survival of cells deep into the scaffold. The channels have smaller dimensions compared to the mould shafts used to define them [11]. This shrinkage of the collagen matrix is due to critical point drying with liquid CO_2 [11, 12].

Processing does not effect the tertiary structure of collagen [11]. Therefore, processed collagen should retain its natural functions, such as cell attachment properties, as these are highly dependent on protein structure. This however remains to be examined.

Freezing the aqueous component of the collagen dispersion results in the formation of ice crystals that aggregate the collagen into the interstitial spaces to create an open-cell pore structure [14] as shown in figure 2. However, the mould and ice crystals need to be removed to expose the internal structures and this is achieved by dissolving in ethanol. Collagen is insoluble in ethanol. The ethanol solvent need to be removed in order to crosslink, rehydrate and prepare the scaffold for cell culturing. Critical point drying with liquid CO_2 serves such a purpose.

For bone tissue engineering, HA particles can be added to the collagen dispersion, as these are the components that make up the natural extracellular matrix of bone. Figure 2 shows such a composite scaffold. The collagen and HA should provide an environment familiar and favourable for the growth of osteogenic cells. Processing does not alter the HA phase. XRD analysis did not detect any phase change in HA after processing as shown in figure 3. Furthermore, FTIR analysis revealed no evidence of changes in the characteristic peaks assigned to HA as shown in figure 4. However, a new peak attributed to CO_2 was revealed after processing. This may be due to the CO_2 used for critical point drying or environmental CO_2 present while acquiring the spectrum.

The greatest challenge facing the technology is whether residual mould material is present on the collagen scaffold after processing. This is currently being investigated using electron probe microanalysis. Research efforts are also aimed at printing a biocompatible mould material, which would eliminate any fears of possible mould residues. The biological performance of these processed collagen and collagen-HA scaffolds still remains to be examined.

CONCLUSIONS

We have developed a process to make collagen or collagen-hydroxyapatite scaffolds with an artificial circulatory system. Moulds made using rapid prototyping technology define the internal and external morphology of the scaffolds. Mould removal is achieved by chemical dissolution and the solvent is removed by critical point drying with liquid carbon dioxide. Channels with predefined dimensions and shape are incorporated into the open-celled collagen scaffold. Composite scaffolds compromising of collagen and hydroxyapatite can also be produced. The process does not alter the phase of hydroxyapatite particles.

ACKNOWLEDGEMENTS

E Sachlos would like to thank the Bodossaki Foundation, Athens, Greece and Department of Materials, University of Oxford for financial support. Also, John Forsdyke for his technical assistance and Prof P Dobson, Department of Engineering, University of Oxford, for use of his critical point drier. We would like to acknowledge the EPSRC through grants GR/N13784 and GR/R20242.

REFERENCES

1. R. Langer, J.P. Vacanti. *Science* **260**, 920-926 (1993).
2. S.L. Ishaug-Riley, G.M Crane, A. Gurlek, M.J. Miller, A.W. Yasko, M.J. Yaszemski, A.G. Mikos. *J Biomed Mater Res* **36**, 1-8 (1997)
3. L.E. Freed, G. Vunjak-Novakovic. *Adv Drug Deliver Rev* **33**, 15-30 (1998).
4. S.S. Kim, H. Utsunomiya, J.A. Koski, B.U. Wu, M.J. Cima, J. Sohn, M. Mukai, L.G. Griffith, J.P Vacanti. *Ann Surg;* **228**, 8-13 (1998).
5. D.W Hutmacher, T. Schantz, I. Zein, K.W. Ng, S.H. Teoh, K.C Tan. *J Biomed Mater Res*, **55**, 203-216 (2001).
6. R. Landers, U Hübner, R. Schmelzeisen, R. Mülhaupt. *Biomaterials*, **23**, 4437-4447 (2002).
7. R.A. Levy, T.G.M. Chu, J.W Halloran, S.E. Feinberg, S. Hollister. *Am J Neuroradiol*, **18**, 1522-1525 (1997).
8. T.M.G. Chu, D.G. Orton, S.J. Hollister, S.E. Feinberg, J.W. Halloran. *Biomaterials*, **23**, 1283-1293 (2002).
9. A.E. Postlethwaite, J.M. Seyer, A.H. Kang. *Proc Natl Acad Sci USA*, **75**: 871-875 (1978).
10. H.K. Kleinman, R.J. Klebe, G.R. Martin. *J Cell Biol*, **88**, 473-485 (1981).
11. E. Sachlos, N. Reis, C. Ainsley, B. Derby, J.T. Czernuszka. *Biomaterials*, **24**, 1487-1497, (2003).
12. N. Dagalakis, J. Flink, P. Stasikelis, J.F. Burke, I.V. Yannas. *Biomaterials*, **1**, 511-528 (1980).
13. C.J. Doillon, C.F. Whyne, S. Brandwein, F.H. Silver. *J Biomed Mater Res*, **20**, 1219-1228 (1986).

Mat. Res. Soc. Symp. Proc. Vol. 758 © 2003 Materials Research Society LL5.6

Biochemical IC Chips Fabricated by Hybrid Microstereolithography

Koji Ikuta, Shoji Maruo, Tadahiro Hasegawa, Takao Adachi, Atsushi Takahashi, Kota Ikeda
Department of Micro System Engineering, Graduate School of Engineering, Nagoya University
Furo-cho, Chikusa-ku, Nagoya 464-8603, Japan

ABSTRACT

The world's first microstereolithography named "IH process" was developed by Ikuta et al. in 1992. Several types of micro stereo lithography including Hybrid-IH process, Super-IH process and Two-photon IH process, have been also developed. Three-dimensional (3D) resolution has reached to 140 nm in the two-photon IH process. The super-IH process and the two-photon process enable direct writing of movable micromechanisms without assembling process or sacrificial layer technique. The hybrid-IH process provides various types of composite devices with other functional elements such as actuators and sensors. These IH processes can be widely used for making polymeric microdevices. We have applied these techniques to create new micro chemical device named "Biochemical IC Chip" proposed by Ikuta et al. in 1994. IH process enables to make the biochemical IC chip including real 3D micro fluidic channels. Various kinds of Biochemical IC chip such as micro pumps, switching valves, reactors, concentrators, have already been fabricated. In chip cell-free protein synthesis has been demonstrated by using biochemical IC chips. The biochemical IC chips will open new bioscience and medicine based on innovative technology. In this paper, we introduce several types of IH process and its application to biochemical IC chips.

INTRODUCTION

Conventional micromachining such as surface micromachining and LIGA process have been widely used to make various kinds of sensors and actuators. However, these methods have some limitations on fabrication of 3D microdevices demanded in recent applications such as micro total analysis systems (μ-TAS) and lab-on-a-chip devices. On the other hand, we have developed several types of microstereolithography to make truly 3D microstructures. The world's first microstereolithography system called "IH process" was proposed and developed by Ikuta and Hirowatari in 1993 [1]. The IH process made possible the layer-by-layer process of 5 μm thickness with modifications to both the optical system and the characteristics of photopolymer. In 1996, mass productive microstereolithography named "Mass-IH process" was proposed and demonstrated [2]. Since this process uses an array of optical fibers to obtain multi-beam scanning with high accuracy, we can fabricate real 3D microstructures under mass and low cost production similar to silicon process. To fabricate functional microdevices, we have developed two-types of IH process named "Hybrid-IH process" and "Multi-polymer IH process". The hybrid-IH process provides a composite microdevice with functional elements such as chemical microparts and actuators [3, 4]. The multi-polymer IH process can produce all-polymer microdevices such as optical waveguides and microvalves using multiple kinds of photopolymer [5].

Conventional microstereolithography systems developed by us and other groups are based fixed surface methods [1, 6] and free surface methods [2-5, 7]. Since these techniques used a layer-by-layer process, the depth resolution and yield rate are limited due to the surface tension and viscosity of piling photopolymer layer. To improve both the resolution and yield rate of microstereolithography, we proposed a novel method named "Super-IH process" [8]. This

method is based on pinpoint inner solidification, which is generated by focusing a blue laser beam inside a liquid photopolymer [9]. 3D scanning of the laser beam permits the fabrication of any 3D microstructure without layer-by-layer processes. The 3D resolution has attained to 430 nm in our latest fabrication system [10]. To obtain further higher resolution and yield rate, two-photon IH process was recently developed [11-15] and subsequently refined by other groups [16, 17]. In the two-photon IH process, a near infrared pulsed laser beam is used to generate two-photon-initiated polymerization, in contrast to UV or blue laser beam used in conventional microstereolithography. Since the rate of two-photon absorption is proportional to the squared intensity of light, the polymerization is strictly confined to a focal point. The resolution of the two-photon IH process attains to 140 nm in our latest fabrication system [18]. The two-photon IH process is also utilized for assembly-free, single-step fabrication of freely movable micro/nano structures [5, 15, 18, 19].

For the practical use of these microstereolithography techniques, we have developed a versatile microfluidic device named "Biochemical IC Family". The biochemical IC chip was proposed by Ikuta et al [20]. Several types of biochemical IC chips including a reactor [21], concentrator [3], homogenizer [22] and active valve and micro pump [4] have been already developed. Recently, in-chip cell-free protein synthesis was demonstrated by using biochemical IC chips [23, 24]. The palm-top protein synthesis devices are promising and powerful tools for not only order-made medicine but also implantable/wearable medical devices in the near future.

MICROSTEREOLITHOGRAPHY

IH process (The world's first microstereolithography)

We proposed and developed the world's first microstereolithography named "IH Process (Integrated Harden Polymer Stereo-Lithography)" [1]. The fabrication principle of the IH process is based on the stereolithography which is used to make 3D mock-up model in macro size. Fig.1 shows the schematic diagram of fabrication apparatus. This system consists of an UV (ultra violet) lamp, XYZ-stage, shutter, lens and computer. To make a 3D microstructure, thin sliced cross sectional shapes of the final product are drawn by UV beam focused on photopolymer through transparent Z-stage. The cross sectional layers are piled up to fabricate the 3D microstructure. Fig. 2 show scanning electron microscope (SEM) images of a bending pipe (100 x 100 x 1000 μm) and a micro coil spring (diameter: 50 μm, length is 350 μm). The 3D resolution of this process attained to 5 μm in lateral and 3 μm in depth.

Unique features of the IH process were as follows: 1) Real 3D structure, 2) High aspect ratio, 3) Simple and low cost apparatus 4) Micrometer resolution etc. These features are much superior than conventional micromachining methods. The IH process has a great potential for various fields of applications.

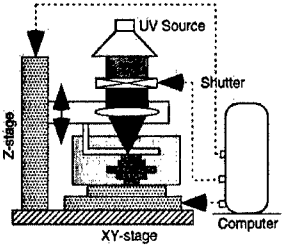

Fig. 1 Schematic diagram of IH process

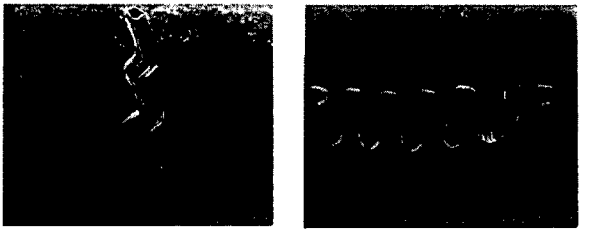
(a) (b)

Fig. 2 3D microstructures made by IH process
(a) Bending pipe (b) Micro coil spring

Mass-IH Process

To improve the mass productivity of microstereolithography, we have developed a method named "Mass-IH Process" [2]. Fig. 3 shows the fabrication system of the mass-IH process. The main technology is the newly developed "Optical fiber Multi-beam scanning" which can satisfy both simultaneous scanning and uniform accuracy on all area. The array of optical fibers (4μm in core diameter) allows the multi-beam scanning. Fig. 4 shows a sample of 3D microstructures fabricated simultaneously. Five micro pipes (220 μm squire, 1150 μm high) with lateral windows were made within 40 minutes. Although the resolution at this time is not high compared to that of the IH process, feasibility as mass productive microstereolithography was verified. Increasing number of fibers and optimizing experimental conditions enable further mass productivity and higher resolution.

Super-IH process

Since conventional microstereolithography systems employ layer-by-layer process, the depth resolution is limited by surface tension and viscosity of photopolymers. To overcome the limitation caused by the layer-by-layer process, we proposed a new method named "Super-IH process" that was based on pinpoint inner solidification by using a tightly focused laser beam [8]. Fig.5 shows the fabrication principle of the super-IH process. The liquid photopolymer is solidified only at the vicinity of the focus, although that is solidified at the surface in the conventional method. By scanning the focus along the shape of the desired structure, any 3D microstructure can be made.

The pinpoint inner solidification results from the nonlinear response of photo polymerization to optical intensity with sufficiently low exposure [9, 10]. It is well known that the liquid/solid transformation of photopolymer is approximated by the threshold system. The photopolymer is not solidified unless the optical exposure exceeds the critical exposure. Accordingly, when a laser beam is highly focused inside photopolymer with optimum exposure conditions, the intensity near the focus is sufficient to solidify the photopolymer, even though the intensity is insufficient at out-of focus regions.

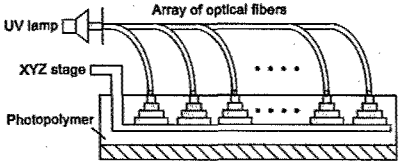

Fig. 3 Schematic diagram of Mass-IH process

Fig. 4 Micropipes made by Mass-IH process

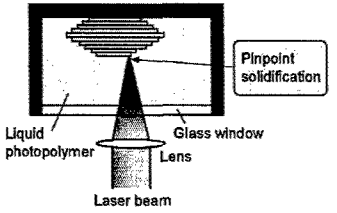

Fig. 5 Fabrication principle of Super-IH process

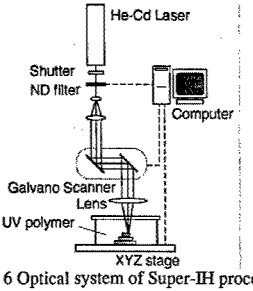

Fig. 6 Optical system of Super-IH process

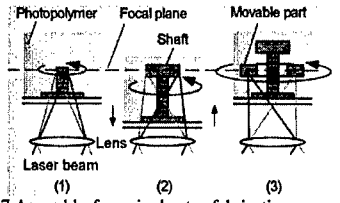

Fig. 7 Assembly-free, single-step fabrication process of movable microstructures


Fig. 8 Microgear made by Super-IH process

Fig. 6 shows a schematic diagram of our fabrication system, which consists of an He-Cd laser (Wavelength: 442nm), shutter, galvano scanners, xyz-stage, and objective lens (N. A.: 1.0 or 1.3). The beam from the laser is introduced into the galvano-scanner set to deflect its direction in two dimensions, and then is focused into the liquid photopolymer with the objective lens. As the beam scans laterally in the liquid photopolymer and the sample-cell stage vertically slides, any 3D structure can be formed in the photopolymer volume. The resolution of our latest fabrication systems attained to 430 nm [10].

The most important feature of the super-IH process is assembly-free, single-step fabrication of movable micromechanisms. In major microfabrication techniques such as surface micromachining and the LIGA process, sacrificial layers are indispensable to make a movable mechanism [25]. Even stereolithography needs supporting columns to hold movable components. On the other hand, the super-IH process requires neither sacrificial layers nor supporting columns, since movable microstructures can be fabricated merely by scanning a focus inside photopolymer as shown in Fig. 7. Fig. 8 shows an SEM image of movable microgear fabricated by the Super-IH process. A microgear (diameter: 47 μm) with an attached shaft was successfully fabricated.

Two-photon IH process

For the further improvement of resolution, we have developed two-photon IH process [11-14]. In the two-photon IH process, a liquid photopolymer absorbs two photons of near infrared simultaneously in a single quantum event whose energy corresponds to the UV region. The rate of two-photon absorption is proportional to the squared intensity of light. Accordingly, near infrared light is strongly absorbed only at the focal point within the photopolymer. This virtue of the two-photon process enables us to fabricate a 3D microstructure by scanning a focus inside the photopolymer.

The fabrication system of the two-photon IH process is similar to that of the super-IH process except for a laser source. In the fabrication system of the two-photon IH process, a mode-locked Ti: sapphire laser (wavelength, 710 nm; repetition, 82 MHz; pulse width, 130 fs) is used, because extremely high optical density is required for generating the two-photon absorption.

The two-photon IH process allows the fabrication of 3D microstructures directly from 3D CAD models. Fig. 9 (a)-(d) demonstrate SEM images of complicated 3D microstructures. The model of the microrobot (16 μm x 13 μm x 28 μm) and The micro V sign (10.4 μm x 10.4 μm x 21 μm) were solidified from the bottom to the top at an interval of 250 nm along the optical axis. The micro beetle and micro locomotive are fabricated in 20 minutes. These results clearly demonstrate the high efficacy of the two-photon IH process for fabricating 3D microstructures with submicron resolution.

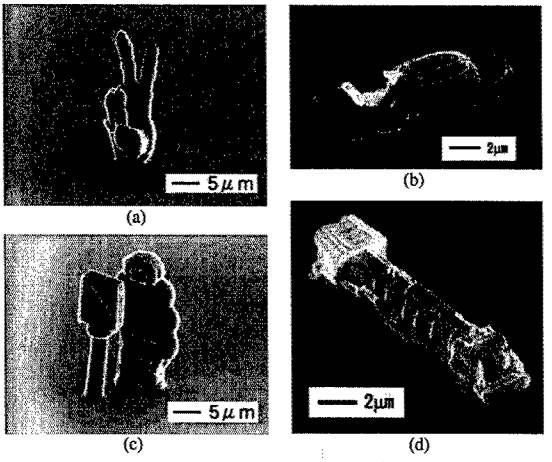

(a) (b) (c) (d)

Fig. 9 3D microstructures made by two-photon IH process
(a) Micro V sign model (b) Micro beetle model
(c) Micro robot model (d) Micro locomotive model

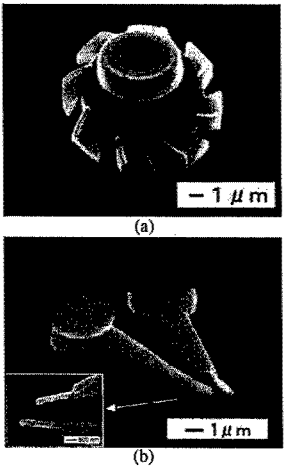

(a) (b)

Fig. 10 Movable micromachins made
by two-photon IH process
(a) Microturbine (b) Nanotweezers

Movable microstructures were also fabricated by using the direct laser writing method shown in Fig. 7. As shown in Fig. 10, various types of micromechanisms including microturbine, microgear train, and nanotweezers were successfully fabricated. The microturbine (external diameter, 14 μm) shown in Fig. 10 (a) was fabricated in only 13 minutes. The probe diameter of the nanotweezers (Fig. 10(b)) is 250 nm. These results demonstrate that two-photon IH process allows the rapid manufacturing of micro/nano machines.

In recent years, the two-photon IH process has been widely used to make complicated 3D microdevices such as photonic crystals and micromechanical components [16, 17]. We have developed optically driven micromachines by using the direct writing of movable micromechanisms. Our micromachines are driven by using a laser scanning manipulation technique [15]. We have already fabricated several types of light-driven micromachines such as microturbine, micromanipulators and nanotweezers [15, 18, 19]. The light-driven micromachines are promising and powerful tools for MEMS and μ-TAS. Although P. Galajda et al. have also used a two-photon process for making optical rotators in recent years [26], their rotators are simple wire-frame types and only offer rotary motion with continuous irradiation of light.

Multi-polymer IH process

We have developed a novel microstereolithography method for producing a hybrid structure using multiple photocurable polymers [5]. This method named "Multi-polymer IH process" has the potential to provide all-polymer functional microdevices. To confirm the validity of the multi-polymer IH process, we constructed a simple fabrication system with a single tank to store multiple kinds of photocurable polymers. The fabrication process is illustrated in Fig. 11. In this case, a 3D microstructure is formed with the polymer A, and then particular layers are formed with the polymer B. Each layer is leveled using a squeegee. By changing photocurable polymers layer-by-layer, a 3D structure consisting of multiple photocurable polymers can be easily formed.

As an example of an all-polymer microdevice, we fabricated several optical waveguides

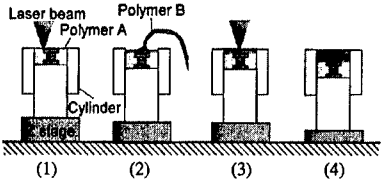

Fig. 11 Fabrication process of Multi-polymer IH process

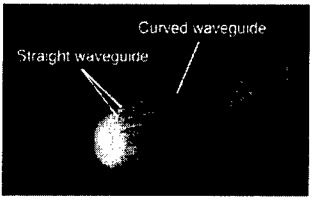

Fig. 12 Optical waveguides made by Multi-polymer IH process

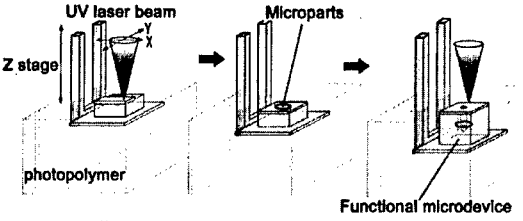

Fig. 13 Fabrication process of Hybrid-IH process.
Functional microdevices are produced without bonding process.

with two kinds of photopolymer having different refractive indexes. Fig.12 shows a prototype of the straight waveguides and a curved waveguide. The width of the core was about 150 μm. The clad and core were made of a low refractive index polymer (n: 1.51) and a high refractive index polymer (n: 1.55), respectively. Both photopolymers are transparent to visible and near-IR light. To verify the performance of the waveguide, we measured the propagation loss of a straight waveguide by using the prism-coupling method with an He-Ne laser. The propagation loss of the waveguide was about 14 dB/cm.

Hybrid IH Process

Another approach to make functional microdevices is to integrate existing elements such as actuators and sensors into a polymeric microstructure. To perform the integration of microparts, we have developed a simple method named "Hybrid-IH process" [3]. The fabrication process of the hybrid-IH process illustrates in Fig. 13. Microparts such as microactuators and membranes are inserted in a polymeric microstructure during the fabrication process. Unlike conventional micromachining techniques, since this process doesn't need additional bonding process, leak-free packaging is easily realized. This process is widely used to make transparent, functional polymer microdevices. We have utilized this process to fabricate micro chemical devices such as micropump [4], microvalves [4] and microconcentrators [3]. In the following chapter, we introduce the micro chemical devices fabricated by using the hybrid-IH process.

BOCHEMICAL IC CHIP

Concept of Biochemical IC chip

The authors have been conducting unique biochemical micro devices named "Biochemical IC" proposed by Ikuta et al. in 1994 [20]. This device originally named "MIFS (Micro Integrated Fluidic System)" contains both miniaturized fluidic circuits made of polymer and silicon circuits in one chip. Although the concept for miniaturization of chemical systems on a chip seems similar to μ-TAS and Lab-on-a-chip, the biochemical IC differs from these chips in various meanings.

Fig. 14(a) shows basic concept of the biochemical IC consisting of 3D micro fluidic channels (upper part) fabricated by the IH process and electric parts (lower part) made by silicon process. Fig. 14(b) shows the modular IC concept of "Biochemical LSI" which satisfies more complicated capability at higher level. [2, 27]. The biochemical IC has the following features in comparison with other micro chemical devices.

1) Modular device architecture
2) 3D micro integrated fluidic system
3) Containing micro fluid driving devices
4) Hybrid structure of polymer, silicon and other materials
5) User assembled chip-set family
6) Wearable/implantable applications

This biochemical IC is based on modular IC concept similar to the today's IC/LSI family (C-MOS/TTL). Each biochemical IC chip in a disk (or cell) shape contains different functional devices such as multiple micro valves, pumps, chemical concentrators and micro reactors. Users can construct their own biochemical systems by using several types of biochemical IC chips. Since active fluidic devices such as pumps and valves are miniaturized in chips, the biochemical IC chips will be applied to wearable and implantable microdevices unlike general μ-TAS and lab-on-a-chip.

Prototypes of Biochemical IC chips and experimental verification

By using the hybrid-IH process, we have already developed several types of biochemical IC chips including a reactor [21], concentrator [3], homogenizer [22] and active valve and micro pump [4]. In this section, we present fluid driving chips such as pump and active switching valve.

Fig. 15 (a) shows a prototype of a micropump chip (size: 14 x 14 x 3.0 mm) containing three micropumps driven by shape memory alloy (SMA) actuators. Each pump designs are reciprocating pumps, consisting of two check valves, a deformable chamber and a SMA actuator as shown in Fig. 15 (b). Pump rate for water are in the order of 10 μl/min.

Fig. 16 (a) shows a prototype of a switching valve chip to select direction of flow dynamically. This valve chip is actuated by two SMA actuators as shown in Fig. 16(b). This valve design is one inlet-two outlet connection valve, consisting of two silicone rubbers as valves and SMA actuators. The switching time in active phase was better than 0.5 seconds and the response time of the opposite way in the passive phase was about 2 seconds.

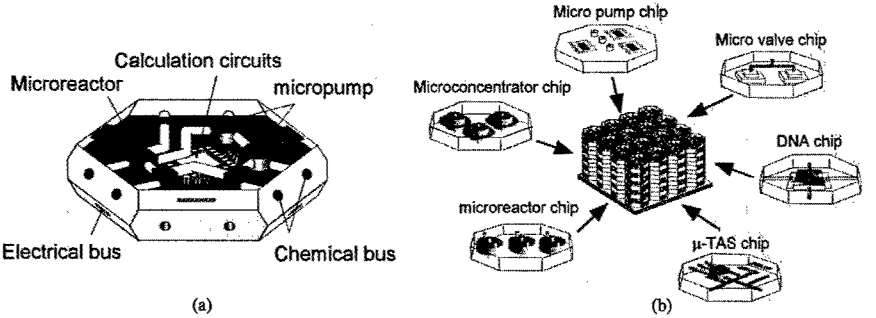

Fig. 14 Basic concepts of Biochemical IC chip and Biochemical LSI
(a) Bicochemical IC chip (b) Biochemical LSI

To demonstrate the validity of these chips, a simple experiment of neutralized reaction using sodium hydroxide and phenolphthalein was demonstrated. Fig.17 (a) shows an experimental setup using biochemical IC chips. The first upper layer is a micro pump chip to supply sodium hydroxide through the inlet. The second layer is a micro reactor chip. The third layer is a micro switching valve chip to switch to another outlet. The fourth layer is a connector chip. Fig. 17 (b) shows biochemical IC chips held in a holder unit. Each chip is connected with thin silicone rubber films, and held by spring force. Our original coupling method named "silicone rubber coupling" enables good sealing under high pressure (>400 kPa) [28, 29].

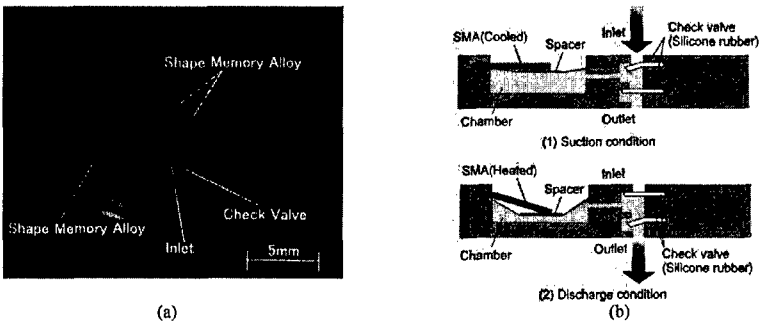

Fig. 15 Micropump chip (a) Prototype (b) Operation principle

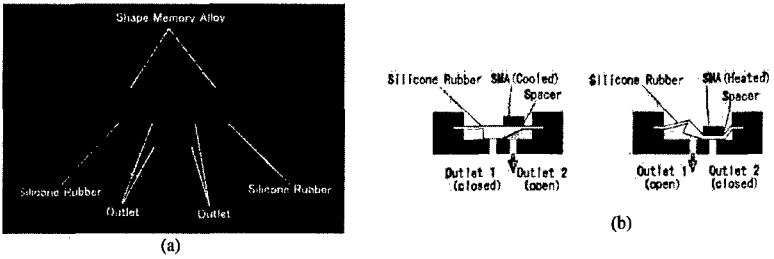

Fig. 16 Switching valve chip (a) Prototype (b) Operation principle

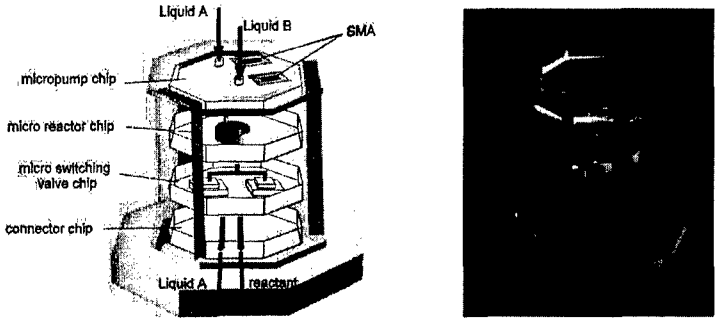

Fig. 17 Experimental setup for neutralized reaction using biochemical IC chips
(a) Schematic diagram (b) Biochemical IC chips held in a holder unit

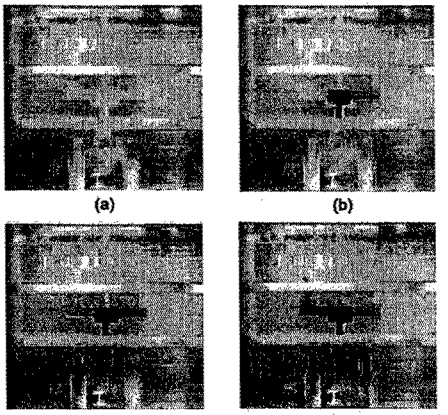

Fig. 18 Experimental results of neutralized reaction using biochemical IC chips
(a) Before neutralized reaction (b) After neutralized reaction
(c) Flow through left outlet (d) Flow changed to right outled

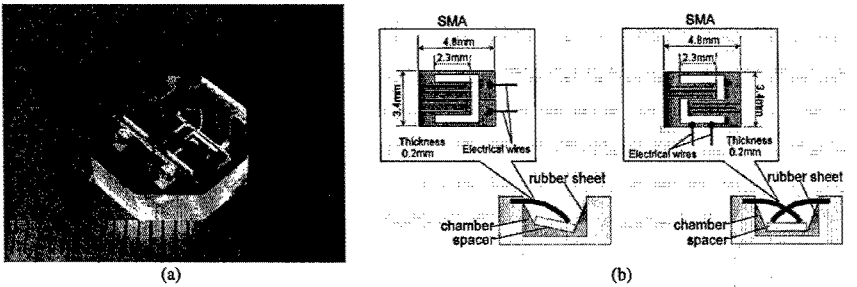

Fig. 19 High-performance micropump chip applicable to liquids and gases
(a) Prototype (b) Modification of SMA cantilevers

Fig.18 is the sequential photos for the demonstration while the neutralized reaction is proceeding in transparent biochemical IC chips. Phenolphthalein and sodium hydroxide were supplied by using the micropump chips, and then they were mixed in the reactor chip. Finally, the mixed reagent was successfully divided into two outlets by using the switching valve chip. The experiments indicates the validity of the modular concept of the biochemical IC chips.

Recently, we have developed a high performance micropump chip that can flow not only liquids but also gases (12 μl/min, 25kPa for water, 11 μl/min., 5 kPa for air) [30]. Fig. 19 (a) shows a prototype of the micropump chip. Two micropumps are included in a chip. To achieve such high performance, we improved the design of SMA actuators, check valves and chamber. The modification of the SMA actuators are illustrated in Fig. 19 (a). The SMA cantilevers can push down the spacer stably compared to the former design shown in Fig. 15.

Cell-free protein synthesis by using biochemical IC chips

Cell-free protein synthesis is one of key technologies in post genome research and tailor made examination. We have first demonstrated cell-free protein synthesis from DNA by using biochemical IC chips [23]. A luminous protein of firefly called "Luciferase" was synthesized

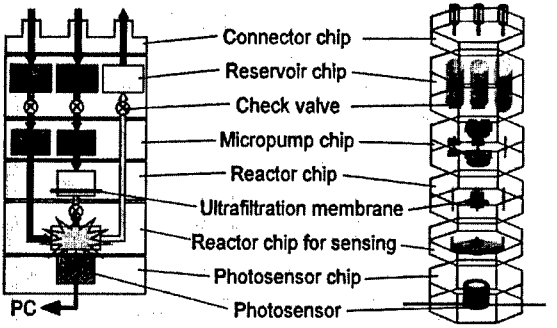

Fig. 20 Biochemical IC chip-set with a built-in micropump chip for cell-free protein synthesis

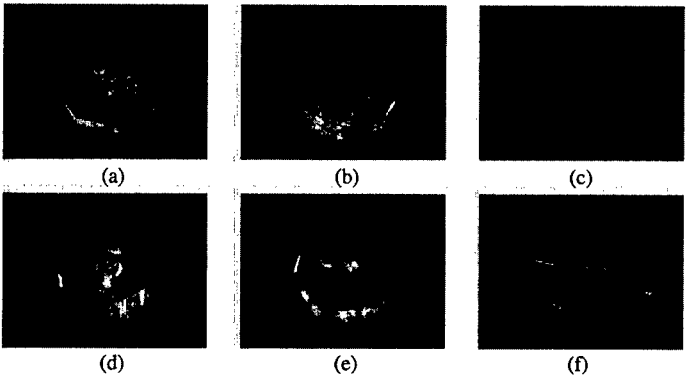

Fig. 21 Prototypes of Biochemical IC chips (a) Connector chip (b) Reservoir chip (c) Micropump chip (d) Reactor chip (e) Reactor chip for sensing (f) Photosensor chip

without living cells in 8 hours. In the first demonstration, however, we used external pumps to supply reagents. Recently, we succeeded in developing a micropump chip for cell-free protein synthesis [24]. Since the micropump chip used new check valves with double silicone rubber films, it has sufficiently long lifetime for protein synthesis.

Fig. 20 shows the basic design of biochemical IC chip-set for cell-free protein synthesis. This synthesis system is constructed with six types of biochemical IC chip: connector chip, reservoir chip, micropump chip, reactor chip, reactor chip for sensing, photosensor chip. The micropump chips supply reagents from the reservoir chips to the reactor chip. The reactor chip includes an ultrafiltration membrane to synthesize protein, which is then introduced into the reactor chip for sensing with the micropump chip. The protein is optically detected at the detection chip, which has a built-in a avalanche photodiode, by mixing an assay reagent for luminescent detection. Fig. 21 shows the prototype chips. By using the hybrid-IH process, micropart such as an ultrafiltration membrane, silicone rubber, SMA actuator, are hybridized with a polymeric structure.

To perform the experiments, each chip is set in a holder unit. Since each chip is connected with thin silicone rubber films by using our proposed silicone rubber coupling method [28, 29], dead volume is minimized without any leakage. Fig. 22 shows the entire experimental setup for

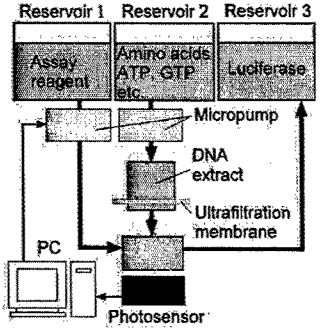

Fig. 22 Experimental setup for cell-free protein synthesis

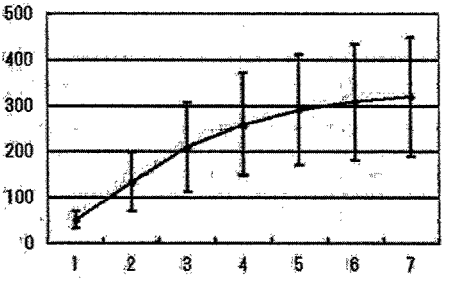

Fig. 23 Experimental result of cell-free protein synthesis

DNA-originated cell-free protein synthesis. Solution A (DNA, S30 Premix, Amino acid complete, SW) and solution B (S30 Extract) are mixed in the reactor and synthesized. Luciferase is filtered through the ultrafiltration membrane (YM100). An assay regent is mixed to measure the protein concentration via luminous intensity. Fig. 23 shows an experimental result of Luciferase synthesis. We succeeded in synthesizing protein in 7 hours by using the built-in micropumps. The palm-top protein synthesis device is promising tools for not only tailor made medicine but also bioscience researches.

CONCLUSIONS

We have developed several types of microstereolithography such as the IH process, the super-IH process, the two-photon IH process and the hybrid IH process. The resolution of the microstereolithography techniques are scalable from 100 μm to 100 nm. By using these techniques, we can fabricate functional polymer microdevices such as the biochemical IC chips as well as micro/nano machines such as microgears and nanotweezers. We have already demonstrated the validity of our modular approach of biochemical IC chip with chemical and biochemical experiments such as cell-free protein synthesis. In the near future, the biochemical IC chips should contribute not only the biomedical applications but also basic science.

ACKNOWLEDGMENTS

This research was supported by Grant-in-Aid for Scientific Research (A) and Grant-in-Aid for Young Scientists (B) from the Ministry of Education, Culture, Science and Technology, and a research grant from the Japan Society for the Promotion of Science (Research for the future program: JSPS-RFTF-96I00103). The authors thank to Mr. K. Hirowatari, Mr. T. Ogata, Mr. S. Kojima, Mr. T. Ninagawa, Mrs. Y. Nakatani, Mr. M. Ogawa, and Mr. S. Ito for their assistance in experiments.

REFERENCES

1. K. Ikuta and K. Hirowatari, Proc. of IEEE International Workshop on Micro Electro Mechanical System (MEMS 93), 42-47 (1993).
2. K.Ikuta, T.Ogata, M. Tsuboi, S. Kojima, Proc. of MEMS 96, pp.301-306 (1996).
3. K.Ikuta, S.Maruo, T.Fujisawa, A.Yamada, Proc. of the IEEE International Conference on Micro Electro Mechanical Systems (MEMS 99), pp.376-381 (1999).
4. K.Ikuta, T.Hasegawa, T.Adachi and S.Maruo, Proc.of MEMS 2000, pp.739-744 (2000).
5. S.Maruo and K.Ikuta, Proc. of MEMS 2001, 151-154 (2001).

6. T. Takagi and N. Nakajima, Proc. of MEMS 93, 173-178 (1993).
7. A. Bertsch, S. Zissi, J. Y. Jezequel, S. Corbel and J. C. Andre, Microsystem Technologies 3, 42-47 (1997).
8. K. Ikuta, S. Maruo and S. Kojima, Proc. of MEMS 98, 290-295 (1998).
9. S. Maruo and K. Ikuta, Applied Physics Letters **76**, 2656-2658 (2000).
10. S. Maruo and K. Ikuta, Sensors and Actuators A **100**, 70-76 (2002).
11. S. Maruo, O. Nakamura and S. Kawata, Optics Letters **22**, 132-134 (1997).
12. S. Maruo and S. Kawata, Journal of Microelectromechanical Systems **7**, 411-415 (1998).
13. S. Maruo and K. Ikuta, Proc. of 10th International Conference on Solid-State Sensors and Actuators (Transducers 99), 1232-1235 (1999).
14. S. Maruo, K. Ikuta and H. Korogi, Proc. of SPIE **3937**, 106-112 (2000).
15. S.Maruo and K.Ikuta, Proc. of MEMS 2001, 594-597 (2001).
16. B. H. Cumpston, S. P. Ananthavel, S. Barlow, D. L. Dyer, J. E. Ehrlich, L. L. Erskine, A. A. Heikal, S. M. Kuebler, I. -Y. S. Lee, D. McCord-Maughon, J. Qin, H. Reckel, M. Rumi, X. Wu, S. R. Marder and J. W. Perry, Nature **398**, 51-54 (1999).
17. S. Kawata, H. B. Sun, T. Tanaka, and K. Takada, Nature **412**, 697-698 (2001).
18. S. Maruo, K. Ikuta and H. Korogi, Proc. of the IEEE Conference on Nanotechnology (IEEE-NANO 2001), 507-512 (2001).
19. S. Maruo, K. Ikuta and H. Korogi, Proc. of Micro Total Analysis Systems 2002 (μ-TAS 2002), 937-939 (2002).
20. K. Ikuta, K. Hirowatari and T. Ogata, Proc. of MEMS 94, 1-6 (1994).
21. K. Ikuta, S. Maruo, Y. Fukaya and T. Fujisawa, Proc. of MEMS 98, 131-136 (1998).
22. K. Ikuta, Y. Sasaki, H. Maegawa, S. Maruo and T. Hasegawa, Proc. of μ-TAS 2002, 745-747 (2002).
23. K. Ikuta, A. Takahashi and S. Maruo, Proc. of MEMS 2001, 455-458 (2001).
24. K. Ikuta, A. Takahashi, K. Ikeda and S. Maruo, Proc. of μ-TAS 2002, 37-39 (2002).
25. K.D. Wise and K. Najafi, Science **254**, 1335-1342 (1991).
26. P. Galajda and P. Ormos, Appl. Phys. Lett. **78**, 249-251 (2001).
27. K. Ikuta, Proc. of Artificial Life V, 17-24 (1996).
28. T. Hasegawa and K. Ikuta, Proc. of μ-TAS 2001, 377-378 (2001).
29. T. Hasegawa and K. Ikuta, Proc. of μ-TAS 2002, 694-696 (2002).
30. K. Ikuta, T. Hasegawa and T. Adachi, Proc. of Transducers 01, 916-919 (2001).

Mat. Res. Soc. Symp. Proc. Vol. 758 © 2003 Materials Research Society LL5.7

Computational Design, Freeform Fabrication and Testing of Nylon-6 Tissue Engineering Scaffolds

Suman Das[1], Scott J. Hollister[2], Colleen Flanagan[2], Adebisi Adewunmi[1], Karlin Bark[1], Cindy Chen[1], Krishnan Ramaswamy[1], Daniel Rose[1], Erwin Widjaja[1]
[1]Mechanical Engineering Department
[2]Biomedical Engineering Department
University of Michigan
2350 Hayward St.
Ann Arbor, MI 48109-2125

ABSTRACT

Advanced and novel fabrication methods are needed to build complex three-dimensional scaffolds that incorporate multiple functionally graded biomaterials with a porous internal architecture that will enable the simultaneous growth of multiple tissues, tissue interfaces and blood vessels. The aim of this research is to develop, demonstrate and characterize techniques for fabricating such scaffolds by combining solid freeform fabrication and computational design methods. When fully developed, such techniques are expected to enable the fabrication of tissue engineering scaffolds endowed with functionally graded material composition and porosity exhibiting sharp or smooth gradients. As a first step towards realizing this goal, scaffolds with periodic cellular and biomimetic architectures were designed and fabricated using selective laser sintering in Nylon-6, a biocompatible polymer. Results of bio-compatibility and *in vivo* implantation studies conducted on these scaffolds are reported.

INTRODUCTION

Tissue engineering [1, 2] is an interdisciplinary field that combines engineering and life sciences to develop techniques that enable the restoration, maintenance or enhancement of living tissues and organs. A majority of these techniques utilize three-dimensional scaffold structures composed of natural or synthetic polymers [3-10]. These scaffold structures are typically endowed with complex internal architecture, channels and porosity that provide sites for cell attachment and proliferation, as well as for conveying cells, growth factors and biomolecular signals to promote tissue regeneration at an implantation site. The composition of most tissue engineering scaffolds is such that the scaffolding material is biodegradable, and it erodes away over time after implantation, eventually being replaced by newly formed tissue.

Recently, solid freeform fabrication (SFF) [11] methods have been employed for fabricating bioimplants and tissue engineering scaffolds [12-20]. In principle, SFF methods are capable of constructing three-dimensional scaffolds with complex architectures incorporating multiple, functionally graded bio-materials and porosity. The overall goal of our research is to develop homogenization theory based computational design techniques and laser sintering based freeform fabrication methods for constructing such heterogeneous tissue engineering scaffolds using multiple biomaterials. This goal is to be achieved via the following three research objectives. First, computational techniques are being developed to locally optimize scaffold architecture, material composition and mechanical properties yielding three-dimensional digital representations of functionally tailored scaffolds. Second, solid freeform fabrication techniques

based on laser sintering are being developed that can construct such scaffolds using multiple biomaterials possibly with the incorporation of drugs or bioactive factors *in-situ*. Finally, mechanical and biological (*in vivo, in vitro*) testing and CT/MRI image analysis is being conducted to evaluate structure and function of both scaffold materials and regenerate tissue. As a first step towards realizing this goal, we have chosen to investigate monolithic Nylon-6 as a scaffold material for tissue engineering applications.

METHODS AND MATERIALS

Scaffold Design Methods

Scaffold design requirements should be addressed on both macroscopic and microscopic scales. On the microscopic scale (100 μm-1 mm), the scaffold internal architecture must fulfill temporary tissue function, enhance tissue regeneration and vascularization, and facilitate nutrient/biofactor delivery. On the macroscopic scale (> 1 mm), the scaffold's external shape must replicate human anatomy. These two scales must be integrated to produce a single design that can be embodied in a format appropriate for SFF. In our studies, we have used both periodic cell-based designs and biomimetic designs to construct scaffolds using SLS.

Periodic Cell-Based Designs

In periodic cell-based designs, a unit cell with specific microstructure is repeated to create an entire scaffold. This technique can be used in combination with topology optimization methods to design microstructures with effective physical properties matching native tissue properties. Additional details of homogenization theory based topology optimization techniques for bioimplants are available elsewhere [21,22]. Figures 1a,b show 8 mm cubic and 8 mm diameter cylindrical periodic scaffolds with 800 μm orthogonal channels and 1200 μm pillars that were designed using such optimization methods. These designs result in scaffolds with a pore or void fraction of approximately 53.7%.

Biomimetic Designs

The design of biomimetic scaffolds relies on micro-CT, micro-MRI or confocal microscopy data to assemble scaffold architectures. In biomimetic designs, scaffolds mimic natural tissue structure and seek to replicate all aspects of tissue structure and function. We used micro-CT derived architecture of human proximal femur trabecular bone as the basis for creating biomimetic scaffolds in Nylon-6. Figures 1c,d show a volumetric rendering of human trabecular bone micro-CT data along with a faceted representation appropriate for use in SFF machines.

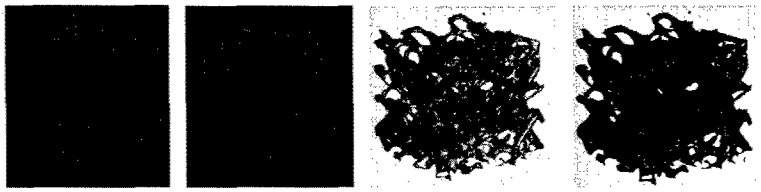

Figure 1. (a) Cubical and (b) Cylindrical periodic scaffold architectures. (c) Volumetric rendering of trabecular bone microstructure derived from micro-CT image data for biomimetic design. (d) Corresponding triangular facet data for SFF.

Scaffold Fabrication

The choice of Nylon-6 as the material for fabricating scaffolds during this study was prompted by Risbud and Bhonde's recent data [9] on the biocompatibility of polyamide 6. Their aim was to develop polyamide 6 membranes blended with gelatin (a natural polyamide) and chondroitin sulfate (a biopolymer) using the phase precipitation method and to evaluate their *in vitro* biocompatibility. A large collection of biocompatibility test data demonstrated that such polyamide 6 composite membranes are biocompatible and prospective candidates for tissue engineering. Several other studies have documented the use of Nylon in suture materials and for dialysis membranes [23], in burn dressings [24], and as cell culture substrata for a variety of cell types [25-27].

Two types of Nylon-6 powders were used in our study. Honeywell Capron 8202 (10-100 μm particle size) was used for fabricating periodic cell-based designs while Atofina Orgasol 1002 ES4 (38-42 μm particle size) was used for fabricating biomimetic structures as well as disks for biocompatibility testing. These powders were processed in a Sinterstation 2000 commercial SLS machine using 200º C preheat, 7 Watts laser power, 49.5 in/s scan speed and 100 μm layer thickness. Porous specimens of both cylindrical and cubical periodic geometry (figure 1), as well as biomimetic architectures (figure 3b) derived from micro-CT data were fabricated. Solid disks (11 mm diameter, 2 mm thick) were also fabricated for biocompatibility tests. The parts were cleaned post-process by simple brushing and careful removal of powder trapped inside the porous channels where necessary.

Biocompatibility Testing

In vitro biocompatibility was determined using the CellTiter 96® AQ_{ueous} One (Promega Corp, Madison, WI) assay, which provides a measure of cell viability related to the level of mitochondrial respiration. This assay is analogous to the MTT assay commonly utilized in biocompatibility studies [28], with the exception that the colored product produced is water soluble [29]. The cells utilized in this study were porcine bone marrow stromal cells (isolated from marrow extracts) and were limited to passage 5 through 8. Additional details of the biocompatibility test procedures are available elsewhere [30].

RESULTS AND DISCUSSION

Figure 2a shows an 8 mm cube with 800 μm channels and 1200 μm pillars fabricated in Nylon-6 by SLS. These specimens will be used for conducting uniaxial tests in unconfined

compression inside a micro-CT machine. Complete 3D strain fields in the scaffold under testing will be computed by comparing images before and after deformation. These tests will provide effective failure stress and local strain values at failure. The results of these studies will be published elsewhere [31]. Figure 2b shows an 8 mm diameter, 6 mm high cylinder with 800 μm channels and 1200 μm pillars fabricated in Nylon-6 by SLS. This scaffold geometry was designed for surgical implantation and histology assessment. Figure 2c shows implantation of cylindrical scaffolds into a Yucatan minipig mandible. These scaffolds were subsequently removed after 6 weeks and assessed for mineralized tissue formation by micro-computed tomography (micro-CT). Figure 3a shows a volumetric rendering of the micro-CT scan conducted on the removed scaffold, showing the ingrowths of mineralized bone tissue into the pore channels of the scaffold. Quantitative image analysis of the micro-CT data revealed that new bone tissue occupied 43.2% of the pore volume. This value is consistent with the range of pore occupation fractions (50.3-65%) attained with hydroxyapatite scaffolds of identical pore geometry implanted for the same 6 week time period at the same site [32]. The lower value of pore occupation for Nylon-6 is likely due to loosely bonded particles on the pore walls causing an adverse cellular response as discussed below, although further experiments are yet to confirm this hypothesis.

Biomimetic architectures derived from CT/MRI data of bony structures are difficult to fabricate by SFF as resolved tissue structures (10-100 μm) are often smaller than the resolution of the SFF machine. Alternatively, these structures can be scaled up and then fabricated to have optimal porosity for bone tissue regeneration (typically 300-1200 μm) [32] while retaining biomimetic architecture. Shown in figure 3c,d are the volumetric rendering of a section of human proximal femur trabecular bone micro-CT data and the corresponding Nylon-6 replica scaled 4X fabricated using SLS. In addition to biological testing of these scaffolds by implantation, we will visualize 3D deformation and failure modes under compression during micro-CT and compare them with failure modes of real bone. These results will be published elsewhere [31].

Biocompatibility tests conducted on the SLS fabricated Nylon-6 disks and their leachable products indicated that cell viability was considerably higher for the cells subjected to the conditioned media containing leach-out products. The results indicated that neither early nor late leaching products were detrimental to the cells. However, cell viability relative to controls dropped when the cells were in direct contact with the media in the presence of disks (CoCulture group). While the level of cell viability was slightly less than 70%, on average, the result still indicates a relatively low level of cytotoxicity. One possible explanation for the reduction in cell viability in the CoCulture group is that the solid free form fabrication method utilized, SLS, resulted in some residual Nylon-6 particulates that were not fully bonded to the construct. This particulate matter may have initiated a detrimental cellular response in the CoCulture group. Particulate matter has been shown to cause osteolysis *in vivo* [33] although this is yet to be confirmed experimentally. The results are still very promising as the fabrication and post-fabrication preparation for biological usage can be further refined and improved. Further details on biocompatibility testing results can be found elsewhere [30].

Figure 2. (a) 8mm cubic periodic scaffold fabricated in Nylon-6. (b) 8mm diameter, 6mm high periodic cylindrical scaffold fabricated in Nylon-6. (c) Scaffold implantation into Yucatan minipig mandible.

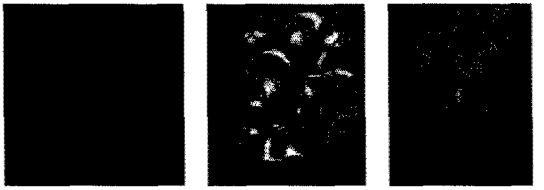

Figure 3. (a) Volumetric rendering of scaffold micro-CT scan. (b) Volumetric rendering of human trabecular bone micro-CT data. (c) 4X scaled replica fabricated in Nylon-6 by SLS (scale in mm).

CONCLUSIONS

This work demonstrates an approach combining computational design, freeform fabrication and testing of tissue engineering scaffolds. Scaffolds with periodic and biomimetic internal architecture were fabricated in Nylon-6 using SLS. Implantation and subsequent histology of scaffolds show presence of regenerate mineralized tissue, consistent with pore occupation fractions attained using monolithic hydroxyapatite scaffolds. The biocompatibility tests show that Nylon-6 scaffolds fabricated via SLS support cell viability quite well. Biocompatibility may be improved by better methods of post-fabrication cleaning or treatment of SLS fabricated scaffold constructs to eliminate loosely bonded polymer particles. Although not bioresorbable, such Nylon-6 scaffolds are biocompatible and could serve as drug/cell delivery devices as well as models for future work on bioresorbable polymers. This work sets the stage for construction of functionally tailored tissue scaffolds in a single step via SLS of multiple materials. Scaffolds incorporating graded architectures with multiple biopolymers and their composites with calcium phosphate ceramics are being explored using a newly designed multiple powder deposition system.

REFERENCES

1. R. Langer and J. Vacanti, Science, **260**, 920-926 (1993).
2. L. G. Griffith and G. Naughton, Science, **295**, 1009-1014 (2002).
3. A. Rothen-Weinhold et al., Europ. J. Pharm and Biopharm, **48**, 113-121 (1999).
4. F. Stancari et al., Quintessenz (Germany), **51**(1), 47-52 (2000).
5. S. D. Putney, Pharmaceutical News, **6**(2), (1999).
6. T. Furukawa, Y. Matsusue, T.Yasunaga, Y. Shikinami, M. Okuno and T. Nakamura, Biomaterials, **21**, 889-898 (2000).

7. C. Mauli Agarwal and Robert B. Ray, J. Biomed. Mater. Res., **55**, 141-150 (2001).
8. L. G. Griffith, Acta Materialia, **48**, 263-277 (2000).
9. M.V. Risbud and R.R. Bhonde, J. Biomater. Sci. Polymer Edn., **12**(1), 125-136 (2001).
10. A.G. Stamboulis et al., Adv. Eng. Mater., **4**(3), 105-109 (2002).
11. J.J. Beaman et al, *Solid Freeform Fabrication: A New Direction in Manufacturing*, Kluwer Academic Publishers, 1997.
12. L.V. McIntyre, H. Greisler, L. Griffith, P.C. Johnson, D.J. Mooney, M. Mrksich, N. Parenteau and D. Smith, in *WTEC Panel Report on Tissue Engineering Research*, 2002, pp. 11.
13. S. Yang, K. Leong, Z. Du and C. Chua, Tissue Engineering, **7**, 679-689 (2001).
14. G. T-M. Chu et. al., *Mat. Res. Soc. Symp. Proc.*, **542**, 119-123.
15. J. E. Smay, J. Caesarano III and J. A. Lewis, Langmuir, **18**, 5429-37 (2002).
16. R. A. Giordano et al., J. Biomater. Sci. Polym. Ed., **8**(1), 63-75 (1996).
17. G. Lee, J.W. Barlow, W.C. Fox and T.B. Aufdermorte, *Solid Freeform Fabrication Symp. Proc.*, 15-22 (1996).
18. J. M. Taboas et al. (in press), Biomaterials.
19. I.W. Zein et al., Biomaterials, **23**(2), 1169-1185 (2002).
20. L. Weiss, et al., U.S. Patent No. 6,143,293.
21. S. J. Hollister and N. Kikuchi, Advances in Bioengineering, American Society of Mechanical Engineers, Bioengineering Division (Publication) **BED 28**, 403-404 (1994).
22. S.J. Hollister, R.D. Maddox, and J.M. Taboas, Biomaterials, **23**, 4095-4103 (2002).
23. S. Yamashita, A. Mochizuki, T. Nakazaki, Y. Seita, J. Sawamoto, F. Endo, N. Yui, N. Ogata, K. Kataoka, T. Okano and Y. Sakurai, ASAIO J., **42**, 1019 (1996).
24. P. Bugmann, S. Taylor, D. Gyger, A. Lironi, B. Genin, A. Vinda, G. La Scala, J. Birraux, C. Le Coultre, Burns, **24**, 609-612 (1998).
25. B. A. Naughton, R. A. Preti and G. K. Naughton, J. Med., **18**, 219 (1987).
26. G. Catapano, M. C. Di Lorenzo, C. Della Volpe, L. De Bartolo and D. Migliaresi, J. Biomater. Sci. Polymer Edn., **7**, 1017 (1996).
27. J. Gerlach, P. Stoll, N. Schnoy and E. S. Bucherl, Int. J. Artif. Organs, **13**, 436 (1990).
28. A. Doyle, J. B. Griffiths and D. G. Newell (Eds.), *Cell and Tissue Culture: Laboratory Procedures*, John Wiley and Sons, New York, 1998.
29. Promega Corporation, Technical Bulletin No. 245.
30. Suman Das et al, Rapid Prototyping J.,**9**(2), 43-49 (2002).
31. Suman Das et al (in press), J. Mater. Res (2003).
32. Scott J. Hollister (private communication).
33. J. J. Jacobs, K.A. Roebuck, M. Archibeck, N. J. Hallab and T.T., Clinical Orthopedics and Related Research, **393**, 71–77, 2001.

ACKNOWLEDGEMENTS

The authors gratefully acknowledge Honeywell Plastics for a generous donation of Nylon-6 powder.

AUTHOR INDEX

SUBJECT INDEX